



The
University
Of
Sheffield.

Assessment of TPUs For Use in The Laser Sintering Process

By:

Piotr J. Gęca

A thesis submitted in partial fulfilment of the requirements for the degree of
Doctor of Philosophy

The University of Sheffield
Faculty of Engineering
Department of Mechanical Engineering

13/10/2016

Abstract

Additive Manufacturing (AM) technologies and especially the Laser Sintering (LS) systems have made an enormous impact on the manufacturing market in the last decade and their adoption continues to grow. Currently, the market of sinterable polymer powders is heavily dominated by polyamides (PAs), which fail to address all the possible LS application niches. Thermoplastic Elastomers (TPEs) and more specifically Thermoplastic Polyurethanes (TPUs) have the potential of broadening LS applications, by offering alternative, rubber-like properties to manufactured parts.

Laser Sintering is a highly demanding process in regards to materials' thermal properties, as well as bulk properties of its powder form. In the first part of project we assessed TPU powder's compatibility with the Formiga P100 LS system. We found that the greatest obstacle to powder's safe use was its poor ability to flow and the resulting incompatibility with the powder deposition system. Improvement of flow properties was attempted by use of annealing process as well as addition of flow agent (FA). We found neither solution to produce satisfactory bulk properties, but we note that higher levels of FA are likely to increase the additive's effectiveness.

In the second part of the project we assessed the performance of twelve diverse batches of TPU, to form a better understanding of factors influencing the mechanical performance of sintered parts. Based on a new paradigm, the sintering process was split into issues of particle coalescence and densification. We found that the particle size and melt viscosity had a strong effect on the strength of interparticle bonds formed in a limited sintering time. When long sintering time was simulated by oven-sintering, we found that parts' density was chiefly determined by powders' ability to cross over into closed-pore densification stage. Powders with Specific Surface Area of $90\text{m}^2/\text{kg}$ and less were unable to densify and formed a stable open-pore structure instead. Avoiding this threshold condition is the first priority in designing future powder batches.

Acknowledgements

Foremost, I want to thank my supervisor and thesis advisor, Dr. Candice Majewski for her help and guidance throughout the project. Her encouraging words, high spirit and trust built my confidence as a researcher. I also want to thank Prof. Patrick Fairclough and other academics whose advice was invaluable when grasping new knowledge. In addition, my thanks to the technical staff of the laboratories, whose practical knowledge enabled me to perform my work.

I would like to thank the commercial project supervisor, Dr. Rajan Hollmann, who has shown great hospitality and consideration for my training during visits to Germany and in our communication.

Finally, I want to express my deepest gratitude to my parents, who had always nurtured my thirst for learning. Their unyielding support and hard work was what allowed to me to focus on academia and self-improvement. Without their help, I could not reach this moment. My accomplishments are theirs as well. Thank you.

Table of Contents

List of Figures	i
List of Tables	v
List of Abbreviations and Symbols	vi
1 Project Introduction	1
1.1 Additive Manufacturing Principles and Applications.....	1
1.2 Laser Sintering Technology	3
1.3 Commercial Materials in Laser Sintering	6
1.4 Project Goals	7
1.5 Structure of the Thesis.....	7
2 Literature Review	9
2.1 Polyurethanes and Polyurethane Processing Literature	9
2.1.1 Thermoplastic Polyurethanes Synthesis and Structure.....	9
2.1.2 Annealing Effects in TPU	12
2.2 Polymer Laser Sintering Literature	13
2.2.1 Selected LS Process Parameters.....	13
2.2.2 Selected LS Material Parameters	15
2.3 Bulk Solids Literature.....	18
2.3.1 Bulk Solids Introduction	18
2.3.2 Bulk Solid Flowability Definition	20
2.3.3 Selected Bulk Solid Flowability Measurement Methods.....	22
2.3.4 Selected Factors in Bulk Solid Flowability	26
2.4 Sintering and Coalescence Literature	27
2.4.1 General Sintering Introduction.....	28
2.4.2 Polymer Coalescence Modelling Introduction	30
2.4.3 Viscoelastic Coalescence Modelling.....	32
2.4.4 Densification	38
2.4.5 Discussion	40
2.4.6 Conclusions	42
3 Methodology	43
3.1 Thermal Properties.....	43
3.1.1 Temperature Scan Calorimetry	43
3.1.2 Isothermal Calorimetry.....	44
3.1.3 Thermogravimetry.....	44
3.2 Bulk properties and Handling	45

3.2.1	Moisture Control	45
3.2.2	Powder Annealing	46
3.2.3	Bulk Density Testing.....	48
3.2.4	Static Control	50
3.2.5	Powder Cake Bulk Density.....	51
3.2.6	Particle Size Distribution.....	51
3.2.7	Unconfined Compressive Yield Strength	52
3.3	Linear Regression	53
3.4	Monolayer Specimens Sintering and Testing.....	54
3.4.1	Specimen and Grip Design	54
3.4.2	Monolayer Sintering Process.....	55
3.4.3	Tensile Testing and Measurements	57
3.5	Oven Sintered Tensile Specimens.....	57
3.6	Hot Stage Microscopy.....	59
3.6.1	Introduction to HSM Coalescence Measurements.....	59
3.6.2	HSM Setup and Methodology.....	60
4	Preliminary Studies.....	61
4.1	Thermal Properties of Experimental TPU	61
4.1.1	TPU Formulation.....	61
4.1.2	Features of Typical TPU DSC Signal.....	62
4.1.3	Annealing Peak Emergence	63
4.1.4	Melting and Recrystallization Peak Shift.....	65
4.1.5	Isothermal Crystallisation.....	68
4.1.6	Thermogravimetry.....	69
4.2	Formiga P100 Features and Parameters	70
4.3	Build Failures and Effects of Annealing.....	73
4.3.1	Buils With Virgin Powder	73
4.3.2	Buils With Annealed Powder	75
4.3.3	Discussion of Build Failures and Annealing Effect	76
4.3.4	Comparison to Prior Research	79
4.4	Exposure Parameters Tests.....	80
4.4.1	Study Plan and Experiment Design.....	80
4.4.2	Build Process and Results	82
4.4.3	Conclusions	83
4.5	Preliminary Tensile Properties Study.....	84
4.5.1	Study Plan and Experiment Design.....	84

4.5.2	The Build Process	84
4.5.3	Specimen Testing.....	86
4.5.4	Discussion of Employed Measurements	89
4.5.5	Discussion of Tensile Testing Results	90
4.5.6	Specimen Features and Abnormalities.....	90
4.5.7	Powder Cake Bulk Density.....	94
4.5.8	Conclusions	94
5	Flow Agent Effects Study.....	96
5.1	Study Plan and Experiment Design	96
5.2	Bulk Properties Study	97
5.2.1	Bulk Density	97
5.2.2	Particle Size Distribution.....	98
5.2.3	Unconfined Compressive Yield Strength	99
5.2.4	SEM Imaging	100
5.2.5	Discussion of Aerosil Effects on Bulk Properties	101
5.3	Tensile Specimens Build Process	103
5.3.1	Tensile Specimens Test Results.....	104
5.4	Monolayer Specimens Test Results.....	106
5.5	Comparison of Traditional and Monolayer Test Results	108
5.6	Conclusions.....	110
6	Viscosity and Particle Size Effects Study.....	111
6.1	Study Plan and Experiment Design	111
6.2	Batch Properties.....	111
6.3	DSC Measurements.....	114
6.4	Monolayer Specimens Testing and Analysis	115
6.5	Oven and Hot Plate Sintering Observations	122
6.6	HSM Assessment of Closed Pore Structures.....	125
6.7	HSM Assessment of Melting Temperature.....	129
6.8	Oven Sintering Study.....	132
6.9	Tests on Convex/Concave Voids	135
6.10	Discussion of Results.....	138
6.10.1	Bulk Properties	138
6.10.2	DSC Measurements	140
6.10.3	The Monolayer Study	141
6.10.4	Observations on Open and Closed Pores	145
6.10.5	Observations on Concave Voids	147

6.10.6	Oven Sintered Specimens and Concave Pore Impact.....	147
6.10.7	Bulk Density and Final Part Density.....	149
6.11	Conclusions.....	151
7	Project Conclusions.....	154
7.1	Major Experimental Findings.....	154
7.1.1	MFR and Particle Size Effects.....	154
7.1.2	The Densification Stage Threshold.....	154
7.1.3	Effects of Flow Agents.....	155
7.1.4	Effects of Powder Bed Bulk Density on Part Density.....	155
7.1.5	TPU's Sensitivity to Annealing.....	156
7.2	Recommendations for Future Work and Material Development.....	156
7.2.1	Results Verification on Full Thickness Specimens.....	156
7.2.2	Increased Flow Agent Content Study.....	157
7.2.3	Annealing Effects Study.....	158
8	Appendices.....	159
8.1	Preliminary Tensile Properties Study Data.....	160
8.2	Flow Agent Effects Full Thickness Specimens Data.....	162
8.3	Flow Agent Effects Monolayers Data.....	163
8.4	Viscosity and Particle Size Effects Batches DSC.....	165
8.5	Viscosity and Particle Size Effects Oven Sintered Specimens Data.....	168
8.6	Viscosity and Particle Size Effects Monolayer Data.....	169
8.7	Results of Regression Viscosity and PSD Study Monolayer Data.....	173
9	References.....	175

List of Figures

Figure 1.1: Chart placing Laser Sintering in the context of other Additive Manufacturing processes.	4
Figure 1.2: Schematic of a representative Laser Sintering system and its major components.....	5
Figure 1.3: Flowchart of Laser Sintering process, including pre- and post-build operations.	5
Figure 2.1: Schematic of molecular structure and microstructure of TPU	10
Figure 2.2: Comparison of DSC signals from repeatedly recycled TPU batch, taken from (Plummer et al, 2012).	13
Figure 2.3: Changes to viscosity while melting amorphous (ABS) and semi-crystalline (PA12, PA2200) materials. (Adapted from (Drummer et al, 2010))	16
Figure 2.4: Changes in the specific volume while melting and recrystallizing amorphous and crystalline polymers. (Adapted from (Gibson and Shi, 1997))	17
Figure 2.5: Differential Scanning Calorimetry curve showing the supercooling property of PA12.	18
Figure 2.6: Shape of two flow functions.....	22
Figure 2.7: Schematic of Jenike shear cell tester (From (Schulze, 2007))	23
Figure 2.8: Funnel flow test apparatus, version with 100ml cup for apparent bulk density measurement. (From (D-20)).....	24
Figure 2.9: Copley Scientific BEP2 Angle of repose tester. Angle is measured as a function of the radius of cone's base and height.	25
Figure 2.10: Jagota-Lin model of coalescence, reducing it to three steps. Elastic Adhesion (a), Zipping (b) and Stretching (c) (From (Lin et al., 2001))	36
Figure 2.11: Chart of different modelling issues in polymer laser sintering.	40
Figure 3.1: Rotating drum used for drum-annealing, with the front cap removed. Entire assembly fits inside an oven.....	47
Figure 3.2: Round agglomerates from the drum-annealing process.....	48
Figure 3.3: Tapped bulk density tester.....	50
Figure 3.4: Unconfined Compressive Yield Strength testing of a caked TPU powder specimen.....	53
Figure 3.5: Custom grips used for testing monolayer strip specimens. Black benchmarks indicate the place where strip loses contact with the grip surface.....	55
Figure 3.6: Schematic of powder bed when sintering monolayer specimens.	56
Figure 3.7: Compacted 'green' dogbone and the same specimen after oven sintering.....	59
Figure 3.8: Hot stage microscopy setup during timelapse experiment. Note the aperture in middle of the ceramic stage to allow illumination from underneath.....	60

Figure 4.1: Features of a standard DSC temperature scan on virgin TPU (solid line) and second temperature scan on same sample (dashed line).	63
Figure 4.2: DSC signal from TPU annealed at 110°C for 12hrs to create strong annealing peak B. Annealing also removes peak A visible in the virgin material.	64
Figure 4.3: Evolution of DSC signal with varying annealing time at 90°C.	64
Figure 4.4: Annealing peak position vs. annealing temperature.	65
Figure 4.5: Annealing peak position vs. annealing time.	65
Figure 4.6: Changes to DSC signal when the sample was repeatedly re-melted at 220°C for 1min.	67
Figure 4.7: Changes to recrystallization peak as result of high-temperature degradation.	67
Figure 4.8: DSC melting signals from the high temperature annealing experiment.	68
Figure 4.9: Signals from isothermal crystallisation experiment. Signals were offset in time for clarity.	69
Figure 4.10: TGA plot and close-up with 1% and 2% weight loss points highlighted. Note that 1% and 2% loss was calculated from peak weight value of 100.3%.	70
Figure 4.11: EOS Formiga P100 sintering system. Note the two upended containers on top of the machine, feeding to the internal hopper.	72
Figure 4.12: Interior of Formiga P100 build chamber.	72
Figure 4.13: Picture illustrating appearance of powder bed when using poorly flowing powder (non-annealed A02 from Flow Agent Effects Study).	74
Figure 4.14: Picture of right side trough during sintering on non-annealed A02 (Flow Agent Effects Study),	74
Figure 4.15: Picture of powder bed during attempted sintering of non-annealed powder (V26 from MFR Effects Study).	75
Figure 4.16: Picture of powder bed during sintering of annealed A02 batch during Flow Agent Impact Study.	76
Figure 4.17: Schematic of correctly working powder deposition (left) and the issue of powder build-up (right).	78
Figure 4.18: Flow chart of two prevalent modes of build failure when powders features small particles, or large particles/clusters.	79
Figure 4.19: Diagram of the grid used for testing exposure parameters. Darker tiles were more heavily exposed. The underlying line shows the order in which tiles were exposed.	82
Figure 4.20: Result of testing exposure parameters on annealed AC88A12 Batch.	83
Figure 4.21: XZY type specimens stacked on powder bed. Order of axis labels lists specimen's largest dimension first.	85
Figure 4.22: Picture of XZY samples during production with annealed powder.	86
Figure 4.23: Representative stress-strain curves of several preliminary tensile study specimens. Note the lack of any yield point and the lack of strain-hardening effect.	87

Figure 4.24: Graphs of Preliminary Tensile Properties Study samples.	88
Figure 4.25: Picture of several XZY tensile specimens after being tested to failure.	93
Figure 4.26: Enhanced contrast picture of two ends of XZY tensile specimens.	93
Figure 4.27: Bulk densities of powder when aerated (poured), tapped and as recycled powder cake. Error bars omitted because of negligible size on this chart.	94
Figure 5.1: Results of Bulk Density testing on Flow Agent Effects study batches. Error bars omitted because of their indiscernible size on this chart.	98
Figure 5.2: Graph of PSD results for Flow Agent Effects study batches.	99
Figure 5.3: Box chart (quartiles and median) of Unconfined Compressive Yield strength of caked Flow Agent Effects study batches.	99
Figure 5.4: Unconfined Compressive Yield Strength specimens after test completion. Angular appearance confirms failure in shear mode.	100
Figure 5.5: SEM images of A04 batch of powder in virgin (higher) and annealed (lower) forms.	101
Figure 5.6: Diagram of tensile specimens in XYZ orientation.	103
Figure 5.7: Box chart (quartiles and median) of tensile tests results from Flow Agent Effects study.	105
Figure 5.8: Toughness vs. Specimen Density in Aerosil effects study. Combined scatter and Box Charts.	106
Figure 5.9: Flow Agent Effects study monolayer specimens Load vs. Strip weight. Combined scatter and Box Charts.	108
Figure 6.1: Selected DSC traces of selected batches.	115
Figure 6.2: DSC signals of batches milled from the same granulate batch.	115
Figure 6.3: Monolayer work data correlation with MFR and SSA.	119
Figure 6.4: Viscosity and PSD Effects monolayer study- all specimens which could sustain 25mm elongation.	121
Figure 6.5: Viscosity and PSD study batches of powder melted in oven for 15min @ 170°C	123
Figure 6.6: Reflected light pictures of sintered specimens' underside. In every picture dark areas correspond to points of adhesion, light areas to air gaps.	124
Figure 6.7: Densities of oven-sintered powder batches, split by the observed pore structure.	125
Figure 6.8: Microscopy images of closed-pore powder batches.	127
Figure 6.9: Selected frames from hot stage melting of V34.2	128
Figure 6.10: Selected frames from melting of V34.1	129
Figure 6.11: Hot Stage Microscopy images showing differences in melting temperature range between V25/V26 representing early melting onset and V28/V30 which represent a more common temperature range.	131
Figure 6.12: Example Stress/Deflection curve of oven sintered specimens. Curve becomes highly linear starting at ~100mm, in non-recoverable strain section.	133

Figure 6.13: Box chart (quartiles and median) of stress in oven sintered specimens at 5mm (recoverable extension) and 100-200mm (unrecoverable extension).....	133
Figure 6.14: Slope of the linear ductile region between 100mm and 200mm.	134
Figure 6.15: Oven sintered specimens. Stress developed at 200mm deflection versus specimen density.....	134
Figure 6.16: Density of oven sintered specimens versus pre-sintering bulk density of powder in mould.....	135
Figure 6.17: Hot stage microscopy pictures of V34.1 and V34.2.....	137
Figure 6.18: Hot Stage Microscopy image of V34.1 after re-milling to reduce particle size.....	138
Figure 6.19: Poured Bulk Density of Viscosity and PSD study batches versus Specific Surface Area. Note that Batches V33-V37 were milled by Mill A and V25-V30 by Mill B.	139
Figure 6.20: SEM image of batch V29, capturing both extremely rough particle on the left and cleanly crushed one on the right.	140
Figure 6.21: Residual values from linear regression of Viscosity and PSD study monolayer data.	143
Figure 6.22: Residual values from linear regression of Viscosity and PSD study monolayer data, plotted versus fitted value.	145
Figure 6.23: Microscopy pictures of oven-sintered V34.1 and V34.2 tensile specimens.	149
Figure 6.24: Numerical simulation of changes to thickness and mass of deposited powder layer, accounting for added depth of sintering-induced pits.	151
Figure 8.1: Combined Residuals plots for linear regression of Viscosity and PSD study monolayer data.....	174

List of Tables

Table 2.1: Summary of molecules in TPU copolymer	11
Table 2.2: Molar ratios of TPU components depending on hardness rating (Drobny, 2007).	11
Table 2.3: Simple summary of polymer sintering stages.	33
Table 4.1: Formulation of TPU in Preliminary Study	62
Table 4.2: Technical Specifications of Formiga P100 sintering system.	71
Table 4.3: Exposure settings for initial sintering trials. Top row contains Energy Density levels used in each group. Left column contains laser power used to expose each specimen in a group. Middle section of the table contains laser speed (in mm/s) necessary to achieve desired ED given the laser power setting on the left.	82
Table 4.4: Parameters of XZY build in Preliminary Tensile Properties study.	85
Table 5.1: Particle Size Distribution results for Flow Agents Effects study batches. SSA: Specific Surface Area, Dv(x): Volume Diameter (percent undersize)	98
Table 5.2: Parameters of XYZ build in the Aerosil Effect study.	103
Table 5.3: Parameters of monolayer build in Aerosil Batches Monolayer study.	107
Table 6.1: Summary of material parameters and selected study results. Special batch attributes: (1) V25 was milled using unique, high-speed mill settings. (2) V34.2 had different flow additive than other batches. (3) V37 had sodium-based IR absorber additive	113
Table 6.2: Machine parameters during monolayer sintering in Viscosity and Particle Size Effects study.....	116
Table 6.3: Adjusted Square Residuals of linear regression models in monolayer study.....	119

List of Abbreviations and Symbols

ABS	Acrylonitrile butadiene styrene
ADS	Adipic Acid
AM	Additive Manufacturing
ANCOVA	Analysis of Covariance
ANOVA	Analysis of Variance
BD	Bulk Density
BDO	Butanediol
BDP	Bulk Density (Poured)
BDT	Bulk Density (Tapped)
DSC	Differential Scanning Calorimetry
EaB	Elongation at Break
ED	Laser Energy Density
FA	Flow Agent
FEP	Fluorinated ethylene propylene
FFC	Flow Function Coefficient
HDI	hexamethylene diisocyanate
HDO	Hexanediol
HS	Hard Segments
HSM	Hot Stage Microscopy
LS	Laser Sintering
MDI	Methylene diphenyl diisocyanate
MFI	Melt Flow Index (identical to MFR)
MFR	Melt Flow Ratio (identical to MFI)
PA	Polyamide
PCL	Polycaprolactone
PEBA	Polyether block amide
PEEK	Polyether ether ketone
PEG	Polyethylene glycol
PEMA	Poly Ethyl Methyl Methacrylate
PMMA	Poly(methyl methacrylate)
PSD	Particle Size Distribution
PTFE	Polytetrafluoroethylene
RM	Rotational Moulding
SS	Soft Segments

SSA	Specific Surface Area
TGA	Thermogravimetric Analysis
TPE	Thermoplastic Elastomer
TPU	Thermoplastic Polyurethane
UCM	Upper Convected Maxwell (model)
UCYS	Unconfined Compressive Yield Strength
UTS	Ultimate Tensile Strength
VIF	Variance Inflation Factor
ρ_b	Density of Bulk Powder
ρ_s	Density of Solid
σ_1	Consolidation Stress
σ_c	Yield Stress

1 Project Introduction

1.1 Additive Manufacturing Principles and Applications

The term *Additive Manufacturing* (AM) can be best defined when contrasted against the related definition of subtractive manufacturing. Term subtractive manufacturing encompasses many conventional fabrication methods which rely on the principle of removing pieces of stock material until it takes on the desired form. Metal machining or wood carving both fall into that category. Common features of all those processes include generation of a large amount of material waste and cutting tools being a limiting factor in determining final shape. While modern CNC machines can sculpt extremely complex shapes, tools still need to be able to reach all recessed areas, putting pressure on designers to factor in available tools during the design phase. Frequently a necessary design change will include assembling final part out of smaller components e.g. welding propeller blades to a shaft. Many other manufacturing processes such as moulding and forging use tooling created using subtractive methods. Limitations of the subtractive processes, therefore, extend to a much wider range of final products.

Additive Manufacturing bypasses limitations on subtractive processes using the principle of layer-by-layer 'printing' of parts. Any 3D object can be deconstructed into 2D layers, analogously to the way a patient's CT scan is deconstructed into series of 2D slices. Layers can be comprised of polymer resin, metal powder, or another amorphous material which can be then selectively hardened and fused to form the final part. The term '3D Printing' can be seen as referring to the ease of 'printing' each two-dimensional layer in the 3D stack. Just like an inkjet printer can produce any image on paper for the cost of ink used, AM system can, in theory, produce arbitrarily complicated 3D geometry without added cost. This concept of 'free complexity' still drives the discussion about AM as future-oriented technology. In many cases, the powder or resin which did not become fused can be recycled and reused in future build jobs. This means that in theory, the AM can achieve 100% material efficiency, which is another ideal characteristic.

To answer when AM should be chosen over more conventional processes it is useful to look at the evolution of the technology and particularly the market shift from Rapid Prototyping (RP) to Additive Manufacturing. Prototyping is a process of creating usually one-off parts, which serve the purpose of early verification of appearance, ergonomics, assembly process, etc. Using early '3D Printing' technologies to manufacture prototype elements allowed for much faster translation of digital 3D designs into tangible objects. The combination of streamlined CAD iteration process and fast translation into physical prototypes gave rise to the Rapid Prototyping field. Because those objects were not meant to be final products, the mechanical and appearance requirements were relaxed. This stage of additive processes adoption was important to its further development, as the early additive systems could not meet more stringent requirements.

The emergence of AM from rapid prototyping was a gradual process which required advancements in all constituents of the system: machine, software and materials. The development goal was to improve the final parts' mechanical and aesthetic qualities and ensure their reproducibility. Machines required greater ability to monitor and control process variables. Software needed to become more user-friendly and time-efficient. Materials needed to address end-use requirements. Once AM became feasible, there has been a push to the adoption of machines with larger build volumes, capable of producing large batches of parts. Other advancements included automation of part cleaning and post-processing.

The cost-benefit analysis of additive versus traditional methods became more complex than it was in the case of RP. RP benefited greatly from the ability to produce unique parts. In AM this benefit is not necessarily utilised. Even when manufacturing simple objects, small to medium sized batches can be price-competitive with traditional moulding or machining processes. Great cost savings come when AM eliminates the need for post-processing steps, such as surface treatments or assembly. AM bone implants can, for instance, have integrated porous surface features which facilitate fusion to bone. Normally, this kind of surface would need to be deposited by plasma coating or welding. Of course, the benefit of manufacturing arbitrarily complex parts is also a large factor in the choice of AM over other methods. A good example of design choices possible with AM is the result of redesign contest for engine mounting bracket, conducted by General Electrics. Part

manufactured using Selective Laser Melting achieved 83.4% weight reduction thanks to complex, hollow structure (Kellner, 2013). Weight savings are especially valuable in aerospace industry and today this industry is one of largest adopters of AM. Parts as demanding and critical as turbine blades can today be manufactured using AM, what might be the best illustration of the advanced state of some AM technologies.

1.2 Laser Sintering Technology

The Laser Sintering (LS) technology is an Additive Manufacturing method which operates on the principle of fusing layers of powder particles using laser energy. Compared to other polymer-AM technologies on the market (see Figure 1.1), LS has the advantage of using raw thermoplastics, identical to ones used in other industrial processes, like injection moulding. Polymers used in LS do not require photoinitiators like stereolithography resins, or even light-absorbent inks like High Speed Sintering.

Figure 1.2 illustrates principle components and operation of a simple LS system. Illustration explains steps of the main build loop of sintering and re-applying fresh powder. Figure 1.3 lays out steps before and after the main build task.

Laser Sintering is both one of the earliest developed 3D printing technologies and the most important Additive Manufacturing technologies today. It was first developed in mid-80's at the University of Texas and the technology was purchased by 3D Systems Inc. in the early 90s. Core technology patents were later challenged by German company EOS, which eventually was granted a licence to use the technology in their own systems. The two companies still remain the largest suppliers of LS hardware, although the core technology patents began to expire around the year 2015. The software and materials market is less centralised, with several companies developing LS-compatible materials and various software solutions for build preparation and quality control.

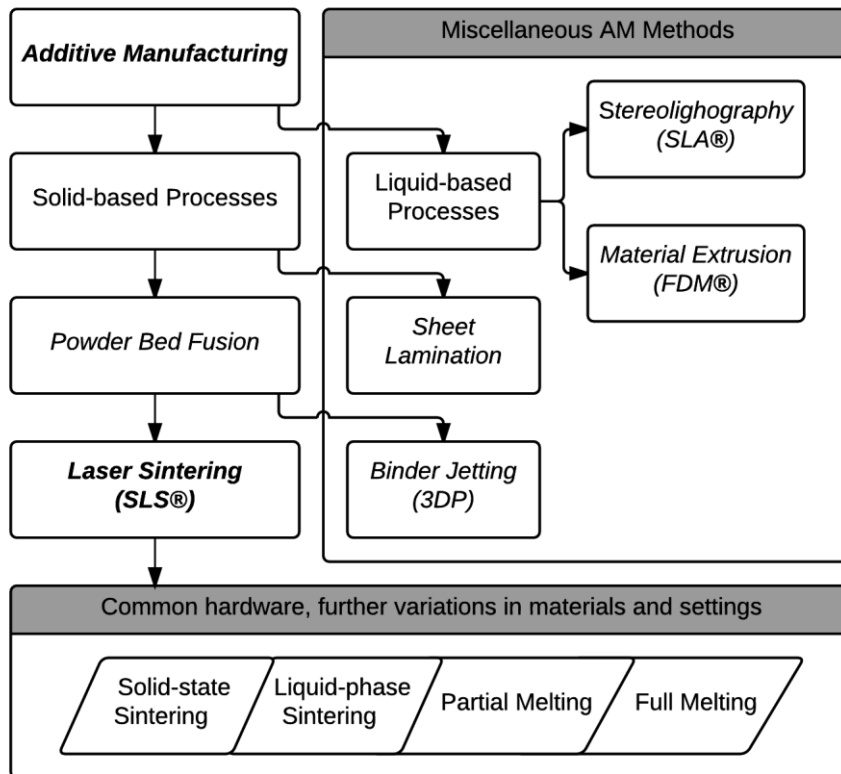


Figure 1.1: Chart placing Laser Sintering in the context of other Additive Manufacturing processes.

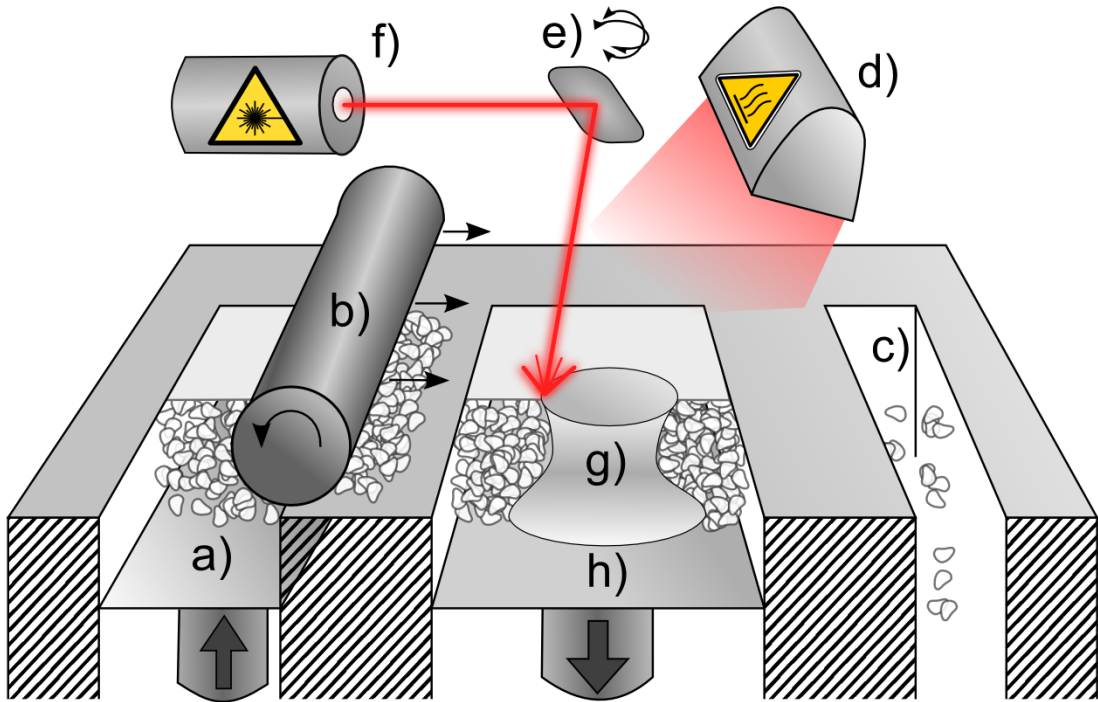


Figure 1.2: Schematic of a representative Laser Sintering system and its major components. Powder feed platform a) moves upwards. Counter-rotating roller b) deposits a layer of powder on build platform and excess is thrown off to chute c). Heating element d) warms up the new powder layer on the build platform. Scanning mirror e) reflects laser beam from source f), melting powder into a new layer of part g). On completing the layer, build platform h) lowers one layer thickness and next powder layer is delivered.

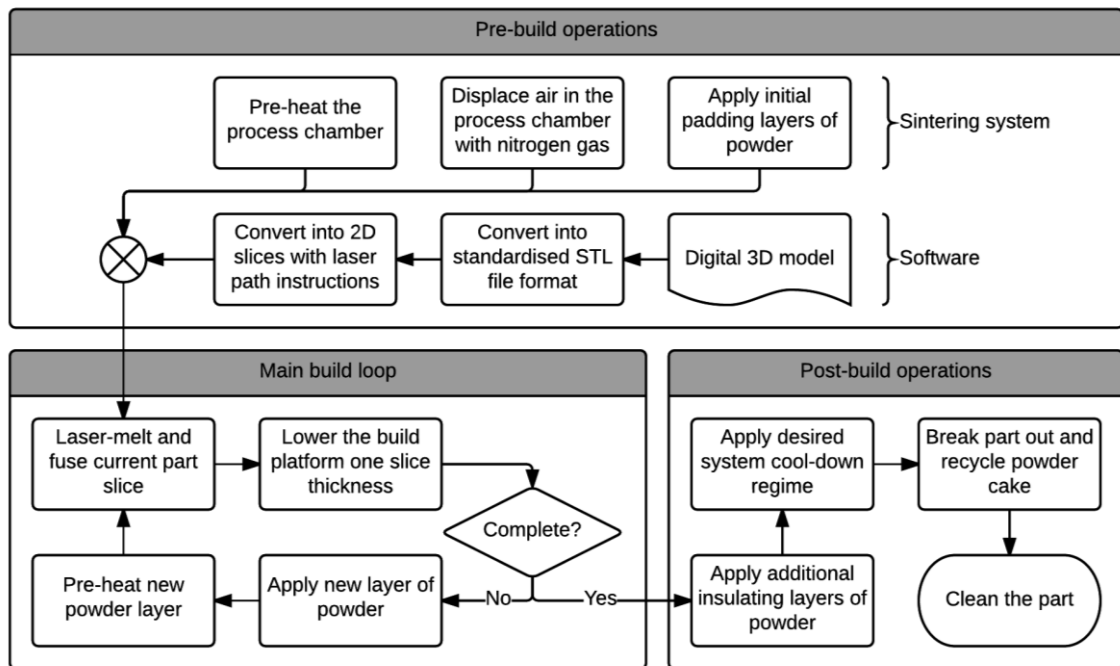


Figure 1.3: Flowchart of Laser Sintering process, including pre- and post-build operations.

1.3 Commercial Materials in Laser Sintering

Although both metal-based LS and polymer-based LS share almost identical operation principles, it is important to note that there are important differences stemming from nature of each material. In general, metal sintering has seen wider adoption at the production of end-use parts. This can be attributed mainly to the process compatibility with very desirable materials, such as titanium alloys which are a staple of highly lucrative Aerospace and Medical industries. Many other engineering and aesthetic metals are compatible with LS, including variety to steel, aluminium and brass alloys. It is impossible to overstate the importance of material selection to the ultimate success of AM technology. In this regard, polymer LS had been at disadvantage, since the complex nature of polymer behaviour made the search for new materials much more difficult. Today, the golden standard for LS polymers is Nylon, especially polyamide 12 (PA12). Reasons for this will be explored further in Chapter 2.2.2.

Out of 13 materials available directly from EOS today, 10 are various grades of polyamide. The variety of materials available from the second market leader- 3D Systems is even smaller- 8 out of 9 materials are DURAFORM® brand blends of polyamide. In the case of both companies the portfolio of materials had been diversified by offering PA with fillers, such as stiffness-boosting glass beads or alumide which imparts a metallic appearance. Both companies offer polystyrene, which is a low-performance polymer useful only for the production of investment castings due to its resistance to crystallisation-induced warping. The introduction of new, high-temperature EOS systems allowed this company to expand their portfolio by being first to offer high-performance, high-temperature engineering polymer PEEK. Lastly, EOS is offering PEBA, which is the only soft, elastomeric material in range.

It is noteworthy that although elastomers have many important engineering functions, PEBA is the sole offering in this category from major suppliers. When the scope of the search is expanded to third-party suppliers, the variety of material increases. Thermoplastic Polyurethanes (TPUs) had been viewed as good candidates for LS process for some time and some are offered commercially under brands Luvosint®, Desmosint™ and TPE-210. TPE-210 has been developed by Advanced Laser Materials company. Both Luvosint® and Desmosint™ are based on the same formulation

originally developed by BAYER. End-use applications of those elastomers are limited mostly by the relatively low melting point compared to thermoset elastomers. So far the most successful cases of commercialisation were in the footwear industry, which leverages AM's ability to create products which are highly customised and visually striking. Due to its softness and safety of fully reacted polymer, TPU is particularly suited for products which interface with the human body, good examples being goggle frames, orthoses and gripping surfaces. These types of products could all benefit from mass customisation enabled by AM.

1.4 Project Goals

The goal of this project is an investigation of TPU powders with respect to their compatibility with laser sintering process. Knowledge of the most important material parameters and their relative significance will expedite the further material development process. Material properties under investigation will include TPU's intrinsic properties such as melt rheology as well as bulk properties of its powdered form. During the project, we will have an opportunity to provide feedback regarding the production of new powder batches.

1.5 Structure of the Thesis

Past the introductory chapters, the thesis will begin with literature review exploring several topics relevant to the project. First, we will introduce thermoplastic polyurethanes. Their co-polymer structure results in a complex and dynamic phase make-up, what will become important to forming hypotheses at early stage of the project. Next, we will provide a richer introduction to the laser sintering process, with a focus on process and material variables found important to successful processing. The next two review chapters will provide a detailed review of powder bulk properties and particle coalescence process respectively. We believe that those two topics were not adequately explored in prior laser sintering literature, despite having a direct impact on materials' success. In order to enrich our understanding of those subjects, we will extend review to other manufacturing processes dealing with bulk solids and/or coalescence.

Experiment methodology will be given its own chapter, separate from results of the study. During the project, it became necessary to adopt unusual test protocols, mainly for investigation of bulk and mechanical properties. We believe that the insights gained from developing those test methods are themselves valuable and may aid future material development. Furthermore, some space will be given to a review of common test methods currently used in LS research. Finally, this chapter forms a convenient reference point for all the experiments sharing identical methodology.

The main experimental results chapter will begin with a set of preliminary experiments dedicated to finding safe and optimal process parameters. Chapter 4 begins with DSC and TGA investigation of TPU's thermal properties, including influence of thermal history on the phase structure of TPU. Pervasive problems with powders' ability to flow often led to rejection of batches for full-scale LS build experiments. Here we will introduce the common types of build failures as well as the annealing process which was used to mitigate them. The preliminary part of study will also include tests of safe exposure parameters and a baseline tensile properties investigation, with focus on part and measurements consistency.

To further improve TPU's flow properties we will dedicate part of the study to effects of flow agents on powder's bulk properties and sintered part properties. In Chapter 5 we will introduce several tests of powder bulk properties- tapped bulk density and Unconfined Compressive Yield Strength. Tensile testing portion of the study will introduce a new type of build and test protocol, based on one-layer specimens.

Finally, the project will conclude with a large study on 12 varied TPU batches in Chapter 6, representing a range of viscosities and particle sizes. We hope that the large number of batches in the study will allow us to form an accurate regression model, to estimate those factors' contributions to sintering. Regression model will be based on monolayer specimen data. We make an argument that the monolayer test isolates the coalescence stage from the densification stage of sintering. Therefore, strength of monolayer specimens will be correlated to material properties in a simpler way than full thickness specimens'. The densification stage will be investigated using oven sintering, where we focus on the formation of closed and open-pore structures.

2 Literature Review

2.1 Polyurethanes and Polyurethane Processing Literature

2.1.1 Thermoplastic Polyurethanes Synthesis and Structure

Thermoplastic Polyurethanes (TPUs) are, just like other types of elastomers, potentially highly elastic, rubber-like materials. While their exact properties depend on the specific formulation, some representative applications of TPUs include cushioning foams and sport shoe soles. TPUs derive their elastic properties from the same molecular structure as other elastomers, including rubber. Their molecular structure consists of long, weakly interacting, flexible polymer chains connected into a network. Model of TPU's molecular structure is shown in Figure 2.1. Molecules typically featured in TPU structure are listed in Table 2.1. Network structure in TPU is imposed by hydrogen bonds formed between special segments of the copolymer, as opposed to irreversible covalent bonds in a cross-linked polymer. As a direct result, TPU or other Thermoplastic Elastomer (TPE) can be molten without decomposing like thermoset elastomers or vulcanised rubber. TPU can, therefore, be processed using the same principal methods as standard thermoplastics: blowing, injection moulding, rotational moulding, extrusion etc. This is also the reason why they are a strong candidate for laser sintering.

Segment type	Molecule type	Example Molecules	Size	Polarity	Rigidity
Soft Segment	Long polyester or polyether diol	PTMA, PCL	Large	Low	Low
Hard Segment	Diisocyanate	MDI, HDI	Small	High	High
	Short-chain diol	PEG, 1,4-BDO, 1,6-HDO			

Table 2.1: Summary of molecules in TPU copolymer

The interaction between HS and SS is the fundamental molecular mechanism governing TPU properties. Properties such as softness and elasticity of the final polymer are determined by the ratio of the two components. In soft grades of TPU, the molar ratio between SS and HS is relatively even. As the proportion of HS is increased, hardness of TPU increases (See Table 2.2). The types of molecules used in SS and HS play a role as well. Most commercial TPUs are based on ester SS since they have superior mechanical properties and are cheaper. Polyether TPUs are reserved for niche applications, where e.g. low-temperature flexibility is required (Drobny, 2007).

Hardness rating	Molar ratio Polyol : chain extender : diisocyanate
Below 60 Shore A	1 : 0.5 : 1.5
Above 70 Shore D	1 : 20 : 21

Table 2.2: Molar ratios of TPU components depending on hardness rating (Drobny, 2007).

While TPU can be classified as a semi-crystalline polymer, its morphology is more complex than monomer's such as PA. Formation of the proper crystalline structure is hampered by entanglement of soft and hard segments. The result is the paracrystalline structure, where soft-segment inclusions can be regarded as defect sites in ordered structure (Van Krevelen and Te Nijenhuis, 2009). According to some experts, paracrystallinity should not be regarded as a third, discrete type of phase. Rather, it should be seen as a spectrum of possible mixed-phase structures (Van Bogart et al., 1981) which emerge in TPU as a result of thermal history, ageing, annealing etc. (Yamasaki et al., 2007) The complex phase make-up and its susceptibility to change continue to make TPU a highly challenging material to study.

2.1.2 Annealing Effects in TPU

When TPU is exposed to elevated temperature for sufficient amount of time, diffusion-controlled processes of phase reorganisation can occur. This effect is well known and is referred to as annealing, analogously to reorganisation processes in metals and other multi-phase materials. References to this effect can be found as far back as 70s (Seymour and Cooper, 1973) and it has been studied extensively since then (Yamasaki et al., 2007, Van Bogart et al., 1981, Hesketh et al., 1980, Yoon and Han, 2000, Koberstein and Russell, 1986, Saiani et al., 2001). One of the most in-depth investigations is by Yoon and Han (Yoon and Han, 2000), who coupled DSC measurements with FTIR and NMR spectroscopy to investigate the occurrence of hydrogen bonding and exchange reactions during the annealing process. Signs of annealing were also seen in DSC signals from Plummer (Plummer et al., 2012) in Figure 2.2, whose work will be cited multiple times in this document.

As outlined in in Section 2.1.1, TPU largely consists of mixed phase which contains both hard and soft segments, at proportion mainly determined by the proportion of reagents during synthesis. Within the mixed phase, hydrogen bonding and debonding will be occurring continuously, what allows hard segments to segregate out and form short-order crystalline microphase, with varying density of hydrogen bonds. The degree of phase separation and so the amount of hydrogen bonds present in phase structure depends on composition as well as the thermal history of TPU. As the temperature is increased, hydrogen bonds become weaker, making regions with low hydrogen bond density prone to dissolution. Exposing TPU to an annealing temperature higher than ambient conditions increases the molecular mobility of low-order phases, leaving higher-order and therefore stable phases intact. Liquidised regions are again susceptible to the process of reorganisation and have the potential to increase their density of hydrogen bonds and therefore the degree of phase separation. The degree of separation will increase up to the point where phase structure becomes stable at the annealing temperature. This new, more highly ordered phase can be found in a DSC signal as an endothermic peak, located above annealing temperature.

Effects of annealing on rheological properties of TPU have been explored by Yamasaki et al. (Yamasaki et al., 2007) for extensional flow. According to the findings, increased phase segregation

led to faster strain hardening of TPU melt, what opens a possibility of annealing having an effect on zero-shear viscosity as well. Castro (Castro et al., 1985) found that annealing increased TPU's Vicat Softening Temperature. Softening Temperature is associated with a rapid drop in hardness preceding melting. Higher softening temperature might prevent TPU particles becoming tacky and clumping while exposed to an elevated temperature on sintering powder bed.

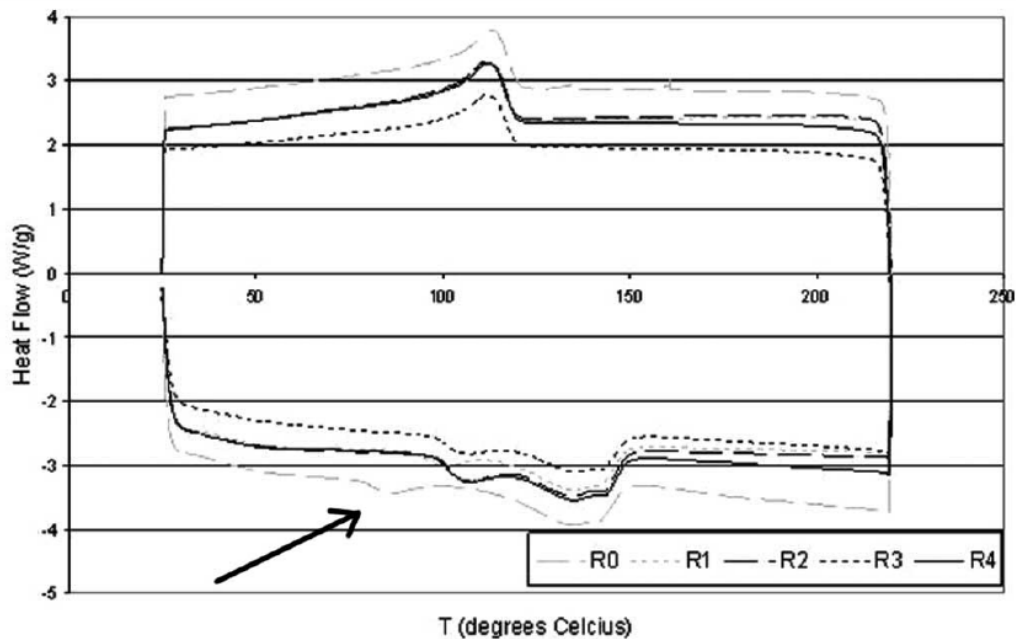


Figure 2.2: Comparison of DSC signals from repeatedly recycled TPU batch, taken from (Plummer et al., 2012). Note that signal is horizontally mirrored compared to other graphs in subsequent chapters. The arrow indicates emergent peak in R0 (virgin) powder, indicating that powder has been probably dried at ~60°C. Peak shifts to ~105°C, following exposure to build chamber temperature of 95°C.

2.2 Polymer Laser Sintering Literature

The goal of literature review at this stage of the project is to gain early insights into the process and material design. Data from prior research should reduce the time required to find optimal process parameters and also show us what issues to anticipate while working with specific materials. This information can be efficiently summarised by focusing on process and material parameters which were previously found important to the LS process.

2.2.1 Selected LS Process Parameters

Energy Density (ED)- The amount of energy delivered to the powder bed by the laser light is often calculated in units of Joules per square millimetre, based on Equation 1:

$$ED = \frac{Power}{Speed \times Spacing} \quad (1)$$

Where Power refers to the wattage of the laser, Speed refers to the speed component of laser dot's velocity and Spacing refers to the distance separating neighbouring laser tracks. Note that it is not necessary to include the size of the laser dot in the equation, but it is assumed that degree of overlap is sufficient to fuse sequential melt tracks.

ED value is usually treated in literature as a comprehensive measure of exposure, but we foresee a possibility of certain parameter combinations having an impact on the sintering results. Lowering laser power while also lowering scan speed would increase the time necessary for exposure. Halving values of both scan speed and laser power would yield the same ED, but delivered in twice the time. Slower delivery of laser energy might be beneficial if it leads to less overheating and longer times polymer spends at melt temperature. This hypothesis will be tested early in the project when we seek optimal exposure parameters.

Laser Scan Strategy- Laser exposure is almost always broken down into at least two stages- shape outlining and filling. Frequent modification to scan strategy is to perform laser exposure on layer contours, before filling the contoured shape. This enhances part's surface definition by avoiding 'end-of-vector' effects on points where the laser changes direction. We found that this modification was also useful in mitigating curl at the layer edges. A noteworthy feature of the laser path planning is that when the sintered layer is subdivided into discrete shapes- e.g. an array of multiple parts- the system will attempt to complete sintering of a single part before moving on to next one. This strategy minimises the time gap between forming subsequent melt tracks. This is important to prevent the tracks from cooling before they fuse with the subsequent track.

Powder Bed Temperature (T_b)- Using laser as energy delivery method results in very large temperature gradients and heating rates. Need to heat polymer by a large amount is likely to result in overexposure and damage to topmost layers of powder (See Section 2.2.2). In addition, a large difference in temperature of powder melt and environment accelerates cooling, reducing time polymer melt is able to coalesce. Pre-heating polymer powder reduces the melt-solid and the melt-environment energy gap. To minimise this gap T_b should be as high as possible while avoiding

transformation of unsintered powder into semi-rigid powder 'cake'. Even before transformation into cake, powder can experience a major drop in flowability (See Section 2.3.4) what could interfere with spreading of an even layer of powder. The EOS Formiga P100 is equipped with a simple infrared pyrometer, reading the temperature of the surface of the powder bed. In this project, Powder Bed Temperature refers to this sensor reading.

Layer Height- Layer Height refers to the increment by which the powder bed is lowered in each stage of the build cycle. Currently, most polymer sintering systems are set up to use 100 μ m layers, which were found to form a good compromise between building speed, interlayer fusion and part definition. This value is also influenced by the practical limit of polymer powder particle size. Sintering of thinner layers would require a use of smaller particles, what in the case of polymers makes powders difficult to handle- an issue which will be further discussed in Section 2.3. It is generally recommended that the average particle diameter should be two-to-three times smaller than layer height. This allows for spreading of a smooth layer and allows most particles to be heated by direct contact with the laser (Goodridge et al., 2012). Note that the true thickness of powder layer which is sintered at each step is likely to be greater than 100 μ m, because of the sintering-induced shrinking of powder volume. This phenomenon will be discussed in Chapter 6.10.7. Software which was used for build preparation in this project was unfortunately locked to the 100 μ m layer thickness and therefore this value was constant during the entire project.

2.2.2 Selected LS Material Parameters

At early stages of LS development, ABS, polycarbonate and other amorphous polymers were the primary research materials. Amorphous nature of those polymers led to the adoption of term 'sintering', analogous to the processing of glass. However as mentioned in Chapter 1.3, today the materials market is dominated by semi-crystalline Nylon (especially PA12) and its various filled forms. Nylon is a durable polymer suitable for wide range of engineering applications. However, its dominance in the market could only be achieved due to a special combination of properties which make it exceedingly compatible with LS. Unfortunately, as it will be shortly shown, most of those properties do not apply to TPU.

The introduction of Nylon should begin with a comparison between the semi-crystalline polymers it is representative of and the amorphous polymers which are comparatively rare on the market.

Viscosity- Depending on the degree of crystallinity and structure, semi-crystalline materials generally possess well-defined melting point T_m . Upon reaching melting temperature the viscosity of polymer drops sharply, as shown in Figure 2.3. In the case of Nylon, viscosity remains nearly unaffected below the melting point. This is important because it allows avoiding polymer softening and caking under elevated process chamber temperature. In comparison, the viscosity of ABS drops gradually, as amorphous polymers lack well-defined melting onset temperature.

In TPU, melting of hard segment domains creates a well-defined melting transition, which is beneficial to the sintering process. However, due to low molecular rigidity, thermoplastic elastomers, such as TPU also often feature a softening point. The softening point is a temperature located below melting temperature, which causes a substantial decrease in hardness. This may increase TPU's tackiness and therefore susceptibility to clump and cake, as was observed by Ziegelmeier (Ziegelmeier et al., 2014).

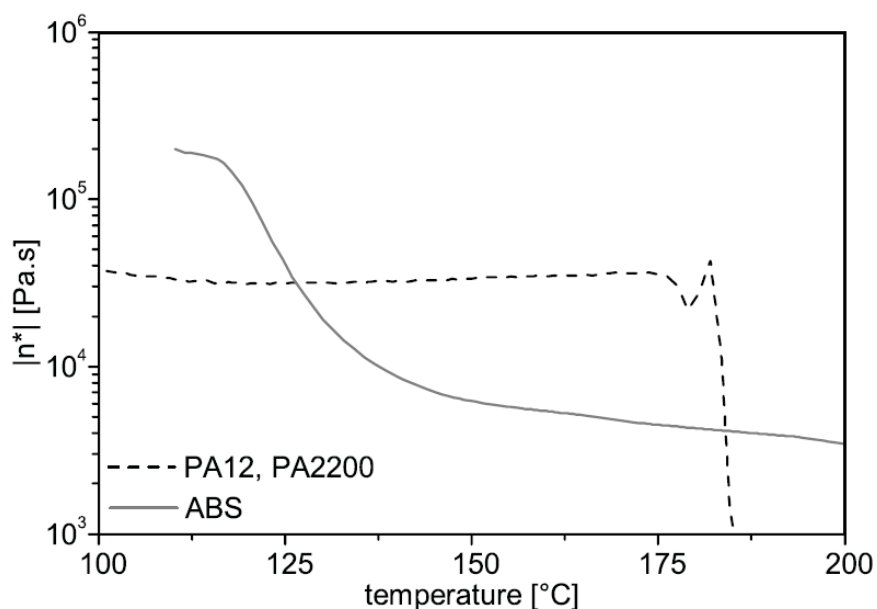


Figure 2.3: Changes to viscosity while melting amorphous (ABS) and semi-crystalline (PA12, PA2200) materials. (Adapted from (Drummer et al., 2010))

Shrinkage- In crystalline regions polymer chains are packed more efficiently than in amorphous phase. Semi-crystalline polymers, therefore, tend to experience a large and sudden drop in volume

as they cool down from melt temperature and crystallise, as shown in Figure 2.4. This poses an especially serious issue in Laser Sintering. The principle of LS relies on rapid melting and solidifying powder layer-by-layer. This leads to temperature gradient where old layers are colder than freshly sintered ones. As a result, unless the shrinkage is carefully controlled, LS part will tend to warp. Amorphous polymers which do not crystallise experience lower amounts of shrinkage and the dimensional accuracy of resulting parts remains a selling point of e.g. polystyrene.

Because TPU's crystalline phase is not well organised (See Chapter 2.1.1) we expect its shrinkage to be minor, compared to semi-crystalline polymers. Injection-moulded TPUs shrink 0.5-2.5% (Drobny, 2007), where as PA6 shrinks nearly 13% (Ehrenstein, 2012). Although the amount of shrinkage is likely to be low, it might be exacerbated by the temperature difference between powder bed and polymer melt. As mentioned in the previous chapter, bed temperature needs to be kept high, but softening of TPU at high temperature might force us to keep T_b much below the melting point.

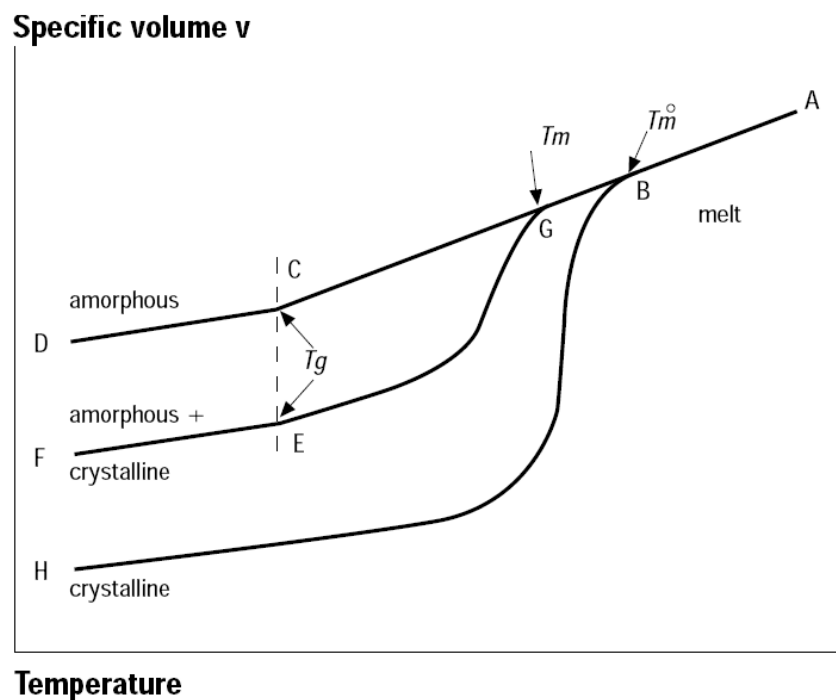


Figure 2.4: Changes in the specific volume while melting and recrystallizing amorphous and crystalline polymers. (Adapted from (Gibson and Shi, 1997))

Supercooling Window- Management of shrinkage in semi-crystalline materials is highly problematic and Nylon's success can be largely attributed to how the shrinkage can be delayed using the supercooling principle. The supercooling principle allows some materials to avoid crystal

formation even when the temperature of liquid phase drops below melting temperature. Melting and crystallisation events can easily be recorded by measuring heat flow with a calorimeter. Figure 2.5 shows such measurement, with two peaks corresponding to the temperature of melting and subsequent recrystallization events. The two events do not overlap in temperature axis, creating a ‘window’ of temperatures where Nylon solidifies but does not crystallise. Similar signal characteristic was found for a number of LS candidate materials, including polypropylene and polyoxymethylene (Drummer et al., 2010). Polymers cooled to the window temperature had their crystallisation process delayed by order of minutes, but only Nylon showed practically indefinite crystallisation delay. It is extremely unlikely that the supercooling approach will be useful in TPU.

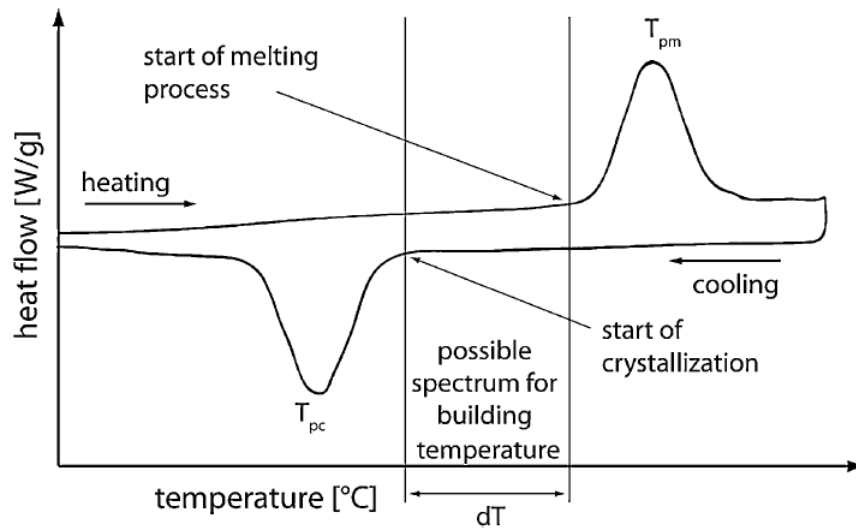


Figure 2.5: Differential Scanning Calorimetry curve showing the supercooling property of PA12. Polymer solidifies but does not crystallise when the temperature is maintained between melting (T_{pm}) and recrystallization (T_{pc}) peaks. (From (Wendel et al., 2008))

2.3 Bulk Solids Literature

2.3.1 Bulk Solids Introduction

Using materials in granular form has millennia-old history, with the most ancient historical examples being arguably flour and dry concrete. Another, more contemporary industry which makes extensive use of bulk solids is the pharmaceutical industry, with estimated 80% of its output (e.g. tablets, aerosols) being produced out of powders (Li et al., 2004). It should therefore not be surprising that significant fraction of literature on the topic of small-grained bulk solids was generated based on materials such as e.g. pulverised silica, paracetamol or dairy powder.

Furthermore, because polymers are a highly diverse category of materials, knowledge based on e.g. Nylon powder may not be directly applicable to TPU powder. Care needs to be exercised in discerning general from specific knowledge when investigating bulk solids.

Clarifying the terminology- the term *Bulk Solid* has broader in definition than the more common term *Powder*. Bulk solid is an assembly of particles which is large enough for a statistical mean of any property to be independent of the number of particles. For instance, adding or subtracting large or small particles from assembly should not have a significant impact on the average particle diameter. Meanwhile, powders are described as a class of bulk solids which have small grains and which have low moisture content, allowing them to retain some degree of flowability. This definition sets them apart from e.g. bulk solids with particle size $>1000\mu\text{m}$, or fine particles suspended in paste or gel. Another difference is that term *powder* is most frequently used in pharmaceutical and food research, while *bulk solid* is preferred in soil, mining and construction industries. In the context of this project, term *powder* can be used interchangeably with *bulk solid*, but latter will be used where research applies to bulk solids in general, rather than specific material.

As mentioned in bulk solid definition, properties of powder are determined statistically and are usually a result of numerous interactions between individual grains. In theory, the behaviour of bulk solid should be possible to model from properties of particles and interparticle forces. The cohesiveness of powder should be calculable from inter-particle attraction due to e.g. static charge. Packing efficiency and therefore the bulk density of powder should be possible to calculate from particle geometry. Unfortunately, models which use this discrete elements approach cannot cope with the complexity of real particle systems. One cubic centimetre of powder with average particle diameter of $100\mu\text{m}$ would contain a number of particles in the order of 10^6 . Each particle may have different shape and size and may interact with multiple neighbours via multiple types of forces. Direct measurement of interparticle forces e.g. by using Atomic Force Microscopy (AFM) has limited power in predicting bulk solid behaviour, since it cannot account for some highly significant factors, such as particle size and role of consolidation stress (Jones, 2003). Models which treat bulk solid as continuum have greater applicability to real world cases. Bulk solid can be seen as a two-phase system of particles (solid phase) suspended in air (gaseous phase). As such, it can exhibit

properties both of liquids (flow) and solids (yield strength) depending on loading and environmental conditions.

For TPU powder to be used successfully in laser sintering, it needs to easily flow in order to fill the build platform in a uniform manner. Once powder settles on the build platform, particles should achieve efficient packing in order to preserve their volume once sintered into a dense part. Meanwhile, powder which is not sintered needs to act as support for sintered parts. Even when exposed to temperature and pressure deep inside build volume, non-sintered powder cannot become too tough, otherwise, it would make part break-out problematic. All those requirements can be described in terms of bulk solid properties, flowability and bulk density being the most significant to our experiments.

2.3.2 Bulk Solid Flowability Definition

In the context of bulk solids, the concept of flowability broadly refers to how efficiently powder can fill containers and be handled using devices such as chutes. In addition, it refers to material's ability to retain flowability when subjected to compacting pressure, elevated temperature or other adverse conditions over time. In qualitative terms, well-flowing powder can be easily poured, sieved and will not block the handling equipment, even after being stored for an extended time. Some simple measures of powder flowability, such as the funnel flow test (D-20) are directly related to handling parameters. However, rigorous study of flow properties necessitates linking the apparent behaviour with a quantifiable physical property of the material. This field of study was pioneered by Andrew W. Jenike who had pioneered the application of rigorous mechanical testing methods to bulk solids.

According to Jenike (Jenike, 1964), bulk solid can be said to flow when it is being deformed plastically by some external stress. Equating flow to plastic deformation allows us to study the problem using well-established mechanics terminology and methods. Plastic deformation and therefore flow occurs at a stress threshold referred to a *yield stress* (σ_c). The point at which powder begins to flow is also sometimes referred to as *incipient flow*. Loose powder which has been recently sieved requires a minuscule amount of yield stress to start flowing and typically will begin to flow under its own weight, allowing it to be poured like a liquid. As such, it is difficult to visualise loose

powder being tested and analysed in a way identical to solid materials. However, it is common for bulk solid to consolidate into semi-solid form when confined and then compressed, just like in process of tableting. As the powder is compressed, its yield strength will increase as a result of particle contacts becoming more numerous and possibly larger due to particle deformation. This process is referred to as consolidation and the compacting stress is the *consolidating stress* (σ_1). Even in semi-solid form, bulk solid can still ‘flow’ when enough stress is applied. Like before, flow occurs at yield stress. This time, the incipient flow state is analogous to a consolidated powder sample becoming crushed in a standard compressive strength test. In conclusion- yield strength of powder is a function of consolidating stress experienced previously by bulk solid.

According to Jenike (Jenike, 1964), the ratio (ff_c) of consolidation stress (Equation (2)) to resulting yield stress can be used to rate the behaviour from highly cohesive ($ff_c < 1-2$) to free flowing ($10 < ff_c$). It is important to note that the ratio is not constant for a given material and that single ff_c value cannot describe flowability under all conditions. Plotting σ_c for a range of σ_1 is necessary to obtain flow function. Representative plot of such flow function is shown in Figure 2.6. While σ_c will almost always increase with σ_1 , the increase becomes smaller and therefore ff_c ratio is often higher at higher consolidation stress values. It is common for materials to behave cohesively at low consolidation stresses and free-flowing at higher stresses. Another common feature of bulk solids is the tendency to become more cohesive when exposed to consolidation stress for a longer time, or when stress is combined with elevated temperature- in a process often referred to as ‘caking’.

$$ff_c = \frac{\sigma_1}{\sigma_c} \quad (2)$$

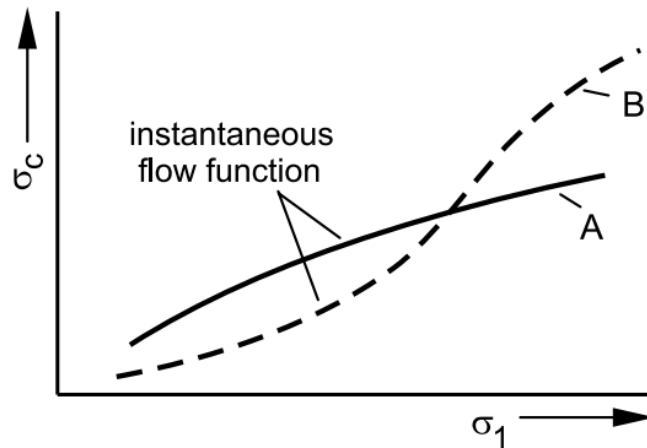


Figure 2.6: Shape of two flow functions. Instantaneous Flow Function emphasises that measurement is performed immediately after compaction, without additional time given to consolidation. Curve A is much more common. (From (Schulze, 2007))

Treating flowability as a function instead of constant value teaches us that investigating TPU powder under one set of conditions may be insufficient. Comprehensive analysis should involve properties of powder as it is being used in production- including storage in machine hopper and flow in elevated temperature atmosphere.

2.3.3 Selected Bulk Solid Flowability Measurement Methods

Although it is difficult to conceptualise how ff_c relates to real world cases, it was widely and successfully used in industry in applications such as design of hoppers, silos and conveying systems (McGlinchey, 2008 pg.74). Flow function is not, however, the only measurement method in use. Frequently it has been displaced by simpler, cheaper to implement alternatives. Some of the methods mentioned below, such as funnel flow test cannot provide absolute measures of flowability since they do not measure the force of particle interactions directly. They can, however, be used to observe the performance of different powder batches comparatively. Compared to flow function, their results are easier to interpret and in the case of properties such as tapped bulk density, they may be more directly applicable in a given case. For instance, when concerned with powder dosing on a production line, only knowledge of bulk density may be necessary.

Unconfined Yield Strength – Although conceptually closest to Jenike’s measurement of consolidation and yield stress, in practice this test is not frequently used. That is because only

cohesive powders which consolidate into semi-solid specimen can be tested using this setup. After being consolidated in a cylindrical mould, powder sample is extracted from the mould and tested in compression until failure, just like any solid specimen. Just like Jenike's technique, the test records consolidation stress from the mould and yield stress from the crush test. Protocol had been standardised in ASTM D2166 (D-06), although in this project the test will be modified to consolidate powder under zero stress, corresponding to natural bulk density (see Chapter 3.2.7 for methodology).

Shear Cells – According to Jenike and Schulze (Schulze, 2007), this is the only fully quantitative method of measuring flowability besides UCYS. Schematic of the Jenike type shear cell is shown in Figure 2.7. The device consists in principle of a stationary base ring and a shear ring, which can be laterally displaced by action of the 'stem' located on the left in the figure. Force acting on the stem is the shear force F_s . As discussed in Chapter 2.3.2, the shear force reading must be accompanied by the reading of stress used to consolidate the sample. Here, it is calculated from the normal force F_n , which is applied directly to bulk solid through the 'shear lid'. Repeat tests for various F_n values are required to arrive at 'yield locus' function, which can finally be used to calculate the yield stress σ_c via Mohr's circle. The entire procedure for the Jenike cell is described in ASTM standard D-6128 (D-18). This type of shear cells is unfortunately uncommon outside of highly specialised labs and in this project we settle on more common techniques.

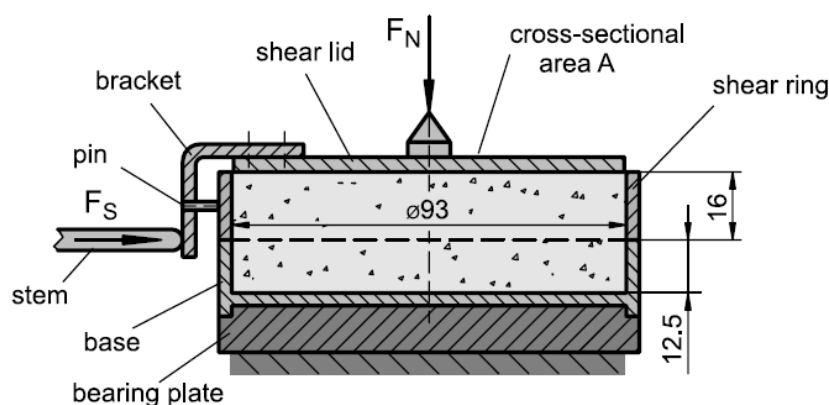


Figure 2.7: Schematic of Jenike shear cell tester (From (Schulze, 2007))

Funnel Flow Test- Due to its simplicity, this test was adopted by many companies, including Association of Rotational Molders and BASF. Funnel test has been standardised in ASTM D1895 (D-20). Schematic of standard funnel is shown in Figure 2.8. This test measures the amount of time

needed for set mass of powder to flow through a funnel of standard geometry. While simple, this test rapidly runs into problems when powder is not well flowing enough to discharge through the funnel. Discharge of powder can be improved by modifying the test with wider funnel openings or stirrers. However, these modifications undermine the value of a standardised test. Standard funnel flow test performed on most TPU powders in this project could not supply quantified data. Instead, behaviour was described in qualitative terms such as ‘tapping required for powder flow’.

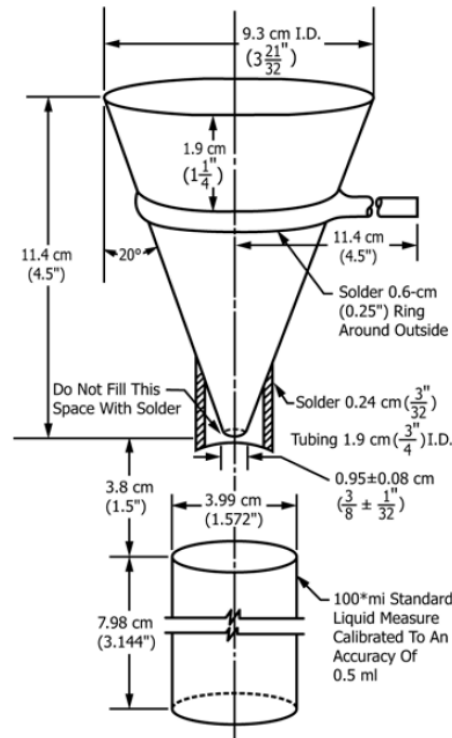


Figure 2.8: Funnel flow test apparatus, version with 100ml cup for apparent bulk density measurement. (From (D-20))

Angle of Repose- Angle of repose usually refers to an angle formed between a conical pile of powder and level surface. However, the same angle can be observed in multiple ways, for instance, as the angle of the avalanche when powder is in a rotating drum, or as the angle at which powder pours out of tipped container. While not clearly related to any one physical property of powder, it remains a useful tool for comparative study and produces an easy to interpret quantified value. The cone angle method is by far the most common and test devices, such as one shown in Figure 2.9, is commonplace. Unfortunately, because it relies on powder flowing under force of gravity alone, powders in which cohesion forces win over particle weight will be difficult to analyse. These

powders do not form neat piles and generally exhibit unpredictable tipping points stemming from clumpy nature.



Figure 2.9: Copley Scientific BEP2 Angle of repose tester. Angle is measured as a function of the radius of cone's base and height.

Poured/Tapped Ratios- When powder is poured into a container, interparticle forces which impede particle movement stop it from achieving theoretical maximum density (or minimum volume). One way to overcome these forces and increase bulk density is to repeatedly drop the container from a small height. When particles are in freefall, cohesive forces are reduced and the shock of drop causes them to shift into a denser configuration. Comparing 'poured' and 'tapped' powder informs us of the magnitude of cohesive forces in the sample. Samples with low cohesive forces achieve high poured density which improves only slightly by tapping. This makes the poured/tapped ratio approach unity. The most common measures of this kind are Hausner ratio and Carr index, which use the ratios of poured and tapped powder volume. In this project, a closely related method will be used which relies on measurement of powder density within a fixed volume. (see Chapter 3.2.3). Both in case of fixed volume and fixed mass measurements, Carr index (K_i) and Hausner ratio (H) can be derived from density measurements using equations (3) and (4) respectively (Schulze, 2007 pg.178).

$$K_I = \frac{\rho_t - \rho_p}{\rho_t} \cdot 100\% \quad (3)$$

$$H = \frac{\rho_t}{\rho_p} \quad (4)$$

Where ρ_p and ρ_t are the poured and tapped bulk density respectively.

2.3.4 Selected Factors in Bulk Solid Flowability

Particle Size and Size Distribution- The relationship between particle size and bulk solid cohesiveness is a direct result of increased number of particle contacts in given volume of material. Small particle size acts as magnifier for all cohesive forces. Note that at the scale of an individual particle, attractive forces actually decrease with smaller size. Smaller particle radius means that smaller area at particle contact is in the proximity of van der Waals and other forces. However, the exponential impact of reduced particle diameter on the number of total particle contacts will always result in increased cohesion of bulk solid. At the scale of individual particles, the mass of particle also diminishes quicker than interaction area. This of course leads to adhesion forces eventually overcoming gravity forces, reducing powder's capacity to flow under its own weight.

Note that the above observations should hold true when comparing powders with similar statistical distribution of particle sizes. When the shape of distribution differs significantly between investigated powders, it has been often observed that powder with the same median particle size, but narrower distribution exhibits higher flowability than powder with wider size distribution (Schulze, 2007 pg.211).

Moisture- Amount of moisture adsorbed on the surface of polymer powder depends chiefly on the level of relative humidity in the atmosphere. On hydrophilic materials, such as TPU moisture adsorption starts with the formation of a monomolecular layer of water. Due to hydrogen bonds between water molecules, it is possible for a multi-molecular layer of moisture to form as well. Still higher moisture conditions may allow accumulation of additional water at the particle's surface, which fills surface pores and points of contact between particles, eventually forming menisci. In presence of menisci, particles will experience adhesion due to the liquid bridge, which is stronger than forces due to van der Waals or static charge. Fortunately, developing this level of moisture in

a material can only happen at greater values of RH. According to bulk solids literature (Schulze, 2007 pg.28) capillary condensation may begin at between 60 – 85% RH, making it extremely unlikely under climate controlled conditions used in this project. Although the presence of mono/multi-molecular moisture layer is far more realistic, its effect on adhesion forces is complex and cannot be generalised (Schulze, 2007 pg.29). In principle, the presence of adsorbed moisture allows material-material contact to be replaced by material-water contact. Depending on characteristics of material, such as Lifschitz-van der Waals constant, material's interaction with water can increase or decrease van der Waals forces. Testing whether moisture adsorption impairs TPU powder flow would be very challenging because of the detrimental effects of drying itself (see Chapter 4.3.3). Existing precautions to the development of moisture in powder as well as drying steps during production make this investigation very low priority.

Static charge- Compared to van der Waals forces, or forces from liquid bridging, static has negligible strength at small distances, such as particle contacts (Schulze, 2007 pg.25). However, considering the low bulk density of TPU powders, it is possible that a substantial number of particle interactions occur at larger distances, where static contributes the majority of attractive force. The problem of static control is a well-understood subject in the field of manufacturing. Accumulation of static charge poses a danger, especially if the bulk solid is flammable e.g. coal dust and flour. Discharging of bulk solid is done with ionised air, which is injected into pneumatic conveyors or 'air curtains' on a production line. Unfortunately, there are no small-scale solutions which can be easily implemented in a laboratory setting. Therefore, our approach is limited to preventing unnecessary static build-up and allowing powder to settle and slowly discharge on its own. In latter stages of the project, some batches of TPU will feature static control additive, which is means to improve conductivity and aid static charge dispersion.

2.4 Sintering and Coalescence Literature

When reviewing sintering theory literature we had expanded the scope of the review to encompass not only laser sintering literature but also basic research into sintering thermodynamics and modelling. We note early that the depth of presented information exceeds in many aspects the

scope of our project. Although a share of focus is given to the effect of polymers' viscoelasticity, further investigation of that topic is not feasible during this project. Still, we believe that this information will contribute to deeper understanding of polymer sintering and possibly find use at more advanced stages of material research.

2.4.1 General Sintering Introduction

The uniqueness of sintering process can be attributed to the possibility that all forces acting to condense particles into a solid may come completely from within the material. Addition of external forces, such as isostatic pressure in metal powder sintering is not strictly required for sintering to occur. It is possible to make an early distinction between the assisted and the unassisted sintering process. In unassisted sintering the main driving force will always be material's tendency to reduce its surface energy. This is the principal reason why particles will tend to fuse into a solid and why smaller particles with higher specific surface area sinter more rapidly. Especially in models which represent idealised experiment conditions all external forces such as pressure, thermal stress or gravity are assumed to be non-existent. Model particles are also assumed to be able to move freely and approach each other as sintering progresses. Temperature of the material is only an indirect factor. Its purpose to relax atomic interactions what enables material to move under internal forces. Effective sintering thus usually requires temperature exceeding material's glass transition temperature T_g , or melting temperature T_m .

Early research into the sintering process had led to discovery of a number of different mechanisms by which internal energies are converted into work and atomic motion. Possible mechanisms of atomic movement include diffusion and viscous flow, but also plastic flow, creep and evaporation. Which types of driving energies and atomic movement mechanisms are available depends chiefly on the type of material. For example, in materials with crystal grain structure the sintering process benefits from energy imbalance resulting from misalignment of crystal lattices at grain boundaries (Fang, 2010 p.20). In fact, the relative effectiveness of metal sintering compared to polymer sintering can be in part attributed to that additional source of driving energy. Because of the complexity of the subject, it is worth to make an early distinction between different sintering mechanisms and focus on the ones relevant to sintering of polymers.

All literature sources agree that when sintering micron-scale polymer particles the overall most important mass transport mechanism is viscous flow.¹ In this mode the energy is supplied by the gradient of surface energies, which develops between convex surfaces of (idealised) round particles and concave curvature of neck between particles in contact. Resisting the flow is the material's viscosity. This leads to widely accepted conclusion that the most important parameters influencing rate of sintering are: particle radius R , specific surface energy γ ,² and polymer viscosity η . These three parameters were used in the earliest successful analytical models of sintering thermodynamics, specifically in Frenkel model (Frenkel, 1945). This model from 1940s, which described idealised viscous flow coalescence can still be applied successfully to sintering of glass spheres. However, decades of experiments conducted on wide variety of polymers led researchers to begin accounting for complex time- dependent and rate-dependent behaviours stemming from viscoelasticity.

Viscoelasticity is the fundamental reason why polymer sintering is unlike metal or glass sintering processes. As discussed by Mazur (Mazur, 1995), viscoelasticity forms a unique function for each polymer formulation and further- for each molecular weight. Kinetics of viscoelastic sintering cannot be therefore characterised by any single material parameter and cannot be solved in closed form. This renders analytical solutions largely inapplicable whenever viscoelastic effects become significant. Furthermore, there exists no general scaling relation for influence of particle size- leading to major, qualitative differences in sintering behaviour of large and small particles of same material. Before development of comprehensive coalescence models, processes of e.g. spray coating and sintering were viewed as disparate- first one driven by surface wetting, the second by capillary pressure. While reviewing the available models it is important to understand their limitations, as they most frequently had been developed to model a narrow range of cases- for instance only high molecular weight, amorphous polymers (Mazur and Plazek, 1994), or only initial stages of neck growth (Milner). Modern, comprehensive models (Jagota et al., 1998, Lin et al., 2001,

¹ Importance of viscous flow will be diminished for smaller particles and for short sintering times, as it will be discussed.

² Note that for isotropic materials e.g. polymer melts specific surface energy is equivalent to surface tension.

Scribber et al., 2005) attempt to model coalescence on multiple timescales, using principles of elastic adhesion and viscoelasticity to improve accuracy of short sintering time predictions.

Coalescence of particles during sintering is only a part of the sintering process as a whole. A simple two-particle model cannot account for events which occur after neck growth between particles leads to the formation of closed pores. The rate of sintering cannot be estimated at all without knowledge of material's viscosity and therefore its temperature. Sections at the end of this chapter will be dedicated to topics of densification and temperature distribution following laser exposure.

2.4.2 Polymer Coalescence Modelling Introduction

Modelling of sintering process has a long history, beginning in the 40s with work of Frenkel (Frenkel, 1945), which was corrected by Eshelby (Shaler, 1949) to satisfy continuity equation. Through experiments performed on glasses and metals, those pioneering researchers were able to observe a major difference in sintering rates of amorphous and crystalline materials. The rate is measured as the growth of radius a of contact between two particles of radius R . As with many types of reactions and processes, the characteristic time to complete sintering was observed to vary exponentially with various material parameters. Influence of particle size on sintering rate was investigated soon after by Herring (Herring, 1950). Equation (5) is a generic scaling equation relating radius of sintering neck a to time t , starting particle radius R and factor K which is a function of material-specific parameters, such as viscosity and surface energy and therefore a function of temperature as well.

$$a = KR^\alpha t^\beta \quad (5)$$

Exponents α and β were found to depend on the dominant mechanism of mass transport. For the viscous, Newtonian flow mechanism, both exponents were found to equal 0.5. Thus, Frenkel's scaling law for Newtonian liquids is:

$$\frac{a}{R} = \left(\frac{\gamma}{\eta R} \right)^{1/2} \quad (6)$$

Where γ is material's surface energy and η is viscosity.

For an extended time, it was assumed that viscous flow is the only mode of practical importance in polymer sintering. This began to change as more real data became available, culminating in work of Mazur and Plazek (Mazur and Plazek, 1994) who began to compile a growing amount of research which was branching into different polymer types and process size/time scales. Despite reports of Frenkel model holding true in some experiments (Rosenzweig and Narkis, 1980), evidence for the special character of polymer sintering was mounting from work on PTFE braids (Lontz, 1964) and latex colloids (Eckersley and Rudin, 1990). Kuczynski's own observations on PMMA particles (Kuczynski et al., 1970) were yielding results different from Rosenzweig (Rosenzweig and Narkis, 1980). While Rosenzweig's observations conformed well to viscous sintering models, Kuczynski was observing significant neck growth at earlier times. Furthermore, depending on experiment temperature the time, exponents ranged from 0.2 at 137°C to 0.9 at 190°C. This was attributed to the non-Newtonian dependency of viscosity on strain rate. Another possible source of discrepancy was that Rosenzweig conducted experiments on relatively large 250-300 μm radius particles, while Kuczynski used particles smaller than 120 μm . In their analysis, Mazur and Plazek have concluded that the apparent agreement of some experimental data with purely viscous models was primarily a result of a limited range of tested particle sizes and sintering times. Their own experiments on a wide size range of PMMA and PEMA particles led to following conclusions:

1. Quasi-elastic, recoverable deformation is an important contributor to sintering of high molecular weight polymers. This is evident from neck ratio at time t : $a(t)/R^3$ being apparently proportional to compliance $J(t)$. Although experiment did not cover low-MW polymers, based on previous research on latex Mazur and Plazek speculate that in low-MW polymers elastic effects will be less important. This is due to high-MW materials displaying a plateau creep compliance value, while low-MW, non-entangled polymers do not. This suggests that viscous flow could occur sooner within the viscoelastic-viscous transition period.
2. Sufficiently small particles should be able to sinter to full density completely within quasi-elastic regime, since their characteristic sintering time τ_1 (time to complete sintering) is lower than the relaxation time τ . The critical particle radius for this condition is $R_c = \gamma\tau/\eta$.

When applied to all studied materials, this equation yielded sub-micron particle size requirement.

3. In high-MW polymers, viscous flow contributions are very small at early sintering times i.e. times shorter than the relaxation time of the polymer.
4. In order for high-MW, sintered polymer to reach the strength of the original material, molecular chains need to diffuse between sintered particles. This process is slower than particle coalescence, meaning that strength of the sintered solid should continue to improve after already reaching final density.

Despite being still widely cited in polymer sintering literature today, Frenkel's original model should be considered only a foundation for more successful contemporary models. It needs to be recognised that between the 1950s and 1990s there was an overwhelming amount of work done on the issue of coalescence modelling- far greater than the number of works cited in this chapter. From this point on the review will focus on the viscoelastic sintering model of Scribber (Scribber et al., 2005, Scribber et al., 2006) who synthesized his model based on works from two major research groups: Pokluda-Bellehumeur (Pokluda et al., 1997, Bellehumeur et al., 1996, Bellehumeur et al., 1998) and Argento-Jagota-Lin (Jagota et al., 1998, Lin et al., 2001, Argento et al., 1997). It will be discussed why we deem Scribber's work to have the highest chance of being relevant to sintering of TPU.

2.4.3 Viscoelastic Coalescence Modelling

Although the modes will be listed roughly in a chronological order, it is important to note that two or more of those processes can and usually do occur simultaneously. While elastic effects may, for instance, make a dominant contribution to contact growth in early stages of viscoelastic sintering, viscous flow's contribution will become more significant as time passes. It is useful to define sintering time thresholds following the same stages. Times t_o and t_v divide the coalescence process into three stages as shown in Table 2.3. Later it will be shown that according to some models those thresholds can be derived from material properties (Lin et al., 2001).

Sintering Stage	Sintering Time	Dominating Mass Transport
Elastic Contact / Adhesion	$t \ll t_o$	Elastic Deformation
Coalescence / Neck Growth	$t_o < t < t_v$	Viscoelastic Flow (or Viscoelastic Adhesion (Lin et al., 2001))
	$t_v < t$	Viscous Flow
Densification	$t_v \ll t$	Vapour Diffusion

Table 2.3: Simple summary of polymer sintering stages.

Elastic Adhesion- When two soft, incompressible particles initially come into contact, they will deform and adhere to one another at the contact surface. This case is described by the theory developed by Johnson, Kendall and Roberts (JKR) (Johnson et al., 1971). Theory's approach is based on balancing the work of adhesion versus work of elastic deformation and it has been confirmed experimentally by observations of solid latex and rubber spheres for a wide range of sizes (Mazur and Plazek, 1994). Although this model treats particles as elastic solids, it has been incorporated into larger models of sintering in a liquid state. Since elastic response precedes viscous flow in viscoelastic materials, JKR theory was used to estimate initial contact geometry for subsequent viscous coalescence in works of Mazur (Mazur and Plazek, 1994) and more recently Milner (Milner). For cases of viscoelastic materials specifically, the equation has been adjusted by Schapery (Schapery, 1989) and Hui (Hui et al., 1998), who treated the neck growth problem analogously to crack healing process, thus arriving at equation:

$$\frac{a}{R} = \left(\frac{9\pi J_e \gamma}{R} \right)^{1/3} \quad (7)$$

Where J_e is material's equilibrium compliance.

According to Lin (Lin et al., 2001) the JKR adhesion step takes place at $t \ll t_o$, where t_o is the threshold time between elastic and viscoelastic adhesive contact and is given by equation:

$$t_o = \frac{R}{2\gamma J} \left(\frac{9\pi J_0 \gamma}{R} \right)^{7/3} \left(\frac{16}{63\pi^3} \right) \left(\frac{R}{\delta_c} \right) \quad (8)$$

Where δ_c is a cut-off distance at which the adhesive force in area surrounding neck region is assumed to disappear.

Final neck ratio in this model is time-invariant, i.e. it depends only on material and particle parameters. The rate of achieving the final ratio is also extremely rapid as well, increasing with $t^{1/7}$ (Hui et al., 1998) instead of $t^{1/2}$ from Frenkel's viscous flow. In practice, Lin (Lin et al., 2001) found Equation (7) unreliable in modelling Polypropylene melts. Using that equation the obtained neck radius ratios were higher than 1, while realistic values should all be less than 1. It is likely that JKR theory cannot be directly applied to polymer melts with significant viscous component and that this stage's contribution would also be negligible at the particle size scale of tens of microns.

Viscous Sintering and Zipping-Stretching Crossover- Most of the contact growth between particles at the size scale of tens of microns occurs by viscous flow. Most sintering models treat this stage as a single event, making it possible to apply uniform scaling laws once viscoelastic effects cease to be significant. However, when observing coalescence it is possible to distinguish two apparently different stages. At early stages of growth, the neck is sharp at the root and particle contact seems pinched. As contact grows, there seems to be an instance where the sharp cusp starts to smooth out (Figure 2.10). Models developed by Jagota (Jagota et al., 1998) and Lin (Lin et al., 2001) make a distinction between the two modes of neck growth and postulate that the initial zipping mode is partially driven by adhesive forces just outside the neck curvature. These forces- primarily Van der Waals force pull surfaces of particle together. As contact radius grows the separation of surfaces outside of neck decreases and adhesive forces diminish, leading to the conventional surface-tension-driven flow. Here we will use terms coined by Jagota (Jagota et al., 1998) referring to the first stage as *zipping* and the second one as *stretching*. It needs to be reiterated that according to Jagota, both zipping and stretching modes occur within viscous flow regime- after elastic adhesion and viscoelastic period. This contrasts with subsequent work of Lin, who treated the zipping stage as part of the viscoelastic period which transitioned into the stretching stage as viscous behaviour took over. Jagota expects the shift in time exponent to occur even for materials such as silicate glasses, which usually are not treated as viscoelastic since the time spent in viscoelastic relaxation is negligible compared to experiment times. This alternative explanation might become useful if low-viscosity TPUs used in this project are found to not have a significant relaxation time. Jagota bridges the gap between models of adhesive contact prevalent in

spray coating and surface curvature drove models prevalent in sintering literature. In order to succeed, Jagota's model had to explain the high coalescence rates of small ($<1 \mu\text{m}$) particles and explain the change of behaviour to slower rates as particle size increases.

Thresholds for crossover in coalescence behaviour were not based on time like in Lin's model, but instead, Jagota expected them to happen at calculated neck ratios. The ratio also depended on the original size of the particle. At $R \leq 200\text{nm}$ the zipping-stretching crossover will occur at $a/R \sim 0.5$. At $R \geq 10\mu\text{m}$ crossover will happen at $a/R \sim 0.1$. Crucially, at neck ratio 0.5, it becomes possible for a closely packed system of particles to coalesce to full density, in which instance the entire coalescence process can be theoretically completed within zipping mode- confirming conclusions of Mazur. In absence of zipping stage, the model predicts that there would be a 100-fold increase in sintering rate when reducing particle radius R from 100 to $1\mu\text{m}$. The addition of zipping mode makes the rate increase 1000-fold. Jagota's model confirms Mazur's conclusion that during the zipping stage it becomes impossible to define a scaling relationship between coalescence rate and particle size. Here, this is a direct consequence of incorporating Van Der Waals forces, which do not scale with R . There is a remarkable degree of qualitative agreement between work of Jagota and Mazur, despite work being conducted on different polymers with Jagota's having minuscule relaxation time and Mazur's in order of 10^6s .

A competing theory of zipping-stretching crossover comes from unpublished work of Milner (Milner). This approach is worth attention, because it manages to arrive at the same predictions without invoking adhesive forces, but instead by recognising that viscous flow can occur according to two different boundary conditions. Condition one is analogous to the problem of droplet spreading on a flat substrate and in that mode the velocity field of viscous flow must be zero at the spreading surface. In condition two the velocity field at the surface has a radial, outward component because of capillary forces pulling material towards the curvature of contact rim. This model opens up the possibility of observing zipping-stretching if Van der Waals forces were insignificant, which is a possibility. Because those forces diminish with the cube of distance- they are eight times lower for two spheres system than for sphere-plane system (Jagota et al., 1998).

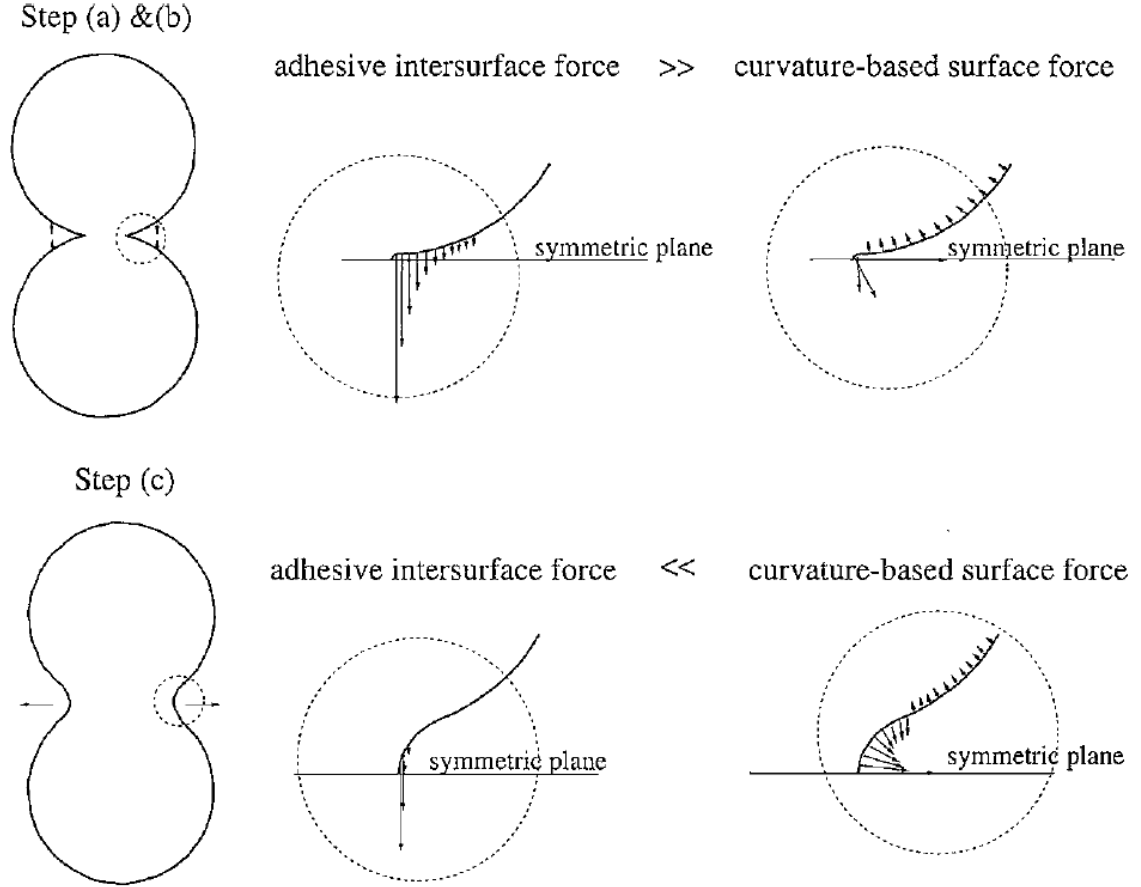


Figure 2.10: Jagota-Lin model of coalescence, reducing it to three steps. Elastic Adhesion (a), Zipping (b) and Stretching (c) (From (Lin et al., 2001))

Viscoelastic Adhesion- Lin's model (Lin et al., 2001) is unique in modelling early viscoelastic coalescence as an adhesion problem. Lin places it at a time between JKR adhesion and viscous flow. $t_0 < t < t_v$ where t_v is given by equation:

$$t_{viscous} = \frac{1}{16} \left(\frac{63\pi^3}{2} \right)^{2/5} \frac{R}{J2\gamma} \left(\frac{\delta_c}{R} \right)^{4/5} \quad (9)$$

In this mode the contact growth is still extremely fast, as it scales with $t^{1/7}$ via equation:

$$\frac{a}{R} = \left(\frac{63\pi^3}{16} \right)^{1/7} \left(\frac{\delta_c}{R} \right)^{2/7} \left(\frac{J\mathcal{M}}{R} \right)^{1/7} \quad (10)$$

Lin was able to obtain good fit with experimental results from Mazur (Mazur and Plazek, 1994) on PMMA particles. However, fitting of model to data resulted in the critical separation value δ_c to be adjusted to value of 50nm. This value is unrealistically high, as Lin admits that value of 17nm used by Jagota was 'quite large'. Schultz (Schultz, 2004p.19) notes that this is likely to be a result of Lin's

model omitting curvature based forces at this stage of coalescence. It seems that time thresholds cannot be used to simply divide the process into discrete phases and that adhesion forces act simultaneously to conventional curvature based forces.

Viscoelastic Sintering and Transient Models- Constructing a model relevant to viscoelastic deformation required several important modifications to Frenkel's model. Firstly, in its original form the model was only correct for spheres of constant volume, not accounting for the significant increase in radius at latter stages of coalescence. A correction by Pokluda (Pokluda et al., 1997) allowed the model to be applied to much later stages of coalescence, by appending the model with the calculation of growing particle radius. The second important development came from Bellehumeur (Bellehumeur et al., 1998) who extended Pokluda's model to viscoelastic materials by incorporating Upper Convected Maxwell (UCM) model into his numerical solution. In its simplest form, the Maxwell model describes viscoelastic liquid with three parameters: viscosity of dashpot η_0 , compliance of spring J_0 and relaxation time τ . At long times Maxwellian material behaves like a fluid with viscosity $\eta = G\tau$ where G is the instantaneous shear modulus. At times shorter than the relaxation time, instantaneous compliance is equal to:

$$J(t) = \frac{1}{G} + \frac{t}{G\tau} \quad (11)$$

Bellehumeur's model was found to conform well to experimental results on polypropylene copolymer resins (Bellehumeur et al., 1998). The UCM model predicted that high relaxation times (i.e. further departure from viscous liquid behaviour) would lead to slower rates sintering, relative to Newtonian model. It needs to be addressed that in Bellehumeur's experiment the relaxation times were not determined experimentally, but rather adjusted arbitrarily to fit the model's predictions to data and might not be realistic. Bellehumeur's time scaling exponent 0.5 was in agreement with viscous sintering models, suggesting that his materials did exhibit significant viscoelastic properties. Bellehumeur's model was also successfully used by Muller (Muller et al., 2012) to predict coalescence rates of a range of 'model polymers' which were liquid at room temperature. However, Bellehumeur's model contradicts findings of Mazur and Plazek (Mazur,

1995) who found viscoelastic effects to accelerate coalescence relative to Newtonian model. The likely cause of the discrepancy is the difference in viscosities. Mazur's polymers were approximately five orders of magnitude more viscous than Bellehumeur's. This contradiction sparked Scribber's hypothesis (Scribber et al., 2005) saying that steady state approximation of UCM model is inappropriate for cases of highly viscous polymers, or alternatively for cases where experiment time does not greatly exceed material's relaxation time. In TPUs the copolymer structure was found to make both viscosity and relaxation time highly sensitive to changes in block length and molecular weight (Velankar and Cooper, 1998). This opens up the possibility of observing both Newtonian and non-Newtonian behaviours in different TPU formulations.

Scribber updated Lin's model by incorporating UCM constitutive behaviour without assuming steady state. This alteration accounted for transient viscosity behaviour in early times where viscoelasticity is significant. As a result of this adjustment, Scribber (Scribber et al., 2006) was able to obtain correct qualitative predictions during tests on three isotactic polypropylenes with different molecular weights. When the transient UCM model was run based on experimentally determined material parameters- it correctly predicted coalescence rates higher than Newtonian at early sintering times. Increasing relaxation time from experimentally determined 1.54s to 3s increased the early neck ratio from ~ 0.4 to ~ 0.5 at 20 seconds. Note that in this experiment neck ratio of 0.9 was achieved at ~ 400 s. The conclusion that longer relaxation times boost neck growth seems to agree with models of Jagota and Lin, who predict that early, viscoelastic coalescence stages are more rapid. If the relaxation time is prolonged, material will take longer to reach the strictly Newtonian coalescence rates. This conclusion opens a possibility that sintering of TPUs could be improved by finding formulations maximising the relaxation time if this can be achieved without an excessive increase in viscosity.

2.4.4 Densification

In the final stage of polymer sintering, we will see closed pores formed out of gas which used to occupy space between particles. While it's possible to analytically derive the size of pores at the moment of closing, it requires gross simplification of the particle system- usually into some form of close-packed structure of equal sized spheres (Sun et al., 1991). All sources of empirical data agree

that all other things being equal- lower initial bulk density will lead to entrapment of larger amount of gas in bubbles (Crawford and Kearns, 2003). At the point of pore isolation, coalescence models discussed above cease to be relevant and the rate of densification is reduced (Kontopoulou and Vlachopoulos, 1999). Unsurprisingly- it is beneficial to achieve as high density as possible before pores close. Once pores are separated from surrounding atmosphere their size and shape will be controlled by a gas diffusion process. One of the widely cited numerical models of that process occurring in polymers was created by Kontopolou (Kontopoulou and Vlachopoulos, 1999). The model is based on the simultaneous solution of diffusion, conservation of momentum and continuity equations. The rate of change of bubble radius R is calculated based on two equations:

$$\frac{dR}{dt} = \frac{1}{4\eta} [(P_g - P_f)R - 2\sigma] \quad (12)$$

$$\frac{d}{dt} \left(\frac{P_g}{R_g T} R^3 \right) = 3R^2 D \left(\frac{\partial c}{\partial r} \right)_{r=R} \quad (13)$$

Where P_g is the pressure inside the bubble, P_f is the system pressure, R_g is the universal gas constant, T the system temperature, σ the surface tension and c the concentration of air in the system.

According to work of Kontopoulou, the dominating factors in the rate of bubble dissolution are bubble size and overall void volume in material bulk. The latter influences whether polymer melt becomes saturated with gas before bubbles can dissolve. The impact of viscosity is marginal and only significant when bubbles shrink to a fraction of their original size. Mechanically, this is caused by viscosity generating a normal force resisting shrinkage of a bubble. Viscosity was shown to have no correlation with gas diffusivity in molten or solid polymers. Rather, diffusivity depends on the molecular size of gas and on the molecular structure of the polymer. This leads to the conclusion that there is no practical way of addressing densification stage by material modification, short of significantly altering its molecular structure. When designing LS TPU the priority should clearly be placed on optimising for coalescence stage and initial bulk density.

2.4.5 Discussion

The main limitation of this review chapter which needs to be recognised is that the understanding of the sintering process is fragmented amongst the issues of coalescence, densification and temperature distribution. Each of those areas is quite complex in itself and relationships between all those areas are likewise complex and often not obvious. Attempts to integrate all those problems into a singular model were rare and not successful at predicting experimental results. To illustrate just how complex the sintering process is, Figure 2.11 lists different areas of which would need to be accounted for in truly comprehensive sintering model and possible ways in which they interact.

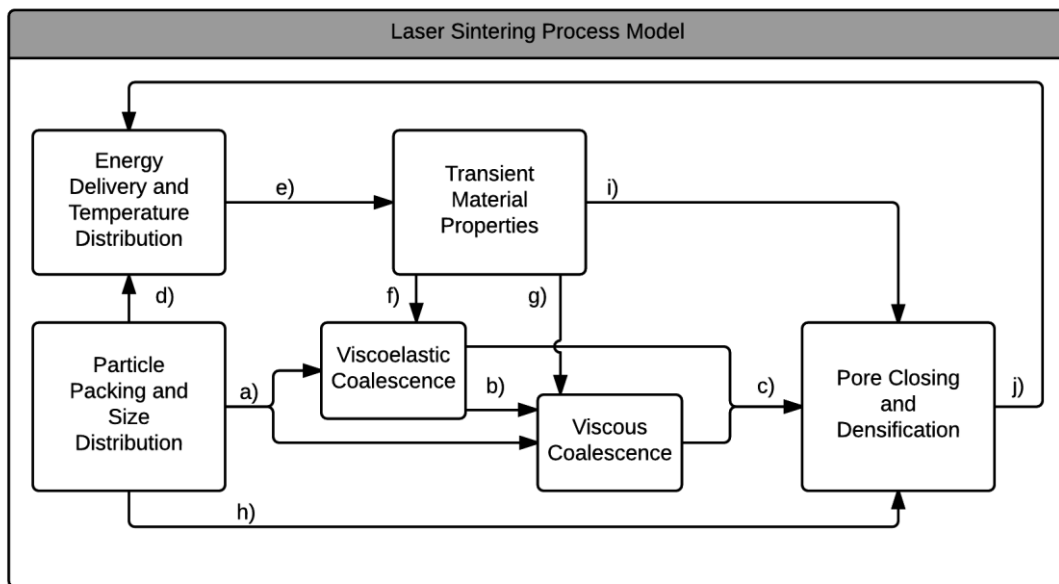


Figure 2.11: Chart of different modelling issues in polymer laser sintering.

From the start, *Particle Packing and Size Distribution* has wide-reaching consequences throughout the process. Their immediate result on sintering is the influence a) on the rate of viscous and viscoelastic coalescence. As stated by Mazur- it might be impossible to develop a simple scaling relationship in this instance. It is certain that Particle Packing also will influence interaction d) with a laser beam and resulting melt temperatures. For instance, a larger amount of gaps between particles would lead to deeper penetration of laser beam, letting it interact directly with deeper-lying particles. However, there could be a possible trade-off as the less dense powder is worse at heat conduction (Li et al., 2010). Temperatures which develop in polymer melt, as well as heating

and cooling rates, will determine e) its various temperature-sensitive properties, the major one being viscosity. This is yet another massively challenging topic which had not been modelled with sufficient accuracy. At early times, where viscoelastic effects are important coalescence will be affected f) by compliance $J(t)$ and later affected g) primarily by viscosity η_0 . Link b) between viscoelastic and viscous stages of coalescence will diminish with increasing sintering time, when viscous flow contributions dominate. However, the link may still be important if the coalescence process is interrupted prematurely, for instance when melt temperature cannot be maintained long enough in LS process. Regardless of specific mechanism- sufficient growth of contact neck between packed particles should lead c) to the formation of closed-pore structure. The neck/particle radius ratio at which pores become isolated is heavily dependent h) on particle size as well as the packing efficiency. Densification after pore closing is the last stage of sintering and it may be dependent i) on yet another set of material properties such as solubility and diffusivity of gas. Finally, there is likely to exist some feedback mechanism j) between densification and temperature distribution. Since not all particles on powder surface can be illuminated by laser directly, some particles will rely on thermal conduction to achieve melting temperature. A good degree of densification and therefore low pore content would improve the thermal conductivity of the bulk material, facilitating melting of deeper lying particles and also re-heating underlying layers what could improve interlayer fusion.

Despite this level of complexity, we find fairly good agreement between existing simulations and experimental data, but only in studies dealing with amorphous polymers, mainly polycarbonate(Childs et al., 1999, Williams and Deckard, 1998). Meanwhile, studies dealing with semi-crystalline materials such as Nylon (Childs and Tontowi, 2001, Schultz, 2004) have less success at reconciling experimental and simulation data. Some factors which make those materials more difficult to simulate are the latent heat of melting and viscosity changes during melting. Because of sharp viscosity drop at T_m threshold, small errors in predicted temperature can lead to major errors in predicted density. As TPU has more in common with melting behaviour of semi-crystalline polymers, we believe that simulation of TPU melting would likewise be very challenging to develop.

Facing true complexity of the sintering problem, we concede that rather than attempting an integrated approach, it is more realistic to draw conclusions from each of the modelling areas separately. Because densification process depends on gas diffusivity, it cannot be controlled by means other than changing polymer entirely. Therefore, no useful conclusions can be drawn from densification models. The main factors in temperature distribution models are related to processing conditions, not material parameters. Coalescence models are the most important to us since they are the most heavily impacted by material properties.

2.4.6 Conclusions

Despite the overwhelming complexity of the sintering process, modern viscoelastic sintering models offer interesting potential avenues for future research. In particular, correlating viscoelastic properties with sintering time would be novel and valuable finding in the context of laser sintering. One of the early indicators that viscoelasticity might be a factor in LS is that laser sintering process is relatively rapid, what might increase the importance of short timescale events, where viscoelasticity dominates.

The review drew our attention to the multi-stage character of the sintering process. Not accounting for viscoelastic effects, we can still subdivide the sintering process into issues of particle coalescence (before pore closing) and densification (after pore closing). In the latter part of the project, this observation will contribute to the adoption of the single-layer sintering experiment. It is informative, that upon reaching densification stage, sintering is no longer sensitive to the standard set of material properties since diffusivity of gas is controlled mainly by molecule type. The final size of pores is in effect determined entirely in the coalescence phase, by the amount of gas remaining in pores before their closure. Bulk density and arrangement of particles, therefore, seem to be important factors in sintered part density.

3 Methodology

3.1 Thermal Properties

3.1.1 Temperature Scan Calorimetry

In principle, DSC apparatus is used to detect any endothermic and exothermic events occurring within a material sample. DSC system accomplishes this by measuring temperature and power consumption of two highly sensitive and inert platinum furnaces- typically one containing sample within a sealed aluminium container and the second an empty container. The difference in power consumption, while maintaining temperature or heating up both furnaces, is due to thermal properties of the sample and endo/exothermic events it generates. The most common use of DSC is observing thermal events during steady rate heating and cooling of a sample (temperature scan).

Valuable approach when performing measurements on TPU is to perform the same measurement twice, which is done without the sample leaving the furnace. First temperature scan reveals phase structure of virgin, as-delivered material. As the first scan melts and recrystallizes the sample, it partially resets and homogenises material's phase structure, removing certain features visible during the first scan. The second scan can, therefore, act as a baseline and is important at highlighting subtle phase transitions in the virgin material.

During DSC measurements the heating rate was set to 10°C/min unless mentioned otherwise. This rate forms a good compromise between accuracy and signal strength. The samples weighed 10±0.2mg in all tests. Powder samples were tested within sealed aluminium pans. During temperature scan, the temperature was set to 200°C maximum.

Typical program steps were as follows:

- 1: Equilibrate at 20°C
- 2: Heat to 200°C at 10°C/min
- 3: Hold isothermal for 1 min
- 4: Cool to 20°C at 10°C/min
- 5: (optional) Repeat steps 2-4

3.1.2 Isothermal Calorimetry

While the temperature scan method is by far most common, an alternative approach is to monitor furnace energy flux while maintaining steady furnace temperature (isothermal). Since crystallisation and melting transitions are not instantaneous, it is possible to stop the temperature scan within the range of melting or crystallisation temperatures and observe their rate. One use for this type of experiment is the identification of the supercooling region, as discussed in Chapter 2.2.2 and tested by Drummer et al. (Drummer et al., 2010) on a range of candidate materials.

In this type of experiment, the rate of temperature scan determines how fast the system can be brought to isothermal hold temperature. If crystallisation or another event occurs rapidly, it might be complete before furnace reaches the target temperature and proper data acquisition starts. High rates allow to capture more rapid events, but without dedicated quenching system, we were limited to the rate of 50°C/min. Sample weight was identical as in temperature scan experiments: 10±0.2mg.

Typical program steps were as follows:

- 1: Heat to 200°C at 20°C/min
- 2: Hold isothermal for 1 minute
- 3: Cool to set hold temperature at 50°C/min
- 4: Hold for 10 minutes, registering DSC signal

3.1.3 Thermogravimetry

Thermogravimetric Analysis (TGA) is one of the standard methods of investigating thermal decomposition in polymers. It operates by heating up a sample of the material, usually under Nitrogen atmosphere and measuring changes to weight as material decomposes into gaseous by-

products. This simple method is often supplemented by spectroscopy of evolving gases which are indicative of the type of reactions taking place. In this project, TGA scan was performed at a standard rate of 10°C/min, from 50 to 700°C, under Nitrogen atmosphere.

3.2 Bulk properties and Handling

3.2.1 Moisture Control

Elastollan® TPU technical data sheet

(BASF)(BASF)(BASF)(BASF)(BASF)(BASF)(BASF)(BASF)(BASF) contains directions for handling and drying of granulate. The sheet cited here is for TPU grade C85A. It is similar to the AC88A12 formulation used in the preliminary studies. Both formulations are based on polyester and the hardness rating is approximately correct. Both these factors influence water adsorption rate and recommended drying temperature respectively. Because of hygroscopic nature of TPU, moisture control requires minimisation of exposure to air. Optimal level of adsorbed moisture in TPU during processing is lower than 0.03%. Once exposed to air at 50% relative humidity and 23°C, it would take 1-2 hours for dry TPU to adsorb over 0.03% moisture. Conditions in project's laboratory are similar, with ~50% RH and temperatures within 20±1°C. However, since material in this project is in powdered form with much greater surface to volume ratio, we can expect its capacity to absorb moisture to be greater. Powder also needs to be sieved at different stages leading up to sintering, what increases its exposure to air.

Technical data sheet again specifies suggested drying times and methods. For grade C85A recommended temperature is 80-90°C, for time of 2-3hrs. Recommended temperature is 10°C higher if using non-dehumidified air or if TPU grade is of greater hardness. It seems that this recommendation is made for starting humidity of 0.4%. According to the same technical sheet, powder conditioned at laboratory ambient conditions should not accumulate more than 0.2% of moisture.

Drying steps needs to be performed directly before sintering in order to be effective. Using the directions from technical sheet as a rough guide, drying temperature was set to 90°C and time to 1h minimum. It was performed in a large, 500l oven. For improved drying, powder was spread in

~10mm thick layers and placed on trays stacked interchangeably with trays containing silica gel. There was no forced flow of air, but due to large volume of the oven it was presumed that convective flow of air would be of benefit. This drying step was performed directly before build. Since standard build chamber temperature was also set to 90°C, the drying step was conveniently combined with the powder pre-heat step, allowing powder manually fed into the machine to be both hot and dry.

In test cases where TPU was not being sintered, but for instance tested for bulk density, drying step was not implemented. Just like annealing, drying TPU powder inevitably led to clustering and drop in bulk density (See Chapter 5.2). In cases where properties of virgin powder are reported, TPU was only sieved and conditioned to ambient laboratory conditions. Since moisture control could not be implemented in those cases, measurements belonging to one test were carried out in short series, on the same day. This way, measurements remained accurate in comparison to rest of data from the same test. Comparisons of data from separate tests may be less accurate.

3.2.2 Powder Annealing

Initially, annealing was performed simply by heating powder spread on trays, in a way identical to the drying method in Section 3.2.1. Powder annealed this way tended to form a cohesive cake, which had to be re-constituted into loose powder by forcing it through a sieve. The tray approach was quickly replaced by annealing inside rotating drum (Pictured in Figure 3.1). The benefit of rotating drum was that constant tumbling prevented powder from settling into a solid cake. Although the drum would form a deposit of cake on the inside walls, around 70% of material could be passed through a 400µm sieve with only light hand agitation. Material which failed to sieve tended to consist of round, pebble-like agglomerates which had formed as result of tumbling motion (See Figure 3.2).

Tumble-annealing was successful in improving annealed powder's flow and bulk density, relative to tray-annealed powder. Tumble-annealed A02 powder (studied in Chapter 5) had on average ~40% greater poured bulk density and ~25% greater tapped density than powder annealed on trays.

Due to the bulky nature of the drum, as well as presumed insulating properties of the powder deposit on inner walls, annealing was done over a prolonged time to ensure thorough annealing of

the entire volume of powder. The oven which contained the drum was set to 90°C for 10hrs. Then, the heaters were turned off and while still rotating, the drum was allowed to cool to ambient temperature over additional 6hrs. Powder was sieved using a 400µm sieve and any agglomerates not passing under light manual agitation were discarded.



Figure 3.1: Rotating drum used for drum-annealing, with the front cap removed. Entire assembly fits inside an oven. Propulsion is by one roller's shaft extending through the back of the oven. Green FEP coating minimises adhesion to inner walls while annealing. Motorized with an electric motor, the drum rotates at approximately 70rpm when loaded.



Figure 3.2: Round agglomerates from the drum-annealing process.

3.2.3 Bulk Density Testing

Bulk density (BD), which is the weight of powder per unit volume is one of the most frequently reported values in this project. The reason why the BD value is so useful is because it quantifies hugely complex flow and compaction behaviour of plastic powder. This behaviour is influenced by numerous factors, such as particle shape, size distribution, moisture, temperature, static charge, viscosity and flow additives (Schulze, 2007, p.35). By setting up different experiments, those factors can be isolated and studied, using the BD value.

Bulk Density was chosen for this project above other quantifiers of bulk behaviour, notably *angle of repose*. Attempts to use the angle of repose measurement (See Figure 2.9) revealed it is unsuitable for powder with very poor flowability and tendency to form clumps. Firstly, TPU powder could not freely pass through the funnel without aggressive agitation. Secondly, the clumpy nature of powder led to asymmetrical shape of the cone and random formation of tall, but very unstable piles, creating ambiguity when taking measurements.

Measurement of BD can be accomplished by measuring either volume of known mass, or mass of known volume. In the first case, a graduated cylinder is used. Like in the case of an angle of repose, clumpy nature of powder made it difficult to take an unambiguous reading from the

graduated cylinder. The second method was preferable, using a steel measuring cup of exactly 100ml volume. This measurement procedure was based on a document published by U.S. Pharmacopeial Convention (Convention, 2012). The amount of powder needed to complete the test was sieved using an 180 μ m analytical sieve. Sieved powder was then gently poured into a measuring cup, to the point of overflowing. Excess powder was removed using a metal blade held perpendicular and in contact with measuring cup's opening. The weight of powder in the measuring cup was recorded. The measurement was performed three times and then the mean value was calculated. The result of this measurement will be referred to as *Poured Bulk Density* to differentiate it from measurements performed on tapping-compacted powder,

The value of BD can be a useful indicator of powder flowability since BD depends on the same collection of factors. The strength of flow-inhibiting factors can be further tested by comparing Poured Bulk Density and density of powder compacted by tapping i.e. *Tapped Bulk Density*. Sudden deceleration after the state of free-fall induces forces which overcome cohesive forces in powder bulk. In powders with very low cohesive forces, poured density will be similar to tapped density. This principle is identical to the one used in the Hausner Ratio test. The crucial difference is that the Hausner ratio relies on volume measurement, which as it was mentioned is unsuitable for clumpy material. Instead, an analogous ratio of densities is used in this project.

Following the same USP guidelines, tapped bulk density test was performed as follows: Measuring cup was fitted with extension, doubling the volume of powder it can contain before compaction. The extended cup was then placed on a mechanical tapping platform (See Figure 3.3), able to tap it 300 times per minute, by lifting the cup at height of 1cm. The extended cup was tapped 500 times. It was determined that beyond that number there was less than 1% further increase in density. After tapping, the extension was removed from the cup and excess powder was scraped off, like in normal BD test.

In practice, density measurements were highly precise, showing on average $\pm 0.7\%$ deviation from the mean. When measuring tapped density, precision was even greater, showing average $\pm 0.3\%$ deviation from the mean. Due to this precision, error bars are omitted in figures reporting bulk densities.

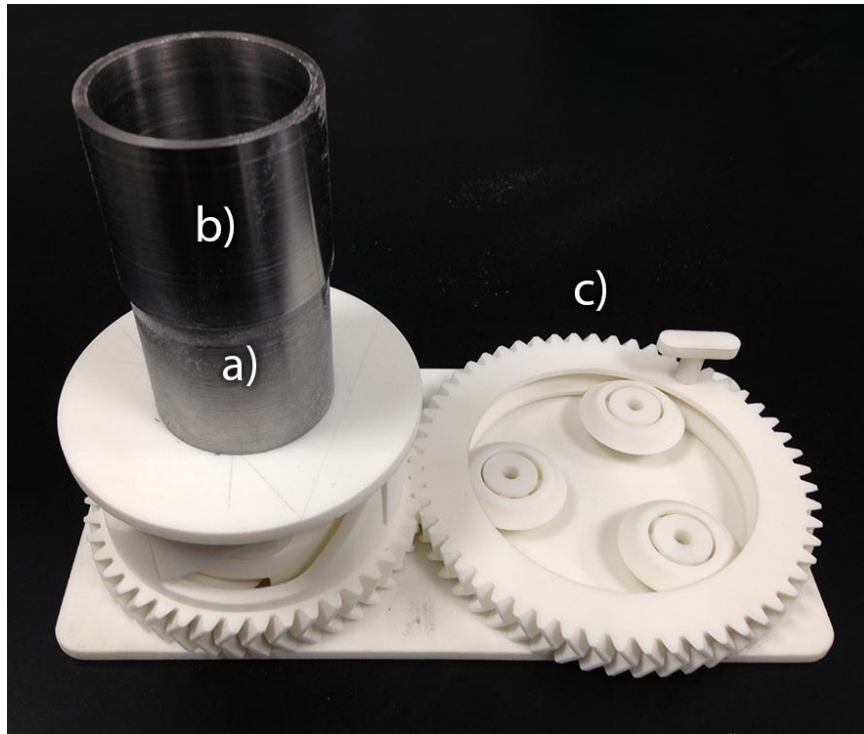


Figure 3.3: Tapped bulk density tester. When operated with crank c), measuring cup a) is being rotated on cam and tapped when it falls under gravity. After tapping, cup extension b) is detached and excess powder removed, leaving 100ml volume of compacted powder.

3.2.4 Static Control

Two greatest potential sources of static build-up were powder sieving and tumble-annealing. The true level of static was not possible to measure in absence of specialised equipment. Instead, bulk density measurement was used to directly quantify possible impact of static on powder flow. Two samples of 0.2wt% Aerosil powder from Flow Agent study were prepared. One sample of powder was tumbled in the annealing drum, without applying heat, for two hours. The second sample was sieved through 400 μ m sieve twenty times. Tapped Bulk Density of tumbled powder dropped by 3.4%. Tapped Bulk Density of sieved powder increased by 2.7%. This result lets us conclude that tumbling-induced static does have a detrimental effect on powder flow (assuming no other unknown mechanism), while sieving either does not generate a substantial amount of static or the increase in static is outweighed by the benefit of e.g. better powder reconstitution. Based on those results, experiments were scheduled such that if powder was to be tumble-annealed, it would rest for at least 24hrs before being used in an experiment, to allow static to dissipate. Note that in practice, tumble-annealing was also the cause of particle clumping, which had a much greater detrimental effect on bulk density.

3.2.5 Powder Cake Bulk Density

This measurement tested the bulk density of semi-solid powder cake which forms around fabricated part in the build chamber. In the case of TPU powder, the cake was found to be solid enough to be cut and retain its shape. Thanks to the solid consistency, it was possible to create a tool for cutting cylindrical 'cores' from the cake at the periphery of build volume. The cutting tool itself was a section of PVC pipe, with a diameter of 31mm, sharpened to cut into powder cake. After core was cut, it was carefully removed out of pipe section, to preserve its shape. Core's length and weight were then measured, allowing to calculate its volume and bulk density.

3.2.6 Particle Size Distribution

The system used for all Particle Size Distribution (PSD) measurements in this project was Malvern Mastersizer 3000, equipped with air suspension system. This type of system uses Laser Diffraction Particle Sizing method, which relies on the difference in angle of light scattered by small and large particles in suspension. Scattered light gathered by an array of detectors is processed by software algorithms applying Mie theory to determine the approximate size of particles responsible for scattering pattern. The accuracy of the measurement depends on powder's conformity to a set of assumptions about its shape and optical properties. For all tests, software was configured to use a set of assumptions developed for rough, milled powders. Pre-set particle absorption index for this type of particle was 0.010. Value for TPU's refractive index was set to 1.463, taken from BASF documentation for Elastollan® TPU. Gas pressure in the air suspension module was set to 3.2 bar. The scattering model was set to 'Mie' option and the analysis model was set to 'General Purpose'.

Size distribution data has statistical quality which can be communicated in several ways. $D_v(x)$ denotes volume-weighted distribution. Thus, value $D_v(10)$ denotes diameter of particles constituting 10% total material volume (or material mass). $D_v(50)$ denotes volume-weighted median diameter. Because this median value is determined by volume contribution, it is skewed towards larger particles in the distribution. An alternative measure is the surface-weighted median diameter $D[3,2]$. This median is determined by surface area contribution and therefore is skewed towards smaller particles. Another reported value is Specific Surface Area (SSA). This value is a

calculated approximation of particle surface area in a given mass of powder. Powders with smaller particles have a greater surface to volume ratio and therefore greater SSA.

Variables used to estimate particle size from diffractometer data are approximate and it is likely that absolute values for particle diameters would be different when measured by a different method, such as camera-based system. However, high precision of Mastersizer system means that relative size comparisons made between different powder batches should be accurate, as long as powder particles do not show major differences in optical properties or shape.

3.2.7 Unconfined Compressive Yield Strength

Due to the project's extended focus on bulk properties, a method was needed to test powder's susceptibility to forming a cohesive cake. One such method, previously used in food and soil testing is Unconfined Compressive Yield Strength (UCYS). In this method, a sample of particulate material is usually compressed in a cylindrical mould, to form a cohesive specimen. The specimen is extracted from the mould and tested in compression in a way analogous to solid material. Because of lack of confinement, particles forming the specimen are free to move against each other as the specimen is compressed. If specimen behaves in a cohesive manner, it will fail in shear mode, when contacts between particles are broken.

The protocol used in this project was developed based on ASTM Standard D2166 (D-06) and comments from Schulze (Schulze, 2007, p.181). Each mould consisted of a 70mm length of aluminium pipe, with the internal diameter of 30mm. Those dimensions are in agreement with ASTM D2166 recommendation. When loading powder into the moulds, an extension was added to the mould to enable overfilling and compaction by tapping. This procedure was analogous to the way bulk density measurement was conducted as described in Chapter 3.2.3 and used the same tapping tool. After tapping the extension was removed and excess powder shaved off. Loaded moulds were placed in an oven for high temperature caking. We found that powder was losing volume during caking, what made it simple to extract the caked specimens by upturning the moulds.

Notably, we modified standard test protocol by not applying compacting pressure to the powder during caking. There are two reasons why this modification benefited this test case. As explained by Schulze, due to friction from mould walls, stress distribution in powder volume is

uneven, diminishing rapidly towards the bottom of the mould. This leads to non-homogeneous strength of powder cake and underestimation of cake strength for given compacting load. Secondly, we believed that density of tapped powder would be more representative of powder in LS system, than heavily compacted powder. We also found that our caked specimens would detach from the mould wall as a result of shrinking.

Compressive testing was performed on a texture analyser equipped with a 500N load cell (Figure 3.4). Test was performed up to the breaking point and the Ultimate Yield Stress was recorded.

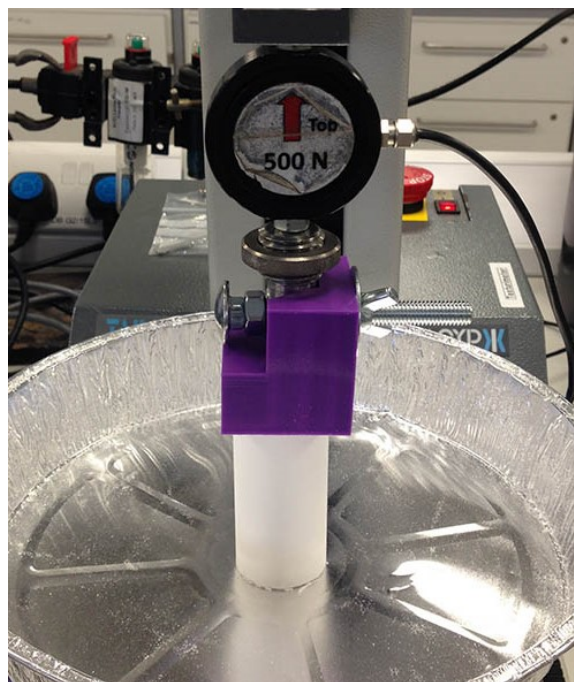


Figure 3.4: Unconfined Compressive Yield Strength testing of a caked TPU powder specimen.

3.3 Linear Regression

Linear regression was performed using Minitab software. This software allows us to perform multiple regression where single response variable (work during extension) can be influenced by multiple predictor variables. What's more, the software has implemented methods for detecting and compensating for correlation between variables. The degree of variable correlation is communicated via Variance Inflation Factor (VIF). VIF is an estimate of inflation of regression coefficients due to predictor correlations. According to software documentation VIF above 5 indicates a moderate degree of correlation. The software also provides an adjusted measure of

squared residuals ($R\text{-sq}(\text{adj})$) which indicates the overall accuracy of regression model when multiple predictors are used. Higher $R\text{-sq}(\text{adj})$ value indicates better regression fit to data. In addition to $R\text{-sq}(\text{adj})$, it is important to monitor the residuals for any patterns. Patterns can emerge when residuals are plotted with respect to e.g the order in which measurements were taken. In a correct linear model, the residuals should have completely random, Gaussian distribution.

3.4 Monolayer Specimens Sintering and Testing

3.4.1 Specimen and Grip Design

Designing a tensile test for monolayer experiment began with considering the required specimen shape. Monolayer specimens are extremely weak compared to standard tensile specimens. Frequently they also had a large degree of porosity, with pores effectively forming holes in specimens. Because of those factors, it was desirable to maximise specimens' width, so that specimen's strength is maximised and the impact of porosity is minimised. Specimens in this experiment had a shape of a rectangular sheet, 25mm wide by 210mm long.

In standard 'dogbone' tensile specimens, wide sections act as strain relief by transferring load over larger cross-section. Wider sections experience less stress and less strain, forcing most of elongation and breaking point to be located in the narrow section. Without strain relief in wide sections, a specimen would frequently break at an area of stress concentration near the gripping surfaces. In the case of rectangular specimens, strain needs to be relieved in another way. The solution was inspired by cylindrical grip design used in testing of ribbons and webbing, such as the one indicated in ASTM standard D6775 (D-13). In this design, strain relief is provided by the gentle curvature of the grip. As strip wraps around the curved section, changing surface angle causes friction force to increase gradually. This is analogous to how dogbone's wide section tapers out in a gradual manner.

Custom grips (Figure 3.5) were designed specifically for monolayer specimens of 25mm width. The radius of curvature of the first curved section is 30mm. The clamping mechanism is self-tightening, allowing it to work with a highly elastic material. Because of very low stresses exerted by strips, it was sufficient to use 3D-printed PLA with negligible flex at maximum stresses.



Figure 3.5: Custom grips used for testing monolayer strip specimens. Black benchmarks indicate the place where strip loses contact with the grip surface.

3.4.2 Monolayer Sintering Process

Powder preparation did not consist of annealing nor drying, as both processes had a detrimental impact on flow and bulk density of powders, as explained in Chapter 4.3.3. Powder was sieved using 180 μ m sieve and conditioned in laboratory atmosphere (20°C, 50%RH) for two hours prior to a build. Several factors suggest that actual level of moisture in powder was significantly reduced directly before sintering. Firstly, during the pre-heat stage powder remains in a moisture-free atmosphere. Secondly, because only one layer of powder is being sintered, moisture only needed to evolve out of \sim 300 μ m thick top layer of powder.

The sintering system was prepared by bringing it up to set-point chamber temperature and leaving it to warm up for two hours, giving all internal surfaces time to reach equilibrium temperatures. Build file containing monolayer specimens was loaded and the build program was put in paused state. This allowed for manual activation of laser exposure. Build chamber was opened and cold, conditioned powder was brought in from outside of the machine.

The powder spreading step was initially done using the recoating arm, but the quality of powder bed surface was often unsatisfactory, despite low temperature and virgin state of powder. It was decided to forego the use of the spreading arm completely and perform spreading manually. The manual technique used P100's own spreading blade, detached from the frame. When spreading, the blade was resting flush with the surface of the build platform. As blade was moved along Y axis of the build platform, reciprocating 'sawing' motion was applied as well (See Figure 3.6). This type of motion was the most successful in producing a smooth layer of powder, as it applied shear forces necessary to overcome cohesive forces between particles. The principle of applying shear to induce powder flow is analogous to the principle of a counter-rotating roller.

Once powder was spread, the chamber was closed which automatically activated overhead heaters. Using the machine's pyrometer readings, the powder was given time to reach the setpoint temperature. The temperature reading indicated a small amount of inertia, which would lead to powder achieving temperature above the setpoint. Laser exposure was therefore applied immediately upon achieving the setpoint before it was crossed.

Immediately after monolayer specimens were sintered, they were taken out of the machine. Remaining powder was spread into an even layer, to be used as a base for next batch. On top of old powder base, 1.5mm layer of fresh, cold powder was spread and the sintering process was repeated.

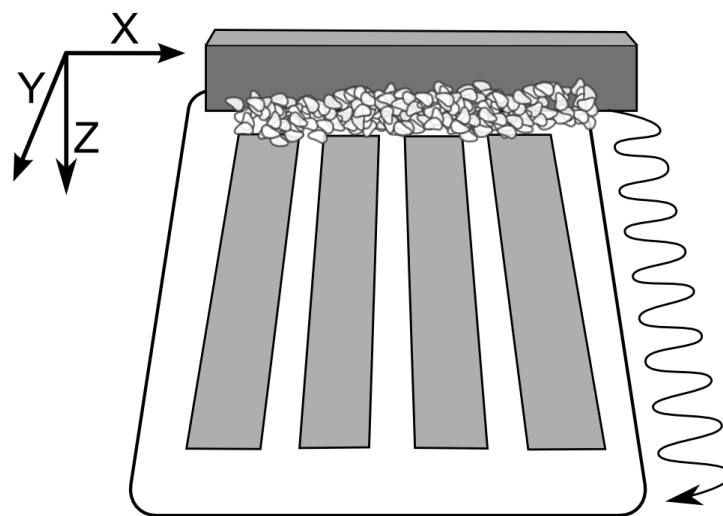


Figure 3.6: Schematic of powder bed when sintering monolayer specimens. Dark areas represent surface to be sintered. Powder spreading was done manually, using spreading blade detached from the automatic arm. The arrow indicates blade's saw-like motion used to shear powder particles into a smooth layer.

3.4.3 Tensile Testing and Measurements

In monolayer experiments, the weight of strip was used as the only specimen-specific measurement. Due to a combination of surface porosity, low thickness ($\sim 250\mu\text{m}$) and softness of the material, the thickness of specimens could not be measured in a meaningful way. Consequently, it would be meaningless to calculate cross-section area and stress. When measuring weight, the only source of inaccuracy was any non-structural, loosely bound powder remaining after sintering. Because of strip specimen's high surface-to-area ratio, loosely adhering powder constituted up to 12% of sample's total weight, which varied depending on powder batch. To compensate for that added weight, the measurement was performed in two stages. Before the tensile test, the weight of all specimens was measured and recorded. After the tensile test, 15 specimens from given powder batch were chosen at random and relatively short, 25mm tabs were cut from them. Tabs were then aggressively cleaned, using a soft pencil eraser to detach any loose material. Average weight-per-millimetre-length was calculated for both tested strips and cleaned tabs. Recorded weight of all strips within powder batch was lowered using the ratio of tab weights before and after cleaning.

During tensile testing, specimens were manually pre-loaded to $\sim 0.05\text{N}$. The initial grip separation was set to 60mm, measured between points where strips break contact with the curved surface (see black markers in Figure 3.5). The software was configured to commence data acquisition when the load reached 0.2N. The system was equipped with a 50N load cell. The rate of the test was set to 500mm/s, identical to the rate used with standard specimens, based on ASTM D412. Testing was performed to the breaking point. In addition to a standard set of tensile test results, software was configured to report values for Load and Work at three extension values: 12.5mm, 25mm, 50mm. Those values were chosen arbitrarily, based on preliminary tests, where a large majority of samples broke at extension significantly higher than 50mm.

3.5 Oven Sintered Tensile Specimens

When discussing stages of sintering in Chapter 2.4.1, we have noted that the initial stage of particle coalescence effectively ends when neck growth leads to formation of closed pore structure. This stage is followed by densification, in which gas needs to diffuse through sintered material in order

to further reduce porosity. At the start of densification, the initial volume of pores is dependent on bulk density and other properties of sintered powder. Further, there are limits to possible density gain during the densification process, related to gas diffusivity and gas saturation of polymer. We conclude that for all processing purposes, there is a limit to the density each powder can achieve, if it is sintering without external pressure, mixing or other intervention. Those conditions are true for the LS process. On this basis, we propose that simply sintering powder in an oven is a viable way of finding the maximum potential sintered density achievable in a LS system. Under this assumption, we conducted mechanical tests on tensile specimens which were sintered in an oven.

The approach to forming the oven-sintered specimens was analogous to the method of ceramic processing where the basic shape is formed by compacting bulk material and the fragile 'green' part is then sintered to full density. The green dogbones were prepared in an aluminium mould conforming to the ASTM D412 Die C standard. The mould itself had a form of a plate with specimen-shaped niches. Powder was poured into the niches and further compressed using a rolling pin. Mould was then preheated to 100°C, to pre-sinter TPU, making green parts less fragile. After removal from the mould, green dogbones were placed on PTFE sheet and sintered at 160°C for 30 minutes.

We found that sintering green parts outside of mould was beneficial to shape consistency and saved specimens from damage in process of extracting them from the mould. Due to the low viscosity of polymer during sintering, the final specimens did not retain the exact shape of Die C, as shown in Figure 3.7. Most importantly- the cross-section lost the rectangular shape, making it very difficult to measure the cross-sectional area for tensile tests. In order to estimate the cross-sectional area, we used measurements of specimen density and mass to first calculate individual specimen's volume. Shrinkage ratio was then calculated based on dimensions of green parts. Shrinkage ratio was then used to approximate the reduced cross-sectional area after shrinkage. When calculating the reduction in cross-section we used the assumption that all shrinkage occurred in the Z axis, flattening the specimen. While this approximation may not be accurate, it should be precise enough to enable meaningful comparison of results.

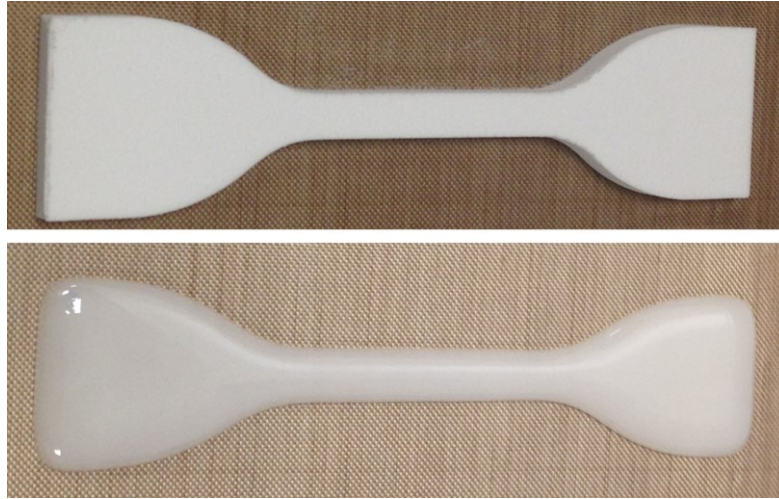


Figure 3.7: Compacted 'green' dogbone and the same specimen after oven sintering. Note the 'milky' white appearance of sintered specimen, which indicates a large concentration of voids. The same TPU would be transparent in fully dense form.

3.6 Hot Stage Microscopy

3.6.1 Introduction to HSM Coalescence Measurements

Hot Stage Microscopy (HSM) allows for observation of microscopic polymer grains as they are heated up and molten in real time. By placing two grains in contact, it is possible to observe the process of their coalescence into a fused drop and quantify the process by measuring dimensions of drops and the neck between them. This type of observations was important for research into sintering models, such as Frenkel's model of viscous coalescence (See Chapter 2.4.2). HSM studies are not however frequently performed. To our knowledge, no such study was performed on LS Nylons. This might be due to a combination of niche equipment, lack of standard methodology and other difficulties which we will mention below.

Coalescence measurements had been previously performed on BASF-supplied TPUs by Plummer (Plummer et al., 2012) and later by Vasquez (Vasquez et al., 2014). Plummer performed HSM on TPU which has been recycled through sintering system multiple times. Despite a major increase in MFI from 27g/min to 37g/min, HSM failed to observe any significant change in sintering rate between batches. Variance in HSM data was described as high. In addition, it appeared that particles were melting while sandwiched between two silica surfaces. This setup might have induced external pressure during melting, interfering with zero-shear flow condition. The quality

of data obtained by Vasquez was likewise low, with some unrealistic fluctuations in recorded rates. In neither case was the data compared to any coalescence model.

In our experience, we found the two-particle experiment to be extremely challenging to perform correctly and with adequate sampling of measurements. Instead of using hot-stage to quantify the coalescence process, we limited the use of the HSM to qualitative observations of melting behaviour of large clusters and layers of particles.

3.6.2 HSM Setup and Methodology

The main part of the hot stage is a ceramic block with a heating element and temperature sensor embedded inside. The block has an aperture in its centre, to enable transferred light microscopy to be performed. This was the main mode of imaging. Powder was melted while exposed to air, without use of top cover-slip. Allowing air to escape the coalescing powder seemed to create a more realistic representation of LS. The hot stage is pictured in Figure 3.8.



Figure 3.8: Hot stage microscopy setup during timelapse experiment. Note the aperture in middle of the ceramic stage to allow illumination from underneath.

4 Preliminary Studies

4.1 Thermal Properties of Experimental TPU

Calorimetry is a common tool in LS research since it allows for accurate localisation of melting and recrystallization events. Knowing temperatures of these two events is most useful when setting powder bed temperature, which should ideally be placed between them (See Chapter 2.2.1) This chapter contains a detailed analysis of a single batch of AC88A12 formulation, which was used in the preliminary part of the study. Other batches used in this project used TPU of identical chemical composition with variations of reagent proportions and molecular weights. Because of this, findings from this chapter continue to be relevant in later parts of this project when discussing thermal properties.

4.1.1 TPU Formulation

Thermoplastic Polyurethane featured in this study was based on formulation designated by the manufacturer as AC88A12. Reagents used in its production are listed in Table 4.1. An important feature of this formulation is the use of aliphatic hexamethylene diisocyanate (HDI), instead of more commonly used aliphatic molecule- methylene diphenyl diisocyanate (MDI). The Higher molecular mobility of aliphatic HDI lowers the viscosity of TPU system, what was the main factor in its choice. One more benefit of HDI use is the reduced susceptibility to thermal degradation and light instability, compared to aliphatic molecules. The trade-off for all those benefits is reduced tensile strength, compared to aromatic-based TPU. An additional side-effect of high molecular mobility of HDI is faster and higher phase segregation. Phase segregation will become an important issue when discussing DSC results further in this chapter. (Prisacariu, 2011)

Segment type	Molecule Type	Constituent Molecules
Soft Segment	Polyester diol	Adipic Acid (ADS), hexandiol 1,6, butandiol 1,4
Hard Segment	Diisocyanate	Hexamethylene diisocyanate (HDI)
	Chain Extender	Hexandiol 1,6

Table 4.1: Formulation of TPU in Preliminary Study

4.1.2 Features of Typical TPU DSC Signal

Temperature scan DSC was the first measurement performed on the TPU. Signal was obtained using temperature scan protocol in Chapter 3.1.1. Standard features of the obtained signal are outlined in Figure 4.1.

The first scan revealed mild endothermic and exothermic events between 30°C and 120°C, leading up to the main melting peak at 145°C. These low-energy events might be a result of reorganisation events in mixed phases within TPU phase structure. The *Wide Endotherm* region likely corresponds to melting of low-order phases, while the *Wide Exotherm* region likely signals temperature-activated phase reorganisation which increases the degree of molecular order.

Melting Peak is a feature highly relevant to processing. We observe that the melting peak is split into two, creating a bimodal peak. Yamasaki (Yamasaki et al., 2007) hypothesises that the first ~130°C peak corresponds to melting of disordered hard phase and the second ~145°C peak corresponds to highly ordered hard phase. It is unlikely that it will be useful to differentiate between those two events during LS processing since TPU will need to be brought to a temperature above both peaks.

Exothermic *Recrystallization Peak* is the only signal present on the cooling curve. It is located at 110°C, but with onset at 120°C. Overlap with the melting peak is significant, making it highly unlikely that supercooling approach can be used- a conclusion which is confirmed by isothermal DSC in Chapter 4.1.5.

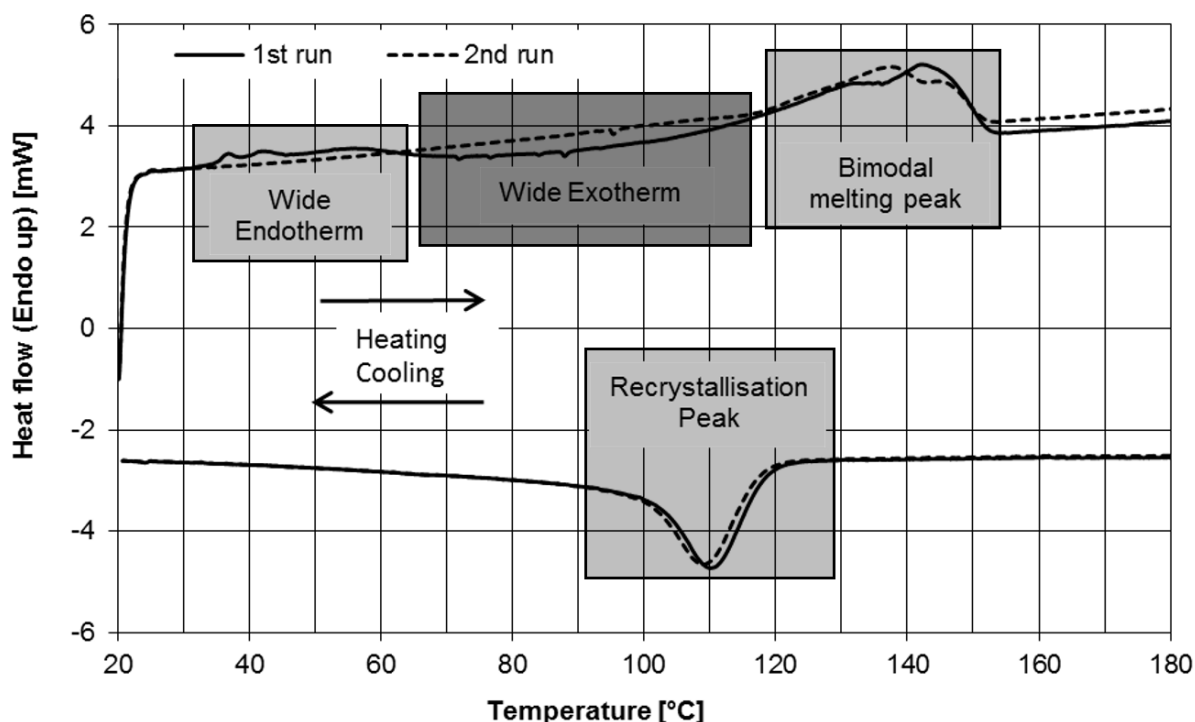


Figure 4.1: Features of a standard DSC temperature scan on virgin TPU (solid line) and second temperature scan on same sample (dashed line).

4.1.3 Annealing Peak Emergence

As discussed in literature review Chapter 2.1.2, the appearance of annealing peak has been observed and analysed numerous times in the literature. In this project, we decided to study this phenomenon closer, based on early observations that annealing improves flow properties of TPU powder, as discussed in Chapter 4.3.2.

Figure 4.2 serves to show appearance of annealing peak, which was made highly prominent by high annealing time and temperature. Position of the annealing peak evolves to higher temperatures with annealing time, as shown in Figure 4.3. As seen in Figure 4.2, example annealing peak emerges at temperature $\sim 10^{\circ}\text{C}$ above annealing temperature of 110°C . The distance between the peaks is higher at lower annealing temperatures, but the relationship remains linear, as shown in Figure 4.4. This linear relationship is consistent with the study by Yamasaki et al. (Yamasaki et al., 2007). The exact position of the peak continues to evolve with longer annealing time, tending towards equilibrium point, as seen in Figure 4.5. In the case of lower temperature annealing, steady state is reached after ~ 30 hrs, raising annealing peak from $\sim 10^{\circ}\text{C}$ to $\sim 15^{\circ}\text{C}$. We suspect that the

low-temperature exothermic signal visible at $\sim 40^{\circ}\text{C}$ in Figure 4.2, in virgin material might effectively be the annealing peak for an ambient temperature of $\sim 20^{\circ}$.

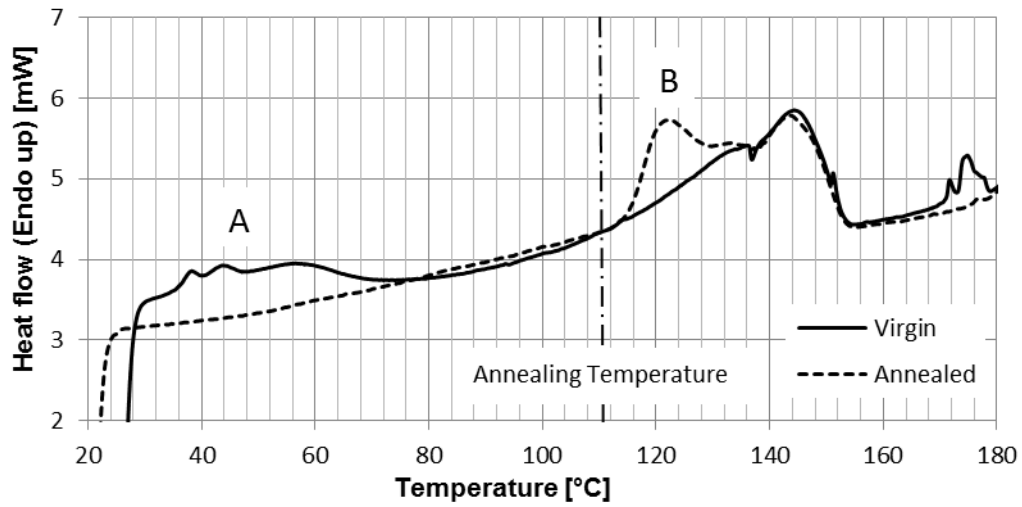


Figure 4.2: DSC signal from TPU annealed at 110°C for 12hrs to create strong annealing peak B. Annealing also removes peak A visible in the virgin material.

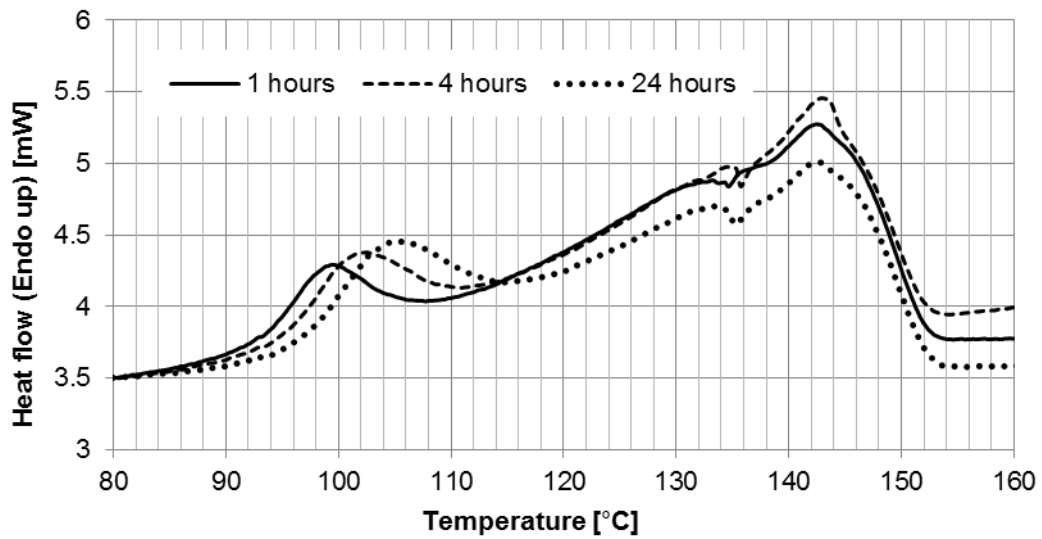


Figure 4.3: Evolution of DSC signal with varying annealing time at 90°C .

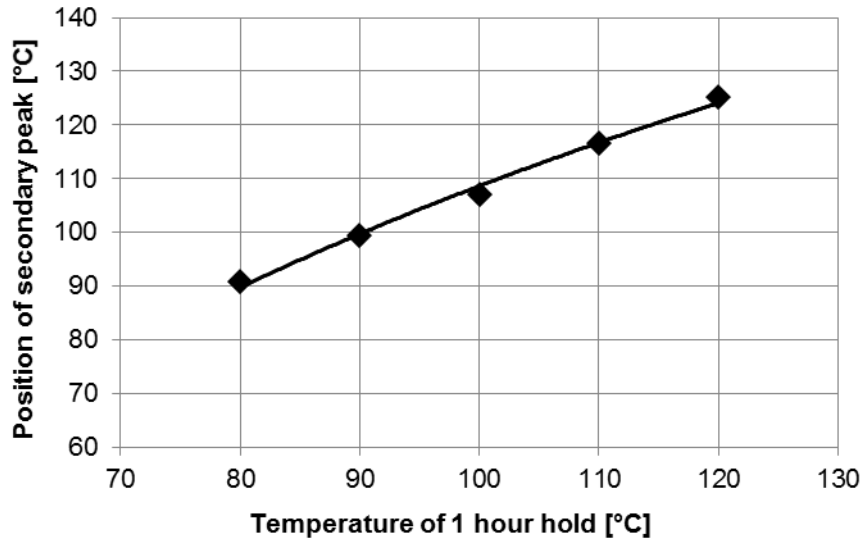


Figure 4.4: Annealing peak position vs. annealing temperature.

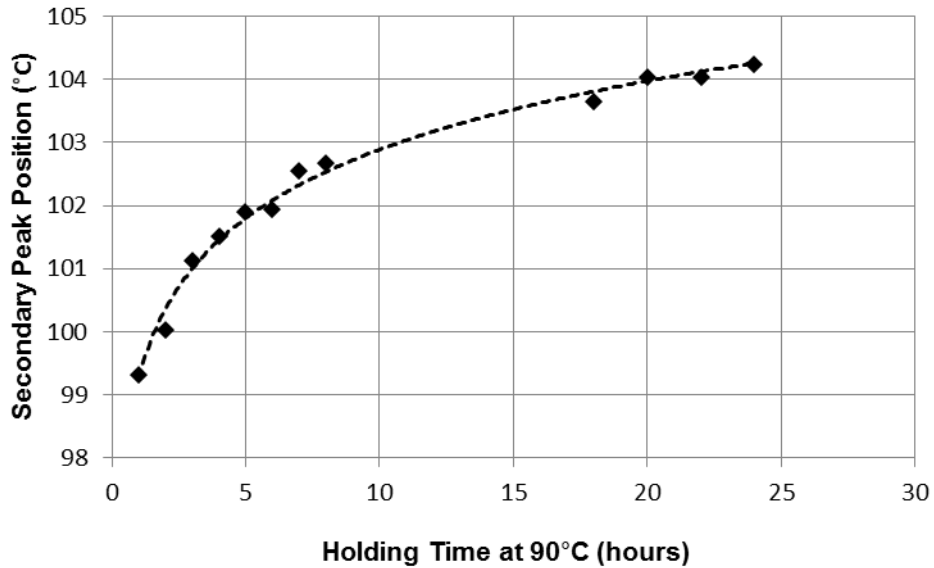


Figure 4.5: Annealing peak position vs. annealing time.

4.1.4 Melting and Recrystallization Peak Shift

One of the properties investigated via DSC was the apparent change in melting signal after TPU was exposed to temperatures significantly above melting peak. As shown in Figure 4.6, TPU goes through high temperature melting cycles in DSC, both the melting peak and recrystallization peak appear to decay. Peaks shift to lower temperatures, become lower and wider. The initial hypothesis was that this change was associated with some kind of molecular degradation mechanism.

Investigating the effect at lower temperatures, we found that when cycles were limited to 190°C no such decay took place (See Figure 4.7).

The second hypothesis explaining decaying peaks involved degradation of phase structure and ordering, rather than the molecular structure of the polymer. A mechanism responsible for the peak shift is proposed by Yoon and Han (Yoon and Han, 2000). They speculate that due to its multiblock copolymer structure (See Chapter 2.1.1) TPU is prone to losing long-range order at high temperatures, without chemical reactions or thermal degradation. When long-range order is lost and TPU transforms entirely into liquid-like state, formation of the hard phase upon cooling is inhibited.

If Yoon's speculation is true, then it should be possible to at least partly recover the long-range order, by annealing TPU at high enough temperature. Figure 4.8 contains DSC signals from a simple experiment designed to test this hypothesis. It contains three signals obtained from the same sample: virgin state, state after spending 5 minutes at 210°C (molten state) and state after being annealed for 90 minutes at 135°C. Molten material had its melting peak shifted from 142°C to 137.5°C. After annealing, the appearance of the peak changed dramatically. It became narrower and the signal at 142°C had recovered to approximately pre-melt strength. This seems to confirm Yoon's hypothesis that the peak shift is not associated with permanent damage to polymer chains, but rather with the loss of long-range order, which can be recovered. This hypothesis will find further confirmation in TGA results (Chapter 4.1.6) where the onset of molecular degradation was found to be significantly above 220°C.

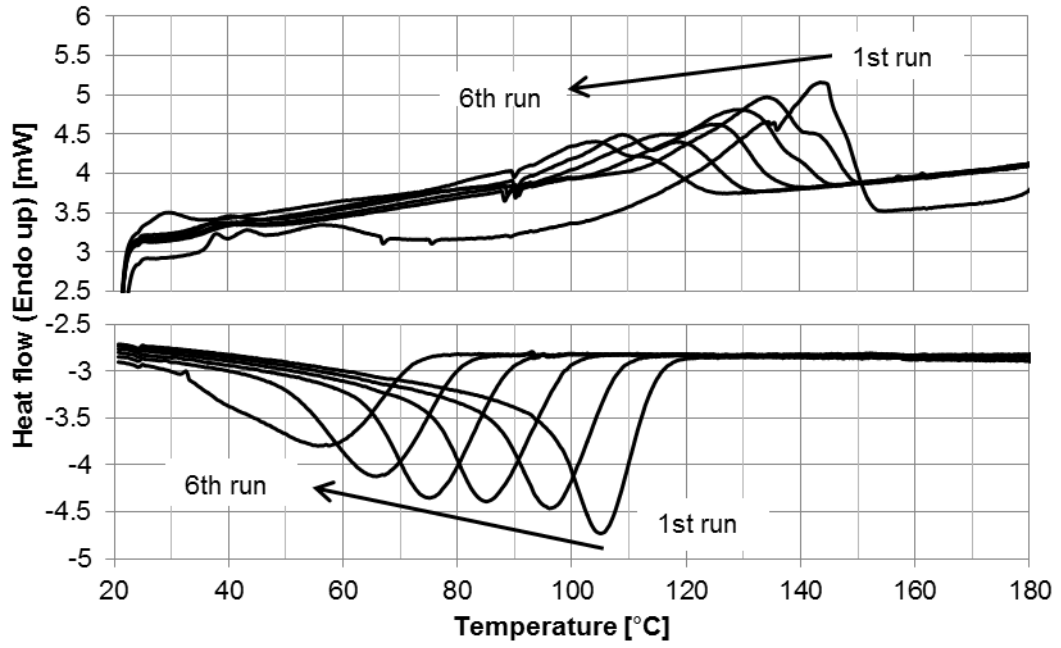


Figure 4.6: Changes to DSC signal when the sample was repeatedly re-melted at 220°C for 1min.

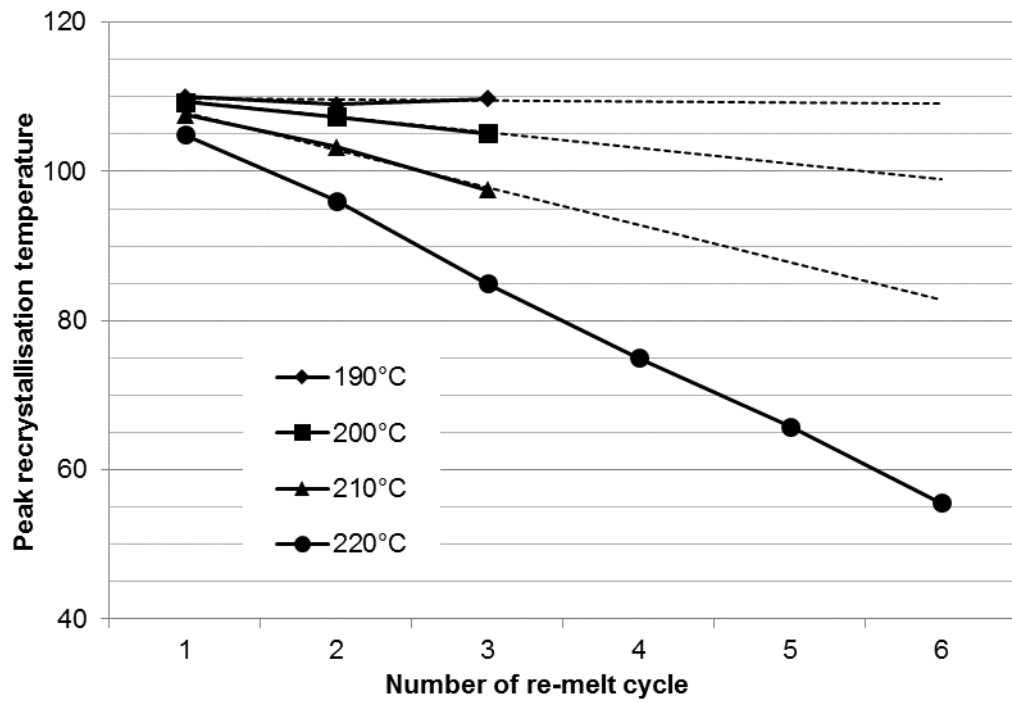


Figure 4.7: Changes to recrystallization peak as result of high-temperature degradation.

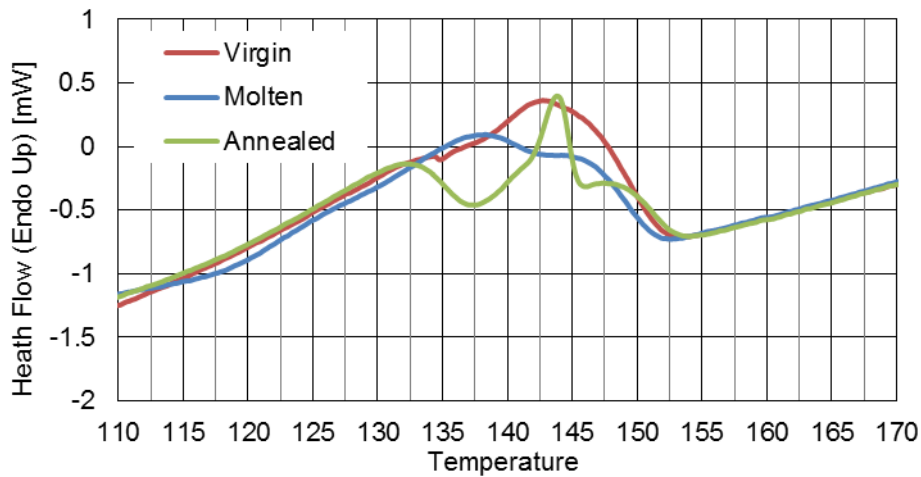


Figure 4.8: DSC melting signals from the high temperature annealing experiment. Material was tested in virgin state (red), after being melted at 210°C for 5min (blue), after annealing at 135°C for 90min (green).

4.1.5 Isothermal Crystallisation

Isothermal DSC was performed according to the protocol in Chapter 3.1.2. Results confirm that for TPU there is practically no holding temperature which delays crystallisation for an extended time. As seen in Figure 4.9, even at 125°C, which is at the onset of recrystallization, the process can be delayed only by five minutes. Experience with TPU in sintering system shows that any temperature in excess of 100°C results in extremely poorly flowing powder, making higher bed temperatures out of our reach.

The true rate of recrystallization might be faster than DSC readings suggest. Faster rate of cooling makes the melting peak move to higher temperatures (recrystallization occurs sooner). This effect is widespread in polymer materials, as demonstrated by Drummer et al. (Drummer et al., 2010) for multiple candidate materials. Given the large difference in melting temperature and chamber temperature (over 60°C), as well as the high surface-volume ratio of laser melt track, we can expect real cooling rate higher than one tested by DSC.

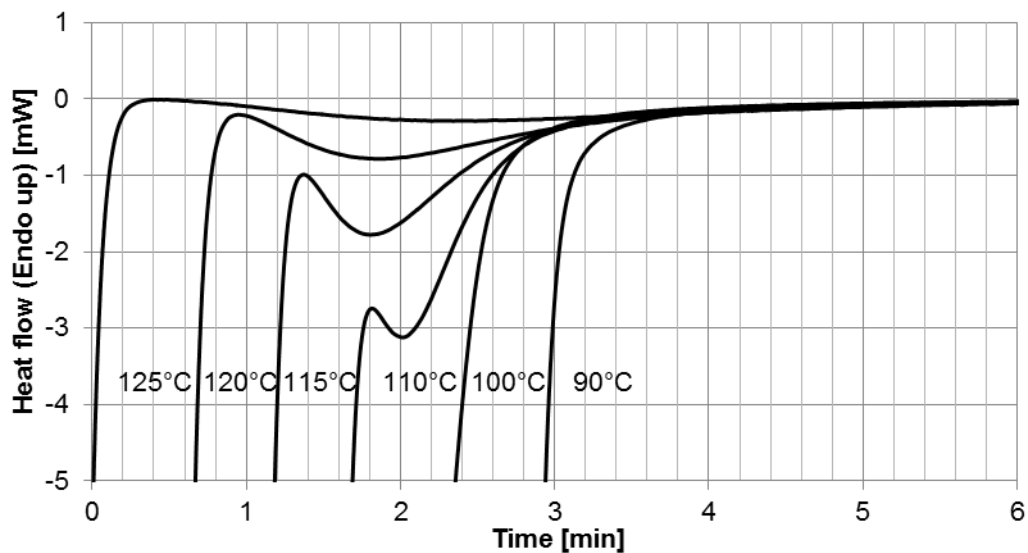


Figure 4.9: Signals from isothermal crystallisation experiment. Signals were offset in time for clarity.

4.1.6 Thermogravimetry

Thermogravimetry (TGA) measurement was performed according to the method in Chapter 3.1.3. Results of analysis are plotted in Figure 4.10. When degradation onset is defined as 1% weight loss, onset was observed at 268.5°C. The obtained weight loss profile is similar to results from literature and contains the characteristic two-segment curve indicating different degradation reactions. According to spectroscopy study by Herrera (Herrera et al., 2002) the first stage (~230-390°C) produces gaseous CO₂, indicating breakdown of urethane bonds in hard segments. The second stage (~390-440°C) produces a more complex gas mixture, including 1,4-butanediol, signalling decomposition of soft segments.

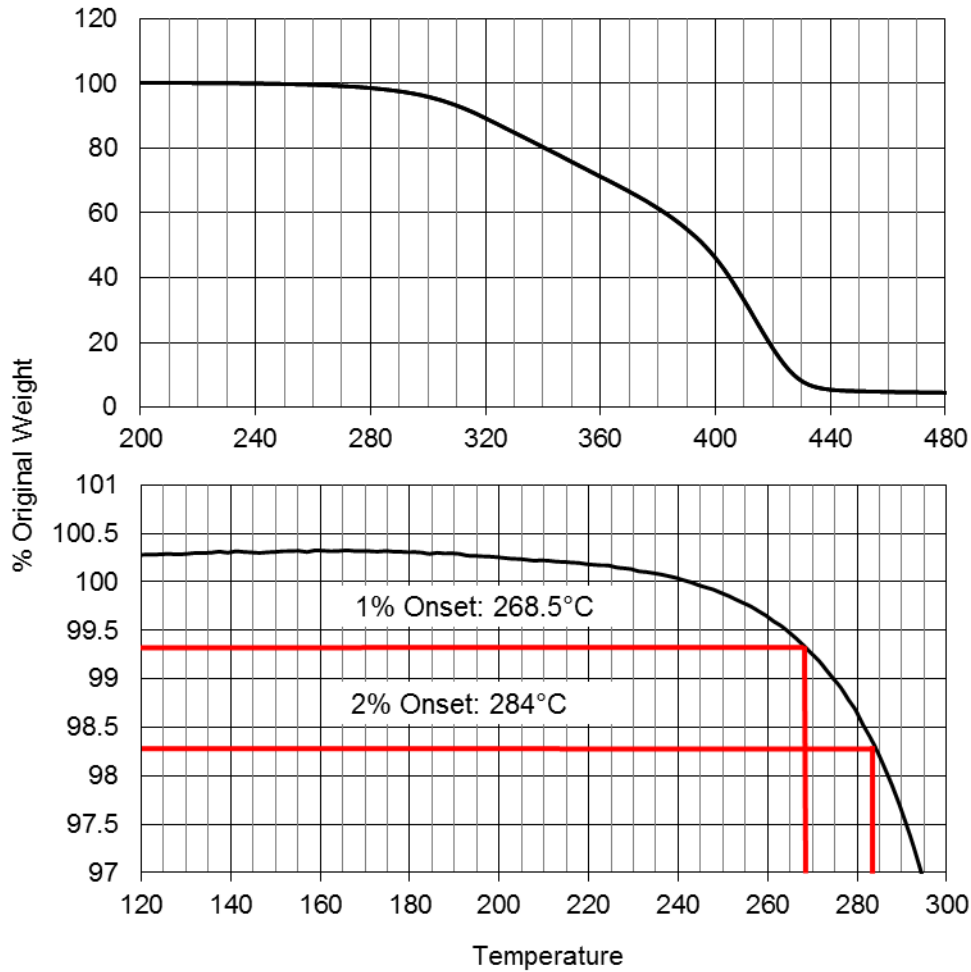


Figure 4.10: TGA plot and close-up with 1% and 2% weight loss points highlighted. Note that 1% and 2% loss was calculated from peak weight value of 100.3%.

4.2 Formiga P100 Features and Parameters

The Formiga P100 system (pictured in Figure 4.11, specifications in Table 4.2), which this study is based on, is a popular commercial laser sintering system from the EOS company. Being primarily a commercial machine, the P100 system was principally designed for sintering of Nylon, which is the ‘golden standard’ in polymer sintering. This is the most apparent in the design of powder delivery and spreading systems. Thanks to the excellent flowability of Nylon powder, those systems could be made simpler and more compact, what reduced machine’s footprint and cost. Unfortunately, these changes also made the system much less forgiving in choice of experimental materials.

Unlike the piston solution in Sinterstation, powder delivery in P100 is based on passive gravitational flow from an overhead hopper. The hopper has a form of a funnel, which feeds into

the left powder trough (Figure 4.12). Dosing from the hopper into the trough is controlled by opening of a long and narrow aperture and it is aided by a vibrating motor on the chute. We quickly found that both the funnel and aperture easily became clogged with most tested TPU batches. This problem was avoided by removing the aperture component to gain access to trough and manually topping up the left trough manually with small amounts of powder at a time, throughout the build process.

The powder spreading system is also simplified when compared to the counter-rotating roller of Sinterstation. It consists of a steel blade, travelling in an arc between two chutes containing powder. In contrast to rotating roller or ‘travelling hopper’ present in other systems, there is no vibration or shearing force applied to powder as it is deposited. The blade system is in effect almost entirely dependent on powder’s innate ability to flow freely, without assistance. We found this system essentially incompatible with poorly flowing TPU. More so than issues with clogging of the hopper, issues with powder spreading became an enormous obstacle to successful specimen production throughout the project.

Laser Type and Wavelength	CO ₂ , 10.2-10.8 μm
Laser Power	75W max
Beam Diameter	0.42mm
Build Bed Dimensions	200x250x330mm
Powder Delivery Solution	Gravity fed chute with vibration
Powder Spreading Solution	Recoating Blade

Table 4.2: Technical Specifications of Formiga P100 sintering system.



Figure 4.11: EOS Formiga P100 sintering system. Note the two upended containers on top of the machine, feeding to the internal hopper.

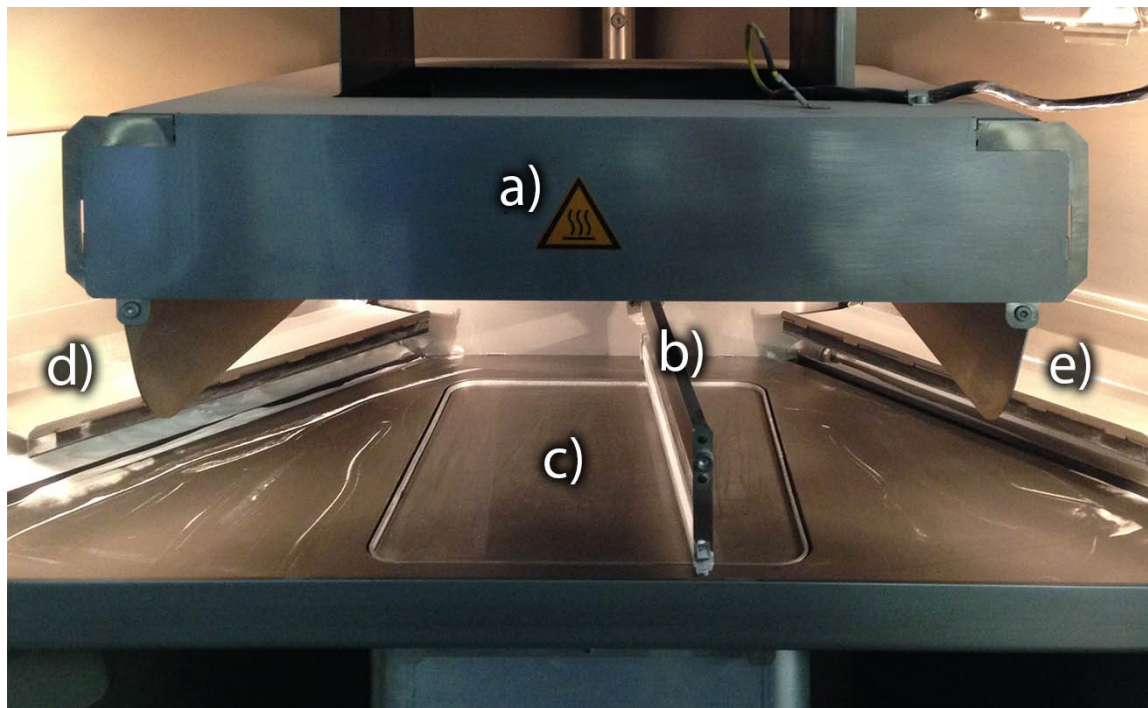


Figure 4.12: Interior of Formiga P100 build chamber. Detailed systems are: a) overhead heater b) spreading arm and blade c) build platform d) left powder trough (with powder feed) e) right powder trough.

4.3 Build Failures and Effects of Annealing

Preliminary attempts at building specimens with the AC88A12 powder quickly resulted in failure, as a direct result of extremely poor powder flow. These issues were not limited to preliminary experiments, as nearly all powder batches used in this project experienced similar issues. When discussing the behaviour of powder we will, therefore, use examples and pictures from different parts of the project, to form a comprehensive picture of the issue.

4.3.1 Builds With Virgin Powder

Issues with powder flow were first spotted during preliminary exposure tests. Although initial 'padding' layers of powder were deposited correctly, powder flow quickly degraded as the pre-heat stage of build achieved target chamber temperature of 90°C. High temperature inside the build chamber caused powder to form cohesive clumps, which could not be spread into an even layer. Further, clumps were cohesive enough to 'scratch' the surface of the powder bed, leaving deep gashes in the direction of spreading blade travel. Another sign of increased powder cohesiveness was the absence of powder from the space between the powder bed and side-troughs (See Figure 4.14).

In Figure 4.13 we see several signs of cohesive powder behaviour, at a chamber temperature of 90°C. The deep, horizontal gaps are the result of under-filling by poorly flowing powder. Vertical 'cracks' on the right side are the result of stresses and shifting generated by excessive friction between the recoating blade and the powder bed. Also, note that there is no powder in areas to left and right of the powder bed. In Figure 4.14 we see a close-up of the right-side trough. The powder is cohesive and retains the shape of trough, as if extruded by parts of the deposition system.

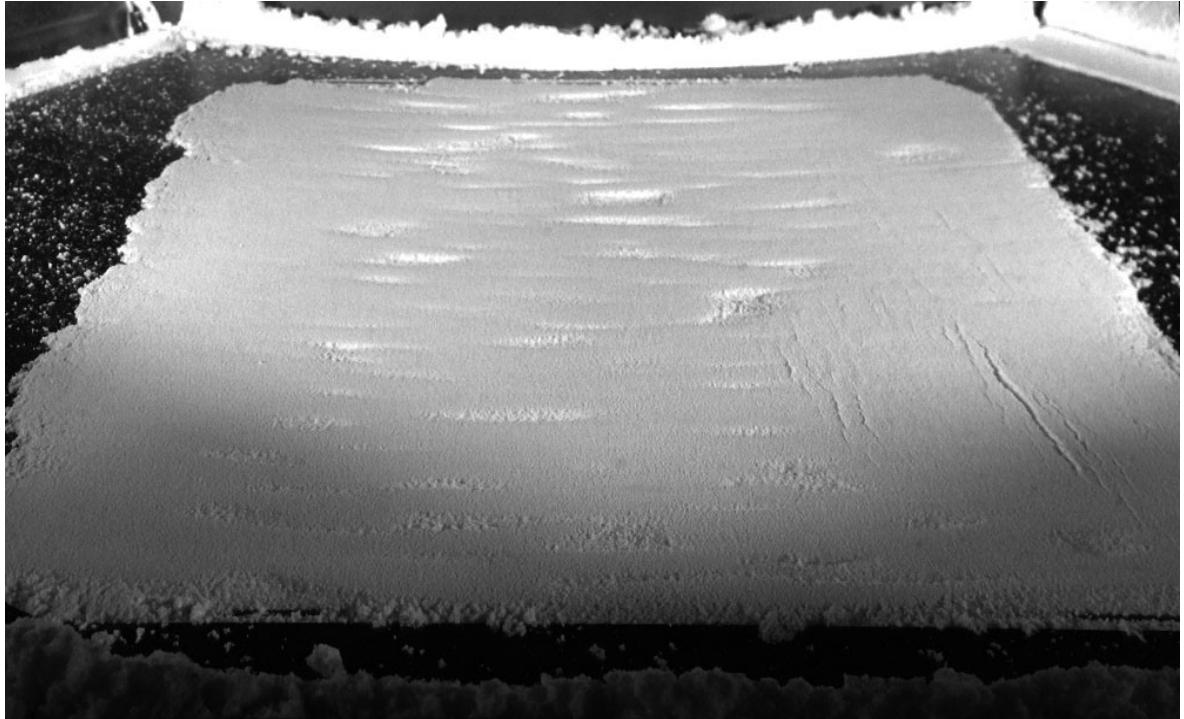


Figure 4.13: Picture illustrating appearance of powder bed when using poorly flowing powder (non-annealed A02 from Flow Agent Effects Study).

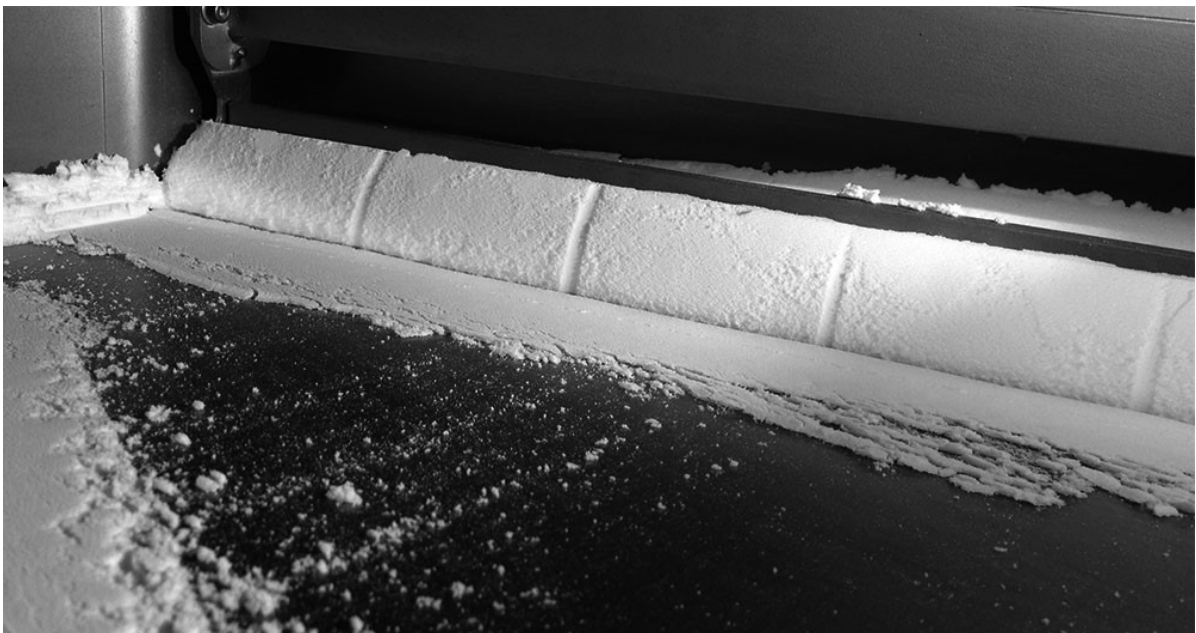


Figure 4.14: Picture of right side trough during sintering on non-annealed A02 (Flow Agent Effects Study),

In Figure 4.15 we demonstrate an attempt at sintering with non-annealed powder. We need to stress that while spreading seems successful, this picture serves only to demonstrate the best possible case. For instance, we show layer #3, very early in the build. Later in the build, the large size of particles in that batch led to catastrophic build-up effects (see discussion in Chapter 4.3.3).

Furthermore, to improve powder spreading beyond the standard method, the spreading system was put under manual control and forced to perform multiple passes on a single layer. Note the differences in powder deposition on top of un-sintered powder bed and on top of sintered parts. Powder deposited on top of sintered parts is smoother than the powder surrounding the parts.

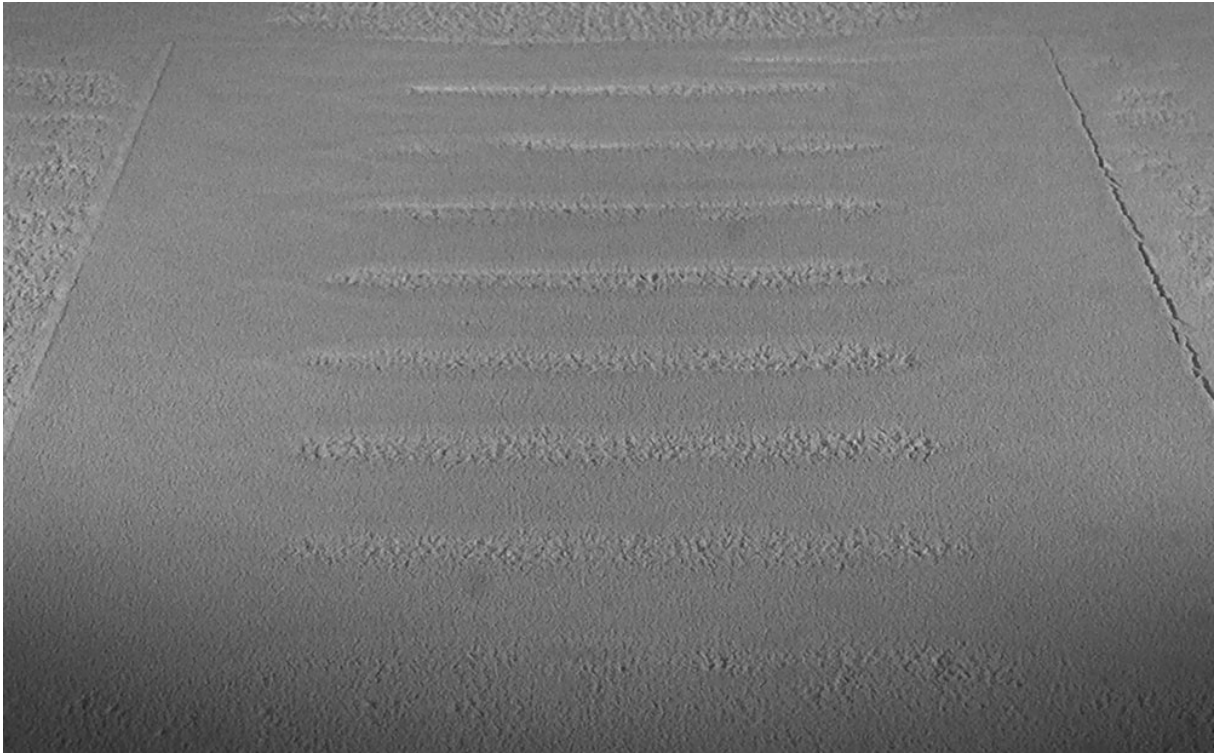


Figure 4.15: Picture of powder bed during attempted sintering of non-annealed powder (V26 from MFR Effects Study). Picture was taken at layer 3, after multiple recoating attempts to remove under-filling defects, such as one visible at the top-most specimen. Early effects of powder build-up are visible as a step on the left edge of specimens. Crack at the right side of specimens indicates shifting of sintered layers due to friction with the recoating blade. Shifting was reduced by ‘glueing’ all specimens together at the wide section.

4.3.2 Builds With Annealed Powder

During preliminary build attempts, we had found that powder which had been recycled and sieved would no longer form cohesive clumps and could be successfully spread. The same was true for dried powder, after oven-drying TPU at 90°C. In both cases, the recycled/dried powder would become clumped and it had to be forced through a sieve to break it up (or reconstitute) before its subsequent use in the sintering system. However, once reconstituted, the powder would be much less susceptible to clumping again. Calorimetry (Chapter 4.1.3) and literature review (Chapter 2.1.2) led us to the conclusion that both drying and recycling were effectively annealing the TPU powder. Because we found the annealing effect to be essential to preventing clumping, we focused

on developing an annealing protocol, which was used consistently in latter parts of the study. The annealing setup and procedure have been described in methodology Chapter 3.2.2.

When building with annealed powder, the issues with flow could be largely avoided. An image of part production with annealed powder is shown in Figure 4.16. The biggest issue encountered with using annealed powder was powder build-up on top of sintered parts. This led to sintered parts eventually raising above the powder bed surface. In mild cases, such as one in Figure 4.16, this led to specimens being shifted around by friction against the recoating blade. In worst cases, build up was sufficient for parts to collide with the blade and become dislodged, as shown later in Figure 4.20.

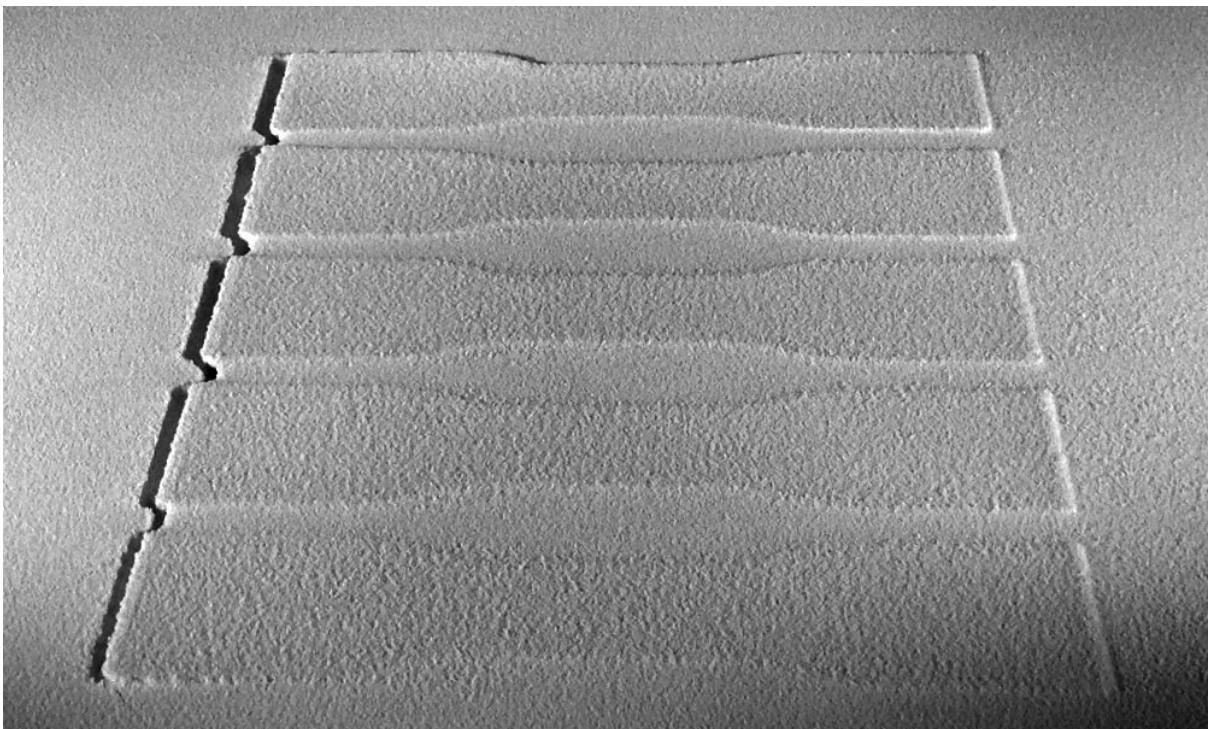


Figure 4.16: Picture of powder bed during sintering of annealed A02 batch during Flow Agent Impact Study. Notice the coarseness of surface compared to deposition of non-annealed powder in Figure 4.15.

4.3.3 Discussion of Build Failures and Annealing Effect

When powder's flowability is reduced as a result of exposure to elevated temperature, the only way it can be spread into a thin layer is by forcing cohesive particles to separate. A shearing force which can force cohesive powder to spread exists only in a narrow zone between the spreading blade and underlying surface. This also requires the powder bed surface to provide friction force opposing the action of spreading blade. This is analogous to spreading of butter with a knife. Butter is easier

to spread on a rough, porous surface. In Figure 4.13 the smooth metal plate does not provide enough friction for powder shearing to occur, which is why the metal surface between bed and trough remains empty of powder. In the same figure, the horizontal gaps in powder are impossible to fill because a gap cannot generate shearing force necessary for deposition.

The shearing forces were also beneficial when producing with annealed powder. In Figure 4.15 we find that powder spreads more evenly on top of the sintered specimens. We believe that the tacky surface of hot, freshly sintered TPU generates additional adhesion, further aiding in powder spreading. We also found the opposite effect to occur when the machine was put in manual control mode during Flow Agent Effects Study. If freshly sintered surface was given additional time to cool before deposition step, spreading was notably worse.

Comparing the appearance of non-annealed powder surface in Figure 4.15 and annealed powder Figure 4.16, we see that the annealed powder creates a visibly rougher surface. Initially, this was not considered a flaw, but investigation by SEM (Chapter 5.2.4) found that annealed powder was comprised of microscopic clusters, much larger than virgin particles. Our current understanding is that rough surface of those clusters is responsible for the improved flowability. As we discuss further in Chapter 5.2.5, the flow-improving additive Aerosil also acts by increasing surface roughness.

Unfortunately, because of their increased size and roughness, those clusters are also likely responsible for the build-up effects during machine operation. A schematic of the build-up effect is shown in Figure 4.17. Powder build-up occurs because of a combination of factors, chiefly large particle size and large interparticle friction. TPU's low bulk density and softness are also likely to contribute. When those factors are present, particles which pass under the recoating blade cannot be compacted and instead press down on and deform the sintered part. After passing under the blade the particles and sintered surface spring back, causing the new layer to be taller than blade's path. This effect is cumulative and subsequent layers will worsen the effect.

The effects of build-up, as well as hot surface tack hypothesis, will find further confirmation in the preliminary sintering study in Chapter 4.5.

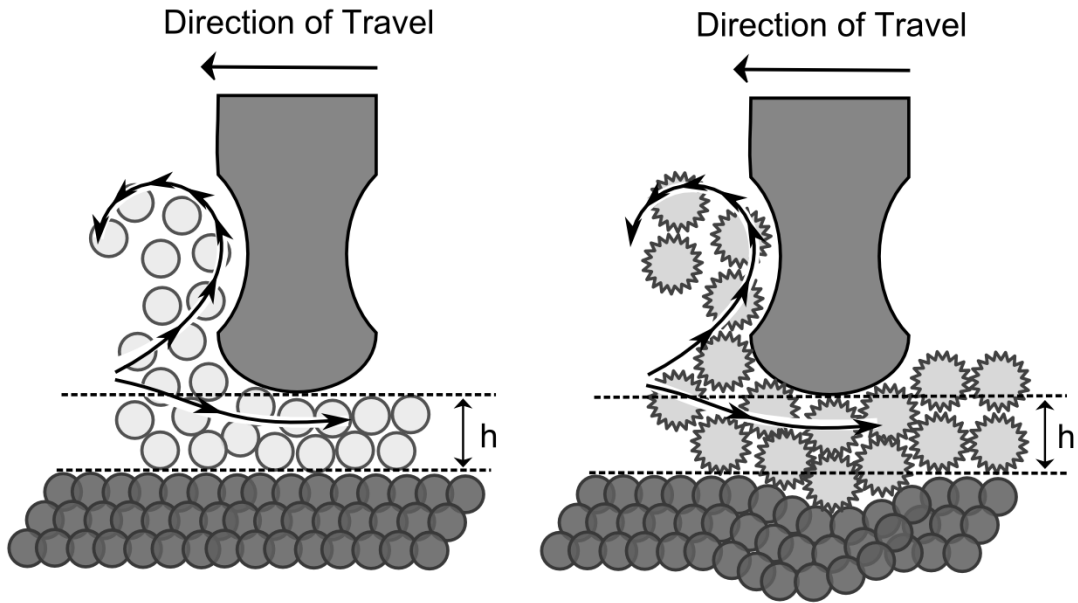


Figure 4.17: Schematic of correctly working powder deposition (left) and the issue of powder build-up (right)

To summarise, both small and large-sized particles present their own set of challenges and trade-offs. The flow-chart in Figure 4.18 summarises the two prevalent modes of failure. In case of clusters and large particles the build-up effects and excessive friction often led to part displacement by the wiper. Small particles on the other hand could not be successfully reconstituted during spreading. Post-sintering depressions or other gaps in powder surface reduce the shearing action occurring between powder bed and wiper. Both the powder build-up and spreading failure cause positive feedback, making the defect worse with each new layer.

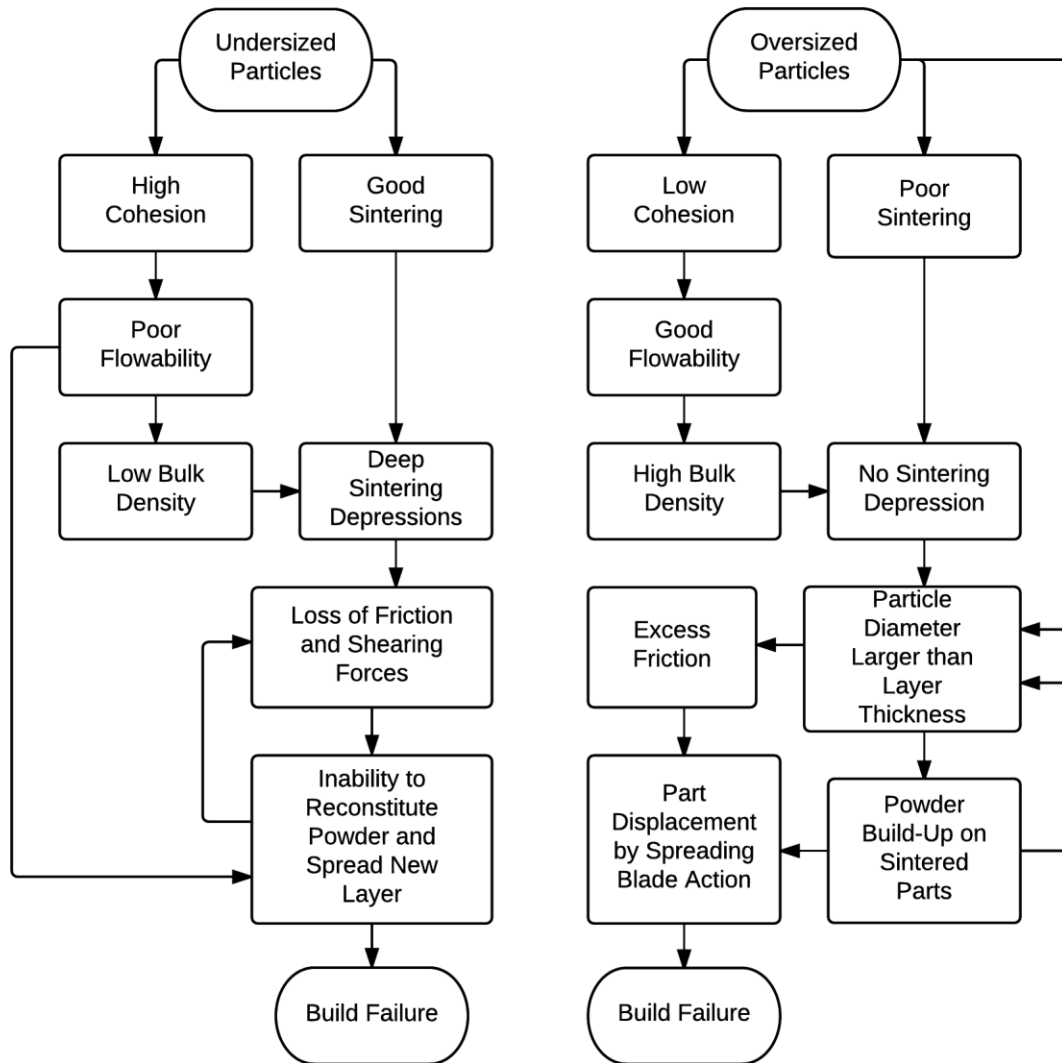


Figure 4.18: Flow chart of two prevalent modes of build failure when powders features small particles, or large particles/clusters.

4.3.4 Comparison to Prior Research

Let us stress again that all of the full-scale sintering experiments performed in this project used annealed powder. Builds using virgin powder were in practice impossible to complete. This might come as a surprise, given that very similar TPU materials were sintered successfully, notably by Ziegelmeier (Ziegelmeier et al., 2015) and Vasquez (Vasquez, 2012). In addition, Vasquez used an identical Formiga P100 system. However, a detailed look at the mentioned research reveals that performance of TPU in this project was, in fact, not worse than in those past cases.

In their work, Vasquez used a drying process on the powder, which has a similar impact on powder characteristics as annealing. Vasquez therefore likely avoided the flow issues in a way

analogous to our own, directed approach. In the case of Ziegelmeier's group, the experiments were conducted on 3D Systems Sinterstation system, which is significantly different than our P100 system. Sinterstation's powder deposition system is based on the principle of the counter-rotating roller. The schematic in Figure 1.2 is based on Sinterstation layout. Compared to P100's passive wiper solution, the rotating roller is able to apply additional shearing forces to powder as it is pushed onto powder bed. This makes roller a much more forgiving system regarding powder flowability. Another factor favouring Sinterstation is the independent control of powder feed temperature and powder bed temperature. This allowed powder feed to remain at 55°C and the powder bed to be heated to 125°C. The two temperature zones allowed for optimisation of both the powder flow and the temperature of the powder bed. P100 is a more compact system and the proximity of the feed-troughs to the powder bed does not allow for separate temperature setpoints to exist. In fact, in our build protocol, we allowed P100 to heat up for an extended amount of time to make sure that the temperatures of troughs were in equilibrium with the central part of the build chamber, as they would be after performing a long, large-scale build. The temperature we adopted for experiments is by necessity a suboptimal compromise. Note that the temperature of 90°C which we settled on lies exactly mid-way between the 55°C and 125°C values adopted by Ziegelmeier.

4.4 Exposure Parameters Tests

4.4.1 Study Plan and Experiment Design

The first priority when attempting to sinter a new material is to determine safe production parameters. Out of processing factors discussed in Section 2.2.1, two which have the greatest impact on both safety and effectiveness of sintering are the powder bed temperature (T_b) and the energy density of laser exposure (ED). Energy density cannot be too high, or it will lead to excessive degradation of material and fuming. Bed temperature needs to be low enough for powder to maintain flowability. Inability to deposit new powder layer not only leads to production defects but in extreme cases, it can lead to dangerous overexposure of already sintered layers.

Exposure parameters can be individually set for every specimen in a build job. The impact of ED variation can be therefore tested quickly and within one batch, which simplifies experiment

design. Prior research (Vasquez, 2012, Kruth et al., 2007) suggests that mechanical performance of LS specimens improves with higher laser exposure, up to the point when the material becomes damaged by heat. The point of polymer's thermal degradation forms the theoretical upper limit of exposure, but effects of degradation can only be tested for after build completion. In practice, the factor which limits ED is the amount of fumes created by the heated material. Fumes are a product of decomposition, but their presence is not indicative of the condition of the bulk of material. Due to sharp temperature gradients in exposure region (Rietzel et al., 2011), it is possible for small-sized particles, or just the surface of larger particles to become overheated, while the bulk of material remains unaffected. Fuming is common in LS and until it becomes excessive, it is not problematic. Vasquez (Vasquez, 2012) compared several polymers in the sintering process and TPU was the only one where there was no registered decline in mechanical properties of specimens, even at maximum safe exposure settings. We believe that the right initial approach is to maximise ED to safe levels, in an attempt to reach a maximum possible degree of sintering.

Powder Bed temperature is identical for all specimens in one production batch, assuming the system can maintain uniform temperature across the bed. Testing the impact of bed temperature requires multiple build jobs, making it much more time-consuming to investigate. Specimens also must also be split between multiple batches, what puts greater significance on between-batch consistency of the process. As mentioned in Chapter 2.2.2, TPU is likely to feature a softening temperature. The approach of keeping T_b just below melting onset is unlikely to be feasible, since at that point TPU will become soft and tacky, making it impossible to spread in layers. In practice, maximum bed temperature will be chosen based on its impact on powder flowability.

Sintering of TPU with an identical formulation and on identical P100 system has been attempted before. Safe parameters were first found by Vasquez (Vasquez, 2012) and then confirmed by Plummer (Plummer et al., 2012). Parameter set included Energy Density of $30\text{mJ}/\text{mm}^2$ and a bed temperature of 95°C . Using these parameters as a starting point, we began the project with a test to confirm these exposure parameters are safe and if the new material cannot accept greater ED. A 6x6 grid of tile specimens was split into nine groups of four tiles each, which were grouped as shown in Figure 4.19. Within each exposure group, tiles would be exposed to

identical energy density, but achieved with a different combination of laser power and speed. This was to verify that results would be consistent within exposure group, regardless of specific laser settings. Exposures tested ranged from 12.5 to 32.5 mJ/mm², in increments of 2.5. Exposure groups and power/speed combinations are listed in Table 4.3. Bed temperature was set slightly below Vasquez’s limit, to 90°C.

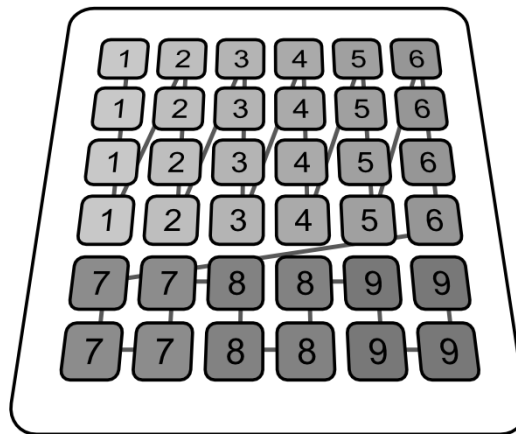


Figure 4.19: Diagram of the grid used for testing exposure parameters. Darker tiles were more heavily exposed. The underlying line shows the order in which tiles were exposed.

Laser Scan Speed (mm/s)		Energy Density (mJ/mm ²)								
		12.5	15	17.5	20	22.5	25	27.5	30	32.5
Laser Power (W)	15	4800	4000	3429	3000	2667	2400	2182	2000	1846
	18	5760	4800	4114	3600	3200	2880	3618	2400	2215
	21	6720	5600	4200	4200	3733	3360	3055	2800	2585
	24	7680	6400	5486	4800	4267	3840	3491	3200	3954

Table 4.3: Exposure settings for initial sintering trials. Top row contains Energy Density levels used in each group. Left column contains laser power used to expose each specimen in a group. Middle section of the table contains laser speed (in mm/s) necessary to achieve desired ED given the laser power setting on the left.

4.4.2 Build Process and Results

This experiment was performed on the AC88A12 preliminary batch. Powder was annealed according to the protocol from Chapter 3.2.2. Build used the tile specimen layout from Figure 4.19 and exposure settings from Table 4.3. During the build process parts were watched closely to record amount of fuming and stop the build process in event of specimens becoming dislodged.

The build was stopped at the first sign of specimens becoming dislodged. According to our observations, the nine exposure groups could be roughly divided into four outcomes:

1. Tiles between 12.5-17.5mJ/mm² were lightly sintered, evident from the relatively small amount by which sintered surface sank into the powder bed. Because there was no sink to compensate for powder build-up, those tiles were the first to accumulate the critical amount of powder and be dislodged by spreading blade pass.
2. Tiles at 20mJ/mm² shown little to no fuming and overall appearance was satisfactory.
3. Tiles between 22.5-25mJ/mm² began to produce a significant amount of fumes, but also sank markedly deeper into powder bed as powder melted and fused, which made them more resilient to effects of build-up.
4. Tiles between 27.5-32.5mJ/mm² fumed excessively and sank very deep into the powder bed. The deep sintering pits occasionally would not be filled by the recoating arm.

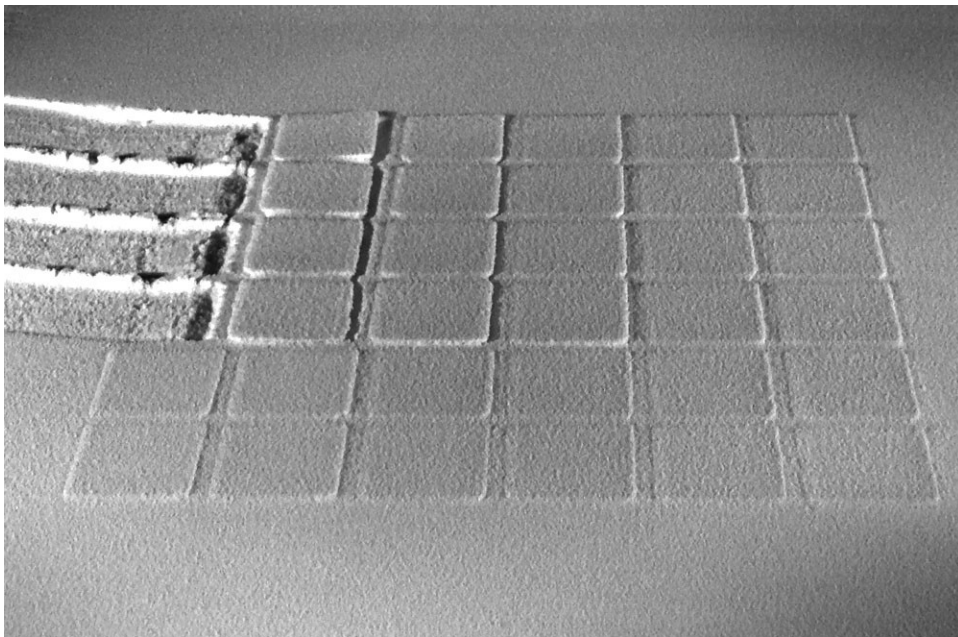


Figure 4.20: Result of testing exposure parameters on annealed AC88A12 Batch. Squares with lowest laser exposure were the first to become dislodged by deposition blade as a result of powder build-up. Build-up is evident in all samples and increases with each new powder layer deposited. There is no apparent difference between specimens within each energy density group. Note that the amount of drag and shift is approximately equal in all members of each exposure group.

4.4.3 Conclusions

The experiment succeeded in its goal to identify safe parameters which can form the foundation for future experiments. The temperature of 90°C forms a good compromise, minimising edge curl while providing satisfactory powder flowability (when powder was annealed). Energy Density of

25mJ/mm² will be preferred in future, as it maximised powder fusion at a tolerable level of fuming. Some amount of fuming is expected during normal LS process and to mitigate that, the Formiga P100 system is equipped with air nozzle keeping the laser window clean. In addition to improved fusion, high ED is more likely to provide protection against effects of powder build-up.

4.5 Preliminary Tensile Properties Study

4.5.1 Study Plan and Experiment Design

The first part of this preliminary study found maximum safe exposure parameters, which were limited by the appearance of excessively dense fumes. We have also found that using lower exposure values resulted in greater risk of parts becoming dislodged. The reason for part dislodging was powder build-up which eventually led to wiper colliding with the edge of sintered part. Further build attempts confirmed the conclusion that while high exposure values lowered the dislodging risk, they did not remove it entirely. Further, we found that colder chamber temperature exacerbated curl on the edges of sintered layers. This meant that at least in the preliminary stage the production parameters were not flexible, but had to be optimised to minimise the risk of failure. For the purposes of tensile testing, only one batch of specimens would be produced.

4.5.2 The Build Process

Through experimentation, we had found that the risk of build failure was the lowest when specimens were manufactured in the XZY orientation (See Figure 4.21). In this orientation the second-longest specimen dimension (width) is aligned with the vertical Z axis. Producing specimens in this orientation minimised the surface area in contact with the recoating blade, which reduced the dislocating friction. Secondly, specimens were becoming embedded deeper in the powder cake, compared to specimens manufactured 'flat'. This anchored them and further prevented dislodging in latter stages of production. As an added benefit, the XZY orientation allows for a large number of specimens to be built concurrently. We had managed to fit 32 ASTM Die 'A' specimens on one production layer. This large sample size, built within single batch gave us an

opportunity to additionally study the consistency of build process. To this end, the specimens were individually labelled. Specimen near the front edge of powder bed was labelled #1.

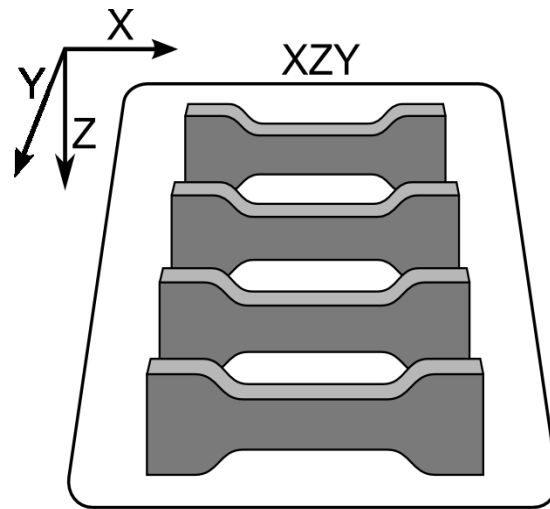


Figure 4.21: XZY type specimens stacked on powder bed. Order of axis labels lists specimen’s largest dimension first.

Temperature of Build Chamber	90°C
Temperature of Removal Chamber	70°C
Laser Energy Density	25mJ/mm ²
Laser Power	21W
Laser Scan Speed	3360mm/s
Laser Scanning Motion	Outline, X axis hatching

Table 4.4: Parameters of XZY build in Preliminary Tensile Properties study.

The build itself was performed using settings from Table 4.4, which we had determined to be the maximum safe parameters. One day before the build, powder was annealed using the established tumbling drum method, as detailed in Chapter 3.2.2. Directly before the build, annealed powder was dried as detailed in Chapter 3.2.1. Drying directly before build also pre-heated the powder to the machine’s chamber temperature. Pre-heating was necessary because in this test powder had to be manually dosed through the chute to prevent clogging. Pre-heating prevented cold powder from outside of the machine from influencing the build process.

As can be seen in Figure 4.22, annealed TPU powder continued to show a large amount of build-up on top of sintered surfaces. Thanks to the XZY orientations the specimens became firmly anchored in the powder cake, what prevented shifting and dislodging.

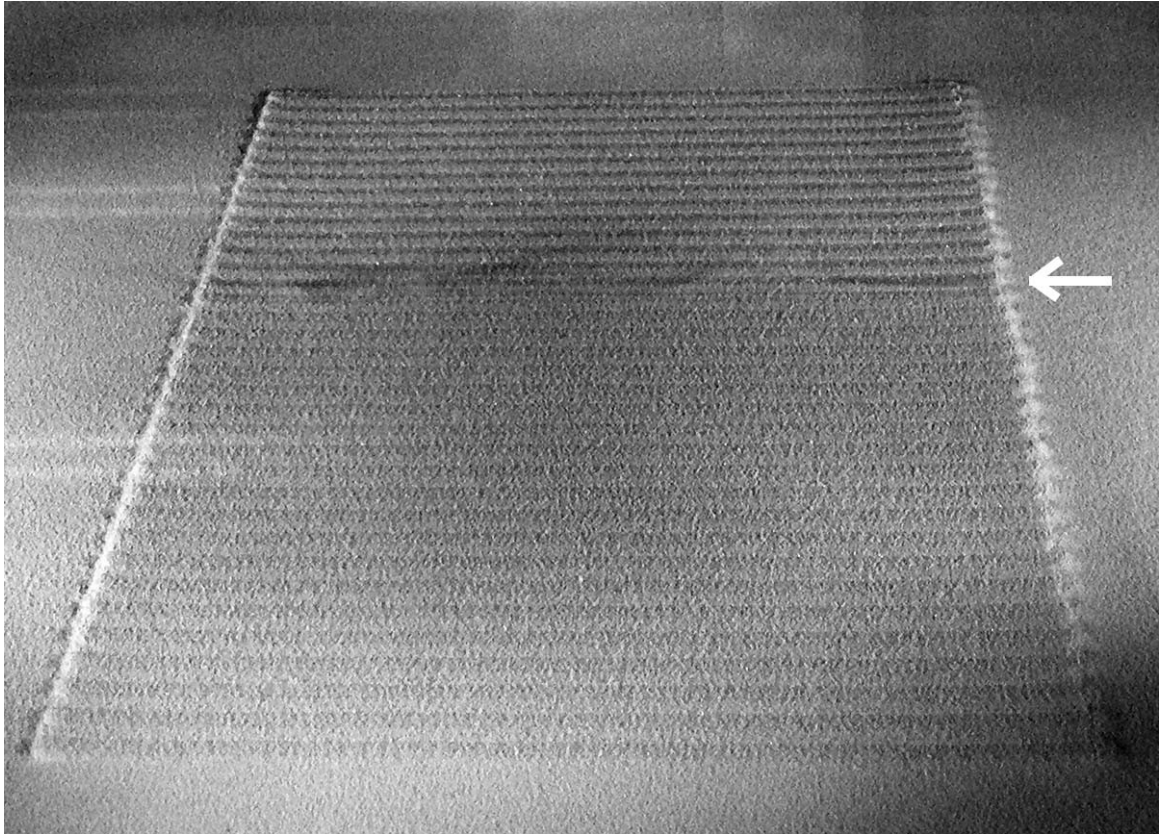


Figure 4.22: Picture of XZY samples during production with annealed powder. Note the problematic powder build-up on sintered parts, which no longer sit flush with powder bed surface. The arrow indicates sample currently being exposed by laser. Note the rising fumes.

4.5.3 Specimen Testing

Before testing, each specimen's dimensions, weight and density were recorded. Width and thickness measurements were taken at three points along the narrow section and averaged. Additionally, we had separately recorded the width of the bulging end sections (see Figure 4.26), believing their abnormal shape can be correlated with other properties of a specimen.

Specimens were tested using a protocol based on the ASTM D412 standard (D-11). Specimens were tested in the order of placement on the build platform, #1 being closest to the front edge of the platform. Testing was performed on a rig fitted with a 2000N load cell and a laser extensometer. The rate of extension was set to 500mm/s. The software was configured to record standard tensile test parameters: Young's Modulus (E), Ultimate Yield Strength (UYS), Ultimate Tensile Strength (UTS) and Elongation at Break (EaB). UYS and UTS were always equivalent and only the latter is reported. Values of Work (W) and Toughness ($J \cdot m^{-3}$) were calculated based on the machine's travel distance and the recorded Load. Work corresponds to the integrated Load-Displacement curve,

Toughness corresponds to the integrated Stress-Strain curve. Both those values are therefore closely related. Figure 4.23 shows several stress-strain curves representative of the obtained specimens.

After testing, based on extremely low weight and outstandingly poor mechanical performance, we rejected specimens 1-2 and 30-32 from the study, bringing the number of samples to 28. In manufacturing practice, it is ill-advised to manufacture parts in close proximity to the powder bed's edge. The need to reject specimens built extremely close to edges was not unexpected. All of the obtained measurements are plotted in Figure 4.24, with details of the data representation explained further in the discussion section.

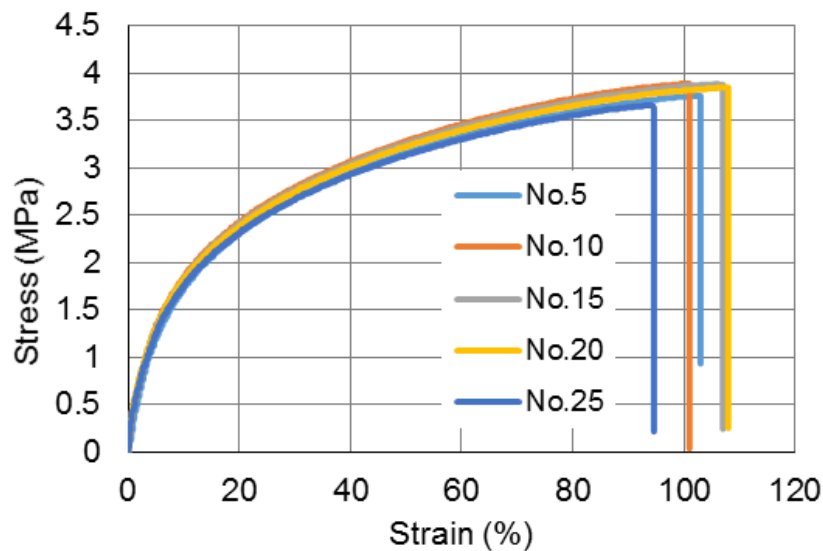


Figure 4.23: Representative stress-strain curves of several preliminary tensile study specimens. Note the lack of any yield point and the lack of strain-hardening effect.

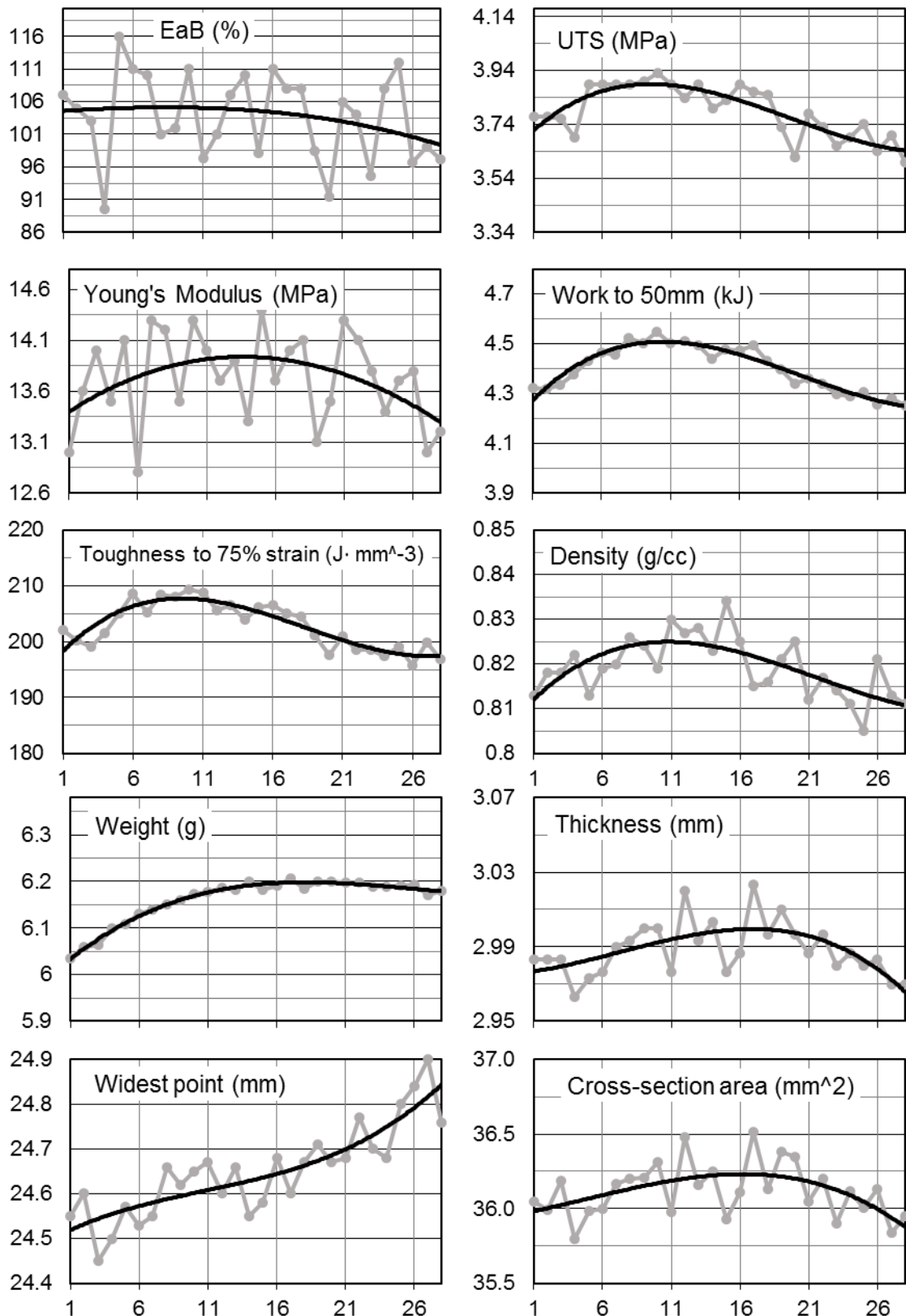


Figure 4.24: Graphs of Preliminary Tensile Properties Study samples. Black lines are third-degree polynomial regression curves fitted to data. All graphs are scaled to represent a range of ± 2.5 standard deviations, for easy comparison of variance levels. Specimen number 1 was sintered near the front edge of the build platform.

4.5.4 Discussion of Employed Measurements

The goal of this preliminary study was to not only to test the specimens but also to establish good practices for further parts of this project. Part of this goal is finding reliable measures and indicators of specimen performance. For easy comparison of different types of data, all results in Figure 4.24 are plotted with all y-axes set to span approximately ± 2.5 times the standard deviation from the mean value. Third-degree polynomial line was fitted to data to visualise data trends. This allows for qualitative estimation of the amount of variance (standard deviation squared) in each type of measurement. Measurements with low variance should be more reliable in discovering correlations and differences between production batches.

Elongation at Break is an example of a property which can be measured with high accuracy, but which has a large random component. The breaking point is likely to depend on the presence of abnormally large pores and other structural weak points, which are distributed randomly between specimens. It can be said that EaB is highly sensitive to local anomalies within each specimen.

Ultimate Tensile Strength like EaB depends on the breaking point, but since the stress-strain curve tends to level off before the break, the exact breaking point has a lesser impact on the read value and variance is reduced.

Young's Modulus calculation appears to have very high variance, likely stemming from extremely narrow linear-elastic region available for interpretation by software (see Figure 4.23). This is also exacerbated by load readings in this region falling below optimal sensing range of the available load cell.

Weight is a good example of high-precision, low-variance measurement. It measures a property which defines the entire specimen at once and therefore does not depend on sampling method in a way that e.g. thickness does.

Density measurement by Archimedes method has more variance than Weight. An entire specimen cannot be measured at one time. Instead, a sampled piece is measured. In addition, the surface of specimens seemed to behave in a hydrophobic manner and form a film of air when

measured in water, contributing to measurement error. Note that this hydrophobic property is, in fact, preferable to water infiltrating into the pores, which would skew results in opposite manner.

Width, Thickness and Cross-section Area all show a large amount of variance. Those measurements are sampled at several points along a specimen, but in the case of a geometrically inconsistent sample it is difficult to provide meaningful, averaged dimensions.

Toughness and Work are closely related and show a low amount of variance. Compared to EaB and UTS, those measures do not rely on the random nature of specimens' breaking point. Their calculation is also free of the ambiguity present in Young's Modulus calculation. Toughness calculation compensates for sample's cross-section area and, in theory, the extension is measured more accurately, eliminating grip slippage, machine flex and other variables. What is apparent, however, is that the unreliable measurement of cross-section is a detrimental source of noise in Toughness calculation. Less complex calculation of Work appears to have less noise and therefore lower variance.

4.5.5 Discussion of Tensile Testing Results

Data for UTS and Toughness is in close agreement with the trend in data. The performance of samples improves from specimen 1 to specimen 10, then declines at a lower rate. This trend seems to be driven entirely by sample density. Dependence on density explains why there is virtually no difference in Work and Toughness results, despite Toughness accounting for external dimensions.

It is unlikely that shift in density is driven by a single factor, but the focus should be on identifying ones with the greatest effect. The most evident difference between the front and rear specimens is how rear samples accumulated more powder, as evident from the *Widest Point* measurements. This led them to collide more strongly with the recoating blade and experience more friction force. That friction aids in powder deposition, but an excessive amount of it could have led to fresh powder being scraped off the sintered surface.

4.5.6 Specimen Features and Abnormalities

During the build process, the powder build-up effect visible in Figure 3 caused samples to be shifted across the powder bed, by the action of the recoating blade. This shifting at beginning of build

process leads to formation of 'horns' at one side of the samples pictured in Figure 4.25. Horns terminate sharply after several layers are built. Their disappearance coincides with layers where sintering of the narrow section started. The narrow section mechanically joined both end sections and created additional friction force against the powder bed, counteracting friction from the recoating blade. Horns are absent on the other side of samples since that side was built last, with the bulk of built specimen acting as an anchor in powder cake. An important observation was that samples with high numbers, which had been exposed last, had visibly more powder build-up on them. More build-up generated more friction and more shifting, evident by larger 'horns' on highly numbered samples. Another sign of increased powder build-up is the steadily increasing maximum width of samples (graph in Figure 4.24). It indicates that due to the build-up, sample was also being pushed down deeper into powder bed by the action of the recoating arm, as illustrated in Figure 4.17. The exact reason why build-up was greater in last-exposed specimens is that those specimens had higher surface temperature and therefore greater tackiness at the moment of powder spreading. Tackiness provides additional shear, necessary for deposition of poorly flowing TPU- a subject which has also been tackled in Chapter 4.3.3.

Detailed investigation of specimens revealed a change in polymer appearance in the wide sections (Figure 4.26). When outer, dark parts were cut off and compared to the middle, narrow section, their density was revealed to be on average 7% greater. Greater density would cause less light to be scattered by the pores, explaining the dark appearance. Change in density happens exactly in planes where machine switched between sintering full length of a specimen and sintering shorter segments forming wide sections of dogbones. The system was set to perform hatching in direction of specimens' longest dimension, what inadvertently maximised time to complete each melt track and therefore time between fusions of sequential melt tracks. During sintering of the narrow section, the total length of one hatching pass was 140mm (i.e. length of a specimen) and given the laser speed, it would be exposed in 42ms. When sintering layers with only end sections present, the software would split every rectangular area into a separate exposure task, making one hatch pass ~20mm long. One melt track would now take 6ms to complete. This particular case illustrates the limitation of using energy density as the sole measure of laser exposure when the

time between track exposures is a significant factor. Unfortunately, exposure cannot be easily reported in terms of e.g. Watts per surface area, because time gap between melt tracks changes dynamically depending on specific layer geometry. When a common cross-hatching technique is used the direction of fill scan at each layer alternates between X and Y axis, making it even less useful to provide a complete measure of energy delivery.

It is not clear by what mechanism the hatch timing controls part density. We propose two mechanisms, which can work separately or in tandem. Firstly- the additional ~36ms time gap between hatching passes could allow molten TPU to cool, therefore wasting part of energy on re-heating old tracks with each subsequent hatching pass. The second mechanism depends on the way powder particles coalesce together in process of sintering. Because of the poor bulk density of annealed powder, shrinkage from coalescence is exacerbated. Additional time gap might be giving molten TPU time to coalesce into narrower melt-tracks, which do not connect well to subsequent melt tracks. This hypothesis is supported by appearance of visible track-aligned striations on monolayer specimens from Chapter 6.4.

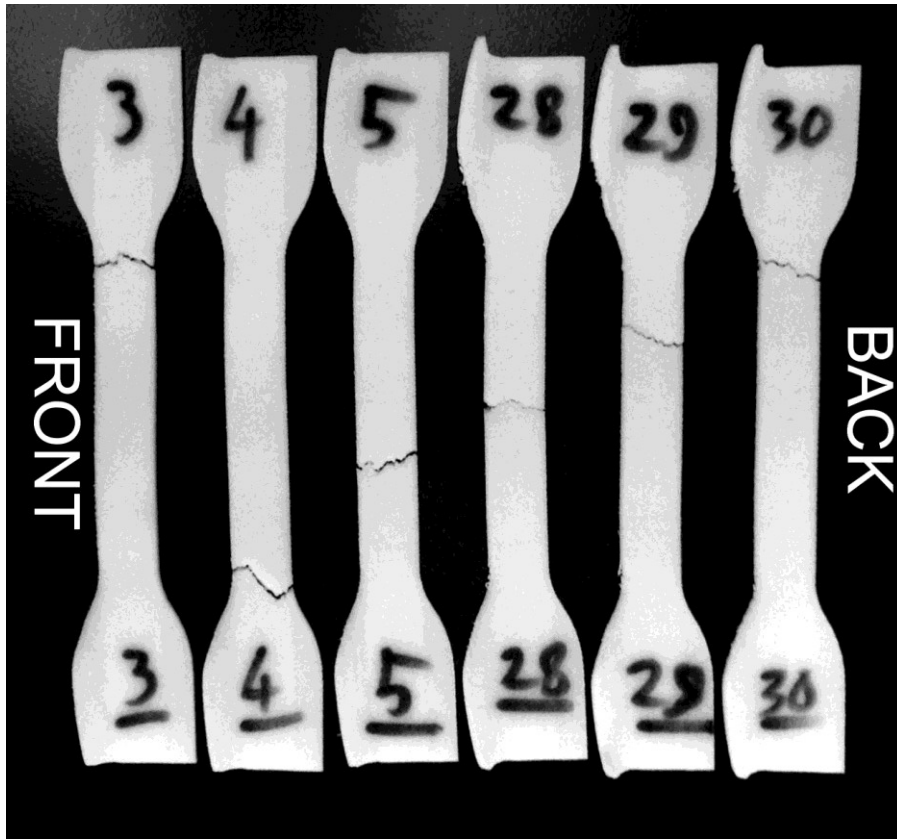


Figure 4.25: Picture of several XZY tensile specimens after being tested to failure. 'Front' and 'Back' label samples' position on the build bed, 'Front' being closer to the operator. Note the 'horn' protrusions which get larger in samples closer to the back of the machine.

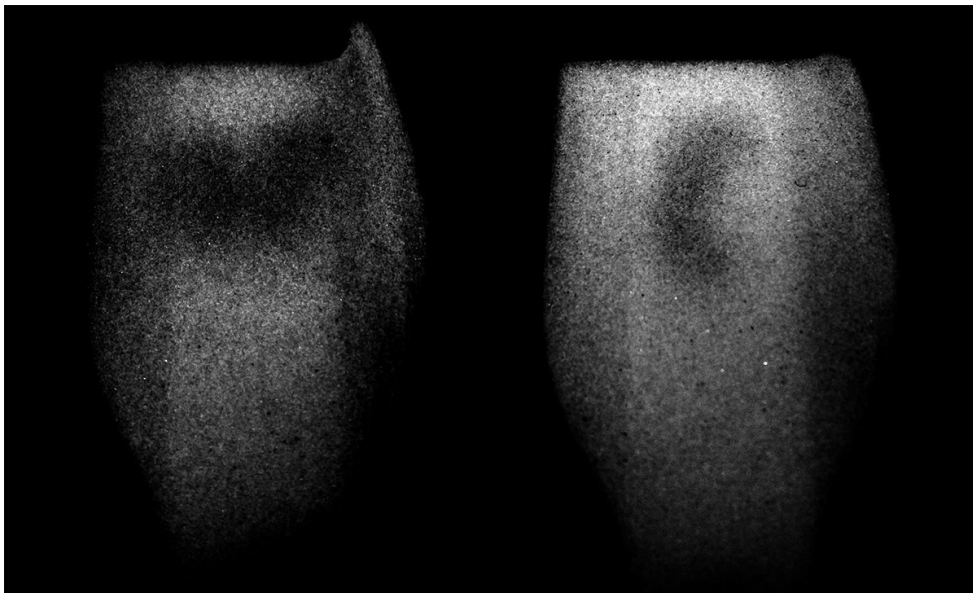


Figure 4.26: Enhanced contrast picture of two ends of XZY tensile specimens. Note that middle section is significantly brighter than outer portions. Dark outer portions are on average 7% denser. Denser, less porous material scatters less light from its surface, giving darker appearance.

4.5.7 Powder Cake Bulk Density

Because of deep XYZ build protocol, The preliminary tensile properties study was the only one where it was possible to investigate density of powder cake on the build platform. XYZ and Monolayer protocols did not create a sufficiently deep cake to make this kind of measurement possible. Cake density was measured using the protocol in Section 3.2.4, using four core samples for the average value. The density of poured and tapped powder was measured using the protocol from Section 3.2.3.

Measured values are plotted in Figure 4.27. Results reveal that powder cake density is intermediate between poured and tapped densities. This result conforms to expectations since powder experiences shear forces during spreading, which provide the benefit of compacting the powder.

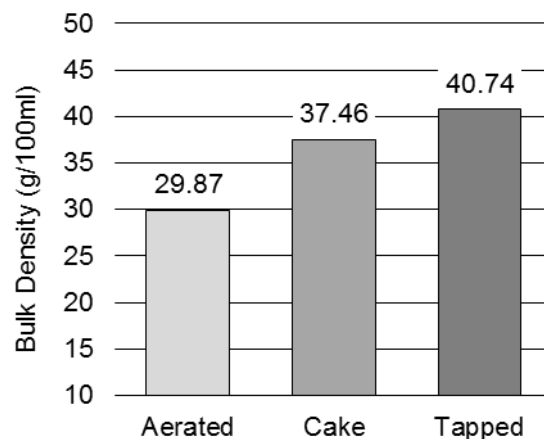


Figure 4.27: Bulk densities of powder when aerated (poured), tapped and as recycled powder cake. Error bars omitted because of negligible size on this chart.

4.5.8 Conclusions

Based on the amount of variance, we find the weight/density and work/toughness measurements to be the most accurate. Although factors such as elongation at break and Young's modulus are important measures of specimen performance, their high variance would make it difficult to detect small-sized effects later in the project. In the following studies, weight/density and work/toughness will be reported, in addition to more conventional measurements.

We found significant discrepancies in the density of sintered specimens, which depended on the length of melt tracks- which in turn caused a lag between their fusion. The difference in the melt

track length in this experiment was approaching the worst case possible, given the dimensions of P100 powder bed. In a practical build case we would expect a similar 7% density difference to appear if e.g. the sintered surface had a shape of a large circle, spanning the entire build surface.

Through the measurements of powder cake density we found that density of powder bed is higher than the density of poured powder, but lower than maximum compaction by tapping. Monitoring this value in future would aid in investigating effectiveness of system's spreading system and it is also a highly practice-oriented measure of powder's flowability.

5 Flow Agent Effects Study

5.1 Study Plan and Experiment Design

Preliminary sintering tests revealed powder flowability to be the greatest obstacle to successful processing. To remedy issues with high-temperature clumping, the annealing process was introduced. The annealing process was beneficial to flow, but it was time-intensive and seemed to introduce particle clusters. Improving powder flow by means other than annealing was therefore highly desired. The addition of fumed silica flow agent such as Aerosil is a common method of improving flow properties and preventing powder caking. Nano-scale particles of Aerosil increase separation of powder particles, minimising adhesive interactions, while also acting as a dry lubricant. Powder batch used in the preliminary study contained 0.2wt% of Aerosil. Our goal in this part of the study was to find out whether Aerosil did have a positive impact on powder flow and whether a larger amount of Aerosil would convey an even greater benefit. Three batches were chosen for this part of the study, based on varying Aerosil content. They featured 0.0, 0.2 and 0.4wt% Aerosil. These three batches are subsequently referred to using designations A00, A02 and A04 respectively. All three batches shared the AC88A12 formulation, identical to the batch in the preliminary study.

At this stage of the project, our attention was drawn to the bulk properties of powders. Since Aerosil's main impact was improving flow and density of powder, we needed to find reliable ways to measure its impact. It was during this study that we had developed the protocols for bulk density measurements (Methods Chapter 3.2.3) as well as Unconfined Compressive Yield Strength protocol (Methods Chapter 3.2.7). Other types of measurements, such as particle sizing and SEM were also used to gain a better understanding of powders' properties.

As a consequence of discovering particle clusters in annealed powders, we introduced the use of special monolayer specimens, as detailed in methodology Chapter 3.4. Monolayer production protocol is based on using cold powder from outside of the machine and spreading it manually, what allows us to use virgin powder, which is free of clusters. In this type of test, the thickness of tensile specimen is limited to just one layer, what means that standard methods of stress calculation

are not applicable. In this study, we hope to find whether the performance of the non-standard monolayer specimens can be correlated with the behaviour of full-thickness tensile specimens.

5.2 Bulk Properties Study

Qualitative differences between the three powder batches were easy to observe when handling the powders. A04 was creating large amounts of airborne dust when poured or sieved. In contrast, A00 created almost no airborne dust. A04 had a smoother appearance and also passed through sieve more easily. A02 batch had handling properties intermediate between A00 and A04. All those signs were early indicators that Aerosil does indeed reduce cohesive forces between particles. We proceeded in attempts to quantify this change in behaviour in several tests.

5.2.1 Bulk Density

Readings of bulk density were taken using standard protocol (See Section 3.2.3) for both virgin and annealed powders. Results are summarised in Figure 5.1. Annealing greatly reduced bulk density in all cases. In all test cases, A04 outranked A02, indicating that increasing A. content might be improving powder flow. However, A00 batch unexpectedly achieved consistently higher densities than either A00 or A04, despite containing no flow agent. The only test case where A00 placed below A04 was Poured Bulk Density of virgin powder.

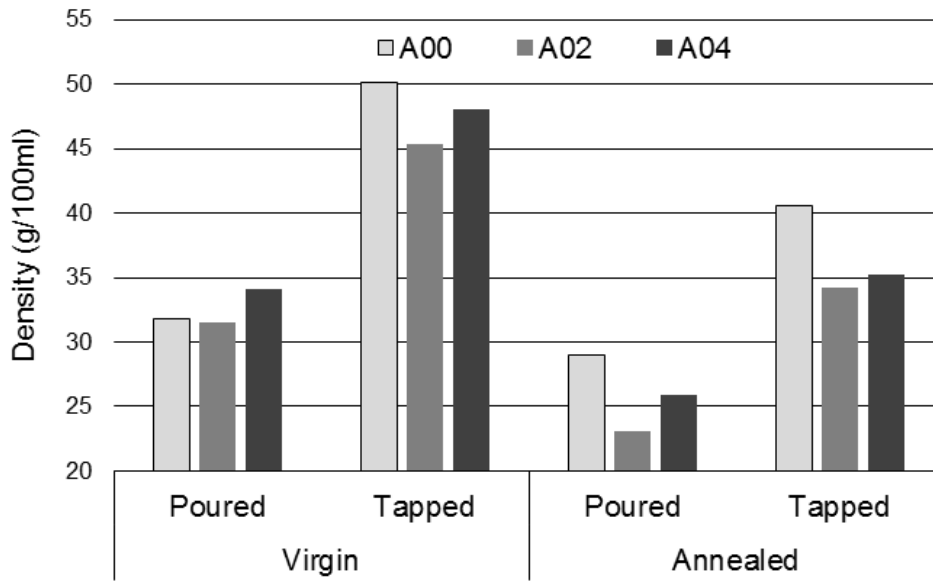


Figure 5.1: Results of Bulk Density testing on Flow Agent Effects study batches. Error bars omitted because of their indiscernible size on this chart.

5.2.2 Particle Size Distribution

Measurements of Particle Size Distribution (PSD) were performed according to the method in Chapter 3.2.6. Multiple distribution descriptors are listed in Table 5.1 and volume density (based on volume diameter D_v) is plotted in Figure 5.2. Relative to powder batches introduced later in the project, the three Aerosil batches show fairly good consistency in size. Measurement suggests that A00 might have a slightly greater amount of oversized particles compared to other two batches which did not generate any signal above the $156\mu\text{m}$ mark.

Batch	A00	A02	A04
SSA (m^2/kg)	105.9	96.0	109.1
$D[3,2]$ (μm)	39.3	43.3	38.1
$D_v(10)$ (μm)	19.3	24.2	19.4
$D_v(50)$ (μm)	56.4	57.8	52.8
$D_v(90)$ (μm)	117.0	107.0	104.0

Table 5.1: Particle Size Distribution results for Flow Agents Effects study batches. SSA: Specific Surface Area, $D_v(x)$: Volume Diameter (percent undersize)

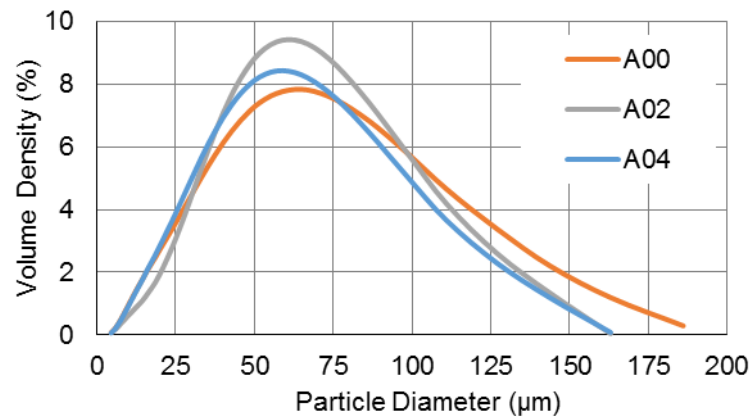


Figure 5.2: Graph of PSD results for Flow Agent Effects study batches.

5.2.3 Unconfined Compressive Yield Strength

The second type of test performed on the powders was Unconfined Compressive Yield Strength (UCYS), as detailed in Chapter 3.2.7. Six specimens were prepared per batch, which was caked in an oven for 2.5hrs at 110°C. The chosen temperature is higher than one used in our build settings, but well within range of powder bed temperatures used by e.g. Ziegelmeier (Ziegelmeier et al., 2015) on TPU. Results are plotted in Figure 5.3 and images of crushed specimens are shown in Figure 5.4. The result clearly shows that batches with Aerosil are less susceptible to caking. Note that Bulk Density is a confounding factor in this study, since strength of the caked powder should increase bulk density, as a function of large number of particle contacts. Relatively high BD of tapped A00 would, therefore, contribute to high UCYS value, but the very low strength of A04 specimen can only be explained by the impact of Aerosil.

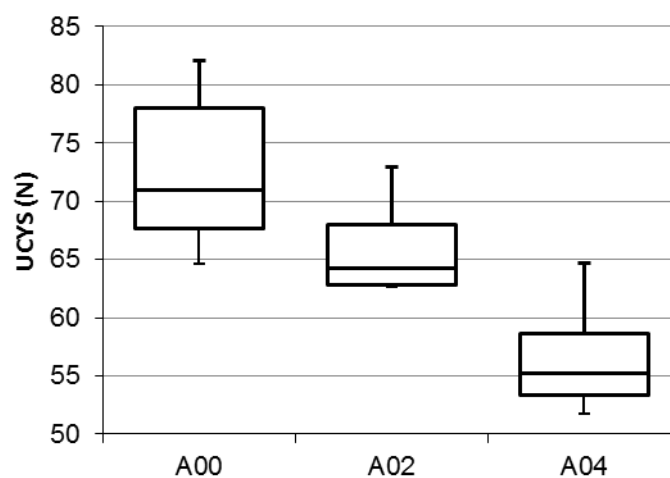


Figure 5.3: Box chart (quartiles and median) of Unconfined Compressive Yield strength of caked Flow Agent Effects study batches.



Figure 5.4: Unconfined Compressive Yield Strength specimens after test completion. Angular appearance confirms failure in shear mode.

5.2.4 SEM Imaging

SEM comparison of virgin and annealed powder (Figure 5.5) draws attention to the appearance of microscopic clusters in the drum-annealed batch. Some clusters consist of an agglomeration of small-to-medium sized particles. The second type consists of small particles adhering to large particle core. Clusters were small enough to flow through 400 μm aperture sieve after drum-annealing, leaving a very small amount of oversized clusters behind. However, at mesh size 180 μm powder would no longer pass freely and it had to be pushed through forcefully. Note that only 400 μm sieve was used in preparation for real builds.

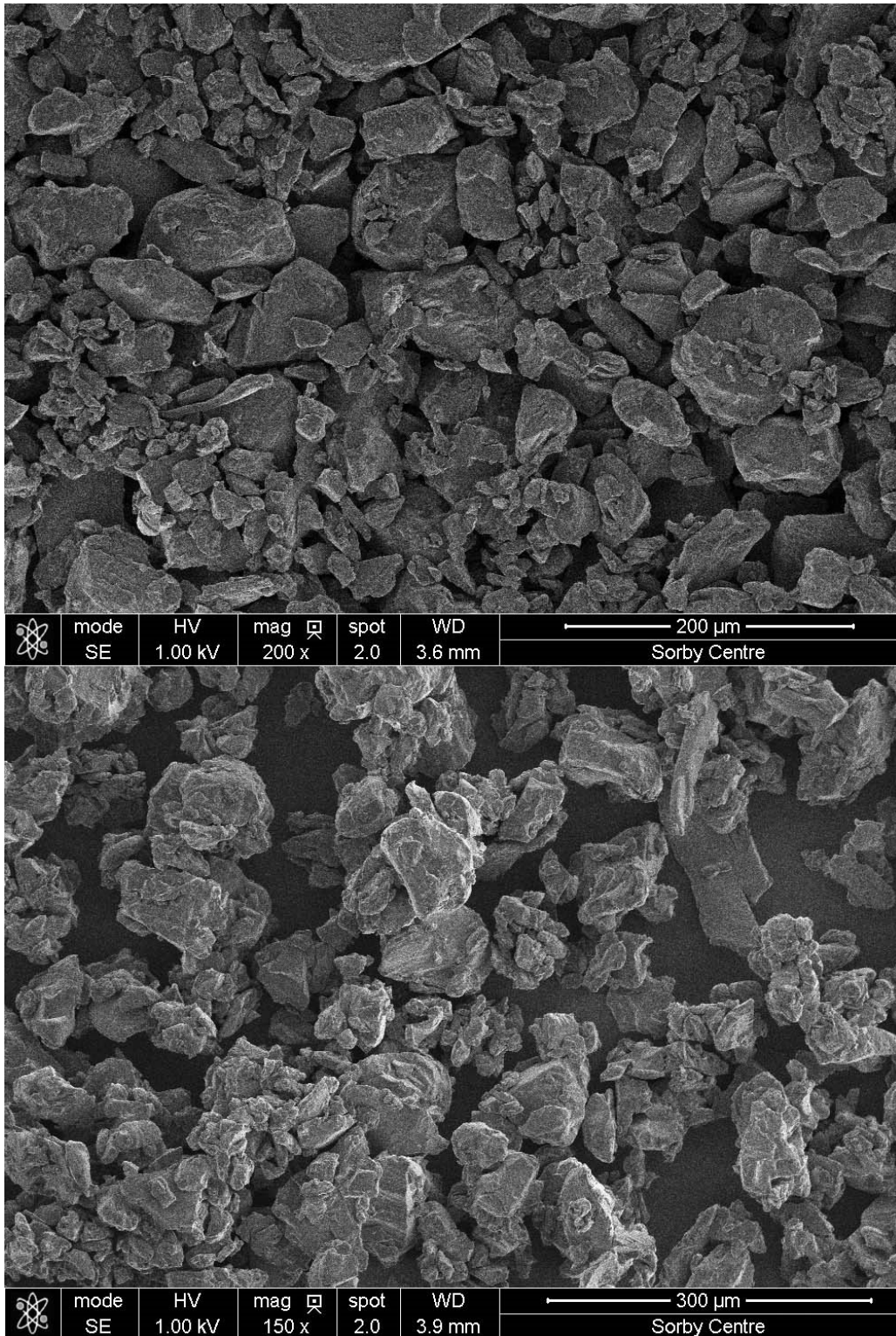


Figure 5.5: SEM images of A04 batch of powder in virgin (higher) and annealed (lower) forms.

5.2.5 Discussion of Aerosil Effects on Bulk Properties

Aerosil particles decrease cohesive forces by attaching themselves to powder particles and increasing their roughness. Surface of rough particles has on average greater separation from other

particles, what diminishes low-range cohesive forces, most significantly van der Waal's force (Tomas and Kleinschmidt, 2009). Note that we found that annealing causes the same mechanism of action, with small powder particles attaching to large powder particles. We confirmed the diminished adhesive forces in the UCYS test, where the strength of powder cohesion was inversely correlated with the amount of Aerosil. However, measurements of poured/tapped densities revealed that Aerosil may impair powder's ability to increase its packing density.

Evonik Industries technical sheet (Evonik IndustriesIndustries, 2015) advises that Aerosil applied to soft and thermoplastic powders may become embedded under particles' surface and become ineffective. The document further states that while Aerosil content below 1wt% may be sufficient for hard materials, soft materials can require up to 5wt% to compensate for powder embedding inside a particle. Additionally, when surface of powder particles is rough, like in cryomilled TPU, FA particles will tend to accumulate in pits and recesses. This renders FA particles ineffective, as they do not present themselves at particle contact points (Schulze, 2007 pg.215) .

It is possible, that Aerosil particles become embedded during the process of annealing when TPU softens. It is also possible that they are already embedded in the virgin material, due to pressure or increased temperature at some stage of processing. Partially embedded Aerosil particles could still impart reduced cohesion, by increasing particle separation. This reduced cohesion would explain airborne dust, higher poured density and reduced susceptibility to caking in UCYS test. However, embedded Aerosil particles can no longer move and roll in response to bulk powder being subjected to shear, removing their dry lubricant property. When embedded, they act to increase inter-particle friction. This increased friction would explain poorer ability to compact when powder is subjected to forced flow, or compacted by tapping.

The detrimental effect of FA on flowability has been previously reported in literature. Schulze (Schulze, 2007 pg.232) reports that when subjected to increasing consolidation stress, grains of salt exhibited marginally better flowability without FA (in this case FA was pepper). At low consolidation stresses, FA had the expected result of improving flowability. It is possible, that the flow impediment is made worse in our case due to the softness of TPU, causing both FA embedding and increased interparticle friction.

5.3 Tensile Specimens Build Process

Temperature of Build Chamber	90°C
Temperature of Removal Chamber	70°C
Laser Energy Density	25mJ/mm ²
Laser Power	21W
Laser Scan Speed	3360mm/s
Laser Scanning Motion	contour, X-axis hatching (specimen parallel), after-contour

Table 5.2: Parameters of XYZ build in the Aerosil Effect study.

During preliminary research, we had used the XZY specimen orientation to alleviate some of the build failure risk. However, we were not satisfied with the consistency and quality of produced specimens. In this study, we made adjustments to the build protocol to allow us to produce more conventional specimens in XYZ (flat) orientation, as shown in Figure 5.6. Build parameters are listed in Table 5.2. The biggest change introduced in this test was forcing the machine into manual operation mode, which gave us full control over build platform depth, deposition system and laser exposure. Due to the build orientation change, only five specimens could be fitted on the powder bed at one time. For each type of powder, 15 specimens were built, split between three batches. Between production of each batch, the powder bed was emptied of sintered specimens and powder cake. Like before, powder was annealed and then dried and pre-heated before build.

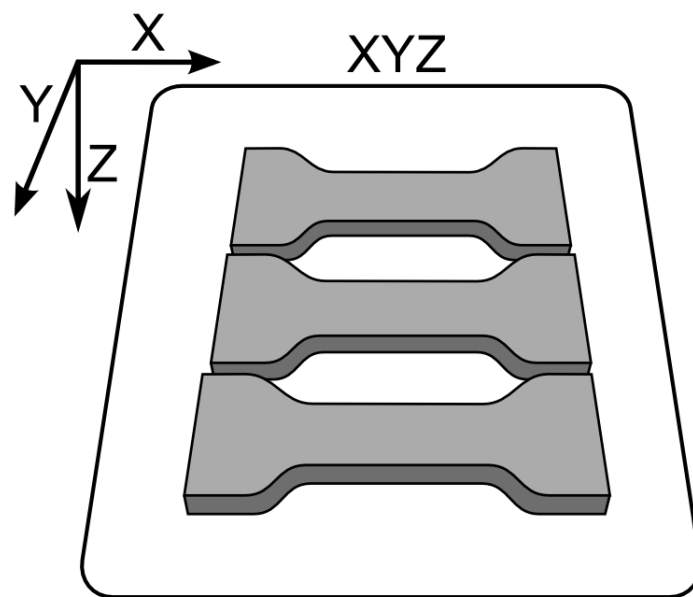


Figure 5.6: Diagram of tensile specimens in XYZ orientation.

By forcing the sintering system into *manual operation mode* we could repeat the recoating step multiple times on the same layer until a consistent layer was formed. Repeating the recoating pass twice was frequently sufficient, but occasionally three or four passes were used until spreading was satisfactory. This procedure had a side-effect of extending the time gap between sintering and deposition of a new layer. Observations from preliminary tensile properties study suggested that this recoating delay had a significant impact on powder spreading- lower delay resulting in more powder agglomeration. This observation was confirmed in this study. When the process was in manual control mode and the sintered surface was allowed additional time to cool (down to powder bed temperature setpoint), it was more difficult for the spreading arm to deposit powder onto the sintered surface. In that situation, additional spreading passes were needed. This strengthens the hypothesis that recoating delay influences powder spreading by lowering surface tackiness.

Important additional post-production step was introduced. Specimens were sintered oversized and were subsequently trimmed to ASTM D412 compliant shape using a Type C cutting die.

5.3.1 Tensile Specimens Test Results

Tensile testing was performed using the same hardware and protocol as in the preliminary tensile study. Note that the dimensions of specimens changed in this study from Die A to Die C, what reduced specimens' cross-sections. Standard tensile values are reported in Figure 5.7. We detect a large amount of overlap in data for A02 and A04. Analysis of Variance (ANOVA) indicates that those two specimen populations are not likely to be different from each other. ANOVA also indicates that A00 significantly outperforms both A02 and A04.

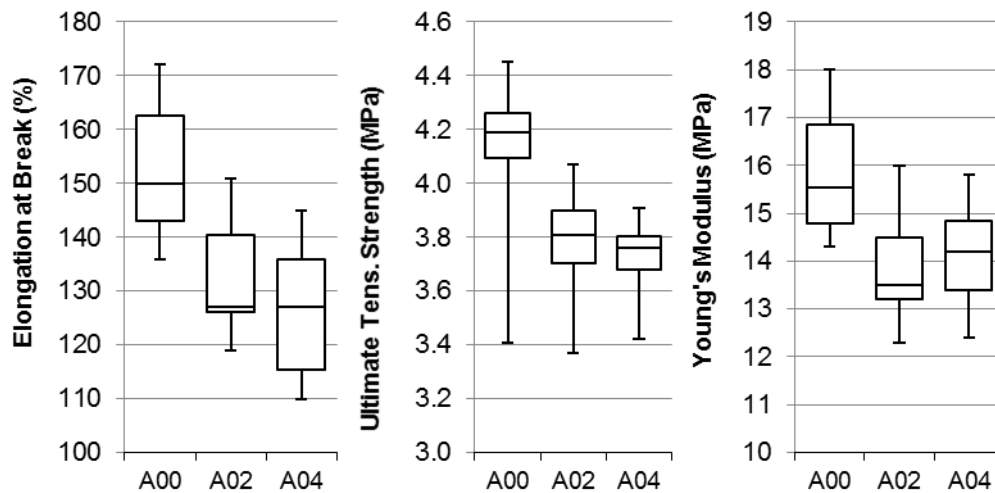


Figure 5.7: Box chart (quartiles and median) of tensile tests results from Flow Agent Effects study.

In the preliminary tensile study, we had seen tensile properties follow the same trend as specimen density. Because of high levels of porosity, specimen density is in effect an indirect measure of average specimen cross-section, accounting for the presence of pores. Because of the obvious causal link between density and developed stress, we decided to correlate mechanical performance with specimen density. In the preliminary study, we found Toughness to be a highly reliable measurement with low variance. In Figure 5.8 we plot all specimens' Toughness (up to 100% strain) versus their density. The result is an apparently linear relationship, which becomes clearer for high-density A00 specimens. As before, we see no significant separation in results of A02 vs A04. A00 continues to outperform both batches in terms of density and toughness. Sintered density reached around 68-71% for A02 and A04. This result is very similar to values from the preliminary study, which also used 0.2wt% Aerosil. A00 specimens achieved a significantly greater density of around 71-73%.

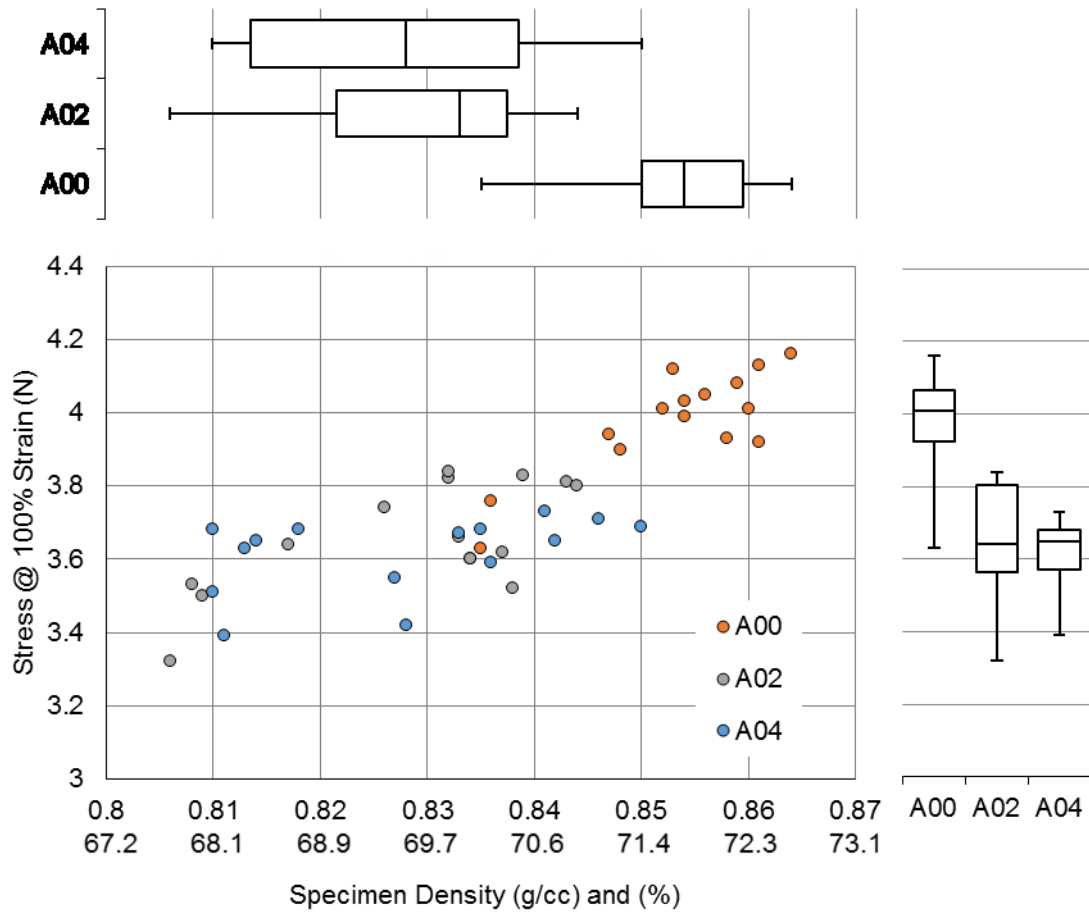


Figure 5.8: Toughness vs. Specimen Density in Aerosil effects study. Combined scatter and Box Charts.

5.4 Monolayer Specimens Test Results

Monolayer specimens were manufactured and tested according to protocols in Section 3.4. Machine parameters used during production are listed in Table 5.3. Due to non-standard nature of monolayer specimens, their mechanical performance cannot be directly compared to full-thickness dogbones. Crucially, because cross-section area of strips cannot be meaningfully measured, we are forced to collect measurements of load and weight, instead of stress and density. Likewise, without a meaningful measure of specimen volume, Toughness which is expressed in joules per volume needs to be replaced with Work expressed in plain joules.

Temperature of Build Chamber	90°C
Temperature of Removal Chamber	70°C
Laser Energy Density	35mJ/mm ²
Laser Power	17.5W
Laser Scan Speed	2000mm/s
Laser Scanning Motion	Y axis hatching

Table 5.3: Parameters of monolayer build in Aerosil Batches Monolayer study.

We assumed that the relationship between strip's Work and Weight would be analogous to that of Toughness and Density of full-thickness specimens. In Figure 5.9 we see that relationship between both values is highly linear. There is a large degree of overlap in weights of specimens from the three batches, but ANOVA confirms that all batches form discrete distributions. A04 produced lightest specimens, A00 heaviest and A02 placed in the middle.

ANOVA of data for Work shows no significant difference between A00 and A02, while A04 placed significantly lower. However, note that A00 specimens are significantly heavier than A02. This leads to a conclusion that A02 specimens can perform more work per unit of mass. Statistically, the difference between A00 and A02 batches is confirmed using Analysis of Covariance (ANCOVA), using specimen weight as a covariate. The difference in performance can be visualised as a shift in the offset of the linear regression line, as shown in Figure 5.9.

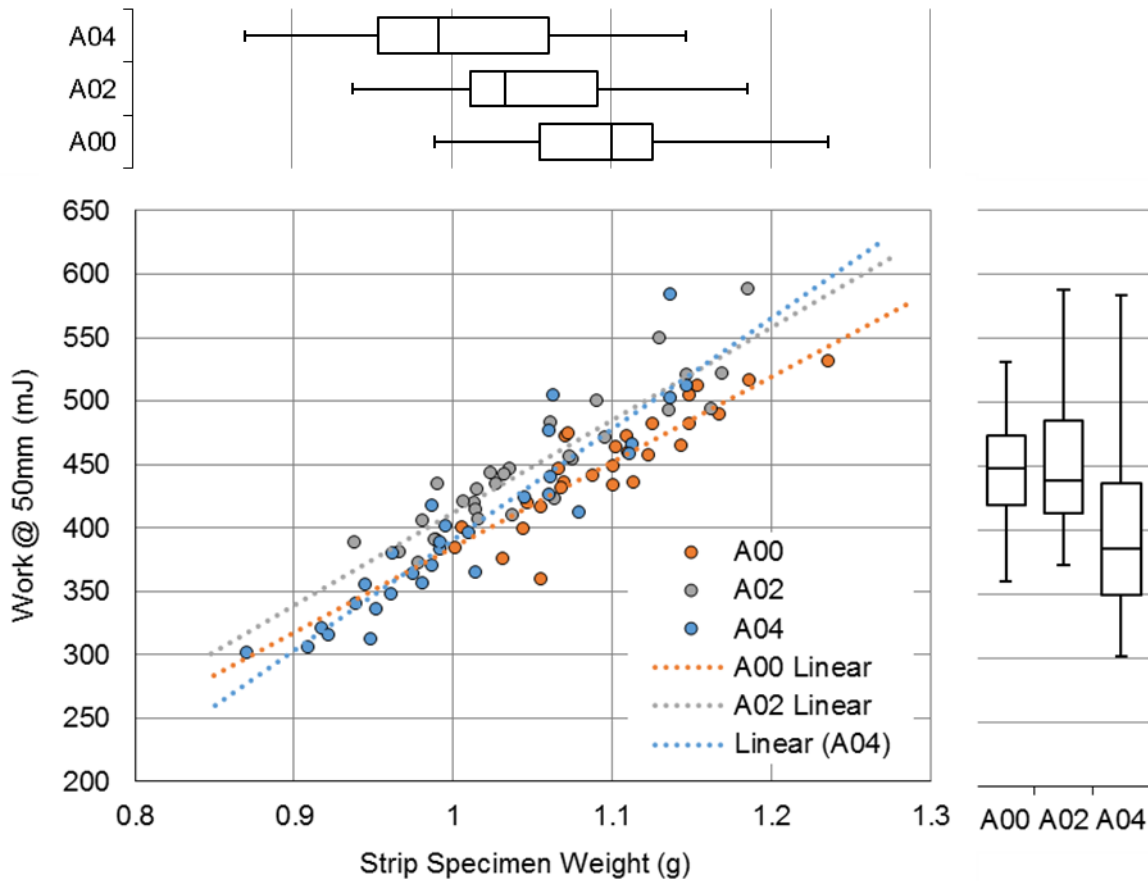


Figure 5.9: Flow Agent Effects study monolayer specimens Load vs. Strip weight. Combined scatter and Box Charts.

5.5 Comparison of Traditional and Monolayer Test Results

The first aim of this study was to identify the impact of Aerosil on mechanical performance of sintered parts. We expected the primary impact to be due to changes to powder's bulk density. Discovery of powder clusters in annealed powder complicates interpretation of the results. Clusters in annealed powder are responsible for the dramatic drop in bulk density, what was likely to change powders' performance, compared to as-delivered virgin powders. However, the effect of clustering seemed evenly distributed amongst the batches and it did not impact materials' relative ranking. The difference in BD of A00 and A02 is still $\sim 5\text{g}/100\text{ml}$ and it is similar between A00 and A04. Because of the overall drop in density this difference has increased from $\sim 10\%$ to $\sim 12.5\%$ density drop. We had hoped that comparison of results of full-thickness and monolayer specimens would help us understand the impact of clustering (since no clusters were present in monolayers), but we found the results to be inconsistent between the two types of tests.

In results from full-thickness specimens, we observed that A00 specimens were denser and outperformed both A02 and A04 in all measures of mechanical performance. We observed no significant difference between A02 and A04 specimens. Specimen density reached around 68-71% for A02 and A04. This result is very similar to values from the preliminary study, which also contained 0.2wt% Aerosil. A00 specimens achieved a significantly greater density of around 71-73%. In the preliminary study, we found that bulk density of powder bed is intermediate between poured and tapped densities. If this continues to be true, A00 had the highest BD and A02/A04 had much lower BD. Mechanical performance and BD seem correlated in this test, but with only three batches in the experiment, the correlation cannot be definitely stated.

The results of monolayer tests did not fully confirm the correlation. While in full thickness specimens A02 performed similar to A04, in monolayer specimens A02 performed similar to A00, with A04 falling behind. This change in A02 performance cannot be explained by the different BD of virgin powders. If the correlation with BD were the main factor in monolayer performance, A02 would have the lowest performance and A04 would be close to A00. Another likely factor- which will also be investigated in a later part of the project- is the particle size. Smaller particles coalesce at a higher rate, creating stronger bonds in limited sintering time. If PSD was a leading factor in monolayer results, we would see A04 performing on par with A00 and A02 performing worse than either batch.

Because of the limited number of batches in this part of study forming any definite correlations was going to be challenging. Results of both experiments aren't as consistent as we had hoped, making it more difficult to state whether either BD or PSD were definitely responsible for materials' performance. Monolayer test is certainly more sensitive to a different set of factors than the full-thickness test is. For instance, the thickness and therefore strength of monolayer is more dependent on the depth of sintering, as monolayers' thickness is not constrained by preset layer thickness. When it comes to full-thickness specimens we do not know exact effects the powder clusters would have on sintering behaviour. Because both tests contained unconventional solutions to poor powder flow, neither can be treated as more representative of real material use case.

5.6 Conclusions

Despite uncertainty in tensile test results, this study has clear implications for future LS TPU design process. We found that addition of 0.2-0.4wt% Aerosil reduces powder's ability to compact in a standard tapped density test. This is likely to cause reduced density of powder bed. Methods which exclusively test powder's free flowing ability such as *Jenike Funnel Flow*, or *Angle of Repose* are not sufficient to understand the full impact of a flow agent addition. Measurement of *Tapped Bulk Density* is highly recommended, as it is technically simple and accurate. *Hausner's Ratio* test is equally relevant but measuring volume of clumpy powder makes it hard to perform on TPU. Technical literature suggests that levels of Aerosil used in TPU were too low to convey a benefit, considering TPU is a soft, thermoplastic material. It is possible that increasing amount of Aerosil to level as high as 4-5wt% will lead to improvement in bulk density. However, evidence that higher bulk density leads to higher mechanical performance remains inconclusive.

At the start of the research project, unpublished data produced by BASF partners indicated that addition of Aerosil does have a detrimental effect on mechanical properties. We found no data to contradict this finding. However, detailed study of individual specimens shown that lower strength was associated with lower part density. We found no evidence that Aerosil detracts from mechanical properties by forming inclusions in final sintered part. As mentioned, experiments should proceed on batches with a significantly higher amount of Aerosil, to make its effects more significant.

6 Viscosity and Particle Size Effects Study

6.1 Study Plan and Experiment Design

Fulfilling all goals of the project required that we gain an understanding of the impact of TPU's intrinsic properties, the most important one being viscosity. To accomplish this, 12 new versions of the AC88A12 powder were introduced into the study. These batches featured undisclosed variations to proportions and molecular weights of reagents to offer a variety of viscosity profiles. Additionally, the manufacturer introduced other potentially beneficial variations, such as antistatic or IR-absorbing agents. Although the size of particles was not part of initial study design, we quickly uncovered major inconsistencies in PSD amongst different batches. Since particle size is another dominant factor in sintering theory, it became an important factor in the study as well.

All 12 batches in this study were very difficult to build with, resulting in frequent build failures as discussed in Chapter 4.3. As a result, we made a decision to forego full scale builds entirely and focus on obtaining good quality data from monolayer specimens

6.2 Batch Properties

Information accompanying the summary Table 6.1.

Mill- Milling was performed by two contractors, who will be referred to as Mill A and Mill B. Mill A seemed to consistently produce powders with smaller particle sizes than Mill B. Mill B also worked with most of the batches with low MFR. This is probably entirely incidental, but during analysis of results, we will be cautious of the possible correlation impacting the statistical analysis.

Flow Agent- Based on poor results from Flow Agent Effects study, Aerosil was replaced by a new flow agent (FA). New additive is AluC, which is a similar fumed silica product from Evonik Industries. An exact grade of the product was not disclosed and therefore the reason for change is unknown. Same FA was used for all batches with exception of batch V34.2, in which case the FA remains undisclosed. The amount of flow agent had remained at 0.2wt% in all powder batches. Standard practice was to add FA after final sieving of milled powder. However, in the case of some batches, 25% of FA was added to TPU granulate before milling.

Antistatic Additive- Some of the batches featured 'antistatic additive' which is usually a compound which improves polymer's conductivity to allow for static dispersal in normally strongly insulating polymer. While concentrations or type of chemical were not disclosed, relative amounts of additive are shown in the summary table. It is likely that the antistatic agent product is similar to the ORTEGOL® solution from Evonik Industries.

Particle Size Distribution- Because of the statistical nature of PSD, several values are supplied to describe the size distribution in a thorough manner. For an explanation of these terms please refer to Chapter 3.2.6.

Melt Flow Ratio- Measurements of TPU viscosity were supplied by the manufacturer in form of MFR values. Because MFR measurements are performed in low-shear, they are most applicable to low-shear processes such as blow moulding and thermoforming (Drobny, 2007). We believe this makes MFR method suitable for sintering as well. Values are reported both for the milled powder and for source granulate. MFR values obtained for powders are smaller in most, but not all cases. Considering the difficulty of removing gas from powder melt, presence of bubbles might be skewing the measurements slightly. Note that batches V35, V34.1 and V34.2 were milled from the same batch of granulate and therefore share the same result for granulate MFR.

DSC Peaks- Values of the annealing peak, melting peak and melting peak end are supplied for each batch, see Chapter 6.3 for details on measurements.

Oven Sintered Density- Density of powder samples after they had been sintered in an oven, see Chapter 6.5.

Monolayer Test Rank- For easy reference, we summarise the result of the monolayer study, by issuing performance rank to each batch. Ranks were assigned based on the order in which regression lines appear in Figure 6.4, starting from the top.

Pore Structure- For easy reference, we summarise pore structure later observed in each batch during oven sintering and hot plate sintering.

Batch No.	Mill	FA before mill?*	Antistatic Additive	Poured BD (g/100ml)	Tapped BD (g/100ml)	Specific Surface Area (m2/kg)	D[3,2]	Dv(10)(µm)	Dv(50)(µm)	Dv(90)(µm)	Powder MFI (g/10min)	Granulate MFI (g/10min)	DSC Melt Peak (°C)	DSC Melt End (°C)	DSC Annealing Peak (°C)	Oven Sintered Density (g/cc)	Monolayer Test Rank	Pore structure	Special
25	B	Y	N	49.07	59.76	131.90	39.90	19.6	58.9	109	33.78		139.3	149.41	98.89	1.117	7	Semi-closed	(1)
26	B	N	N	49.56	59.37	107.90	48.80	25.6	67.8	128	33.54	35.25	138.9	149.18	107.01	1.095	8	Semi-closed	
27	B	N	N	52.02	64.49	90.65	58.10	31.6	79.3	148	14.25	11.82	143.8	151.25	103.51	0.744	10	Open	
28	B	N	N	51.67	63.14	89.13	59.00	32.2	80.9	148	28.04	32.64	144.3	152.72	107.23	0.781	9	Open	
29	B	N	N	52.39	63.10	81.13	64.90	38.3	86.6	153	3.99	6.47	145.8	153.72	108.52	0.747		Open	
30	B	N	100%	47.96	62.53	79.22	66.40	37.5	90.5	160	19.32	22.82	144.3	152.51	103.9	0.729	11	Open	
33	A	Y	25%	34.13	49.85	132.80	39.60	19.7	56.3	113	35.48	41.35	144.4	153.96	103.33	1.094	2	Convex	
34.1	A	N	50%	36.73	51.33	112.40	46.80	23.2	66.7	133	39.97	44.74	144.3	153.32	103.12	1.098	6	Concave	
34.2	A	N	50%	34.53	50.06	128.00	41.10	20.9	57.9	109	39.67	44.74	145.3	153.35	103.16	1.073	3	Convex	(2)
35	A	Y	50%	32.86	49.30	141.00	37.30	18.2	53.1	104	39.15	44.74	144.9	153.35	102.62	1.087	1	Convex	
36	A	Y	N	35.77	49.81	117.10	44.90	22.5	65.1	122	30.31	31.79	144.4	153.27	103.88	1.109	5	Concave	
37	A	Y	N	34.30	48.99	136.30	38.60	18.9	56.0	106	28.5	27.72	144.9	153.02	103.05	1.105	4	Convex	(3)

Table 6.1: Summary of material parameters and selected study results. Special batch attributes: (1) V25 was milled using unique, high-speed mill settings. (2) V34.2 had different flow additive than other batches. (3) V37 had sodium-based IR absorber additive

6.3 DSC Measurements

All of the 12 batches were investigated using standard DSC protocol outlined in Section 3.1.1. Through analysis of melting peak, 9 out of 12 samples were identified to have virtually identical signal in the melting region. Batches V25 and V26 likewise appeared to have a very similar melting peak, but appearing at a lower temperature and with a gap between melting peak and end of the peak. V29 appears to be intermediate between the main group and V25/26 outlier group. Figure 6.1 and Figure 6.2 contains signals from several batches illustrating the grouping. Values of Sintering Peak, Melting Peak and Melting Peak End can be found in Table 6.1 and complete list of DSC traces can be found in Chapter 8.4.

Annealing and melting peaks can be analysed to provide additional information about the thermal history of the samples and therefore the processing steps. Since all the batches were annealed in granulate form, at an oven temperature of 100°C, we can infer that bulk of batches such as V25 and V35 did not achieve the target temperature. If this were the case, their annealing peaks would be positioned at ~110°C (See Figure 4.4). Position and size of the peaks can serve as a fingerprinting technique as well. Batches V34.1/V34.2/V35 have identical annealing and melting peaks and it has been confirmed by the manufacturer that they have been milled from the same batch of annealed granulate. Batches V25 and V26 have identical melting peak, but the different position of annealing peak, one at 100°C, second at 108°C. This seems to indicate that these powders originated from the same batch of granulate, but the granulate was annealed in two separate batches.

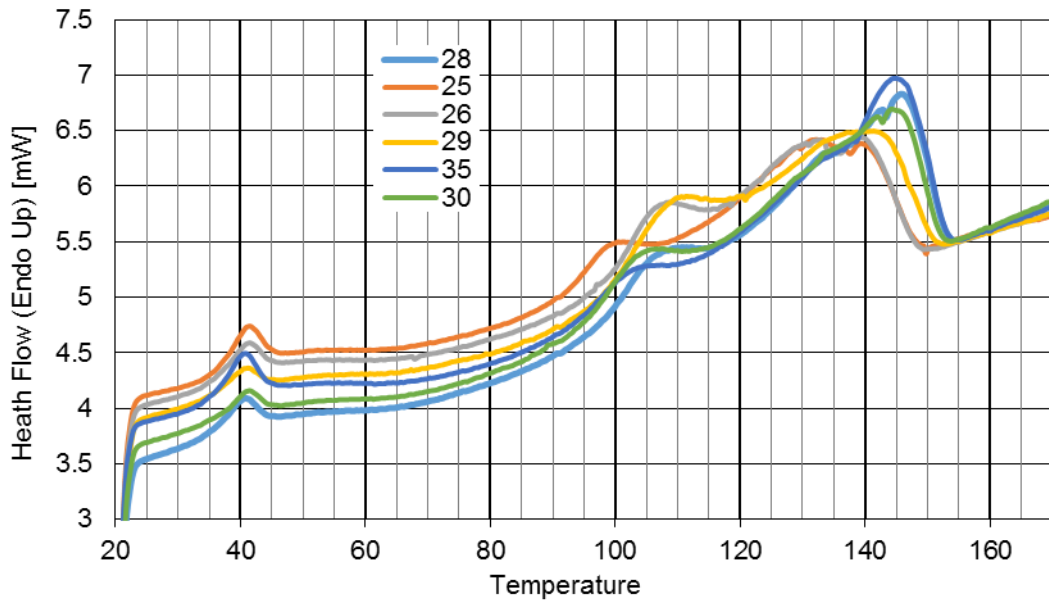


Figure 6.1: Selected DSC traces of selected batches. The lack of vertical overlap between curves is due to natural drift of the DSC system, which is magnified when looking at very low strength signal. Signals were vertically aligned at 155°C position to facilitate comparison of peaks. See Appendix 8.4 for all curves.

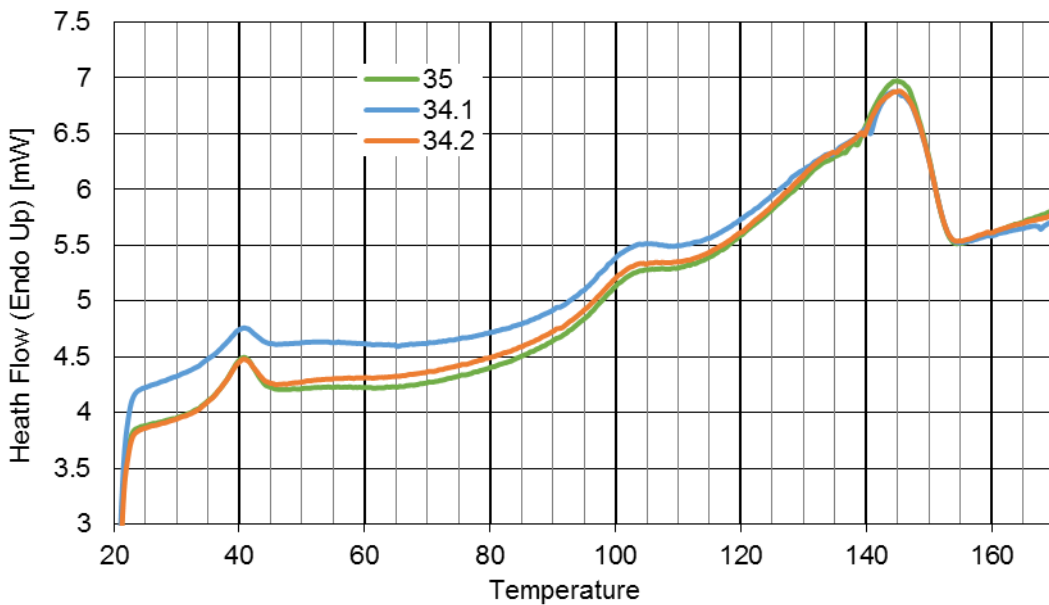


Figure 6.2: DSC signals of batches milled from the same granulate batch.

6.4 Monolayer Specimens Testing and Analysis

The monolayer study was conducted according to methodology laid out in Chapter 3.4, using machine parameters contained in Table 6.2.

Temperature of Build Chamber	90°C
Temperature of Removal Chamber	70°C
Laser Energy Density	35mJ/mm ²
Laser Power	17.5W
Laser Scan Speed	2000mm/s
Laser Scanning Motion	Y axis hatching

Table 6.2: Machine parameters during monolayer sintering in Viscosity and Particle Size Effects study. As before, we performed integration on the load-displacement curves to obtain work put into the specimen up to an arbitrary extension. To make it possible to compare both very fragile and very durable specimens, the maximum extension during measurement was 25mm, which corresponded to less than 50% strain of the strip specimens. Note that the specimens from batches like V35 and V33 could sustain strain of over 250%, exceeding maximum travel distance of the tensile tester. The only batch which had to be rejected from the study based on extremely poor performance was V29, which featured both extremely low MFR and highest particle size of all the batches. Due to errors in machine setup as well as some premature specimen failures, not all batches are represented by 30 data points, but the lowest number is 20 specimens in the case of batch V30.

The analysis of data began with the observation that there is a large spread in Work values and that this variance can be correlated, as in the case of flow agent study, with the weight of each individual specimen. It is possible that the variance in specimen weights is due to the highly manual powder spreading process in monolayer protocol. Unfortunately, manual spreading was unavoidable in making the protocol work with poorly flowing powders and could not be eliminated. A linear relationship between specimen weight and its work to an extension made specimen weight easy to integrate into the linear regression model. Figure 6.4 shows work done by specimens in the study plotted against their weight.

It is important to note that batch V25 was also eliminated from the pool of results because of extreme non-conformity with the regression model. Specifically, non-conformity arose when variables included any PSD values derived from Malvern system. All of the V25 data points were flagged by Minitab software based on very high residuals. Residuals of V25 ranged from -70 to -100, while the range of residuals for all other batches remained within ± 50 . As such, we considered

it beneficial to remove V25 data entirely from the regression model. The discussion will contain speculation on the cause for the outlier status.

We began the linear regression fitting process by assuming that most of the variance in Work values is correlated with variance in specimen mass. Larger mass directly translated to a larger number of particles and a larger number of sintering necks to carry the load. Regression accounting only for specimen strength achieved R-sq(adj) of 58.77%. Further improvements to R-sq(adj) are listed in Table 6.3.

With the primary source of variance accounted for we moved on to the well-established factors which are viscosity and particle size. Both those factors are present in the baseline Frenkel coalescence model and as seen in Figure 6.3 both are highly correlated to specimen stiffness. A model which incorporated MFR achieved R-sq(adj) of 78.01%. We are aware that in many sintering models the degree of coalescence is proportional to square root of zero shear viscosity. While we do not possess the information about the exact relationship between zero shear viscosity and MFR, we were cautious to look for signs of non-linearity in the regression model. This procedure will be discussed further below, but no signs of non-linearity were found in the case of MFR.

Particle size had been measured using a diffraction-based system which generates several different statistical descriptors of the distribution. In a regression model, it is undesired to use factors which are highly correlated and redundant, as it leads to a reduction in confidence in coefficient values of each individual factor. Therefore, the best practice is to find only one numerical descriptor of PSD. Two initial candidates are the two different estimates of mean size- volume mean ($D[3,4]$) and surface mean ($D[3,2]$). The volume mean corresponds to mean diameter of particle contributing the most to powder volume. Surface mean corresponds to mean diameter of particle contributing the most to powder surface area. Due to square and cube relationship with radius respectively, former value is skewed towards larger particles and latter to smaller particles. Another PSD result describing entire distribution is the Specific Surface Area (SSA). This value should be proportional to the surface mean since they both share a square relationship with particle radii. We found that regression benefited the most from the addition of Specific Surface, with

R-sq(adj) of 96.53%. This is not a notable improvement over using D[3,2] measure, as both those values are heavily influenced by small particles in a distribution.

At this point, we once again investigated the degree of multicollinearity in the model. As mentioned- higher SSA batches tended to also have higher MFR. Also, higher SSA and MFR batches tended to produce heavier specimens. VIF values for all three variables ranged from 1.92 to 2.8. This value indicates only a moderate level of collinearity which should not significantly impact the quality of regression coefficients.

Lastly, we attempted to incorporate Poured Bulk Density into the model. This resulted in further increase of R-sq(adj) to 98.13%. However, at this point, the VIF readings increased significantly. SSA had VIF of 5.24 and BD VIF at 4.92. At this level of correlation, it is recommended to take action. Compensation measures include summing correlated variables into one value or standardising variables. However, we know that in this case, BD is a function of SSA. We believe that the reason why BD improves fit in this scenario is because it correlates with particle size so highly, it becomes another indirect measure of particle size distribution. BD data was acquired using method completely independent from other measures mentioned above. Including both SSA and BD in the same model effectively doubles the readings of particle size data, improving the quality of predictions. We recommend using only SSA or D[2,3] for regression.

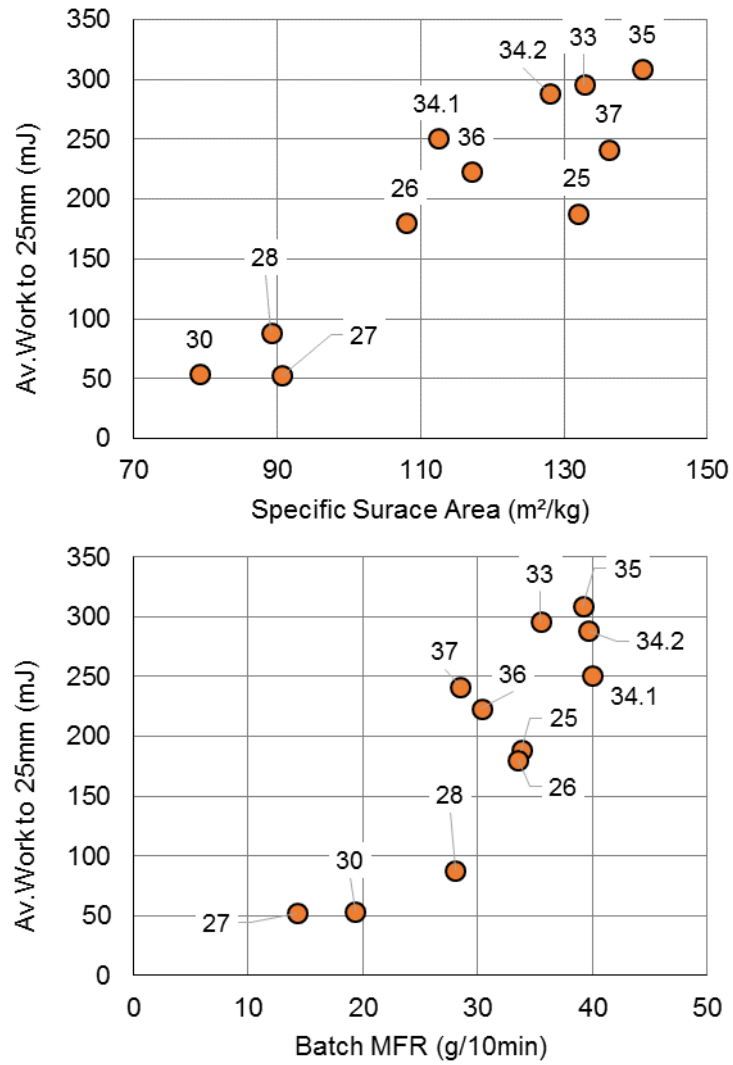


Figure 6.3: Monolayer work data correlation with MFR and SSA.

Response Variable	Predictor Variables	Adjusted Square Residuals
Work to 25mm	Weight,	58.77%
	Weight, MFR	78.01%
	Weight, MFR, D[4,3]	87.34%
	Weight, MFR, D[3,2]	95.69%
	Weight, MFR, Specific Surface	96.53%
	Weight, MFR, Bulk Density	95.33%
	Weight, MFR, Specific Surface, Bulk Density	98.13%

Table 6.3: Adjusted Square Residuals of linear regression models in monolayer study.

The best regression model we could obtain calculated regression coefficients of 2.42 for MFR and 2.88 for SSA. The degree of model fit is very high, with R-sq(adj) 96.53%. Regression

coefficients represent a change in the response variable (Work) for one unit of predictor variable change if other predictors were to remain constant. Increasing SSA by $1\text{m}^2/\text{kg}$ would increase specimen's work by 2.4mJ. Increasing MFR by $1\text{g}/10\text{min}$ would increase specimen's work by 2.88mJ. Because typical numerical values of SSA in this study were larger than values of MFR, SSA had more power to influence the specimens. The difference between highest and lowest SSA was $\sim 60\text{m}^2/\text{kg}$, while the difference in MFR was $\sim 30\text{g}/10\text{min}$. This translates to a potential change of 172mJ by SSA alone and a potential 72mJ change by MFR alone.

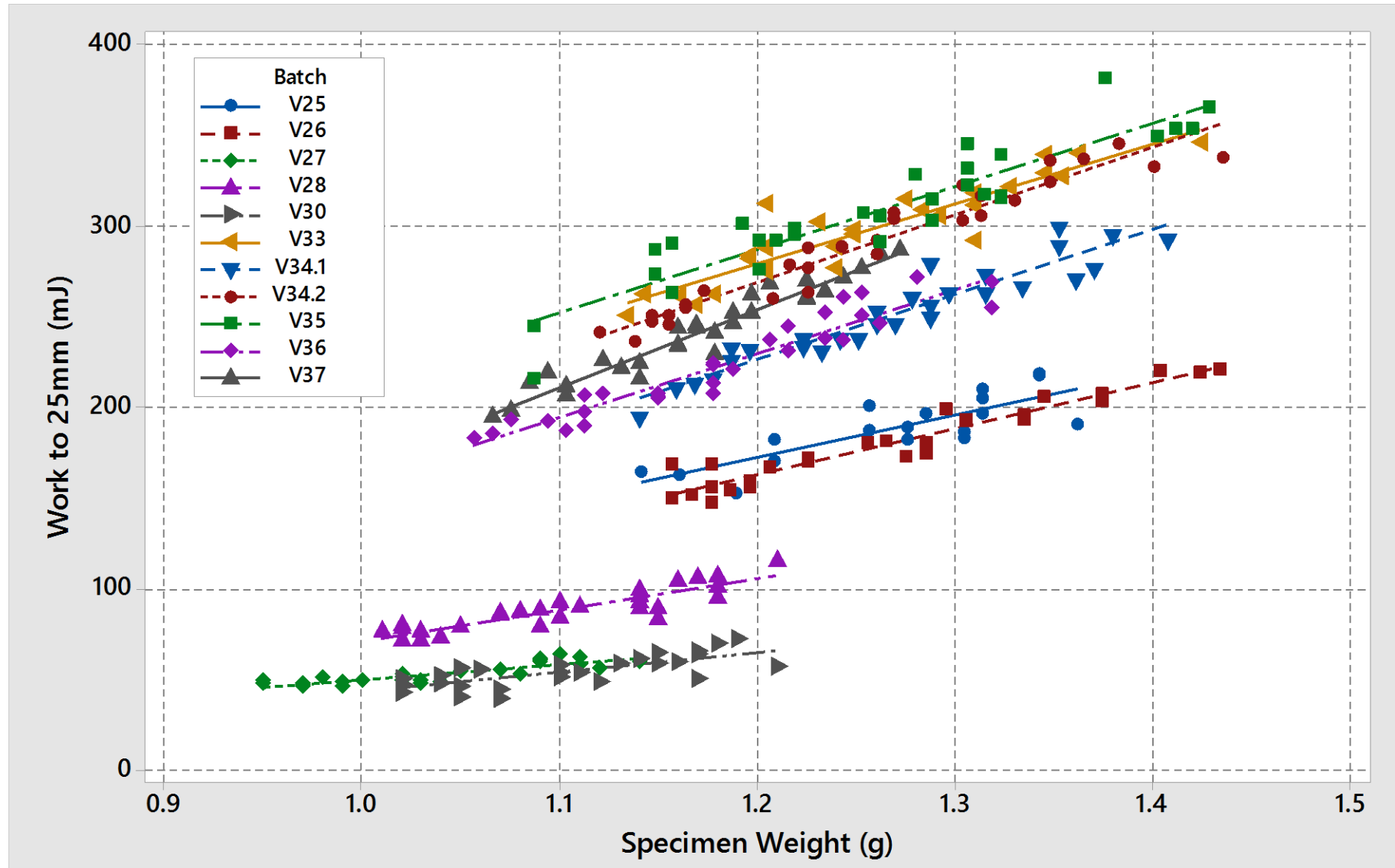


Figure 6.4: Viscosity and PSD Effects monolayer study- all specimens which could sustain 25mm elongation.

6.5 Oven and Hot Plate Sintering Observations

Differences in melting and coalescence behaviour of the 12 powder batches were so drastic that they could be qualitatively assessed by melting them in an oven. Figure 6.5 contains pictures of small doses of powder which had been melted on a PTFE sheet at a temperature of 170°C, for 15 minutes. Batches V33 to V37 appear very well sintered. Their surface is smooth and glistening, what indicates a lack of open pore structure. Note that the samples were not sieved prior to melting. Batches V33 to V37 had a larger tendency to clump in storage and those clumps remain visible after melting, due to limited viscous flow. Batches V27 to V30 have very opaque, rough appearance. Note the vertical cracks appearing e.g. in V29. They appeared as result of flexing the PTFE sheet after specimens were already sintered. Batches V25 and V26 can be seen as intermediate. While almost translucent, they were rough to touch and matte in appearance.

In order to observe pore structure, we sintered samples of powders on glass slides. Slides were placed on a hot plate set to 170°C for 5 minutes, to ensure complete melting to stable structure. Reflected light images show adhesion points between TPU and the glass substrate. Images from this imaging method are shown in Figure 6.6. Batches V33-V37 are characterised by small, isolated voids. Batches V27-V30 show very little adhesion and points of adhesion are isolated. V26 and V26 shown intermediate structure, where pores are closed but are very large and have a complicated shape.

We had verified the open-pore structure in batches V27-V30 by attempting to melt them in a vacuum oven. This produced no change in behaviour, proving that gas is free to move through the sintered powder volume and therefore that pore structure is open.

We measured the density of oven-sintered specimens using Archimedes method. Four specimens were tested per powder batch. Results are presented in Figure 6.7 and density averages are listed in summary Table 6.1.

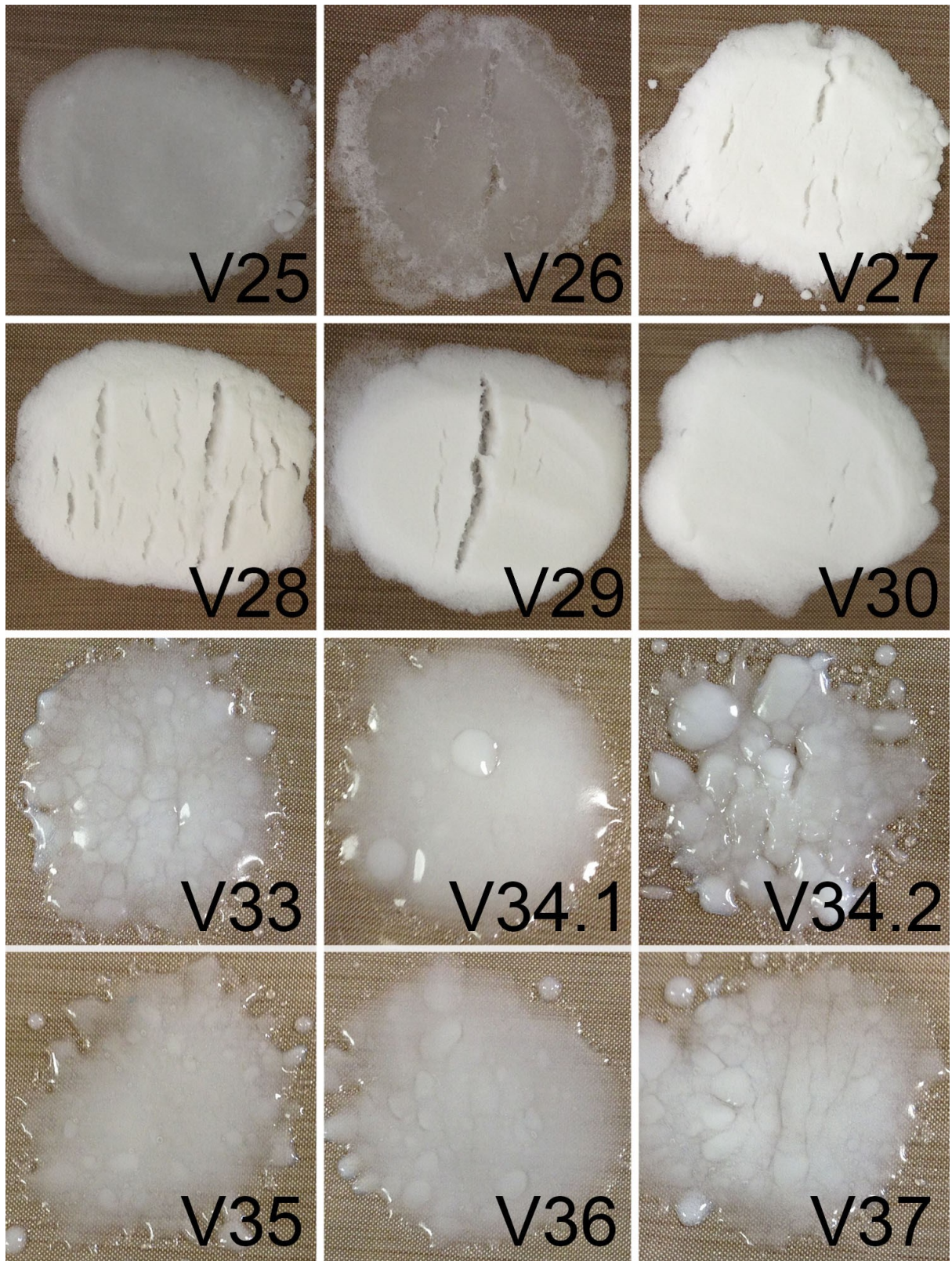


Figure 6.5: Viscosity and PSD study batches of powder melted in oven for 15min @ 170°C

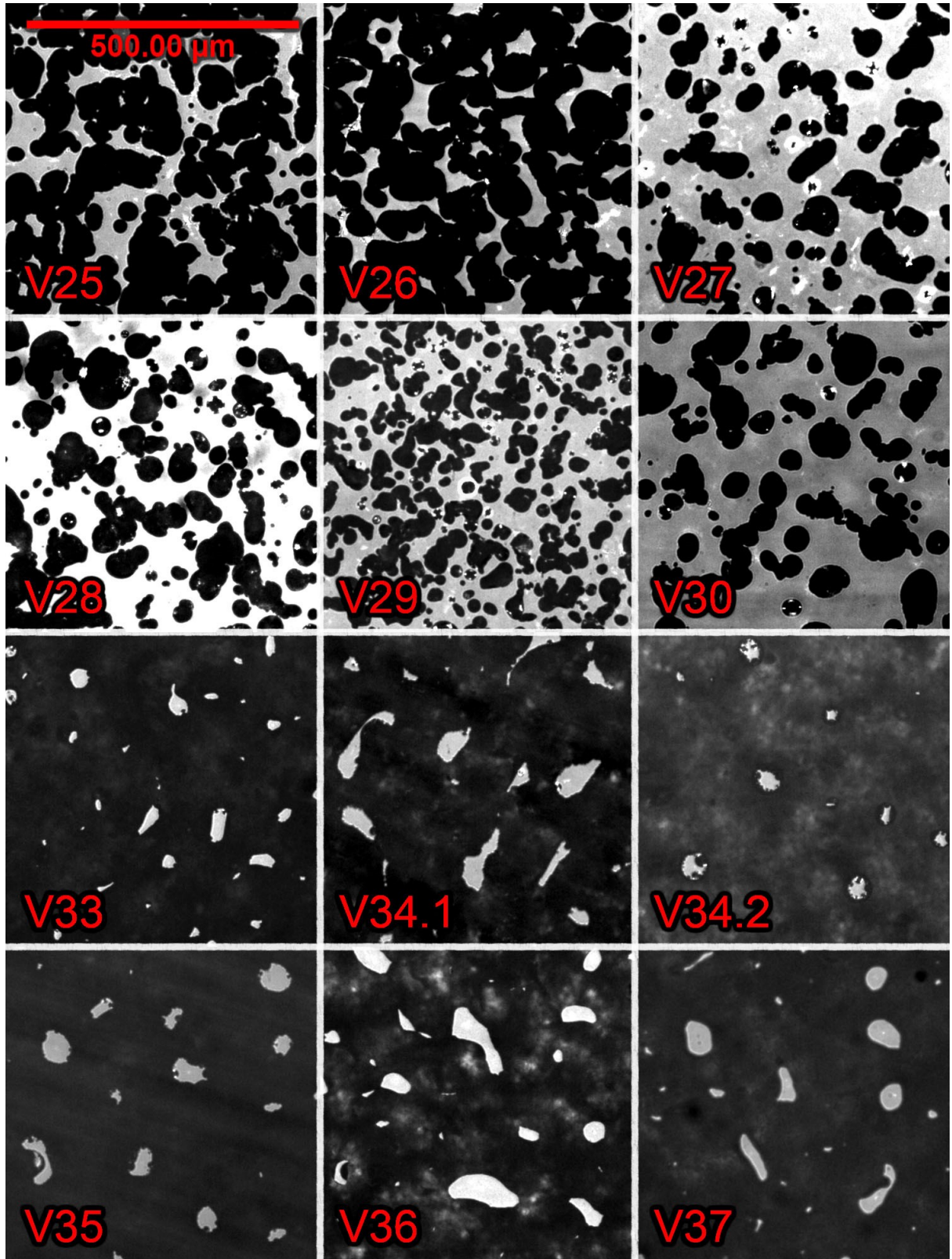


Figure 6.6: Reflected light pictures of sintered specimens' underside. In every picture dark areas correspond to points of adhesion, light areas to air gaps.

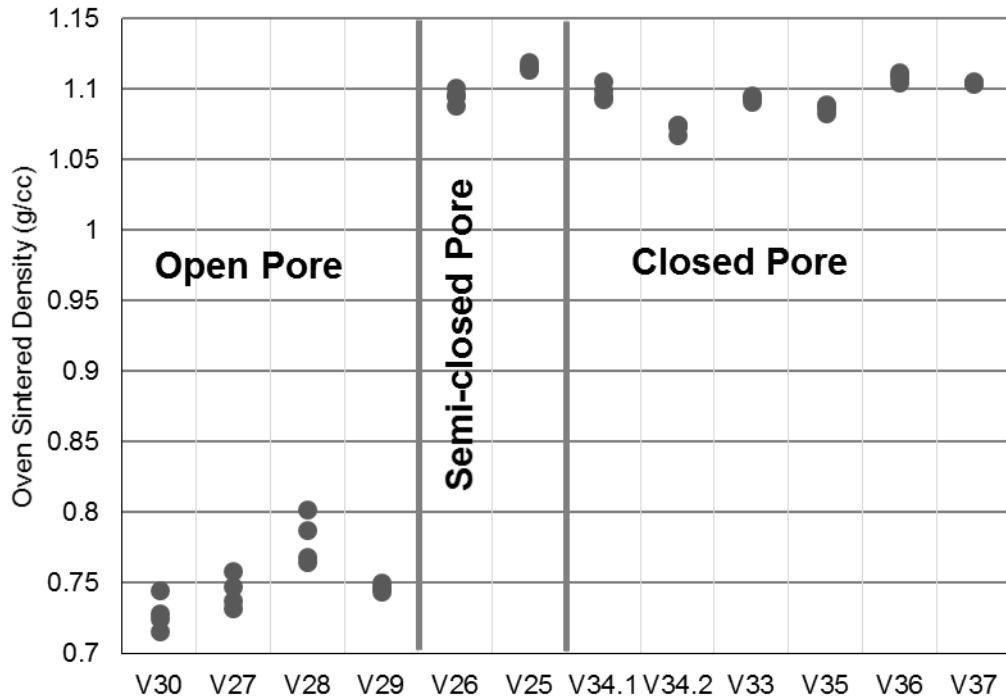


Figure 6.7: Densities of oven-sintered powder batches, split by the observed pore structure.

6.6 HSM Assessment of Closed Pore Structures

In this study, we utilised the Hot Stage Microscopy observations mainly in a qualitative manner. By melting portions of powder large enough to form closed pores, we could use it to study the pore formation and densification process. With the exception of the adhesion patterns shown in Figure 6.6, it was very difficult to use optical methods on the open-pore batches. They were too opaque for transmitted light observations and their surface was too rough to present a clear image. HSM could be used to observe pore structure of closed-pore batches only. Microscopy images of those batches are shown in Figure 6.8.

A very unusual observation was made in melting behaviour of batches V34.1 and V36. Unexpectedly, in these batches pores appeared ‘crushed’, with concave walls and sharp corners. Coalescence process of those two batches is shown in detail in Figure 6.9 and Figure 6.10. According to all models of Newtonian fluid coalescence, concave-walled voids should not be stable. Capillary forces driving viscous coalescence should be highest in the formed crevices. We speculate that the

convex-concave shape of voids is important to understanding problem of coalescence of TPU and this topic will be explored further in Chapter 6.10.5.

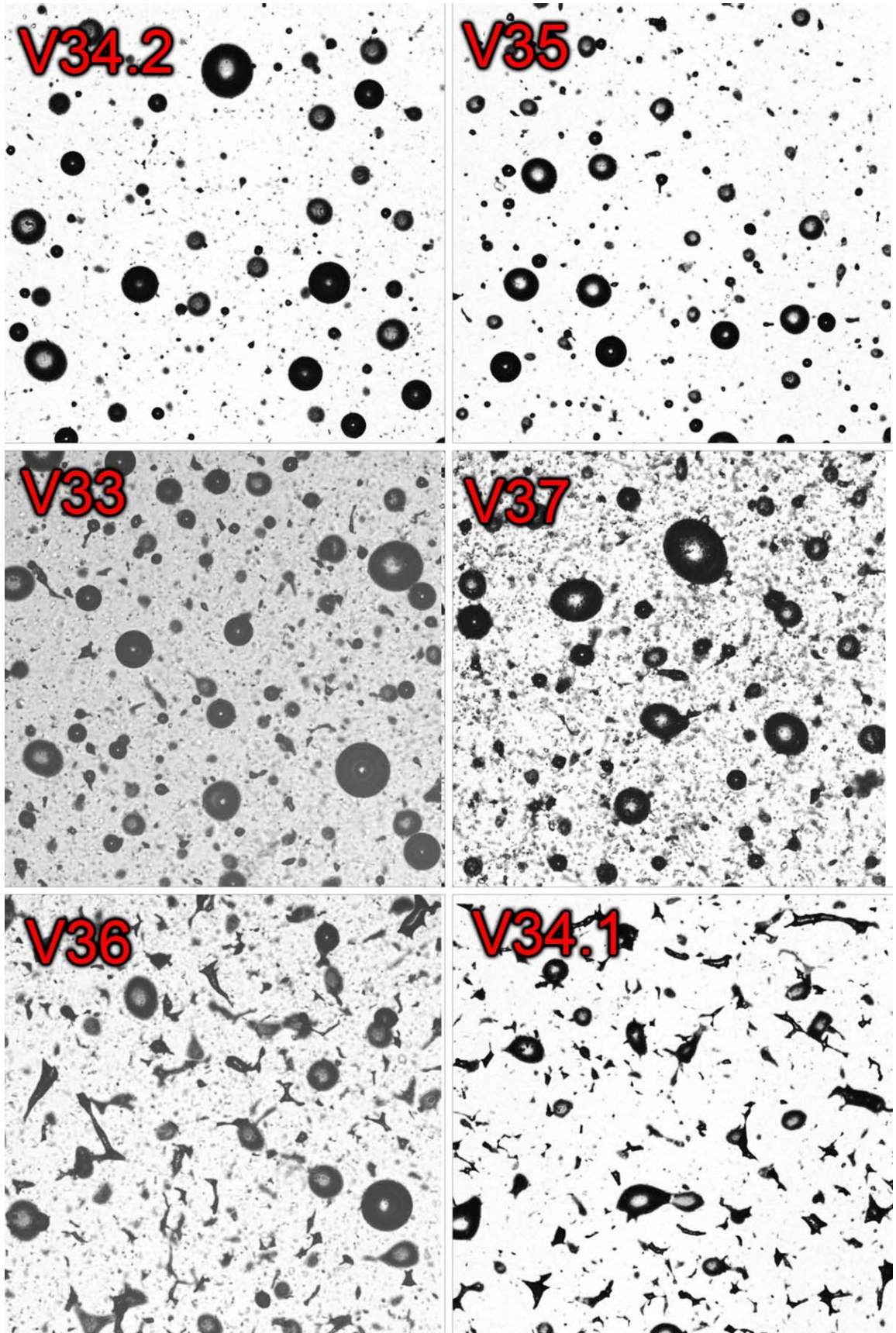


Figure 6.8: Microscopy images of closed-pore powder batches.

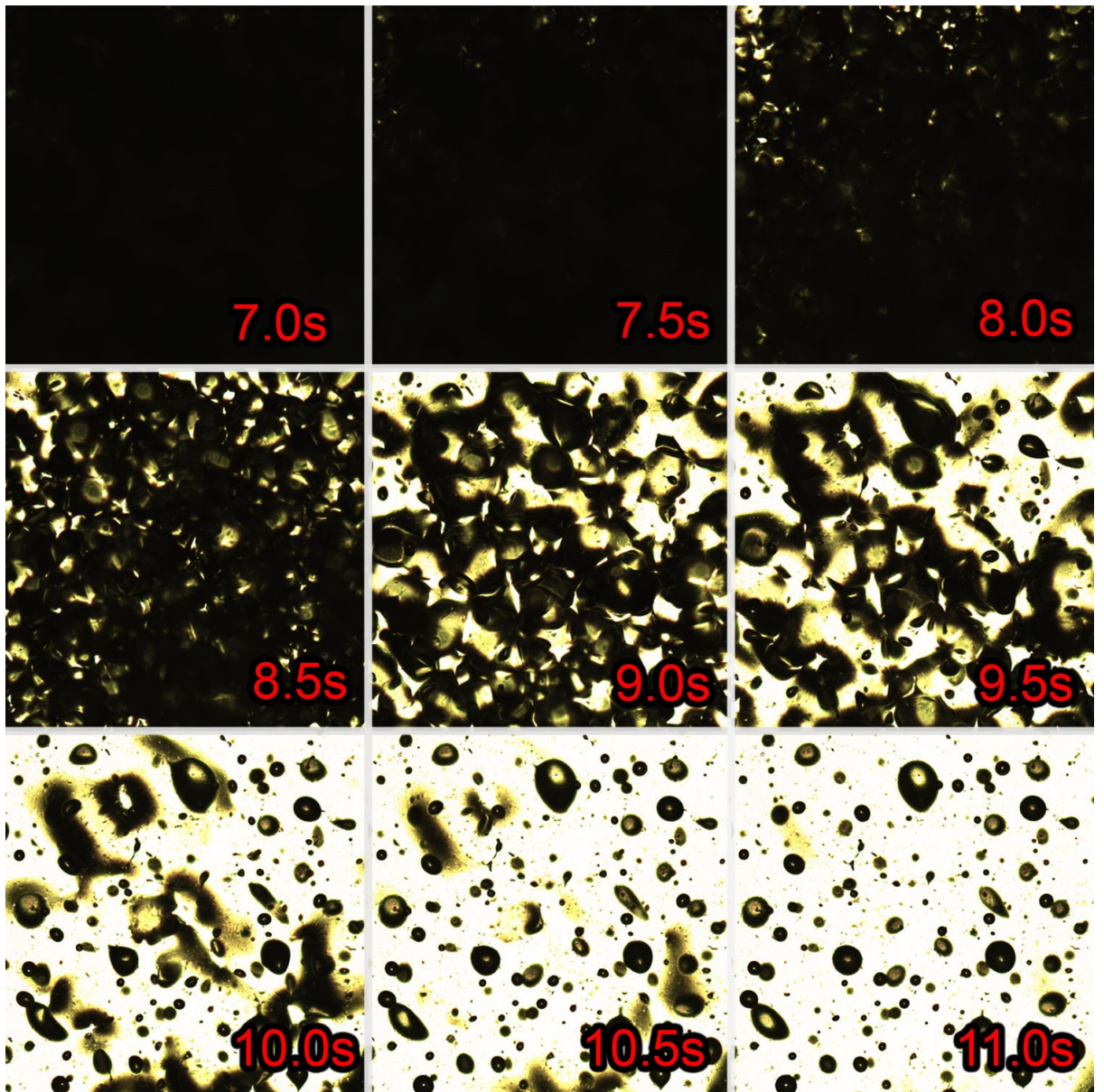


Figure 6.9: Selected frames from hot stage melting of V34.2

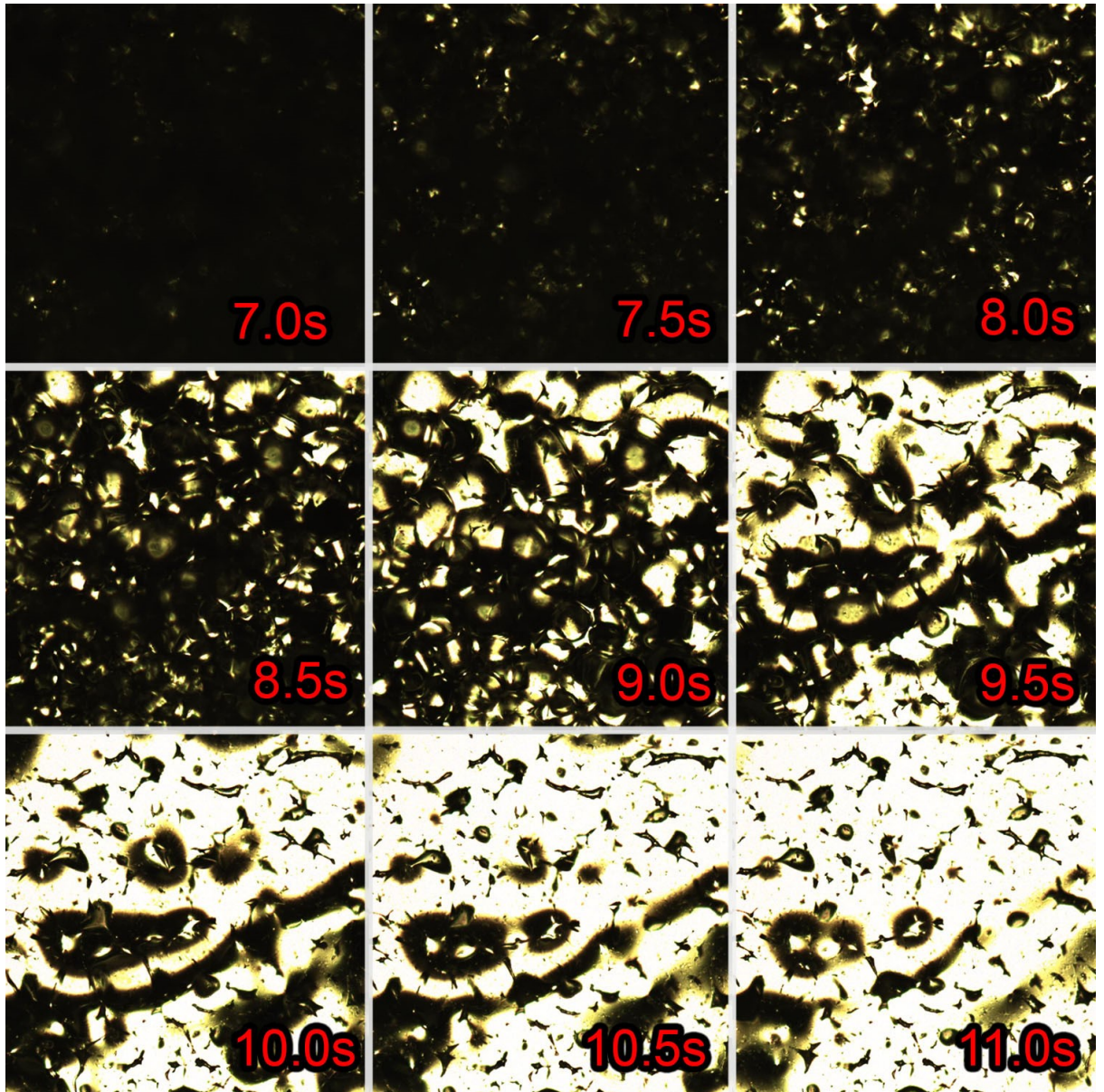


Figure 6.10: Selected frames from melting of V34.1

6.7 HSM Assessment of Melting Temperature

According to DSC traces, almost all batches show an almost identical melting peak, with exception of batches V25 and V26. To test whether the different trace did translate into truly different melt behaviour, we had observed the melting process on hot stage. The temperature was increased at a slow rate of 10 degrees per minute, to avoid problems with heating inertia, temperature equilibration and delay in picture acquisition. According to DSC trace, V25 and V26 finished melting at exactly 150°C. All the other batches completed melting at 155°C. Figure 6.11 shows HSM images

at 145-155°C, capturing the difference in melting. V25/V26 clearly begin melting at lower temperature and achieve coalescence sooner than batches V28/V30.

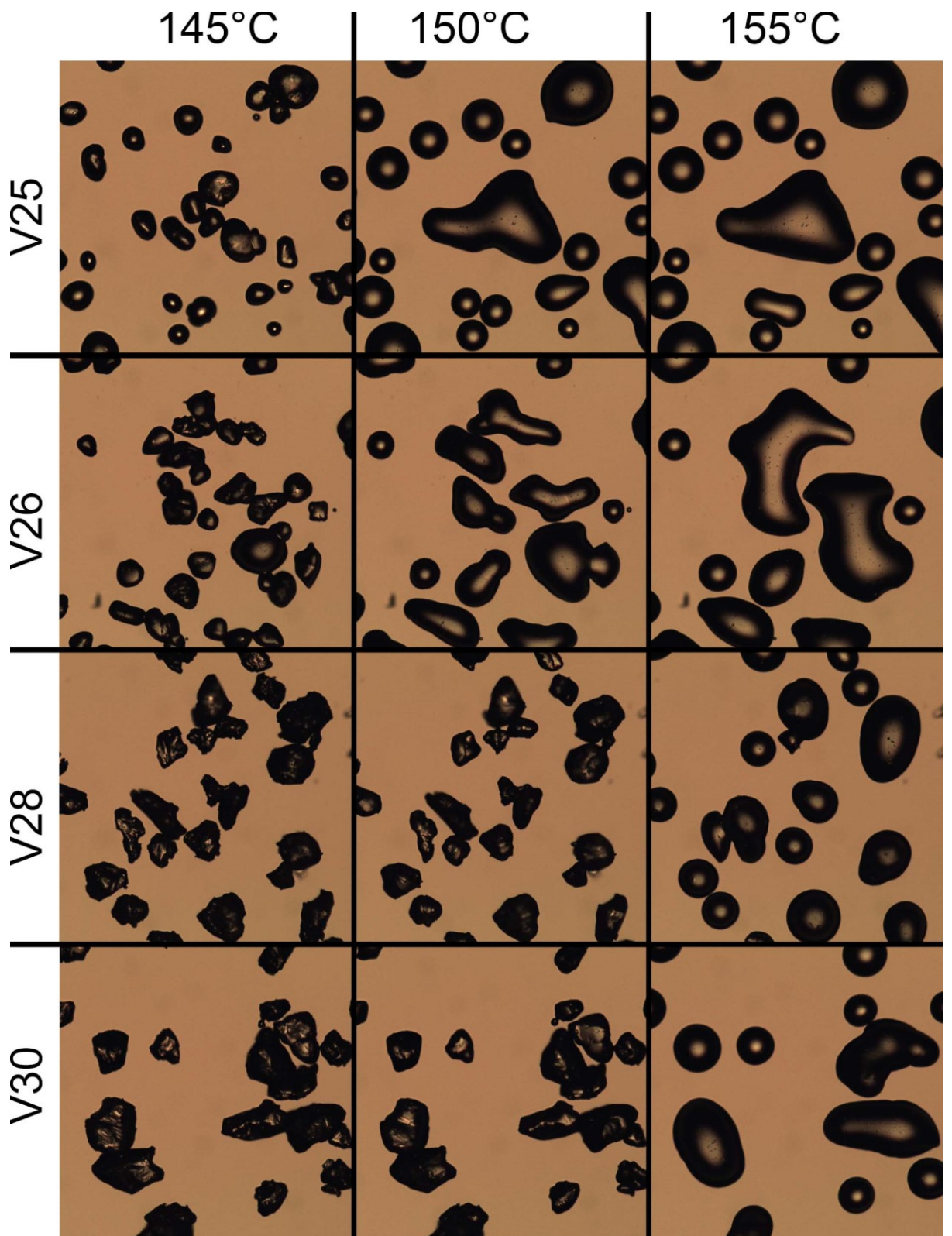


Figure 6.11: Hot Stage Microscopy images showing differences in melting temperature range between V25/V26 representing early melting onset and V28/V30 which represent a more common temperature range.

6.8 Oven Sintering Study

The monolayer tests were very useful in rating potential performance, based on the degree of coalescence. However, without tests performed on full-sized specimens, the link between monolayer results and true performance could not be confirmed. In face of tremendous difficulties with full-thickness LS builds, we decided to supplement our understanding with tests on oven-sintered specimens. Specimens were manufactured using oven sintering method from methods Chapter 3.5. For this experiment, we decided to test Batches V34.2 and V34.1. This was due to our desire to understand the impact of convex and concave voids on mechanical properties and these batches were excellent examples of low and high concave voids content.

In the preliminary tests, we found that recoverable strain of the oven sintered samples would be below approximately 50N region. In order to perform measurements above recommended 5% capacity of the load cell, we performed tests on texture analyser equipped a 500N load cell. A typical signal is shown in Figure 6.12. Stress measurements were taken at three points: 5mm, which would be within recoverable strain region, 100mm which was approximately at the start of linear non-recoverable region and 200mm which was close to the maximum possible extension. Those measurements are shown in Figure 6.13. Additionally, Figure 6.14 shows the measured slope of the non-recoverable strain region, which also shows significant difference in stiffness.

Realising that specimen density might account for some of the variance in the results, we measured the density of each specimen, using wide dogbone sections as samples. The bulk density of pre-sintering powder could be calculated based on knowledge of individual specimen's mass and the fixed volume of moulds. The value of stress sustained by samples at 200mm deflection is plotted in Figure 6.15 against specimen density. Figure 6.16 shows the density of specimens plotted against the bulk density of pre-sinter part. Note that we differentiated data points belonging to each sintering batch to show the variability caused by manual nature of specimen fabrication. Each batch consisted of 6 specimens, two batches produced for each powder.

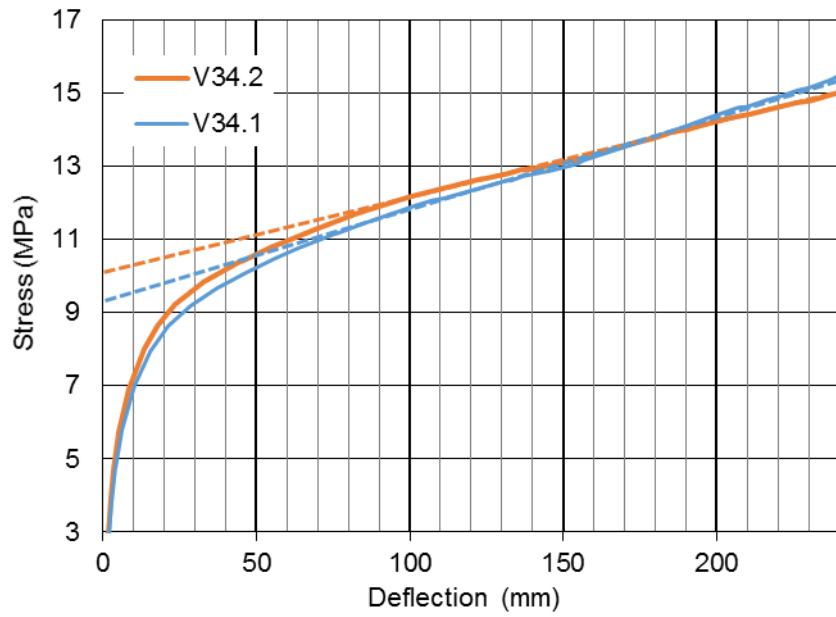


Figure 6.12: Example Stress/Deflection curve of oven sintered specimens. Curve becomes highly linear starting at ~100mm, in non-recoverable strain section.

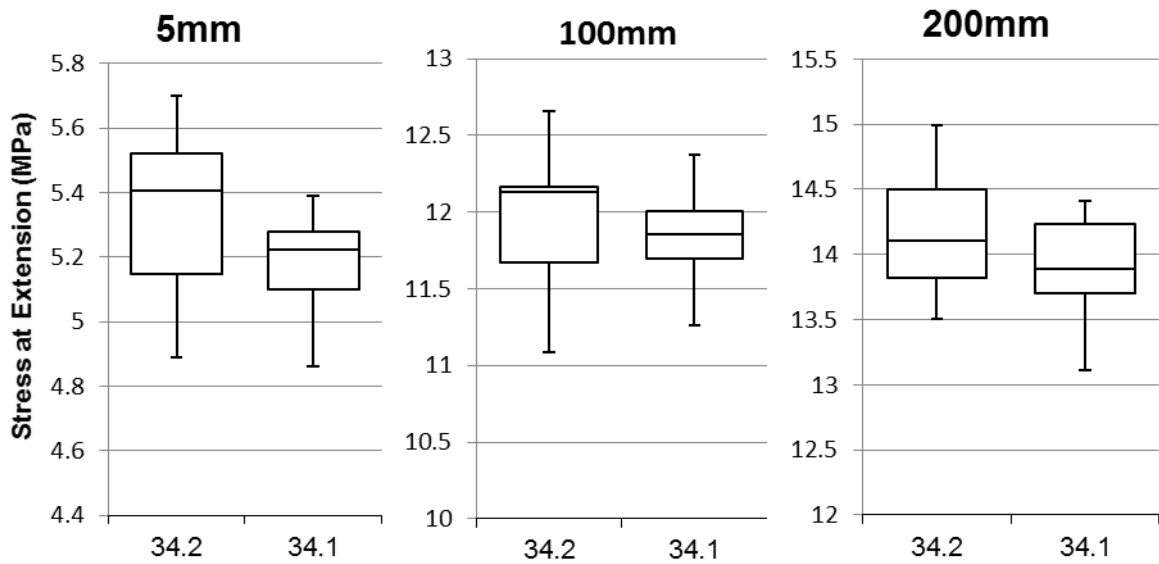


Figure 6.13: Box chart (quartiles and median) of stress in oven sintered specimens at 5mm (recoverable extension) and 100-200mm (unrecoverable extension).

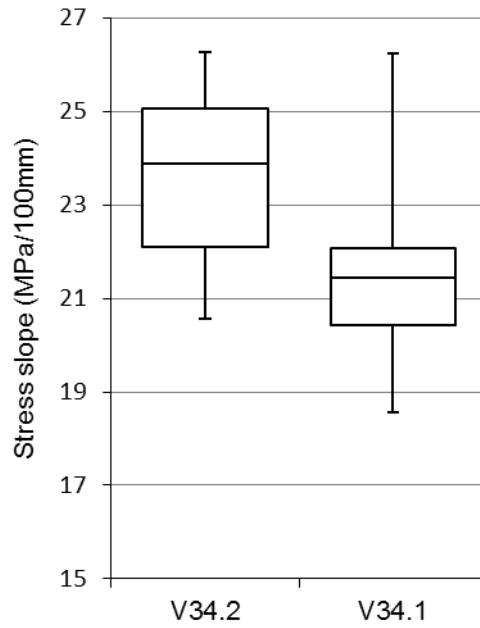


Figure 6.14: Slope of the linear ductile region between 100mm and 200mm.

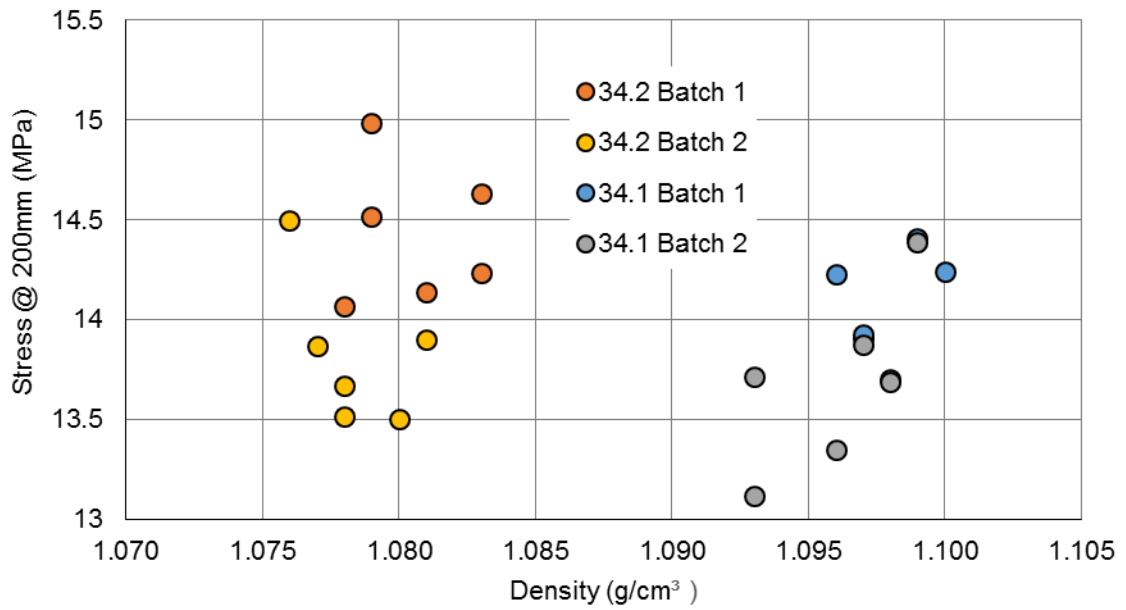


Figure 6.15: Oven sintered specimens. Stress developed at 200mm deflection versus specimen density.

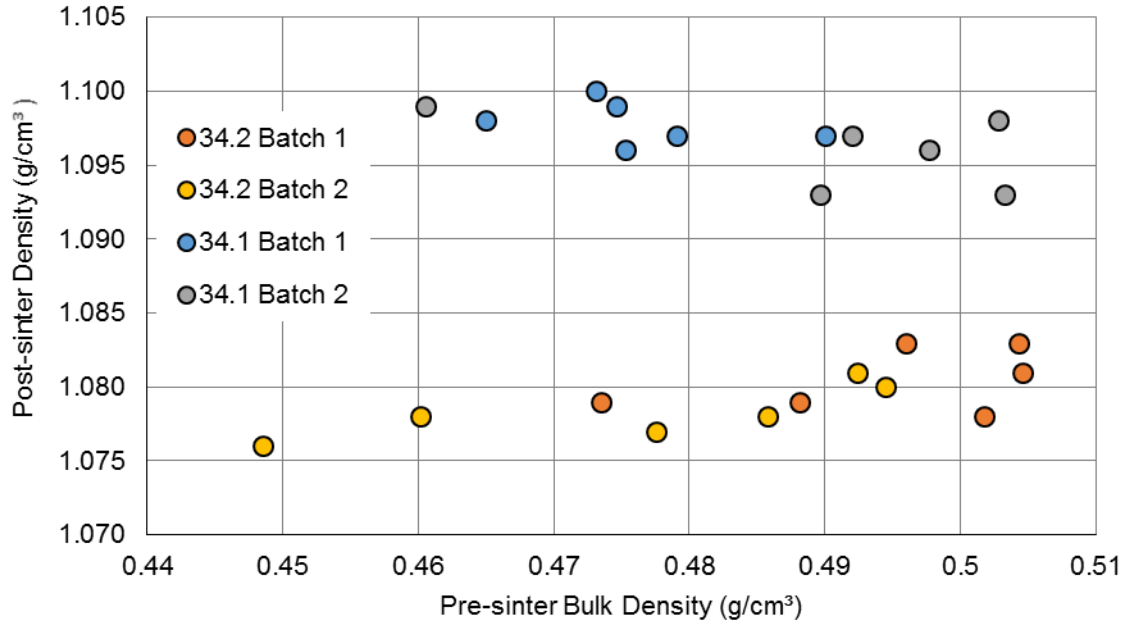


Figure 6.16: Density of oven sintered specimens versus pre-sintering bulk density of powder in mould.

6.9 Tests on Convex/Concave Voids

The concave voids were first observed in batch V34.1. The observation was made even more interesting by the fact that the sister-batch V34.2 shown completely expected, bubble-like convex voids. Note that both those batches were milled out of the same granulate and neither DSC nor MFI showed any discrepancy. The only intended differentiating factor was that V34.2 featured a different flow agent. Seeing that it is the V34.1 which can be seen as an outlier in the high-coalescence group, we do not think that FA is responsible for the difference. V34.1 is an outlier with respect to PSD and especially the size of largest particles in distribution. Compared to V34.2, median particle diameter $D_v(50)$ was 115% the size, but the upper size $D_v(90)$ was 122%. At $D_v(90)$ of 133 μm , V34.1 had by far largest particles of the high coalescence group. V34.1 also had the lowest SSA and the lowest bulk density of the group.

Concave voids were not unique to V34.1, but in the case of other batches, their occurrence was less frequent, as can be seen in Chapter 6.6. The frequency of concave voids increases in batches with larger particle size. Both V34.1 and V36 show a large number of concave voids and both featured much larger particles than other batched in high coalescence group. It is possible to

consider concave voids as an intermediate form between the open pore structure of the low coalescence group and the spherical voids in high coalescence batches.

In order to confirm that it was the particle size which was responsible for the void shape, we needed to perform two tests to attempt to change melting behaviour of V34.1 and V34.2. Firstly, to eliminate bulk density as possible cause we compared the appearance of powders molten in a typical, loose form and pellets created in a 5-tonne press. Results are shown in Figure 6.17. The tendency to melt into concave/convex voids clearly remained unchanged. An interesting result to note is that thanks to the extreme powder compaction we definitely see that more compacted powder produces a larger amount of smaller voids. This result will be referenced when discussing results of oven sintering of specimens.

The second experiment we needed to perform was altering the particle size distribution to confirm that this would eliminate concave pores. Due to cohesive nature of the high coalescence powders, it was practically impossible to sieve them conventionally. Instead, we decided to re-mill the V34.1 batch using Retsch CryoMill. The machine was set to 2 minutes pre-cooling and 2 minutes of milling at 25Hz. Only ~5g was placed in the chamber at one time. As shown in Figure 6.18, the created super-fine powder melted to convex bubble form and bubbles were very rare and large. The extremely low bulk density might also have been a factor, allowing air to escape powder before closing of the pores.

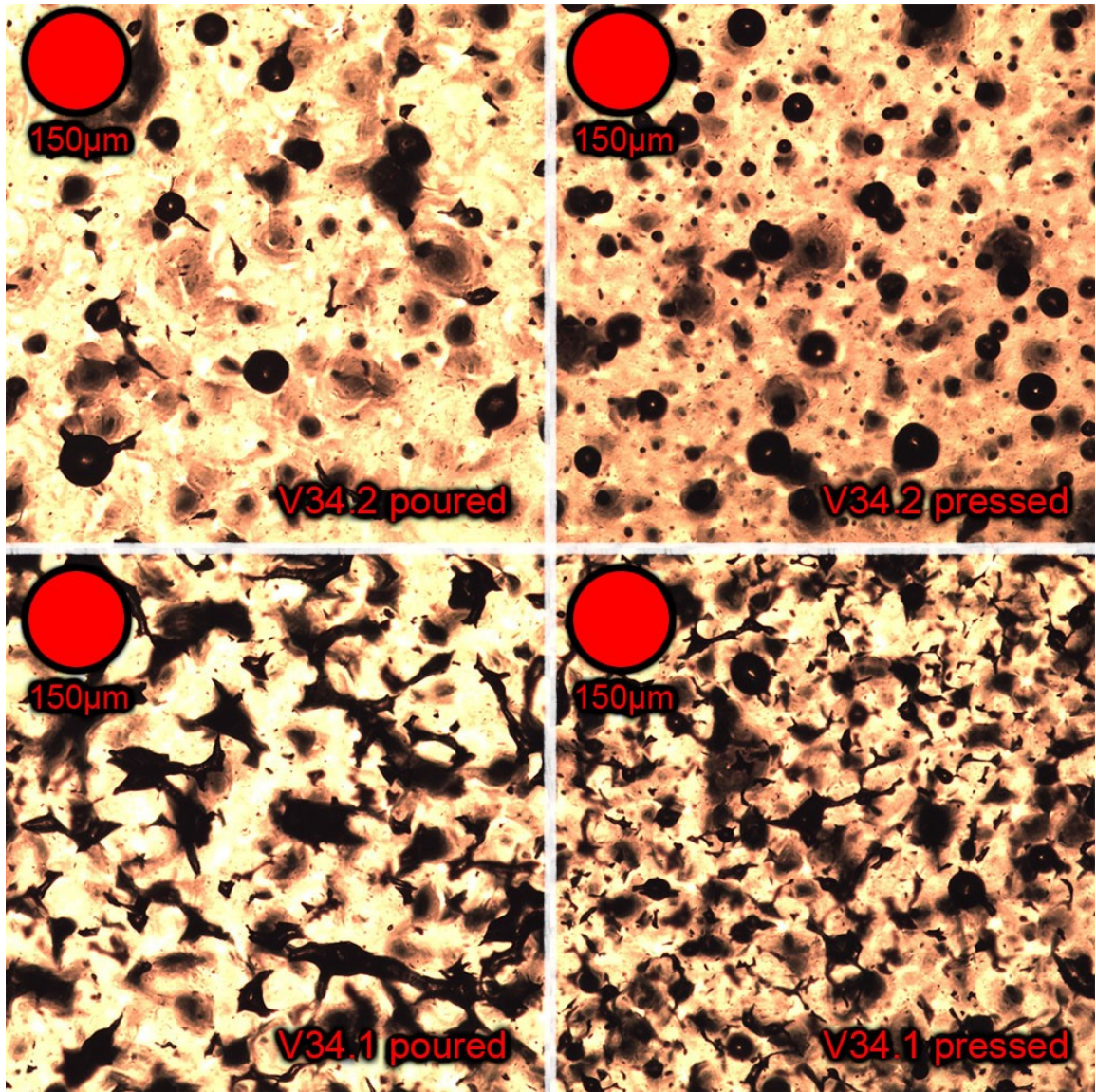


Figure 6.17: Hot stage microscopy pictures of V34.1 and V34.2. Powder in left column pictures was molten in as-poured condition, while powder in right column was compressed using the 5t press. Melting of compressed powder produced a larger number of smaller pores.

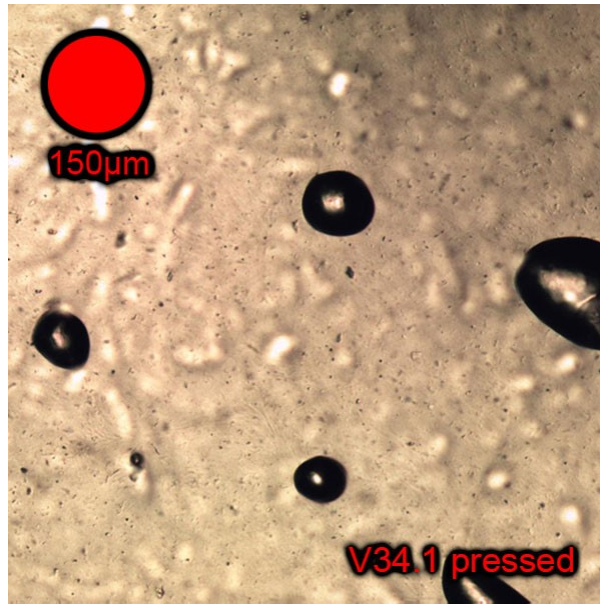


Figure 6.18: Hot Stage Microscopy image of V34.1 after re-milling to reduce particle size.

6.10 Discussion of Results

6.10.1 Bulk Properties

Unfortunately, we were not able to perform a successful full thickness build with any of the 12 batches. During sintering attempts, we kept running into two modes of failure: failure to recoat and part dislocation by the wiper. Former issue was most prevalent in batches V33-V37, that is all the batches from Mill A, which displayed generally smaller particle size. Batches V25-V30 shown better flowability, but they were more prone to part dislocation due to a combination of factors. Low sintered density of those batches prevented the formation of deep sintering pits which can compensate for oversized particles (See discussion in Chapter 6.10.7). When spreading the large particles, wiper generated enough friction to dislocate newly sintered layer. Low cohesiveness of those batches made dislocation more likely since the competing friction of sintered layer against the powder bed was lower than in cohesive powder batches.

Although it might have been possible to use the drum-annealing approach again to enable sintering, we find that approach to be intrinsically flawed and not commercially viable. In retrospect, we still believe that the monolayer study combined with the oven sintering observations was more fair and useful than continuing to use drum-annealed powders. Mind that we determined

that the usefulness of drum-annealing was due to clustering effect it had on particles (See Chapter 5.2.4), rather than any effect on polymer phase structure. In this study, TPU granulate was annealed before grinding, introducing morphological changes without the clustering effect (See Figure 6.20 for SEM image typical for batches in this study). Effect of those morphological changes, if any, was not sufficient to solve our flowability problems.

The largest obstacle to successful production was the simple wiper-type spreading system used in Formiga P100. Wiper design is too reliant on good powder flow and does not generate enough shear to break apart cohesive powder. It is highly probable that most of the batches would be useable in e.g. 3DSystems Sinterstation system, which is equipped with the roller-type spreading system and in which feed powder is allowed to rest at lower temperature.

A clear correlation can be drawn between particle sizes and bulk densities. As discussed in Chapter 2.3.4, smaller particles inevitably generate more interparticle forces as one unit of mass will have greater surface area to carry out the interactions. Correlation between Bulk Density and Specific Surface Area is shown in Figure 6.19. The relationship appears to break down mainly for batches V25 and V26. Monolayer study results suggest that V25 PSD readings are erroneously low.

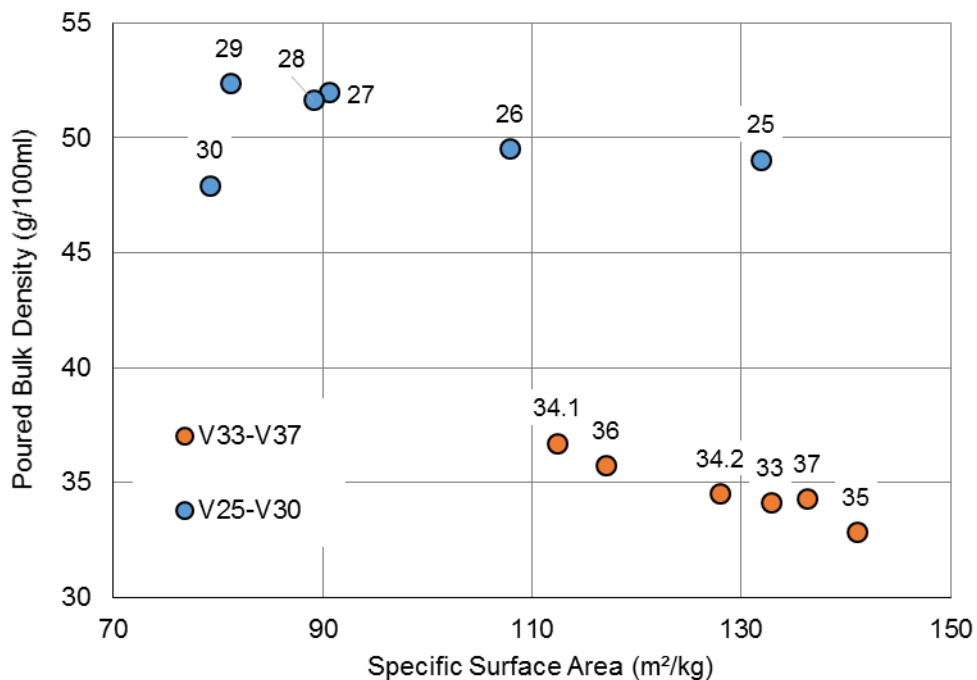


Figure 6.19: Poured Bulk Density of Viscosity and PSD study batches versus Specific Surface Area. Note that Batches V33-V37 were milled by Mill A and V25-V30 by Mill B.

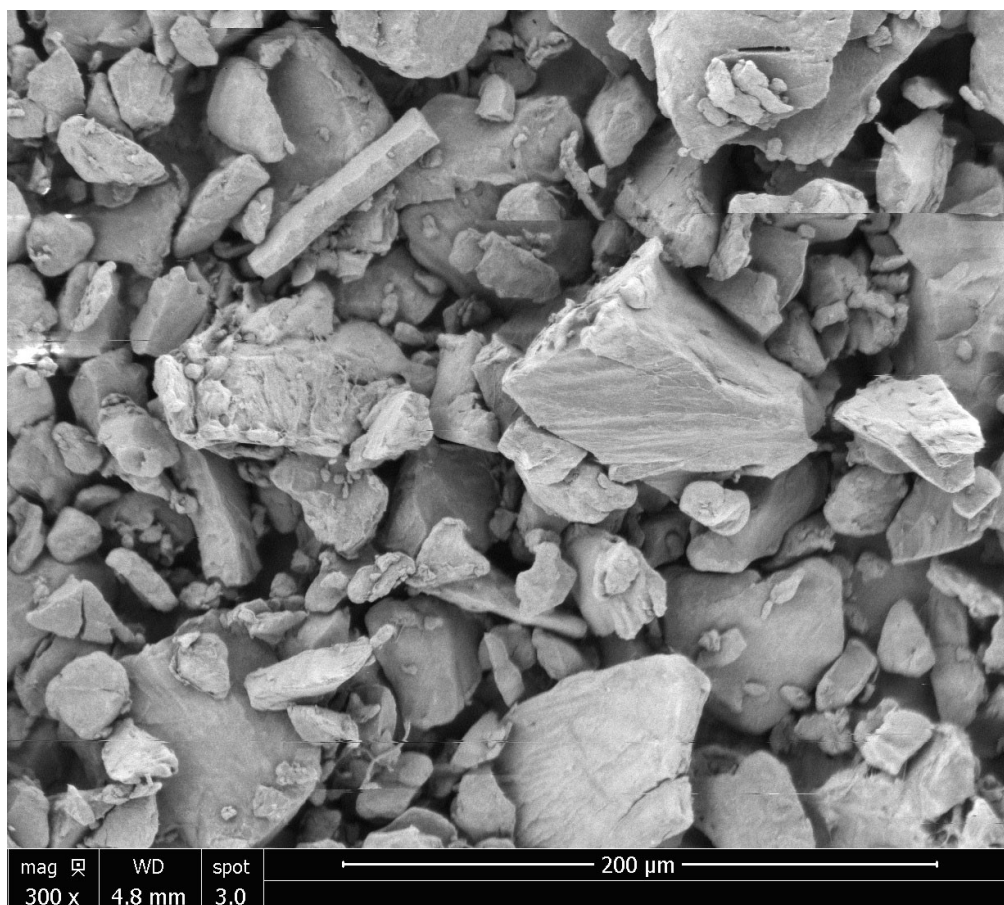


Figure 6.20: SEM image of batch V29, capturing both extremely rough particle on the left and cleanly crushed one on the right.

6.10.2 DSC Measurements

DSC traces of all batches shown similar characteristics and features- most significantly the annealing peak and melting peak. Batches V25/V26 displayed significantly different melting peak, with both the peak and its ending found at temperature $\sim 5^{\circ}\text{C}$ lower than rest of the batches. We did find evidence for lower temperature melting, as shown in Chapter 6.7. Note that the same two batches displayed the unusual semi-open pore structure, as shown in Chapter 6.5. Their unusual way of melting is likely to be somehow linked with the lower melting temperature. V25 was also a major outlier in the monolayer study, but we are still inclined to attribute this error to underestimated size based on PSD reading.

In this study, we found no effects which could be attributed to annealing-induced morphological changes. We speculate that annealing might have had limited effect on powder tackiness at elevated

temperature, but this effect would have been very difficult to detect since the dominating factor in flowability was the unique PSD of each batch and where relevant- annealing induced clustering. Comparison of the annealing peaks in this study with the data in Chapter 4.1.3 suggests that the annealing performed on granulate batches was often insufficiently long for the target morphology to develop. Potential of annealing approach has not yet been fully determined.

6.10.3 The Monolayer Study

As mentioned, V25 was a major outlier from the regression model, showing performance significantly below model's prediction. We believe that the most likely source of non-conformity is error in particle size readings from the Malvern system. Because this batch was the only one where 'high RPM' mill setting was used, we speculate that some change to optical properties or average particle shape influenced the measurements. We have established a close connection between the average particle size and BD, to the point where BD could be substituted for SSA as a factor in regression. If this was done, V25 stopped being an outlier. In the case of V25, we suspect that BD is a more accurate representation of true PSD of V25.

In the review of coalescence literature (Chapter 2.4.1), we had discussed the possibility of polymer particles demonstrating qualitatively different coalescence behaviour below a certain size threshold. This kind of qualitative difference would introduce non-linearity to monolayer results and we found no evidence of it in our dataset.

When discussing correctness of the regression model we need to address the presence of patterns in the regression residuals, which can be a signal of poor fit to data. Complete data on model's residuals and other quality indicators is contained in Appendix Chapter 8.1. One of investigation points is the apparent clustering of residuals on the per-batch basis, as visible in Figure 6.21. In an idealised situation, the residual values should show complete randomness, but instead, we observe the clear tendency of some batches to achieve lower or higher residuals. Although weight, MFR and SSA account for vast majority of data variability, clusters may indicate the presence of an additional, unknown batch variable. However, it is also quite likely that the clusters are a result of using a singular, per-batch measure of SSA and MFR, what allows a single

skewed measurement to skew data of entire batch. Elimination of MFR or SSA from model allows us to see that the MFR measurement has greater clustering effect. We find no discernible pattern in the tendency to over or underestimate batch performance. At this time and do not think that unknown variable hypothesis should be pursued.

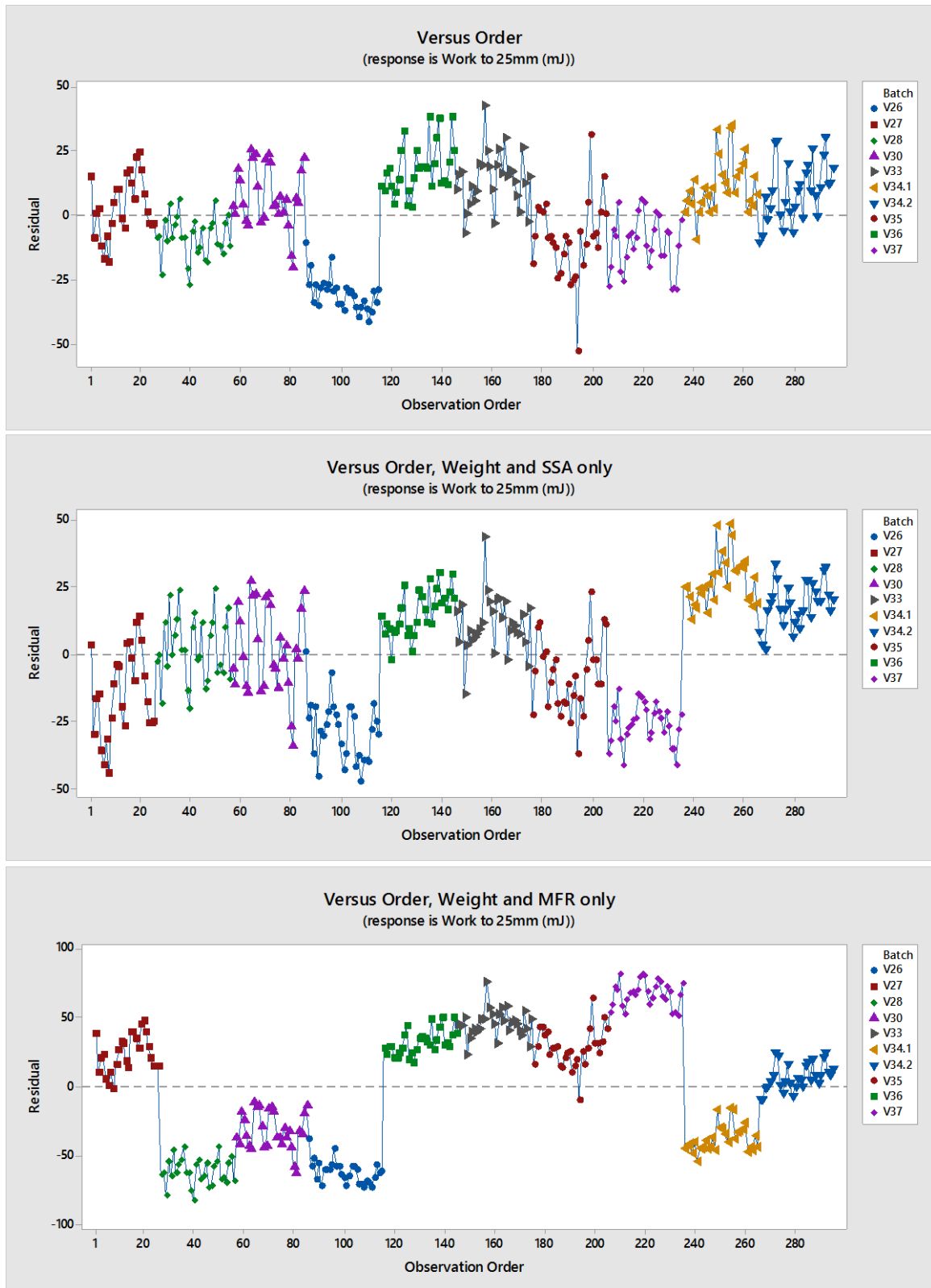


Figure 6.21: Residual values from linear regression of Viscosity and PSD study monolayer data.

To further analyse our linear model we take a look at the plot of Residuals Versus Fits. This plot (Figure 6.22) allows us to see if fitted values tend to become over or underestimated as the fitted value increases. An important use for this way of presenting data is to verify whether quadratic regression would provide better fit to data. Here, U-shape of data points is a possible sign of quadratic relationship somewhere in the model. As mentioned above, attempts to eliminate this U-curve with squared variable values were unproductive. Instead, we believe that the changing slope of residuals can be easily explained by referring to the manner in which specimens changed with improving coalescence.

Observing distribution of data points in Figure 6.4, we see that while each individual batch conforms to a linear relationship with weight, the slopes of regression lines become progressively steeper for higher work specimens. In Batches V27 and V30, 0.1g of powder conveys additional ~12mJ of work. In batches V25 and V25 the same amount of powder conveys additional ~24mJ and in best-performing batches (later referred to as closed-pore batches) the same amount conveys ~35mJ. This difference might be the result of specimens with poorer degree of sintering having larger fraction of material not contributing to mechanical strength. This material is likely to be in form of particles which failed to form sintering necks with more than one neighbour. Naturally, particles located at the specimen's surface have fewer necks and contribute less to strength than particles within specimen's bulk. Although all specimens consisted of only one layer of sintered powder, the specimens with poorer degree of sintering were significantly thinner and therefore had larger surface to area ratio. We would also like to point out the significantly higher slope of V37, where 0.1g of powder conveyed additional 43mJ. This batch was not a very high performer due to its particle size and MFR, but it was the only batch with IR absorbing agent additive. We speculate that this outstanding result might be linked to the additive, although this is impossible to verify when PSD is inconsistent between batches.

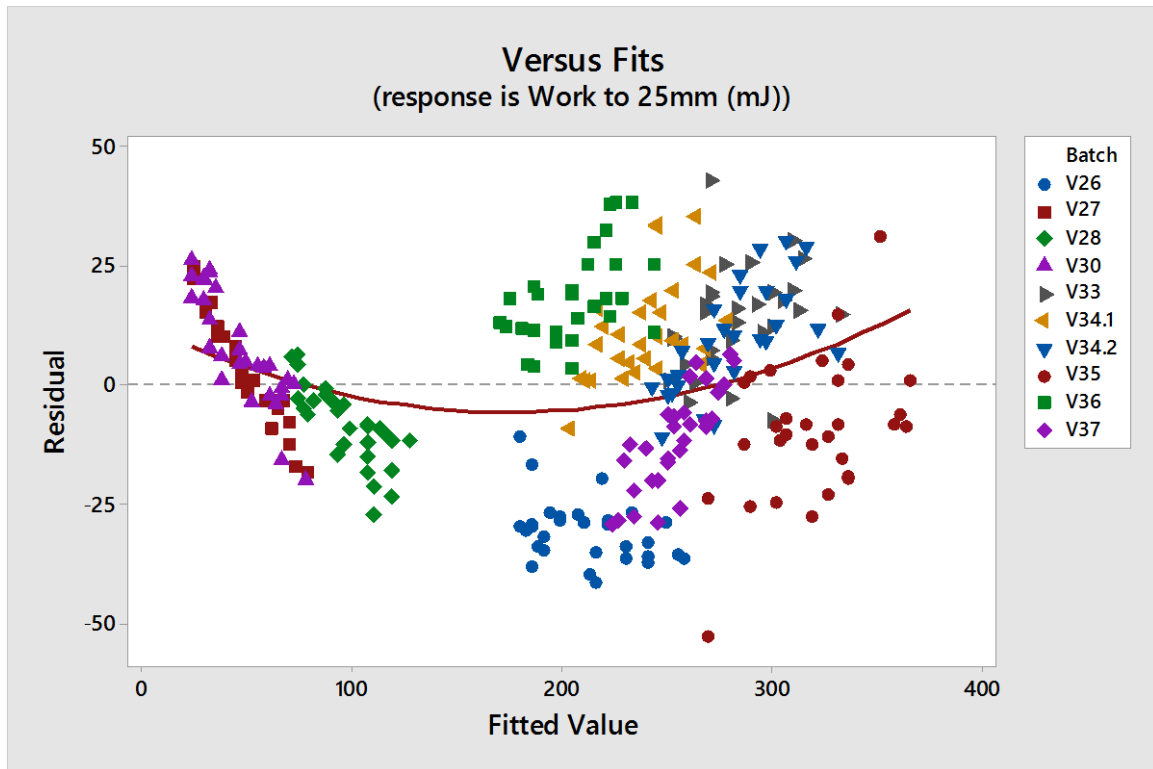


Figure 6.22: Residual values from linear regression of Viscosity and PSD study monolayer data, plotted versus fitted value. Also included is quadratic fit line. Note that lack of fit between line and data suggests that quadratic relationship is not the source of apparent trend in residuals.

6.10.4 Observations on Open and Closed Pores

Regardless of the clear result of monolayer experiment, we are aware that it is a limited simulation of LS process. The test was performed under the assumption that it is representative of coalescence stage. Initial coalescence stage of sintering can be broken down into interactions between individual pairs of particles, as they form sintering necks. This problem can be considered two-dimensional and we believe that flat specimens are a fair representation of it. The process of forming closed pores during densification stage, however, cannot be represented by a two-dimensional specimen. In monolayer test, progressively weaker specimens were characterised by smaller sintering necks between particles, creating larger holes in the flat sheet. Due to flat nature of specimens, we could not observe the critical point where necks were too narrow to create closed-pore structure in full thickness specimen. Nor could we observe void volume which would remain in closed-pore specimens. To observe those effects we supplemented our observations with TPU sintered on a hot microscopy stage and in an oven.

As we discussed in methods Chapter 3.5, we believe that as long as powder samples are small and at rest, oven-sintered powder is a fair representation of maximum possible density achievable in LS system. Samples of powder sintered in oven (Figure 6.5) revealed how limited coalescence of some batches puts them below the threshold of closed pore structure formation. The open-pore structure of batches V27-V30 was stable regardless of time or temperature, up to point of severe yellowing of TPU. The only way in which open-pore batches could be induced to enter closed-pore densification stage was if the flow was introduced by external force e.g. by prodding or flexing the specimen.

Pictures of powder sintered on hot plate confirmed the oven sintering observations exactly. We observe that the 2D image of adhesion points is capable of representing open and closed pore structures. Batches V25 and V26 were revealed to have intermediate structure, where pores appear to have dead ends, but still show a large degree of interconnectedness. Those three distinct groups: *closed pore*, *open pore* and *intermediate* are also clearly seen as data clusters in monolayer results (Figure 6.4).

When we measured the density of oven-sintered specimens we found a rift between densities of open-pore structures and others. The density of semi-closed pores in V25-V26 was on par with the density of closed pore structures. This result is an excellent demonstration of how crucial it is for the sintering process to reach densification stage. Discounting the open-pore samples, we attempted to find factors correlating with the density of closed-pore specimens. No strong correlation could be found among the investigated factors. Possibly noteworthy is the high density shown by all batches with concave pores (V34.1, V36) and the semi-closed pore structure (V25, V26). We also observe that batches V34.2 and V35 which feature purely convex pores had a relatively low density in this test. Notice that the monolayer performance of V34.2/V35 was very high and V34.1/V36 performed much worse. This suggests a possibility that in order to achieve the highest density possible, batch should be just above the densification threshold. Batches which coalesce most rapidly sinter to lower density. This could be related to rate at which pores become isolated, or indirectly by the fact that faster rate correlated with lower bulk density.

6.10.5 Observations on Concave Voids.

Further examination of pore structure in HSM images revealed differences in void shape within closed pore group. Voids could quite clearly be subdivided into ones with concave walls and ones with convex walls. Convex voids appear as round or oblong bubbles, while concave voids had sharp or 'pinched' edges. Concave voids were spotted in most of the powder batches, but their concentration was the largest in batches which also performed relatively poorly in monolayer tests. Batches V34.1 and V36 were the poorest performers out of closed pore group and they also displayed the greatest concentration of concave batches. Just as was the case with open pore structures, concave pores were stable and would only collapse into convex pores when flow was induced by e.g. stirring. We also observed collapse when powder sintered unevenly, due to cold spot over hot stage aperture. This induced viscous flow towards faster-sintering regions. Lack of intermediate-shape pores also indicates that the transformation from concave to convex is associated with some threshold state. Empirical observations clearly support the view that concave pores are an intermediate stage between open pore structure and spherical bubbles.

Increasing powder's bulk density by compressing it in 5-tonne press created a surprising result. In the case of both concave and convex voids, sintering of compressed powder resulted in a larger number of smaller voids. Voids would retain their concave or convex shape as well. Only milling the powder to reduce its PSD allowed V34.1 to melt to convex void form. Because both PSD and MFI had the largest impact on coalescence behaviour in monolayer tests, we would have liked to know if a batch of the same PSD as V34.1 but lower viscosity would sinter to convex void form. Unfortunately, we possessed no batch which would allow for the comparison.

6.10.6 Oven Sintered Specimens and Concave Pore Impact

Stress measurements were performed in the elastic and ductile region of specimen's elongation. Measurements point to V34.2 possessing higher stiffness and toughness than V34.1. However, the difference is minor and because of between-batch variability, it may not be significant. The difference is certainly less significant than the performance in monolayer test, where V34.1 and

V34.2 placed very low and very high within the closed pores group. It is not surprising that oven sintering led to much more uniform performance. During oven sintering, both powders were given sufficient time to achieve their respective maximum density. In the monolayer experiment, the sintering time was limited, what emphasised the differences in the rate of sintering over the ultimate equilibrium state.

A much more significant result is the difference between specimen densities. While the pre-sinter bulk density was similar for both batches, the V34.1 specimens sintered to significantly greater density than V34.2, with no overlap in data points. Even accounting for the variance in stress data we can confidently state that V34.2 specimens are stiffer, despite their lower density. While the relative difference in developed stresses is minor, we believe it can be used to demonstrate that the distribution of pore sizes does have a measurable impact on performance of sintered parts.

Batches V34.1 and V34.2 were chosen based because their propensity to form concave and convex voids, while being almost identical in other regards. Upon microscopy investigation (Figure 6.23) we were surprised to find that all the voids in V34.1 collapsed to a spherical form. We have observed that the concave pores will collapse into concave form when disturbed by viscous flow. We suspect that in the case of the oven-sintered specimens the difference in width of the dogbone sections led to uneven melting, inducing viscous flow from regions which sinter slower to regions which sinter faster. Viscous flow will cause concave voids to collapse and transform into spherical ones. Distribution of bubble sizes in V34.1 is highly skewed towards small sized bubbles. We believe that the small bubbles are created when crevices between concave void's walls become pinched off during collapse into bubble, creating large central bubble and several smaller ones around it.

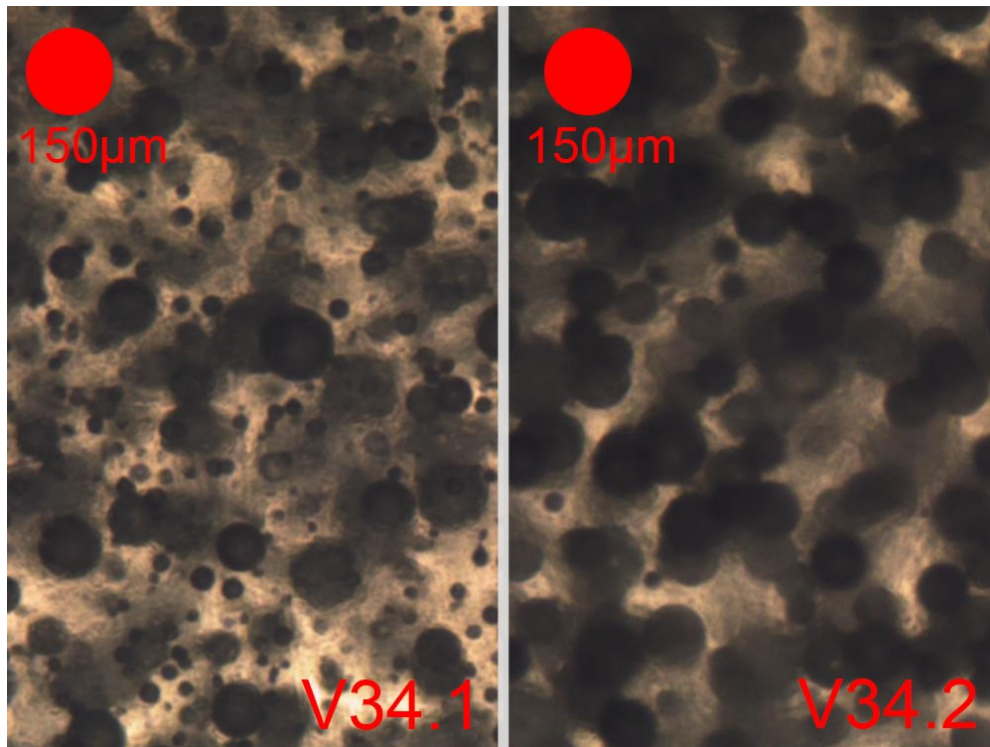


Figure 6.23: Microscopy pictures of oven-sintered V34.1 and V34.2 tensile specimens.

Drastically different distribution of void sizes might explain why increased density of V34.1 samples does not correspond to higher stiffness or toughness. Given the constant total volume, a greater number of smaller voids would increase pore structure's total surface area and total void cross-section. Both these factors could contribute to the reduction of stiffness.

6.10.7 Bulk Density and Final Part Density

An interesting result which was observed during the oven melt test was the apparent lack of impact of pre-sinter bulk density on the final part density. As can be seen in Figure 6.16, the density of green parts varied by as much as 10%, but the density of sintered parts varied only by less than 1%. Variation was also not correlated, leading to the conclusion that bulk density had no significant impact on the density of oven sintered parts. Earlier we made an argument, that oven-sintered specimens are a fair representation of LS specimens, if LS specimens were fully sintered. We believe that the comparison is still valid and that impact of BD on LS outcome should be re-evaluated.

In this project, the only test which correlated low BD with low specimen density was the Flow Agent Effects full-thickness tensile test. There are two reasons why we don't believe it contradicts

oven sintering result. First- degree of sintering in LS machine was not complete. Powders with lower BD might simply require more time to sinter completely, leading to the density difference in LS. Second- powders used in LS were annealed and formed micro-clusters. We cannot rule out the possibility that those clusters sinter differently than virgin TPU powder due to unusual particle arrangement.

Work from Nottingham University group (Ziegelmeier et al., 2015) promised to demonstrate a link between improvements in BD and specimen density, in laser sintered TPU powders. In practice, the data is not convincing. Sieved TPU powder did show BD improvement, as measured by FT-4 powder analyser. Final part density was measured using two methods- volumetry (possibly water displacement, an exact technique not mentioned) and Computational Tomography (CT). CT indicated a minor density increase, but volumetry indicated a greater amount of density drop. Measurement by CT is less direct, as it involves software image processing, including thresholding operation. CT system also possesses limited resolution. We are inclined to put more faith in the volumetry result, which registered part density drop. Mechanical performance of alleged higher density specimens was not uniformly better. While UTS and EaB increased, E-modulus decreased.

Part density insensitivity to BD seems to be contradicted by the principle of layer-by-layer manufacturing. If it is assumed that a part is built from constant-thickness layers, when volume of powder used per part is constant. This would mean that density of part is directly correlated with bulk density of powder. If constant thickness layer assumption is true, it should not be possible for sintered parts to achieve a higher density than powder's BD. Because we know this to not be the case, the assumption about constant thickness deposited layers is most likely wrong.

In practice, sintering causes powder to densify and the sintered areas create depressions in the powder bed. When new layer of powder is deposited, the actual thickness of powder layer is 100 μ m plus the depth of the post-sintering depression. If our assumption about equal final part density is correct- sintering of low-BD powder will create a deeper depression. This directly causes a larger amount of low-BD powder to be delivered during subsequent recoating. This compensating mechanism has a form of a feedback loop, leading to a certain equilibrium value for the amount of delivered powder.

To illustrate this compensation mechanism, let's use an example of two hypothetical powders with different BD. Values will be based approximately on A00 and A02 batches from Flow Agent Effects study. First powder has BD of 0.45g/ml, second one 0.5g/ml. Assuming that they both sinter to the density of 0.8g/ml, the first powder will leave a 43.75 μm depression in the powder bed and the second one a 37.5 μm depression. During second sintering cycle, sintering depressions will be deeper, because new powder layers are 143.75 μm and 137.5 μm deep. Eventually, the thickness of delivered powder will converge on amount exactly compensating for the amount of shrinkage- 177.8 μm for low-BD powder and 160 μm for high-BD powder. In the equilibrium state, the same mass of polymer is delivered, regardless of bulk density. The process of convergence is plotted in Figure 6.24.

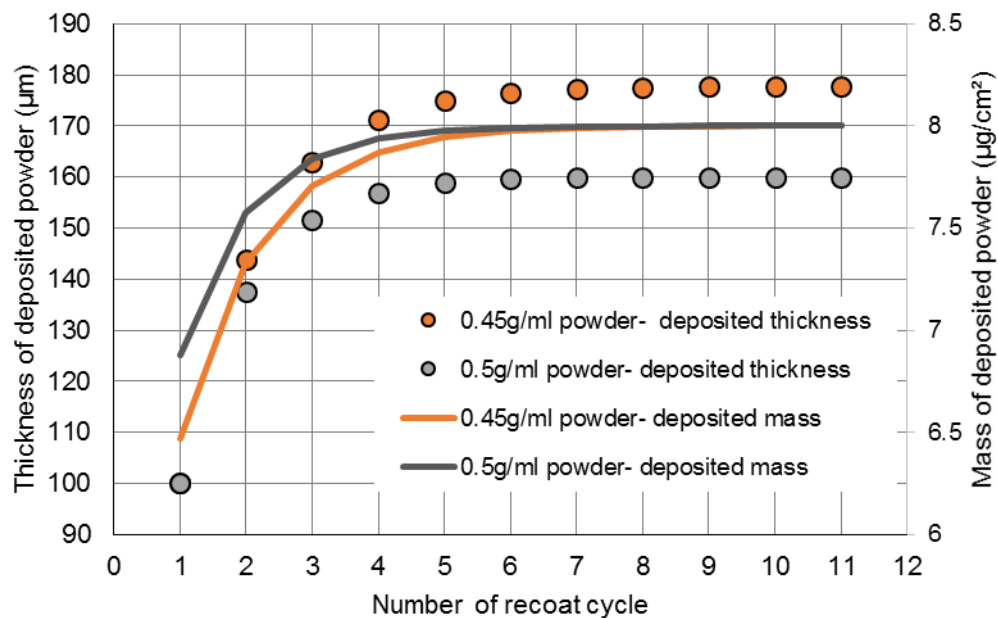


Figure 6.24: Numerical simulation of changes to thickness and mass of deposited powder layer, accounting for added depth of sintering-induced pits. Model assumes equal sintered density, independent from initial bulk density (either 0.45g/ml or 0.5g/ml)

6.11 Conclusions

Splitting the study into monolayer test and subsequent oven melting test allowed for disambiguation of the two issues in sintering, namely coalescence and densification. Monolayer specimens are not significantly influenced by the formation of pores, while fully-sintered oven

specimens are not sensitive to the rate of sintering. Taking this approach allowed us to both confirm well-established assumptions and gain new insights into sintering problem.

The first major result of the study is confirmation of MFR and PSD as two most significant factors determining the rate of coalescence. More specifically, we find that the stiffness of monolayer specimens in the recoverable strain region is linearly correlated both to MFR and SSA. We found SSA to have a larger impact on specimen strength, due to the magnitude of fluctuations in particle size. Along with specimen weight, those two factors were found to account for over 96% of data variance, making the search for additional factors unfeasible with this data set.

We should note that PSD of batches was not one of the experimentally controlled factors. Rather, the amount of variance observed in PSD was mostly due to inconsistencies in the milling process. This is best illustrated with the example of V34.1 and V34.2 which should have had identical sintering properties and only demonstrate the impact of experimental flow agent on BD. Instead, differences in PSD caused them to melt in qualitatively different manner, altering not just rate of coalescence, but also shape and size distribution of pores. Consistency of milling process must absolutely be improved in future studies to not overshadow other factors.

Another important observation was the threshold condition for the formation of closed pore structure. Only TPUs which reach closed-pore densification stage can experience an additional boost in density, making crossing this threshold necessary for any LS TPUs. In batches which sintered to closed pore form, the greatest difference in part density was $\sim 2.5\%$. Density of specimens which did not sinter to closed pore form was around 30% lower than closed-pore ones.

While we couldn't find specific factor controlling the final density of oven-sintered specimens, evidence points to highest density being achieved by powders which barely crossed the densification threshold. We speculate that this is caused by the collapsed, concave void shape and slower coalescence giving more time for gas evacuation from powder bulk. As a result, highest densities were achieved by slowest-coalescing powders, with large particles and small MFI. Pursuing this 'sweet spot' to maximise density would carry the risk of crossing over to open pore sintering, what must be avoided. What's more, limited evidence from oven-sintering study points to high specimen density not necessarily translating to improved mechanical performance. We

believe at this moment that this relationship cannot be fully understood without accounting for the shape and size distribution of pores making up the total void volume.

7 Project Conclusions

When summarising the information gained during this project it is worth looking at the pre-existing hypotheses which guided the research and provided context to our experiments. We had managed to both confirm established hypotheses as well as challenge some pre-existing assumptions. Our experiments have also generated new questions, some of which may have consequences for further material development.

7.1 Major Experimental Findings

7.1.1 MFR and Particle Size Effects

Arguably the most basic assumption about viscous sintering is that its rate increases with lower viscosity and smaller particle size. This has, of course, been confirmed by experimental results from the monolayers study. We had determined through multivariate linear regression that increasing MFR and SSA of powder has a strong effect on the rate of coalescence. This is especially important when available sintering time is short.

7.1.2 The Densification Stage Threshold

Probably the most useful, novel observation in the project was the discovery of densification threshold amongst the 12 batches in the Viscosity Effects Study. Out of 12 batches in this part of the study, four were observed to sinter extremely poorly, reaching sub-par densities compared to most batches. By comparing results of monolayer experiments and oven sintering we had arrived at a conclusion that extremely poor sintered density is associated with the formation of stable open-pore structure. Open pore structure is a consequence of low neck-to-particle radius ratio. The ratio remains low when particle system does not possess sufficient potential energy to fuel mass transport and neck growth. Potential energy in viscous sintering comes mainly from the reduction of free surface energy of the particle system, leading us to believe that the surface area and therefore particle size is the ultimate factor controlling this behaviour. We found that the threshold

between closed and open-pore structure occurred between batches V26 and V27. This translates to SSA between 107 to 90m²/kg or D[3,2] of 49 to 58µm. New powders located within that range or with larger particle size run into risk of developing open-pore structure.

7.1.3 Effects of Flow Agents

When investigating the three Aerosil-modified batches of powder we were advised that while higher Aerosil content improves flowability and bulk density of powder, its presence also impairs the mechanical performance of TPU. In the investigated batches we found that Aerosil in fact impeded powder compaction, what would have a negative effect on the density of powder bed. We attribute this effect to Aerosil particles becoming embedded in the surface of the soft polymer and thus increasing interparticle friction. This leads to a situation where no-Aerosil is preferable to a small amount of Aerosil. However, increasing Aerosil content further might offset the embedding mechanism and improve BD as intended. This type of study is recommended in Chapter 7.2.

While we did find that Aerosil- doped batches produced mechanically inferior specimens, the drop in performance was strongly correlated with decreased specimen density. We found no evidence yet that Aerosil may worsen mechanical performance by creating inclusions.

7.1.4 Effects of Powder Bed Bulk Density on Part Density

For most of the project, it was assumed that high BD of powder bed is beneficial to the density of sintered parts. This effect seemed partially confirmed in the Aerosil effects study. However, results obtained from oven-sintered specimens suggest that bulk density has very limited, or even negligible impact on the final density of sintered parts. There are crucial differences between the two experiments which justify the apparent discrepancy. Firstly, we hypothesise that BD ceases to have a major effect when specimens sinter completely. Secondly, hypothesis assumes that both powders are identical, the only source of difference being more efficient compaction of powder. Aerosil specimens violated both those assumptions. They were not sintered completely and the difference in powder density was due to the formation of unusual particle clusters during tumble-annealing.

7.1.5 TPU's Sensitivity to Annealing

Extensive DSC study of the TPU confirmed many of previously observed thermal characteristics. Most notably, we confirmed that TPU grade used in this project is susceptible to annealing. The annealing-like effect can even be detected in powder after drying at elevated temperature. We hypothesise that increased segregation of phases might have minor effects on TPU's tackiness and melt viscosity. In Chapter 7.2 we propose experiments to investigate those effects further, as they might be an inexpensive method of modifying TPU's thermal properties to better suit LS process.

7.2 Recommendations for Future Work and Material Development

7.2.1 Results Verification on Full Thickness Specimens

Tests performed on monolayers informed us that high MFR and SSA (which is a function of particle size) are equally important in boosting the rate of powder coalescence. The next question which should be answered is: can full sintering be achieved using the MFR and SSA of current batches, or do they need to be increased further to achieve the full potential of sintered parts? This question is very important to the development of commercial grade product. Both high MFR and high SSA are associated with certain trade-offs. TPUs of lower MFR possess more desirable mechanical properties. Lower SSA powder would be easier and cheaper to mill, sieve and handle. In addition, low SSA improves powder flowability, what has many downstream benefits. Minimum MFR and SSA sufficient for full sintering, therefore, form a 'sweet spot' where sintered part's performance should be greatest.

Search for the sweet spot can only proceed by performing a full-scale build and tensile test, this time on an LS system compatible with poorly flowing TPU powder. For instance, EOS P396 system features a 'travelling hopper' type of spreading system, which might help by isolating powder feed from high temperature on powder bed. We recommend that before this study is commissioned, it should be verified that the new system can successfully manufacture specimens out of a high-SSA batch, such as V35. The low-SSA batches which sintered to an open-pore structure can be safely

rejected from the study. Evidence points to them being fundamentally unable to reach densification stage, putting hard, low limit on their final density.

During the full-scale study, the impact of MFR and SSA is likely to change, or even possibly become undetectable, if the new production parameters allow TPU to sinter to full density. Note that the differences in monolayers' coalescence rate could only be detected because many batches did not reach their full potential coalescence. Ideally, the new LS study would be performed twice. The first part of the study would use the sub-optimal sintering parameters from monolayers study. The second part of the study would use new system's full potential to maximise sintering performance. The sub-optimal part of the study would have a greater chance of finding whether the MFR and SSA continue to have the same effect on sintering as they had on monolayers' coalescence.

If the new system is capable of sintering TPU to full density, we suspect that the rate of coalescence will lose most of its significance to the outcome. Mechanical properties of fully sintered specimens also become more consistent, as the amount and volume of voids are decreased. At this stage of development, we believe that the detailed pore structure and the dynamics of pore formation will gain significance. Our observations show that the same grade of powder sinters to different pore size distribution depending on its state of compaction. At the same time, other characteristics of pore structure, namely the likelihood of forming concave voids seemed to depend solely on particle size. Monitoring overall density and void fraction will need to be supplemented with more advanced measurements of pore size distribution and possibly pore shape if concave voids are found again. Once LS specimens can fully sinter, will become useful to compare results from LS specimens to oven-sintered specimens. If such test proves that performance of oven and laser-sintered specimens is comparable, oven sintering could become an excellent low-cost tool for further material prototyping.

7.2.2 Increased Flow Agent Content Study

An important, low-cost study should look into properties of batches with a much greater amount of flow agent additive. FA manufacturer's guidelines suggest that FA levels under 1% are only suitable for hard materials, what makes them too low for TPU. High SSA of LS powders also increases the

amount of FA required, compared to e.g. pellet form. While more Aerosil or other FA could be added to already existing batches, note that the process requires special mixing/homogenising equipment in order for the additive to be effective. In this new study, starting concentration of FA should be no less than 1wt% and it should go up as high as 4 or 5%.

In order for further material development to proceed, it is necessary to gain much tighter control over particle size distribution following cryomilling. The extreme differences in PSD observed in this study could be attributed to splitting the production between two contractors, but even powders manufactured only by Mill A have shown as much as 20% difference in SSA. Variability even this high could be compensated for, if powders were purposefully milled under-sized so that reaching full sintering potential is still guaranteed. However, search for the 'sweet spot' necessitates exercising better control over particle size.

7.2.3 Annealing Effects Study

Lower priority, but potentially useful study could be designed to verify whether the microstructure changes introduced by annealing do have any significant impact on TPU performance. Rather than testing annealing's impact on powder directly, the test could be performed on moulded plates or strips, what eliminates particle shape and size as a variable. Properties which should be investigated include tack and softening temperature. If annealed plates were to exhibit lower tack at processing chamber temperatures, such properties are likely to translate into better high-temperature flowability.

Secondly, the impact of annealing (if any) on TPU's viscosity profile should be investigated. This study should be performed in the low-shear mode to be more relevant to the sintering process.

8 Appendices

8.1 Preliminary Tensile Properties Study Data

Sample No.	Elongation at Break (%)	UTS (MPa)	Modulus (MPa)	Work to 50mm (J)	Weight (g)	Toughness to 75% Elongation	Cross Section Area (mm)	Thickness (mm)	Max. Width (mm)	Density (g/cc)
1	93	3.09	13.3	3625	5.734	169.1	35.5	2.94	24.62	0.778
2	105	3.52	13.6	4070	5.970	188.3	35.6	2.94	24.62	0.800
3	107	3.77	13.0	4321	6.035	202.0	36.0	2.98	24.55	0.813
4	105	3.77	13.6	4316	6.059	200.2	36.0	2.98	24.60	0.818
5	103	3.76	14.0	4334	6.064	199.0	36.2	2.98	24.45	0.818
6	90	3.69	13.5	4378	6.099	201.6	35.8	2.96	24.50	0.822
7	116	3.89	14.1	4431	6.108	205.1	36.0	2.97	24.57	0.813
8	111	3.89	12.8	4463	6.130	208.6	36.0	2.98	24.53	0.819
9	110	3.89	14.3	4455	6.139	205.3	36.2	2.99	24.55	0.820
10	101	3.89	14.2	4522	6.152	208.3	36.2	2.99	24.66	0.826
11	102	3.90	13.5	4502	6.159	208.0	36.2	3.00	24.62	0.824
12	111	3.93	14.3	4547	6.173	209.3	36.3	3.00	24.65	0.819
13	97	3.89	14.0	4503	6.177	208.8	36.0	2.98	24.67	0.830
14	101	3.84	13.7	4510	6.187	205.7	36.5	3.02	24.60	0.827
15	107	3.89	13.9	4494	6.183	206.6	36.2	2.99	24.66	0.828
16	110	3.80	13.3	4439	6.200	204.0	36.3	3.00	24.55	0.823
17	98	3.83	14.4	4478	6.182	206.2	35.9	2.98	24.58	0.834
18	111	3.89	13.7	4475	6.192	206.5	36.1	2.99	24.68	0.825
19	108	3.86	14.0	4493	6.206	205.0	36.5	3.02	24.60	0.815
20	108	3.85	14.1	4431	6.185	204.5	36.1	3.00	24.67	0.816
21	98	3.73	13.1	4399	6.201	201.1	36.4	3.01	24.71	0.821
22	92	3.62	13.5	4337	6.200	197.6	36.3	3.00	24.67	0.825
23	106	3.78	14.3	4361	6.198	201.0	36.0	2.99	24.68	0.812

24	104	3.73	14.1	4339	6.197	198.6	36.2	3.00	24.77	0.817
25	95	3.66	13.8	4295	6.189	198.5	35.9	2.98	24.70	0.814
26	108	3.69	13.4	4291	6.188	197.4	36.1	2.99	24.68	0.811
27	112	3.74	13.7	4307	6.190	199.2	36.0	2.98	24.80	0.805
28	97	3.64	13.8	4255	6.193	195.8	36.1	2.98	24.84	0.821
29	99	3.70	13.0	4279	6.172	199.9	35.8	2.97	24.90	0.813
30	97	3.60	13.2	4252	6.179	196.9	35.9	2.97	24.76	0.811

8.2 Flow Agent Effects Full Thickness Specimens Data

Batch No.	Specimen No.	Elongation at Break (%)	UTS (MPa)	Young's Modulus (MPa)
A00	1	147	3.73	14.3
A00	2	136	4.19	17.2
A00	3	142	4.23	14.3
A00	4	167	4.43	17.0
A00	5	146	4.20	14.7
A00	6	164	4.45	15.6
A00	7	172	4.19	15.5
A00	8	150	4.24	16.4
A00	9	137	3.90	15.1
A00	10	158	4.34	16.0
A00	11	141	4.03	Error
A00	12	161	4.28	18.0
A00	13	164	4.16	15.4
A00	14	144	3.41	17.6
A00	15	157	4.19	14.7
A02	1	127	3.70	13.5
A02	2	141	3.63	14.0
A02	3	126	3.85	16.0
A02	4	126	3.85	16.0
A02	5	151	4.00	14.4
A02	6	140	3.85	12.5
A02	7	143	3.76	13.8
A02	8	129	3.73	13.2
A02	9	120	3.35	12.4
A02	10	119	3.57	13.2
A02	11	130	3.99	13.2
A02	12	124	3.88	14.6
A02	13	126	3.52	12.3
A02	14	126	3.87	13.3
A02	15	141	3.74	14.8
A04	1	134	3.77	13.9
A04	2	145	3.79	14.2
A04	3	127	3.79	14.9
A04	4	144	3.82	14.9
A04	5	135	3.59	13.1

A04	6	110	3.41	13.2
A04	7	125	3.62	14.9
A04	8	120	3.69	15.8
A04	9	117	3.75	13.7
A04	10	114	3.71	13.5
A04	11	113	3.39	12.4
A04	12	128	3.69	13.3
A04	13	138	3.84	14.4
A04	14	137	3.89	14.8
A04	15	114	3.72	14.8

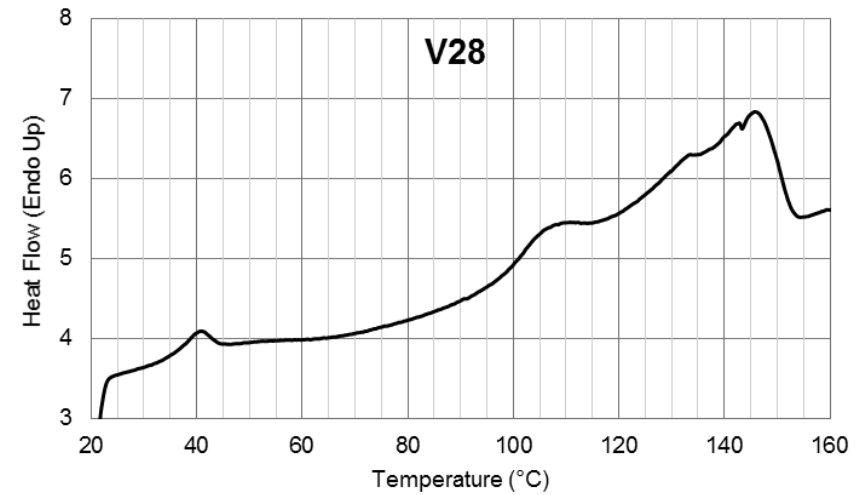
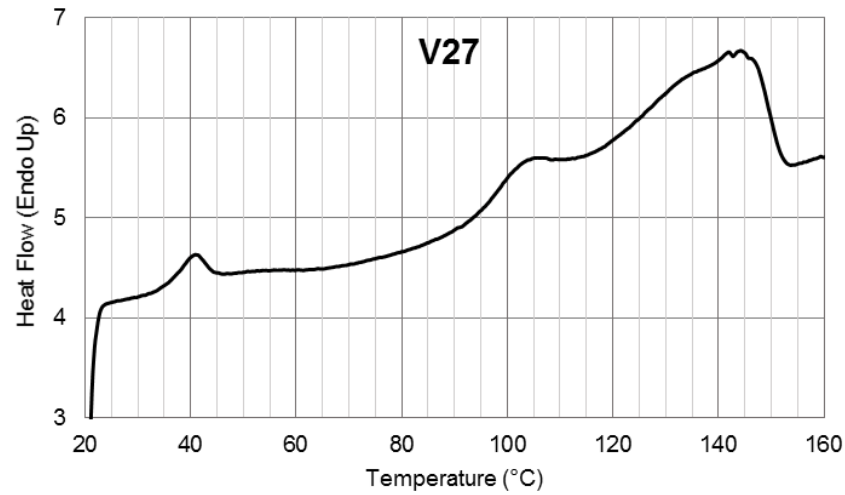
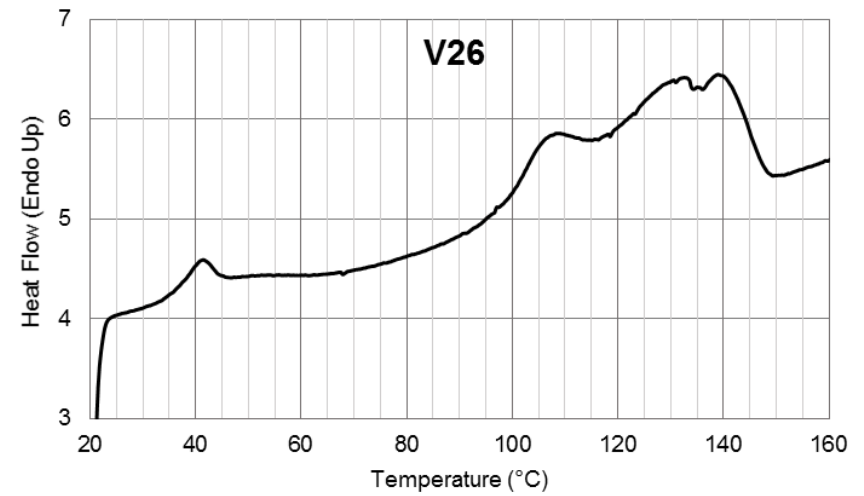
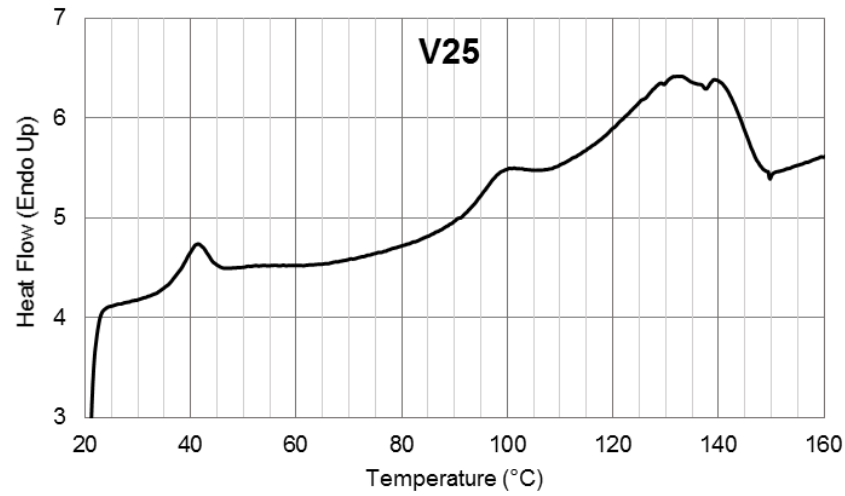
8.3 Flow Agent Effects Monolayers Data

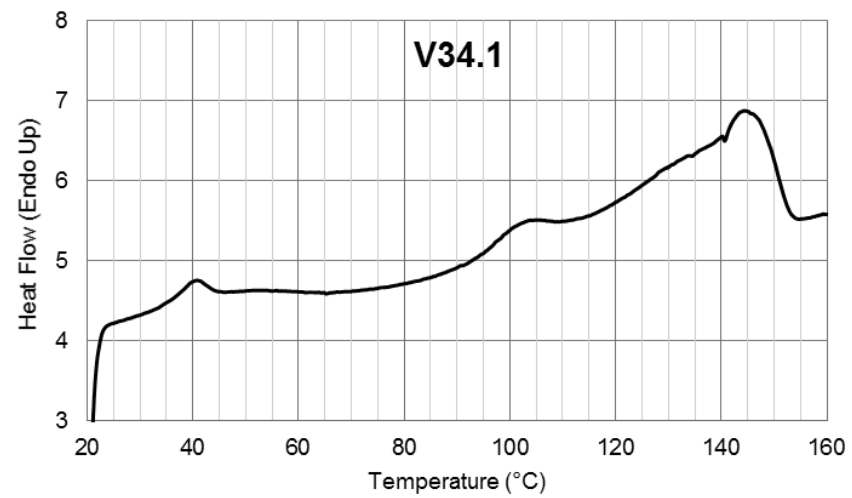
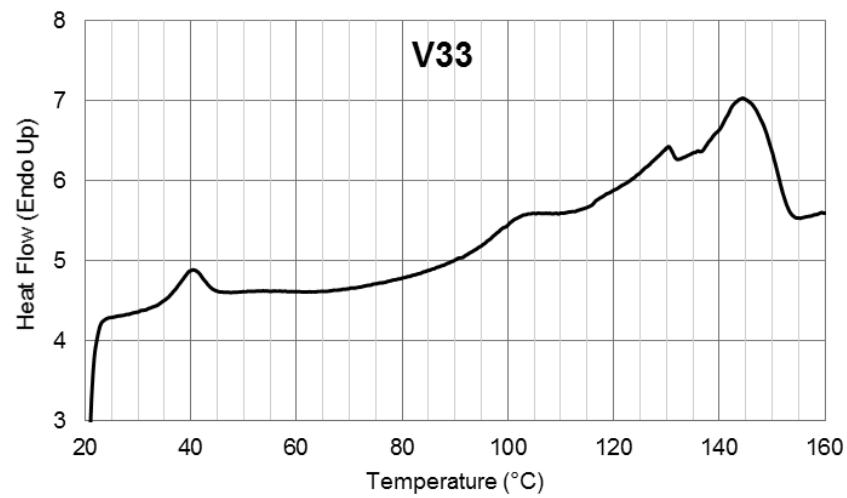
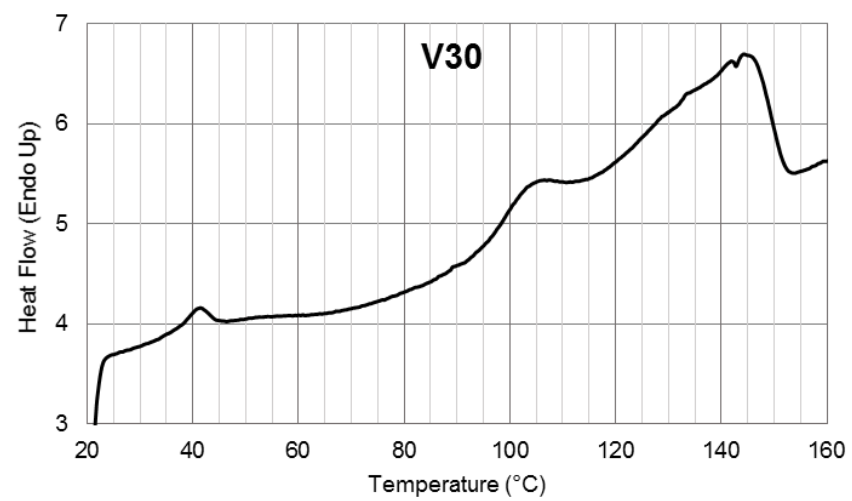
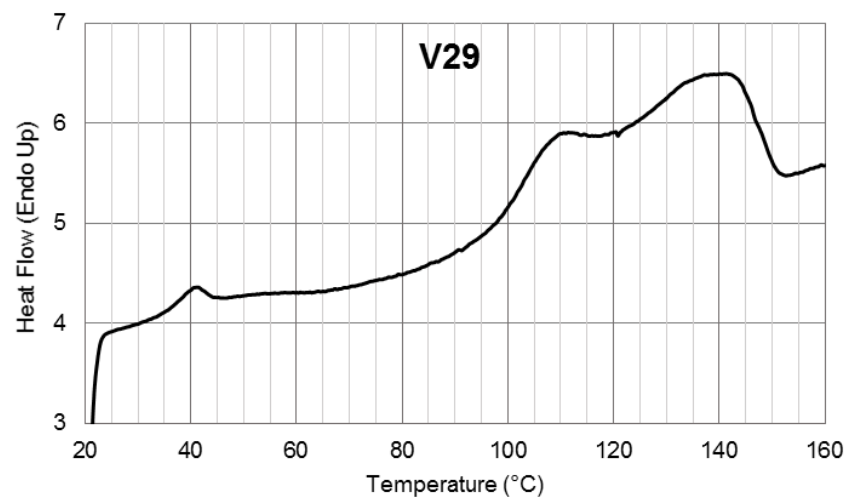
Batch	Specimen No.	Specimen Weight (g)	Work to 50mm (mJ)	Load@50m m (N)
A00	1	1.002	384.119	10.917
A00	2	1.070	435.752	12.526
A00	3	0.989	390.871	11.220
A00	4	1.113	435.846	12.408
A00	5	1.148	481.864	13.889
A00	6	1.056	416.885	11.971
A00	7	1.056	359.937	10.576
A00	8	1.066	446.060	12.731
A00	9	1.071	471.781	13.423
A00	10	1.073	473.882	13.481
A00	11	1.148	504.003	14.227
A00	12	1.031	376.022	10.835
A00	13	1.068	431.360	12.273
A00	14	1.110	459.609	13.074
A00	15	1.102	463.571	13.189
A00	16	1.153	511.455	14.542
A00	17	1.005	400.165	11.415
A00	18	1.047	419.264	11.934
A00	19	1.101	448.568	12.556
A00	20	1.101	433.521	12.326
A00	21	1.167	489.734	13.890
A00	22	1.044	399.643	11.297
A00	23	1.123	457.252	13.127
A00	24	1.126	481.851	13.691
A00	25	1.186	515.728	14.563
A00	26	1.088	440.811	12.736
A00	27	1.109	471.936	13.420
A00	28	1.144	464.691	13.246
A00	29	1.236	531.719	15.065
A02	1	0.989	390.235	11.008
A02	2	1.027	434.382	12.119
A02	3	1.075	454.017	12.837
A02	4	1.162	493.420	13.894
A02	5	1.169	521.983	14.735
A02	6	1.035	446.012	12.697
A02	7	1.073	456.167	12.809

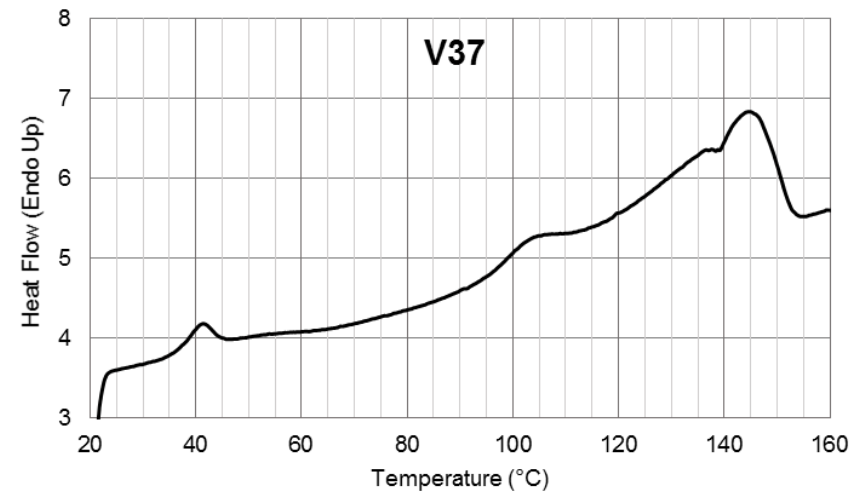
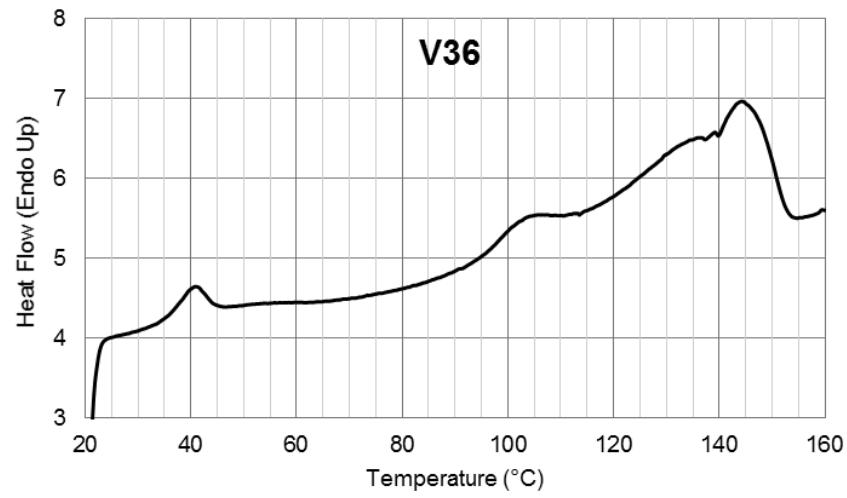
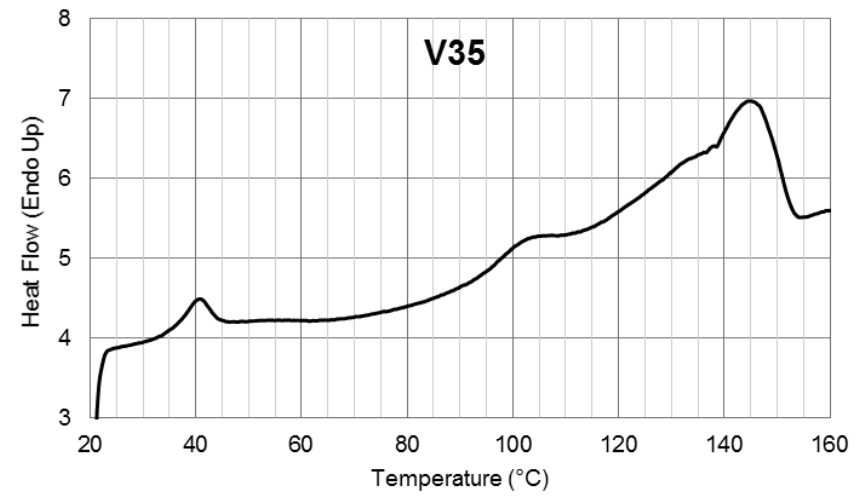
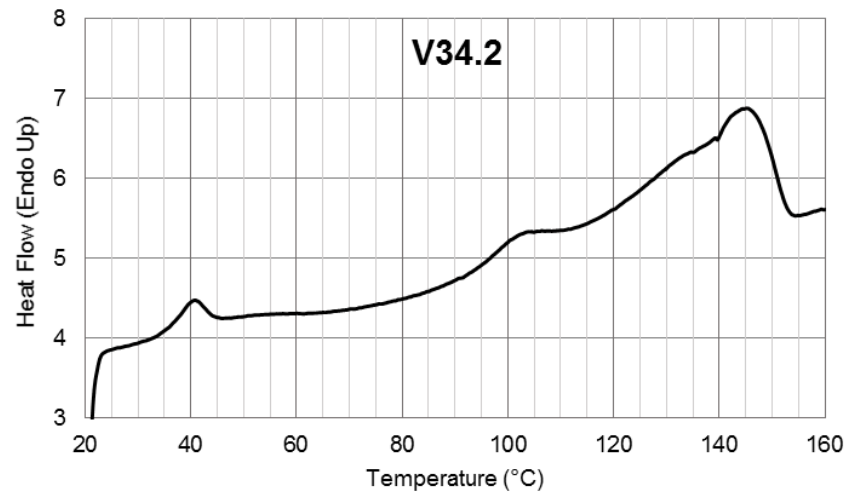
A02	8	1.147	520.800	14.646
A02	9	1.185	588.443	16.468
A02	10	0.990	435.039	12.278
A02	11	1.064	423.101	11.995
A02	12	1.013	419.792	11.947
A02	13	1.129	549.281	15.426
A02	14	1.091	500.618	14.030
A02	15	0.966	381.246	10.748
A02	16	0.981	405.433	11.362
A02	17	1.014	414.195	11.639
A02	18	1.061	482.932	13.586
A02	19	1.016	406.223	11.501
A02	20	1.023	442.786	12.499
A02	21	1.136	492.989	13.837
A02	22	1.095	470.909	13.350
A02	23	1.015	429.835	12.164
A02	24	1.037	409.993	11.690
A02	25	0.978	372.364	10.621
A02	26	1.032	441.607	12.494
A02	27	1.007	420.737	11.937
A02	28	0.938	388.878	11.014
A04	1	0.918	320.328	9.142
A04	2	1.061	440.171	12.482
A04	3	0.939	339.715	9.747
A04	4	0.871	301.483	8.720
A04	5	1.060	476.103	13.466
A04	6	1.113	465.698	13.044
A04	7	0.909	305.966	8.706
A04	8	0.922	315.925	0.001
A04	9	0.975	364.208	10.404
A04	10	1.010	396.442	11.266
A04	11	0.952	335.651	9.591
A04	12	1.014	365.212	10.420
A04	13	0.995	400.865	11.479
A04	14	1.045	423.359	11.979
A04	15	1.111	458.146	12.920
A04	16	0.945	354.974	10.109
A04	17	0.992	383.036	10.904
A04	18	1.079	412.168	0.045
A04	19	1.137	502.114	14.123
A04	20	0.948	312.523	8.911

A04	21	0.962	380.346	10.764
A04	22	0.961	347.444	9.931
A04	23	0.987	370.216	10.480
A04	24	1.060	425.520	12.015
A04	25	1.147	511.565	14.352
A04	26	0.981	355.799	10.178
A04	27	0.992	388.017	10.982
A04	28	0.987	417.013	11.754
A04	29	1.063	504.808	14.221
A04	30	1.137	583.622	16.368

8.4 Viscosity and Particle Size Effects Batches DSC







8.5 Viscosity and Particle Size Effects Oven Sintered Specimens Data

Batch No.	Specimen No.	Weight	Density	Load (N)			Work (J)			Est. Stress (MPa)		
				20mm	100mm	200mm	20mm	100mm	200mm	20mm	100mm	200mm
V34.2	2-1	3.638	1.078	98.605	135.813	157.179	1.446	11.149	25.833	12.157	14.069	5.468
	2-2	3.539	1.079	95.730	131.881	157.628	1.395	10.795	25.309	12.146	14.518	5.484
	2-3	3.658	1.081	98.588	136.204	158.369	1.439	11.145	25.965	12.159	14.138	5.381
	2-4	3.596	1.083	98.406	135.575	160.827	1.461	11.116	26.001	12.334	14.632	5.658
	2-5	3.656	1.083	99.094	135.999	159.080	1.468	11.171	25.887	12.170	14.235	5.635
	2-6	3.433	1.079	96.514	133.286	157.859	1.412	10.868	25.550	12.655	14.988	5.699
	3-1	3.252	1.076	87.008	121.155	145.068	1.282	9.891	23.204	12.110	14.500	5.429
	3-2	3.462	1.077	90.949	126.995	147.565	1.340	10.317	24.159	11.934	13.868	5.319
	3-3	3.570	1.081	92.339	128.093	151.967	1.351	10.486	24.474	11.717	13.901	5.164
	3-4	3.522	1.078	85.842	119.902	146.172	1.255	9.752	23.040	11.086	13.515	4.891
	3-5	3.585	1.080	89.070	123.413	148.406	1.311	10.097	23.681	11.231	13.506	5.052
	3-6	3.336	1.078	85.172	118.120	140.023	1.244	9.664	22.563	11.530	13.668	5.095
V34.1	1-1	3.430	1.100	89.025	125.117	147.014	1.308	10.179	23.749	12.121	14.242	5.277
	1-2	3.553	1.097	91.502	128.489	149.086	1.320	10.424	24.276	11.984	13.905	5.079
	1-3	3.473	1.097	89.541	124.688	145.972	1.332	10.189	23.720	11.897	13.928	5.372
	1-4	3.446	1.096	89.706	125.591	148.096	1.308	10.219	23.827	12.066	14.229	5.256
	1-5	3.441	1.099	87.928	123.092	149.341	1.288	9.995	23.535	11.876	14.409	5.190
	1-6	3.371	1.098	86.627	120.323	139.279	1.271	9.839	22.823	11.839	13.704	5.290
	2-1	3.608	1.096	91.658	126.960	145.515	1.335	10.376	24.028	11.650	13.353	5.078
	2-2	3.339	1.099	89.824	124.482	144.698	1.307	10.169	23.652	12.377	14.387	5.391
	2-3	3.567	1.097	91.935	127.448	149.391	1.332	10.410	24.220	11.840	13.879	5.167
	2-4	3.550	1.093	90.859	125.912	147.491	1.320	10.292	23.970	11.711	13.718	5.107
	2-5	3.649	1.093	89.529	124.477	144.958	1.298	10.129	23.614	11.263	13.116	4.861
	2-6	3.645	1.098	92.983	127.860	150.478	1.380	10.493	24.408	11.635	13.693	5.277

8.6 Viscosity and Particle Size Effects Monolayer Data

Batch	Specimen No.	Specimen Weight (g)	Work to 25mm (mJ)	Load@25 mm
V27	1	0.970	45.558	2.916
V27	2	1.080	52.232	3.275
V27	3	1.030	47.578	2.949
V27	4	1.030	49.322	3.118
V27	5	1.110	57.362	3.555
V27	6	1.120	55.353	3.635
V27	7	1.110	61.644	3.880
V27	8	1.140	59.527	3.714
V27	9	1.070	55.117	3.438
V27	10	1.020	49.367	3.088
V27	11	0.990	45.977	2.861
V27	12	1.000	48.797	3.018
V27	13	1.040	48.422	3.002
V27	14	1.090	59.075	3.659
V27	15	0.970	46.549	2.944
V27	16	0.980	50.331	3.124
V27	17	0.990	48.325	3.034
V27	18	1.020	50.475	3.124
V27	19	0.950	46.989	2.934
V27	20	0.950	49.312	3.070
V27	21	0.970	47.521	2.977
V27	22	1.020	52.585	3.279
V27	23	1.050	53.710	3.667
V27	24	1.100	63.695	4.028
V27	25	1.090	60.359	3.742
V27	26	1.090	60.723	3.758
V28	1	1.160	103.679	6.423
V28	2	1.140	98.745	6.086
V28	3	1.180	95.033	5.955
V28	4	1.070	85.293	5.303
V28	5	1.170	105.330	6.505
V28	6	1.020	77.750	4.851
V28	7	1.140	98.484	6.111
V28	8	1.100	91.720	5.664
V28	9	1.070	86.499	5.340
V28	10	1.020	79.572	4.911

V28	11	1.110	89.690	5.525
V28	12	1.110	89.564	5.558
V28	13	1.150	88.779	5.471
V28	14	1.150	82.547	5.158
V28	15	1.040	72.573	4.524
V28	16	1.020	70.670	4.392
V28	17	1.090	78.562	4.844
V28	18	1.100	83.338	5.105
V28	19	1.030	71.159	4.485
V28	20	1.180	100.472	6.168
V28	21	1.140	88.889	5.557
V28	22	1.090	87.788	5.388
V28	23	1.050	78.450	4.861
V28	24	1.010	76.343	4.758
V28	25	1.180	106.623	6.623
V28	26	1.140	95.188	5.936
V28	27	1.140	91.952	5.706
V28	28	1.080	87.031	5.406
V28	29	1.030	76.228	4.757
V28	30	1.210	114.993	6.975
V30	1	1.140	61.006	3.784
V30	2	1.180	69.465	4.326
V30	3	1.020	41.865	2.583
V30	4	1.050	45.677	2.814
V30	5	1.100	50.303	3.141
V30	6	1.150	57.972	3.604
V30	7	1.160	59.019	3.686
V30	8	1.020	49.634	3.087
V30	9	1.040	51.740	3.207
V30	10	1.050	56.111	3.437
V30	11	1.100	57.324	3.558
V30	12	1.170	63.223	3.948
V30	13	1.170	65.023	4.050
V30	14	1.040	51.246	3.162
V30	15	1.050	55.673	3.451
V30	16	1.060	55.302	3.435
V30	17	1.130	58.400	3.651
V30	18	1.150	64.293	4.022
V30	19	1.190	71.693	4.415
V30	20	1.050	39.619	2.467

V30	21	1.070	38.722	2.484
V30	22	1.070	43.675	2.734
V30	23	1.120	47.995	2.994
V30	24	1.170	50.064	3.135
V30	25	1.210	56.895	3.551
V30	26	1.100	53.183	3.340
V30	27	1.110	53.628	3.364
V30	28	1.040	47.036	2.953
V30	29	1.020	46.436	2.934
V26	1	1.157	168.348	10.134
V26	2	1.256	179.720	10.816
V26	3	1.295	198.770	12.007
V26	4	1.335	195.255	12.377
V26	5	1.206	166.247	10.177
V26	6	1.424	218.730	13.304
V26	7	1.305	192.572	11.810
V26	8	1.344	205.517	12.359
V26	9	1.265	180.943	10.938
V26	10	1.226	171.287	10.455
V26	11	1.176	168.089	10.163
V26	12	1.176	155.421	9.505
V26	13	1.226	170.302	10.426
V26	14	1.196	155.746	9.655
V26	15	1.285	180.453	11.065
V26	16	1.374	203.267	12.334
V26	17	1.404	220.143	13.288
V26	18	1.167	151.441	9.302
V26	19	1.176	155.326	9.473
V26	20	1.196	158.695	9.791
V26	21	1.374	204.437	12.353
V26	22	1.275	172.784	10.542
V26	23	1.433	220.861	13.306
V26	24	1.374	207.206	12.621
V26	25	1.335	192.799	11.596
V26	26	1.285	174.064	10.608
V26	27	1.176	146.802	8.980
V26	28	1.157	149.373	9.201
V26	29	1.186	153.686	9.458
V26	30	1.305	191.699	11.607
V25	1	1.343	218.238	13.135
V25	2	1.160	162.462	9.901
V25	3	1.208	169.926	10.712
V25	4	1.285	196.477	11.804

V25	5	1.304	186.393	11.726
V25	6	1.189	152.568	9.657
V25	7	1.276	182.080	11.324
V25	8	1.304	182.930	11.178
V25	9	1.362	190.146	11.745
V25	10	1.314	196.210	12.138
V25	11	1.256	186.670	11.351
V25	12	1.314	204.872	12.396
V25	13	1.141	163.868	9.889
V25	14	1.208	181.699	10.912
V25	15	1.276	188.324	11.556
V25	16	1.256	200.006	11.771
V25	17	1.314	209.322	12.346
V25	18	1.343	217.348	12.838
V36	1	1.112	196.913	11.671
V36	2	1.178	213.498	12.927
V36	3	1.215	230.861	13.725
V36	4	1.262	245.812	14.603
V36	5	1.318	254.543	15.226
V36	6	1.103	187.271	11.421
V36	7	1.150	204.958	12.352
V36	8	1.187	220.517	13.369
V36	9	1.253	250.338	15.007
V36	10	1.234	252.098	15.050
V36	11	1.112	189.327	11.502
V36	12	1.150	205.377	12.320
V36	13	1.178	207.249	12.650
V36	14	1.243	236.571	14.196
V36	15	1.318	268.606	16.284
V36	16	1.075	192.967	11.698
V36	17	1.122	207.013	12.412
V36	18	1.178	222.859	13.399
V36	19	1.234	238.069	14.454
V36	20	1.281	271.244	16.227
V36	21	1.150	207.229	12.525
V36	22	1.178	223.870	13.457
V36	23	1.215	244.433	14.655
V36	24	1.243	260.246	15.476
V36	25	1.066	184.807	11.128
V36	26	1.056	182.809	11.082
V36	27	1.094	192.249	11.540
V36	28	1.112	206.008	12.342
V36	29	1.253	263.432	15.727

V36	30	1.206	237.163	14.308
V33	1	1.143	262.093	15.459
V33	2	1.354	326.982	19.168
V33	3	1.196	283.649	16.568
V33	4	1.310	291.701	17.526
V33	5	1.178	262.302	15.398
V33	6	1.161	261.388	15.435
V33	7	1.292	305.087	17.953
V33	8	1.205	274.919	16.079
V33	9	1.240	288.675	16.844
V33	10	1.345	328.683	19.269
V33	11	1.310	318.291	18.852
V33	12	1.205	312.207	18.347
V33	13	1.231	301.817	17.911
V33	14	1.205	287.836	16.931
V33	15	1.143	261.772	15.517
V33	16	1.169	255.849	15.450
V33	17	1.205	288.684	16.805
V33	18	1.275	314.782	18.455
V33	19	1.249	297.657	17.749
V33	20	1.345	339.018	19.794
V33	21	1.424	345.914	20.120
V33	22	1.328	321.563	18.911
V33	23	1.284	308.503	18.063
V33	24	1.249	294.947	17.270
V33	25	1.205	276.628	16.462
V33	26	1.134	250.461	14.739
V33	27	1.363	340.415	19.966
V33	28	1.310	311.294	18.368
V33	29	1.240	276.445	16.818
V33	30	1.196	282.061	16.596
V35	1	1.323	316.072	19.162
V35	2	1.253	307.235	18.013
V35	3	1.192	301.260	17.926
V35	4	1.157	290.380	17.101
V35	5	1.306	331.207	19.546
V35	6	1.323	339.485	20.002
V35	7	1.420	353.747	20.990
V35	8	1.306	321.845	18.775
V35	9	1.218	295.134	17.375
V35	10	1.148	273.280	16.235
V35	11	1.201	275.909	17.257
V35	12	1.288	302.494	18.200

V35	13	1.315	317.482	18.735
V35	14	1.402	349.024	20.384
V35	15	1.288	314.602	18.626
V35	16	1.262	290.575	17.335
V35	17	1.157	262.823	15.538
V35	18	1.087	244.698	14.535
V35	19	1.087	215.741	13.589
V35	20	1.411	353.576	20.483
V35	21	1.323	315.745	18.529
V35	22	1.209	291.610	17.195
V35	23	1.280	328.072	19.197
V35	24	1.376	381.109	22.086
V35	25	1.201	292.178	17.285
V35	26	1.218	298.659	17.445
V35	27	1.262	305.372	18.109
V35	28	1.429	365.753	21.696
V35	29	1.306	345.113	20.253
V35	30	1.148	286.388	16.770
V37	1	1.103	206.255	12.515
V37	2	1.141	224.419	13.488
V37	3	1.159	243.766	14.411
V37	4	1.197	252.192	15.063
V37	5	1.206	267.775	15.819
V37	6	1.103	211.687	12.634
V37	7	1.178	229.120	13.631
V37	8	1.159	233.562	13.926
V37	9	1.225	259.577	15.439
V37	10	1.225	260.848	15.643
V37	11	1.122	225.753	13.342
V37	12	1.169	243.465	14.644
V37	13	1.197	262.271	15.539
V37	14	1.262	285.095	16.780
V37	15	1.272	286.483	16.758
V37	16	1.094	218.991	13.039
V37	17	1.131	221.698	13.145
V37	18	1.178	241.081	14.092
V37	19	1.188	251.695	14.837
V37	20	1.225	269.557	15.801
V37	21	1.253	276.210	16.162
V37	22	1.085	212.708	12.641
V37	23	1.159	234.178	13.770
V37	24	1.169	245.673	14.590
V37	25	1.234	263.829	15.743

V37	26	1.066	194.250	11.623
V37	27	1.075	197.645	11.808
V37	28	1.141	215.637	13.004
V37	29	1.188	245.803	14.468
V37	30	1.244	271.682	15.889
V34.1	1	1.168	212.024	12.708
V34.1	2	1.223	232.263	14.154
V34.1	3	1.315	261.820	15.683
V34.1	4	1.361	269.906	16.049
V34.1	5	1.407	292.031	17.268
V34.1	6	1.141	193.975	11.625
V34.1	7	1.177	214.497	12.788
V34.1	8	1.242	236.540	14.201
V34.1	9	1.288	255.034	15.384
V34.1	10	1.371	275.715	16.234
V34.1	11	1.159	209.770	12.542
V34.1	12	1.223	237.077	14.175
V34.1	13	1.251	236.971	14.436
V34.1	14	1.288	278.178	16.455
V34.1	15	1.380	294.262	17.459
V34.1	16	1.187	232.088	13.779
V34.1	17	1.196	231.013	13.897
V34.1	18	1.260	245.536	14.989
V34.1	19	1.288	278.573	16.482
V34.1	20	1.352	298.144	17.681
V34.1	21	1.187	224.927	13.701
V34.1	22	1.260	252.260	15.053
V34.1	23	1.279	259.705	16.061
V34.1	24	1.315	272.344	16.066
V34.1	25	1.352	288.263	16.967
V34.1	26	1.233	230.351	13.725
V34.1	27	1.269	245.113	14.514
V34.1	28	1.288	248.272	15.345
V34.1	29	1.297	262.517	15.611
V34.1	30	1.334	265.964	15.882
V34.2	1	1.138	235.926	14.885
V34.2	2	1.225	263.260	16.196
V34.2	3	1.435	337.206	20.586
V34.2	4	1.146	247.104	14.677
V34.2	5	1.164	256.326	15.130
V34.2	6	1.216	277.982	16.506
V34.2	7	1.304	322.009	19.196
V34.2	8	1.383	344.795	20.236

V34.2	9	1.164	254.226	15.519
V34.2	10	1.155	245.107	14.537
V34.2	11	1.225	276.202	16.888
V34.2	12	1.313	315.999	19.265
V34.2	13	1.146	250.505	15.693
V34.2	14	1.208	259.551	15.558
V34.2	15	1.260	284.074	17.271
V34.2	16	1.304	303.199	18.029
V34.2	17	1.400	332.445	19.795
V34.2	18	1.155	250.303	14.865
V34.2	19	1.225	287.465	16.866
V34.2	20	1.269	303.353	17.970
V34.2	21	1.313	305.301	18.637
V34.2	22	1.365	336.774	19.788
V34.2	23	1.173	263.877	15.785
V34.2	24	1.120	241.326	14.533
V34.2	25	1.260	291.802	17.278
V34.2	26	1.269	306.975	18.357
V34.2	27	1.348	336.180	19.605
V34.2	28	1.243	288.121	17.167
V34.2	29	1.330	313.537	18.600
V34.2	30	1.348	324.137	18.953

8.7 Results of Regression Viscosity and PSD Study Monolayer Data

Regression Analysis: Work to 25mm versus MFR (g/10min), Specific Surface (m²/kg), Specimen Weight (g)

Analysis of Variance

Source	DF	Adj SS	Adj MS	F-Value	P-Value
Regression	3	2660984	886995	2723.20	0.000
MFR (g/10min)	1	40154	40154	123.28	0.000
Specific Surface (m ² /kg)	1	507116	507116	1556.92	0.000
Specimen Weight (g)	1	138972	138972	426.67	0.000
Error	291	94784	326		
Lack-of-Fit	181	87472	483	7.27	0.000
Pure Error	110	7312	66		
Total	294	2755768			

Model Summary

S	R-sq	R-sq(adj)	R-sq(pred)
18.0476	96.56%	96.53%	96.47%

Coefficients

Term	Coef	SE Coef	T-Value	P-Value	VIF
Constant	-538.5	13.5	-39.91	0.000	
MFR (g/10min)	2.422	0.218	11.10	0.000	2.80
Specific Surface (m ² /kg)	2.8844	0.0731	39.46	0.000	2.01
Specimen Weight (g)	281.4	13.6	20.66	0.000	1.92

Regression Equation

$$\text{Work to 25mm (mJ)} = -538.5 + 2.422 \text{ MFR (g/10min)} \\ + 2.8844 \text{ Specific Surface (m}^2\text{/kg)} \\ + 281.4 \text{ Specimen Weight (g)}$$

Residual Plots for Work to 25mm (mJ)

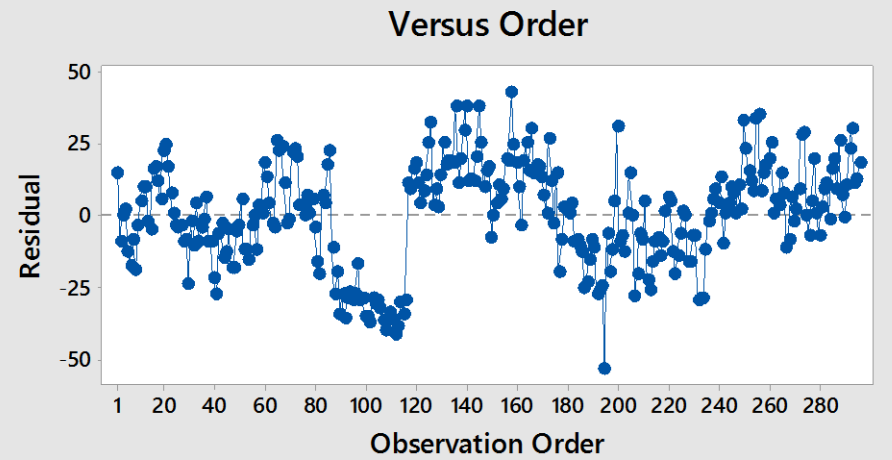
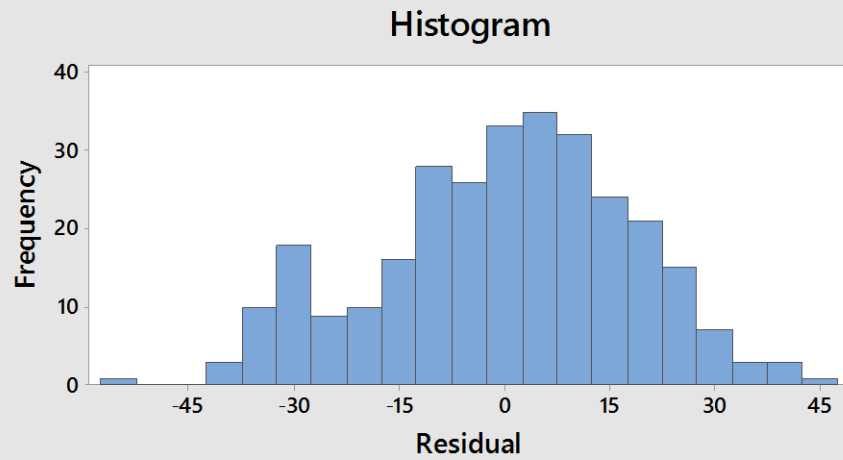
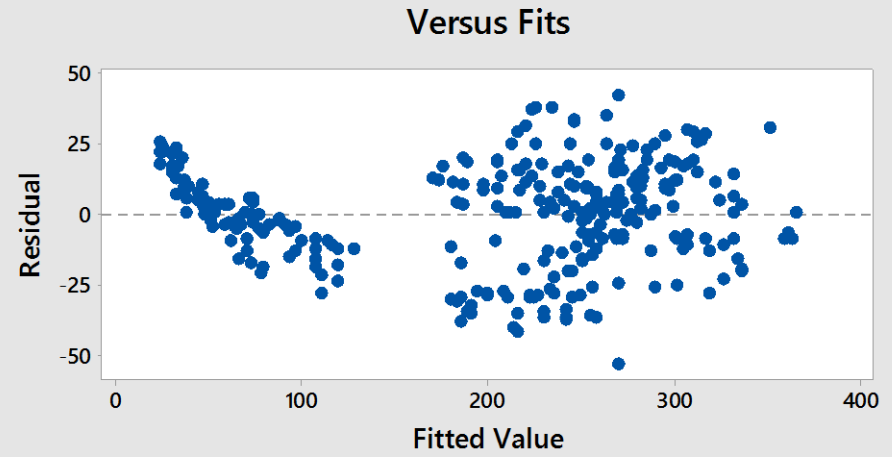
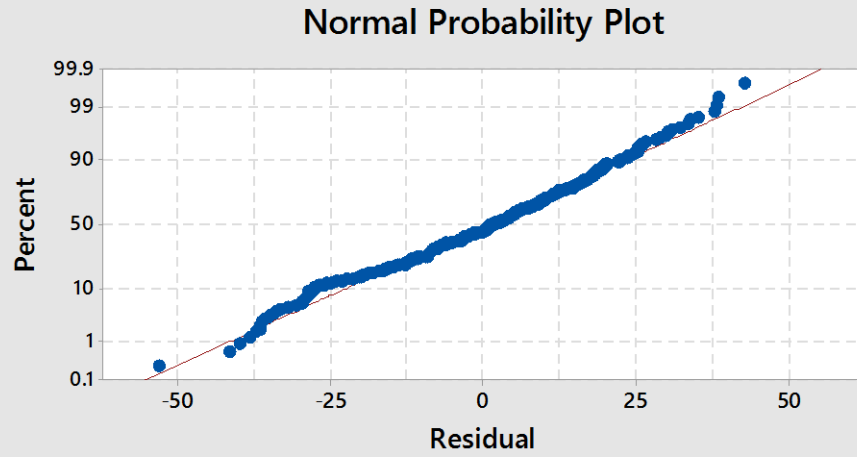


Figure 8.1: Combined Residuals plots for linear regression of Viscosity and PSD study monolayer data.

9 References

- ARGENTO, C., JAGOTA, A. & CARTER, W. 1997. Surface formulation for molecular interactions of macroscopic bodies. *Journal of the Mechanics and Physics of Solids*, 45, 1161-1183.
- BASF. Elastollan® C85A TPU Technical Data Sheet. 2015. Available: www.elastollan.basf.us/pdf/1190A.pdf.
- BELLEHUMEUR, C., BISARIA, M. & VLACHOPOULOS, J. 1996. An experimental study and model assessment of polymer sintering. *Polymer Engineering & Science*, 36, 2198-2207.
- BELLEHUMEUR, C. T., KONTOPOULOU, M. & VLACHOPOULOS, J. 1998. The role of viscoelasticity in polymer sintering. *Rheologica acta*, 37, 270-278.
- CASTRO, A., HENTSCHEL, P., BRODOWSKI, W. & PLUMMER, T. 1985. Influence of Processing Conditions on Mechanical Properties of High Performance CHDI Based TPUs. *Journal of elastomers and plastics*, 17, 238-248.
- CHILDS, T., BERZINS, M., RYDER, G. & TONTOWI, A. 1999. Selective laser sintering of an amorphous polymer—simulations and experiments. *Proceedings of the Institution of Mechanical Engineers, Part B: Journal of Engineering Manufacture*, 213, 333-349.
- CHILDS, T. & TONTOWI, A. 2001. Selective laser sintering of a crystalline and a glass-filled crystalline polymer: experiments and simulations. *Proceedings of the Institution of Mechanical Engineers, Part B: Journal of Engineering Manufacture*, 215, 1481-1495.
- CONVENTION, U. S. P. 2012. <616> Bulk and Tapped Density [Online]. Available: http://www.usp.org/sites/default/files/usp_pdf/EN/USPNF/visions/m99375-bulk_density_and_tapped_density_of_powders.pdf.
- CRAWFORD, R. J. & KEARNS, M. P. 2003. *Practical Guide to Rotational Moulding*, Rapra Technology Limited.
- D-06, A. Standard Test Method of Unconfined Compressive Strength of Cohesive Soil. Astm Int'L.
- D-11, A. Standard Test Method for Vulcanized Rubber and Thermoplastic Elastomers-Tension. Astm Int'L.
- D-13, A. Standard Test Method for Breaking Strength and Elongation of Textile Webbing, Tape and Braided Material. Astm Int'L.
- D-18, A. Standard Test Method for Shear Testing of Bulk Solids Using the Jenike Shear Cell. Astm Int'L.
- D-20, A. Standard Test Methods for Apparent Density, Bulk Factor, and Pourability of Plastic Materials.
- DROBNY, J. 2007. *Handbook of Thermoplastic Elastomers*, William Andrew Inc. Norwich, NY.
- DRUMMER, D., RIETZEL, D. & KÜHNLEIN, F. 2010. Development of a characterization approach for the sintering behavior of new thermoplastics for selective laser sintering. *Physics Procedia*, 5, 533-542.

- ECKERSLEY, S. T. & RUDIN, A. 1990. Mechanism of film formation from polymer latexes. *JCT, Journal of coatings technology*, 62, 89-100.
- EHRENSTEIN, G. W. 2012. *Polymeric materials: structure, properties, applications*, Carl Hanser Verlag GmbH Co KG.
- FANG, Z. Z. 2010. *Sintering of advanced materials*, Elsevier.
- FRENKEL, Y. I. 1945. *Kineticheskaya teoriya zhidkosti* (Kinetic Theory of Liquids), Moscow: Akad. Nauk SSSR.
- GIBSON, I. & SHI, D. 1997. Material properties and fabrication parameters in selective laser sintering process. *Rapid Prototyping Journal*, 3, 129-136.
- GOODRIDGE, R., TUCK, C. & HAGUE, R. 2012. Laser sintering of polyamides and other polymers. *Progress in Materials Science*, 57, 229-267.
- HERRERA, M., MATUSCHEK, G. & KETTRUP, A. 2002. Thermal degradation of thermoplastic polyurethane elastomers (TPU) based on MDI. *Polymer degradation and stability*, 78, 323-331.
- HERRING, C. 1950. Effect of change of scale on sintering phenomena. *Journal of Applied Physics*, 21, 301-303.
- HESKETH, T., VAN BOGART, J. & COOPER, S. 1980. Differential scanning calorimetry analysis of morphological changes in segmented elastomers. *Polymer Engineering & Science*, 20, 190-197.
- HUI, C.-Y., BANEY, J. & KRAMER, E. 1998. Contact mechanics and adhesion of viscoelastic spheres. *Langmuir*, 14, 6570-6578.
- INDUSTRIES, E. 2015. SIPERNAT® specialty silica and AEROSIL® fumed silica as flow aid and anticaking agent. Technical Information TI 1351.
- JAGOTA, A., ARGENTO, C. & MAZUR, S. 1998. Growth of adhesive contacts for Maxwell viscoelastic spheres. *Journal of applied physics*, 83, 250-259.
- JENIKE, A. W. 1964. Storage and flow of solids, bulletin no. 123. *Bulletin of the University of Utah*, 53.
- JOHNSON, K., KENDALL, K. & ROBERTS, A. Surface energy and the contact of elastic solids. *Proceedings of the Royal Society of London A: Mathematical, Physical and Engineering Sciences*, 1971. The Royal Society, 301-313.
- JONES, R. 2003. From single particle AFM studies of adhesion and friction to bulk flow: forging the links. *Granular Matter*, 4, 191-204.
- KELLNER, T. 2013. Jet Engine Bracket From Indonesia Wins 3D Printing Challenge.
- KOBERSTEIN, J. T. & RUSSELL, T. P. 1986. Simultaneous SAXS-DSC study of multiple endothermic behavior in polyether-based polyurethane block copolymers. *Macromolecules*, 19, 714-720.
- KONTOPOULOU, M. & VLACHOPOULOS, J. 1999. Bubble dissolution in molten polymers and its role in rotational molding. *Polymer Engineering & Science*, 39, 1189-1198.
- KRUTH, J.-P., LEVY, G., KLOCKE, F. & CHILDS, T. 2007. Consolidation phenomena in laser and powder-bed based layered manufacturing. *CIRP Annals-Manufacturing Technology*, 56, 730-759.
- KUCZYNSKI, G., NEUVILLE, B. & TONER, H. 1970. Study of sintering of poly (methyl methacrylate). *Journal of Applied Polymer Science*, 14, 2069-2077.
- LI, C., WANG, Y., ZHAN, H., HAN, T., HAN, B. & ZHAO, W. 2010. Three-dimensional finite element analysis of temperatures and stresses in wide-band laser surface melting processing. *Materials & Design*, 31, 3366-3373.

- LI, Q., RUDOLPH, V., WEIGL, B. & EARL, A. 2004. Interparticle van der Waals force in powder flowability and compactibility. *International journal of pharmaceutics*, 280, 77-93.
- LIN, Y., HUI, C. & JAGOTA, A. 2001. The role of viscoelastic adhesive contact in the sintering of polymeric particles. *Journal of colloid and interface science*, 237, 267-282.
- LONTZ, J. 1964. Sintering of polymer material. Fundamental phenomena in the material sciences, Vol. 1, Bonis and Hausner ed. Plenum Press, New-York.
- MAZUR, S. 1995. Coalescence of polymer particles. *Polymer powder technology*, 157.
- MAZUR, S. & PLAZEK, D. J. 1994. Viscoelastic effects in the coalescence of polymer particles. *Progress in organic coatings*, 24, 225-236.
- MCGLINCHEY, D. 2008. *Bulk Solids Handling*, Wiley-Blackwell.
- MILNER, S. T. Early stages of spreading and sintering.
- MULLER, J.-D., LAMNAWAR, K. & MAZOUZ, A. 2012. Relationship between rheological and surface properties for the sintering process of polymers. *Journal of Materials Science*, 47, 121-131.
- PLUMMER, K., VASQUEZ, M., MAJEWSKI, C. & HOPKINSON, N. 2012. Study into the recyclability of a thermoplastic polyurethane powder for use in laser sintering. *Proceedings of the Institution of Mechanical Engineers, Part B: Journal of Engineering Manufacture*, 226, 1127-1135.
- POKLUDA, O., BELLEHUMEUR, C. T. & VLACHOPOULOS, J. 1997. Modification of Frenkel's model for sintering. *AIChE journal*, 43, 3253-3256.
- PRISACARIU, C. 2011. *Polyurethane elastomers: from morphology to mechanical aspects*, Springer Science & Business Media.
- RIETZEL, D., DREXLER, M., KÜHNLEIN, F. & DRUMMER, D. Influence of temperature fields on the processing of polymer powders by means of laser and mask sintering technology. *Proceedings of the Solid Freeform Fabrication Symposium*, 2011. 252-262.
- ROSENZWEIG, N. & NARKIS, M. 1980. Coalescence phenomenology of spherical polymer particles by sintering. *Polymer*, 21, 988-989.
- SAIANI, A., DAUNCH, W., VERBEKE, H., LEENSLAG, J.-W. & HIGGINS, J. 2001. Origin of multiple melting endotherms in a high hard block content polyurethane. 1. Thermodynamic investigation. *Macromolecules*, 34, 9059-9068.
- SCHAPERY, R. 1989. On the mechanics of crack closing and bonding in linear viscoelastic media. *International Journal of Fracture*, 39, 163-189.
- SCHULTZ, J. P. 2004. *Modeling heat transfer and densification during laser sintering of viscoelastic polymers*. Virginia Polytechnic Institute and State University.
- SCHULZE, D. 2007. *Powders and bulk solids: behavior, characterization, storage and flow*, Springer Science & Business Media.
- SCRIBBEN, E., BAIRD, D. & WAPPEROM, P. 2006. The role of transient rheology in polymeric sintering. *Rheologica acta*, 45, 825-839.
- SCRIBBEN, E., EBERLE, A. P. & BAIRD, D. G. 2005. Viscoelastic coalescence of thermotropic liquid crystalline polymers: The role of transient rheology. *Journal of Rheology (1978-present)*, 49, 1159-1175.
- SEYMOUR, R. W. & COOPER, S. L. 1973. Thermal analysis of polyurethane block polymers. *Macromolecules*, 6, 48-53.

- SHALER, A., ESHELBY, J. D. 1949. Seminar on the kinetics of sintering. *Transactions of the American Institute of Mining and Metallurgical Engineers*, 185, 796-813.
- SUN, M., NELSON, J. C., BEAMAN, J. J. & BARLOW, J. A model for partial viscous sintering. *Proceedings of the solid freeform fabrication symposium*, 1991. 46-55.
- TOMAS, J. & KLEINSCHMIDT, S. 2009. Improvement of flowability of fine cohesive powders by flow additives. *Chemical engineering & technology*, 32, 1470.
- VAN BOGART, J., BLUEMKE, D. & COOPER, S. 1981. Annealing-induced morphological changes in segmented elastomers. *Polymer*, 22, 1428-1438.
- VAN KREVELLEN, D. W. & TE NIJENHUIS, K. 2009. *Properties of polymers: their correlation with chemical structure; their numerical estimation and prediction from additive group contributions*, Elsevier.
- VASQUEZ, G., MAJEWSKI, C., HAWORTH, B. & HOPKINSON, N. 2014. A targeted material selection process for polymers in laser sintering. *Additive Manufacturing*, 1, 127-138.
- VASQUEZ, M. 2012. *Analysis and development of new materials for polymer laser sintering*. © Mike Vasquez.
- VELANKAR, S. & COOPER, S. L. 1998. Microphase separation and rheological properties of polyurethane melts. 1. Effect of block length. *Macromolecules*, 31, 9181-9192.
- WENDEL, B., RIETZEL, D., KÜHNLEIN, F., FEULNER, R., HÜLDER, G. & SCHMACHTENBERG, E. 2008. Additive processing of polymers. *Macromolecular materials and engineering*, 293, 799-809.
- WILLIAMS, J. D. & DECKARD, C. R. 1998. Advances in modeling the effects of selected parameters on the SLS process. *Rapid Prototyping Journal*, 4, 90-100.
- YAMASAKI, S., NISHIGUCHI, D., KOJIO, K. & FURUKAWA, M. 2007. Effects of aggregation structure on rheological properties of thermoplastic polyurethanes. *Polymer*, 48, 4793-4803.
- YOON, P. J. & HAN, C. D. 2000. Effect of thermal history on the rheological behavior of thermoplastic polyurethanes. *Macromolecules*, 33, 2171-2183.
- ZIEGELMEIER, S., CHRISTOU, P., WÖLLECKE, F., TUCK, C., GOODRIDGE, R., HAGUE, R., KRAMPE, E. & WINTERMANTEL, E. 2015. An experimental study into the effects of bulk and flow behaviour of laser sintering polymer powders on resulting part properties. *Journal of Materials Processing Technology*, 215, 239-250.
- ZIEGELMEIER, S., WÖLLECKE, F., TUCK, C. J., GOODRIDGE, R. D. & HAGUE, R. J. 2014. Aging behavior of thermoplastic elastomers in the laser sintering process. *Journal of Materials Research*, 29, 1841.